Defect passivation in zinc tin oxide: improving the transparency-conductivity trade-off and comparing with indium-based materials

Thèse N° 9318

Présentée le 14 février 2019

à la Faculté des sciences et techniques de l'ingénieur
Laboratoire de photovoltaïque et couches minces électroniques
Programme doctoral en physique

pour l'obtention du grade de Docteur ès Sciences

par

Oscar Esteban RUCAVADO LEANDRO

Acceptée sur proposition du jury

Prof. R. Houdré, président du jury
Prof. C. Ballif, Dr M. Morales Masis, directeurs de thèse
Dr D. Urban , rapporteur
Dr T. Jager, rapporteur
Dr S. Siol, rapporteur

2019

ÉCOLE POLYTECHNIQUE
FÉDÉRALE DE LAUSANNE

"Crystals are like people
it is the defects in them which tend to make them interesting."
— C.J. Humphreys

Acknowledgements

It is finally over! After four years of hard work, the doctoral thesis is finished. This dissertation would not have been possible without the collaboration of many people, and in the next paragraphs I will do my best effort to express my gratitude to the people directly and indirectly involved.

First, I would like to thank my thesis director, Prof. Christophe Ballif for giving me the opportunity to work at PV-Lab. His teachings in the field of solar cells (spanning from solid-state physics to the global picture of the energy market) and his guidance during these four years were key for the full development of this dissertation. Next, I would like to thank my co-supervisor Dr. Monica Morales-Masis, for believing in my competences and for giving me the opportunity to work the TCO-group (long-live the TCO-group). The DisCo-project and this thesis were only possible because of her scientific cleverness, her daily dedication and her motivation. She is a role model for any young ambitious scientist. In addition, I would like to thank Dr. Daniel Urban, Dr. Sebastial Siol, and Dr. Timo Jäger for agreeing to form the scientific jury of this dissertation, and for reviewing and improving the thesis document. I want to thank Prof. Romuald Houré for chairing the committee of the examination.

I would like to thank Dr. Quentin Jeangros, Dr. Mathieu Boccard and Dr. Aïcha Hessler-Wysser for their support and dedication, regarding scientific and non-scientific issues during these intense four year-period. I would like to thank Dr. Daniel Urban, Dr. José A. Flores-Livas and Miglė Graužinytė for the great discussions in these years which lead to fruitful cooperations. I would like to acknowledge Dr. Takashi Koida for hosting me, sharing his knowledge and for introducing me in a couple of weeks to Japanese traditions, which concluded in very fruitful cooperation. I would like to acknowledge the institution that financed the DisCo project, the Swiss National Found (SNF).

Overall, I would like to thank my colleagues of PVLab for creating an ideal atmosphere which lead to time full of nice moments and fruitful collaborations these four years. In particular I want to acknowledge my fellow Ph.D. students with whom I shared great and the not-so-great moments. Josua, Jérémie, Janina, Flo, Mario, LucaA, LucaG, Ele, Fede, Lionel, Marina, Jordan, Laurie-Lou, Arnaud and Samira. In addition, I want to acknowledge Jean, for all his help these years, for the crazy-Jean-activities, for the MAD activities and for enabling a great office atmosphere. In particular I want to thank Ana and Gizem for sharing with me this great experience, giving me their advice, and above all, thank you for your honest friendship. I also want to express my admiration and gratitude for the Post-docs who accompanied me these years: Olivier, Fan, Sihua, Matthias, AndreaI and Terry. I want show my gratitude to Jan and Angela, with whom I shared a great time, scientifically and otherwise. I want to acknowledge the excellent work performed by the technicians and the administratives from PVLAB: Cedric, Aymeric, Xavier, Frank, Nathanael, Sylvain, Raphaël, Karine, Hassan and Mary-Claude without them the lab would not function as smoothly as it does now.

I want to acknowledge my friends outside PVLab, Juan, Cecilia, Vincent et Nicole, Esteban and Dani: thanks for the unforgettable time, the joy, the nice moments, all the cheese, the meat and the wine! Back in Costa Rica I would like to thank all the people who supported me from the distance. To my friends, whom I always accompanied me in these times, the "Chonete-group" and the "chiwiLegal-group". My family was always present for me, both my molecular- and my nuclear-family. Thanks to all the aunts, uncles, cousins who came to visit me in Neuch, you have no idea how much I enjoyed our time together. I would like to thank my nuclear family, mom, dad and brother! My mother Rita and my father Oscar, you gave me the basic survival-kit of values for to overcome difficulties and face responsibilities; for that I will be always great full. Last, I would like share my gratitude towards Antonella. Her constant support, patience and friendship made the difficult times easier to cope and the fun parts more enjoyable. Sharing these time with you is the source of my happiness and motivation in my life.

Neuchâtel, December 2018 Esteban Rucavado

Abstract

Transparent conductive oxides (TCOs) are essential in technologies coupling light with electricity. Due to its good optoelectronic properties and its production scalability, tin-doped indium oxide (In_2O_3:Sn) is the preferred TCO in industrial applications. Nonetheless indium is scarce in the Earth's crust and its availability might be compromised over the next decades. To address this issue, this doctoral project aims to (i) improve the optoelectronic properties of indium-free TCOs seeking to match those of In_2O_3:Sn, and to (ii) refine the optoelectronic properties of In_2O_3-based films to decrease the indium consumption in applications. To accomplish this, we investigated the links between the defects, the microstructure and the optoelectronic properties of amorphous zinc tin oxide (a-ZTO) and zirconium-doped indium oxide (In_2O_3:Zr).
First, we studied the evolution in the optoelectronic properties and microstructure of a-ZTO when annealed up to 500 °C in oxidizing, neutral, and reducing atmospheres. We show that annealing under atmospheric pressure at temperatures > 300 °C decreases detrimental subgap absorptance while increasing electron mobility (μ_e). Thermal treatments in reducing atmospheres increase free-carrier density (N_e) and detrimental subgap absorptance. None of the thermal treatments resulted in important changes in the amorphous microstructure. Combining these results and density functional theory (DFT) calculations, oxygen deficiencies (V_O) were identified as the source of detrimental subgap absorption. V_O can act as donors but also as electron-scattering and absorption centres. Based on these results, a-ZTO with μ_e of up to 35 $cm^2V^{-1}s^{-1}$, is demonstrated by high-temperature defect passivation. Profiting from its the microstructural stability, a-ZTO was used as a recombination junction in a tandem solar cell that requires a high-temperature step in its processing.
This high-temperature passivation scheme might be problematic for temperature-sensitive technologies. Therefore, we demonstrated an alternative low-temperature passivation method, which relies on co-sputtering a-ZTO with SiO_2 . Using a-ZTO and SnO_2 —two tin-based oxides with different compositions and microstructures—and the results of DFT calculations, we demonstrate that SiO_2 contribution is twofold—(i) The oxygen from SiO_2 passivates the V_O in SnO_2 and a-ZTO. (ii) The formation energy of the ionized V_O ($V_O^{\bullet\bullet}$) is lowered by the silicon atoms, enabling defects that do not contribute to the subgap absorptance. This passivation scheme improves the optical properties without affecting the electrical conductivity (σ), overcoming the optoelectronic trade-off in tin-based TCOs. Finally, we study an indium-based high μ_e TCO: zirconium-doped In_2O_3. Films of In_2O_3:Zr with thicknesses ranging from 15

nm to 100 nm were sputtered in the amorphous state and annealed in different atmospheres. Annealing in air yields fully crystalline films with high transparency and a high μ_e limited by phonon and ionized impurity scattering. 15-nm-thick films exhibit an average absorptance of $< 0.5\%$ (between 390 nm and 2000 nm) and a μ_e of 50 $\mathrm{cm^2V^{-1}s^{-1}}$ increasing to 105 $\mathrm{cm^2V^{-1}s^{-1}}$ for 100-nm-thick films. Alternatively, annealing in a neutral or reducing atmosphere results in higher σ for films thinner than 50 nm as a high N_e is maintained. The reduction in thickness while keeping high lateral σ makes In_2O_3:Zr an alternative to reduce indium in applications such as flexible displays, solar cells and light-emitting diodes. As a proof of concept we applied 40-nm-thick In_2O_3:Zr layer as the front TCO in silicon heterojunction solar cells. The reduction in thickness and the introduction of a secondary anti-reflective coating result in cells with a higher photogenerated current than cells with standard electrodes, while decreasing the use of indium in the device.

Keywords: Transparent conductive oxide, dopants, electron mobility, defects, free-carrier density, electron transport, free-carrier absorption, bandgap, sub-bandgap defect, ionized impurity, phonon scattering.

Résumé

Les oxydes conducteurs transparents (TCO) sont essentiels dans les technologies couplant lumière et électricité. En raison de ses bonnes propriétés optoélectroniques et de sa facilité d'extensibilité, l'oxyde d'indium dopé à l'étain (In_2O_3 :Sn) est le TCO le plus utilisé dans les applications industrielles. Néanmoins, l'indium est un élément rare dans la croûte terrestre et sa disponibilité pourrait être compromise au cours des prochaines décennies. Pour répondre à ce problème, ce projet de doctorat vise à (i) améliorer les propriétés optoélectroniques des TCO sans indium, afin d'égaler les propriétés du In_2O_3 :Sn et (ii) affiner les propriétés optoélectroniques des films à base d'In_2O_3, afin de réduire la consommation d'In dans les TCO et leurs applications. Pour ce faire, nous avons étudié les liens entre les défauts, la microstructure et les propriétés optoélectroniques de l'oxyde amorphe de zinc-étain (a-ZTO) et de l'oxyde de indium dopé au zirconium. Tout d'abord, nous avons étudié l'évolution des propriétés optoélectroniques et de la microstructure de l'a-ZTO lorsqu'il est recuit jusqu'à 500 °C en atmosphères oxydantes, neutres et riches en hydrogène. Nous montrons qu'un recuit à pression atmosphérique à des températures de plus de 300 °C diminue l'absorption intra-bande nuisible aux propriétés optiques tout en augmentant la mobilité des électrons (μ_e). Les traitements thermiques en atmosphère réductrice augmentent la densité des porteurs libres (N_e) et l'absorptivité intra-bande. Aucun des traitements thermiques n'a entraîné d'importante modification de la microstructure amorphe. En combinant ces résultats et les calculs de la théorie fonctionnelle de densité (DFT), les vacances d'oxygène ($\mathrm{V_O}$) ont été identifiées comme étant la source d'absorption intra-bande préjudiciable. Une $\mathrm{V_O}$ peut agir comme donneur mais aussi comme centre de diffusion d'électrons. Sur la base de ces résultats, a-ZTO présentant des μ_e allant jusqu'à 35 $cm^2V^{-1}s^{-1}$, est démontré par une passivation de défaut à haute température. Profitant de la stabilité à haute température de l'a-ZTO, ce matériau a été utilisé en tant que jonction de recombinaison dans une cellule solaire tandem qui nécessite une étape à haute température durant sa fabrication.

Cette méthode de passivation à haute température pourrait être problématique pour les technologies sensibles à de telles températures. C'est pourquoi nous avons également fait la démonstration d'une méthode alternative de passivation à basse température, qui repose sur la co-pulvérisation de a-ZTO avec du dioxyde de silicium (SiO_2). En utilisant deux oxydes à base de Sn, de composition et de microstructures différentes : a-ZTO et SnO_2 , et les résultats des calculs DFT, nous démontrons que la contribution de SiO_2 est double. (i) L'oxygène du

SiO_2 passive les V_O le SnO_2 et a-ZTO. (ii) L'énergie de formation du V_O ionisé ($V_O^{\bullet\bullet}$) est abaissée par les atomes de silicium, ce qui permet l'existence de défauts ne contribuant pas à l'absorptivité intra-bande. Ce schéma de passivation améliore les propriétés optiques sans affecter la conductivité électrique, surmontant ainsi le compromis optoélectronique des TCOs à base d'Sn.

Enfin, nous étudions un TCO à base d'In haute μ_e :In_2O_3 dopé au Zr. Des films d'In_2O_3 :Zr d'une épaisseur de 15 nm à 100 nm ont été pulvérisés à l'état amorphe et recuits dans différentes atmosphères. Le recuit à l'air permet d'obtenir des films entièrement cristallins à haute transparence et à haute μ_e limitée par la diffusion de phonons et d'impuretés ionisées. Les films de 15 nm d'épaisseur présentent une absorbance moyenne inférieure à 0,5% (entre 390 nm - 2000 nm) et un μ_e de 50 $cm^2V^{-1}s^{-1}$, passant à 105 $cm^2V^{-1}s^{-1}$ pour les films de 100 nm d'épaisseur. Alternativement, le recuit dans une atmosphère neutre ou réductrice entraîne une conductivité plus élevée pour des films d'une épaisseur inférieure à 50 nm, car une N_e élevé est maintenu. La démonstration de la réduction de l'épaisseur tout en conservant une conductivité latérale élevée dans une couche de In_2O_3 :Zr constitue une alternative pour réduire l'In dans des applications telles que les écrans flexibles, les cellules solaires et les diodes électroluminescentes. Pour démontrer le concept, nous avons appliqué une couche de 40 nm de In_2O_3 :Zr comme TCO frontal dans des cellules solaires à hétérojonction de silicium. La réduction de l'épaisseur permet d'obtenir des cellules solaires avec un courant photogénéré plus élevé que les cellules avec des électrodes d'épaisseur standard, tout en diminuant l'utilisation d'indium.

Contents

Acknowledgements **v**

Abstract (English/Français) **vii**

List of figures **xv**

List of tables **xxvi**

1 Introduction **1**

1.1 What are transparent conductive oxides? 1

1.2 Fundamental properties of transparent conductive oxides 2

1.2.1 Electron transport in TCOs and mobility limiting mechanisms 3

1.2.2 Defects in crystalline and amorphous materials 4

1.2.3 Dopants in transparent conductive oxides 12

1.2.4 Effect of dopants on the optical properties of TCOs 14

1.2.5 Interband transitions, Burstein-Moss shift and optical bandgap in TCOs 16

1.2.6 Summary of TCO properties 20

1.2.7 Transparent conductive oxide design for silicon heterojunction photovoltaics 25

1.3 This Thesis 28

1.3.1 Thesis outline 28

1.3.2 Contribution to the field 29

2 Thin-film fabrication and characterization techniques 33

2.1 Radio frequency magnetron sputtering 33

2.1.1 Thin-film growth and co-sputtering 34

2.2 Electrical properties 35

2.2.1 Hall effect in the van der Pauw configuration 35

2.3 Optical properties 38

2.3.1 Ultraviolet-visible-near infrared spectrophotometry 38

2.3.2 Fourier transform infrared spectrometer 39

2.4 Structural and chemical properties 40

2.4.1 Transmission electron microscopy and energy dispersive X-ray spectroscopy 40

2.4.2 Electron diffraction 40

2.4.3 Thermal desorption spectroscopy 40

2.4.4 Rutherford backscattering and elastic recoil detection analysis 41

3 Defects and high-temperature defect-passivation of amorphous zinc tin oxide 43

3.1 Motivation and state of the art 44

3.2 Methods 46

3.2.1 Computational Methods. 47

3.3 Electrical properties: Hall mobility and free-carrier density 49

3.4 Effect of thermal treatments on the optical properties of a-ZTO 50

3.5 Film Composition and Microstructure 53

3.5.1 Rutherford backscattering and electron recoil detection analysis 53

3.5.2 Nanobeam diffraction and fluctuation electron microscopy 53

3.5.3 Thermal Desorption Spectroscopy on a-ZTO 55

3.6 Electron scattering mechanisms 57

3.7 Calculations and correlation with experimental results 59

3.7.1 Correlation with optoelectronic properties 61

3.8 A-ZTO as recombination junction for perovskite/Silicon monolithic tandem solar cells 63

3.9 Conclusion 66

4 Alternative low-temperature passivation route for Sn-based oxides 67

4.1 Motivation and state of the art 68

4.2 Methods 69

4.2.1 Experimental details 69

4.2.2 Computational methods 70

4.3 Trade-off in optoelectronic properties of a-ZTO 71

4.4 Co-deposition of SiO_2 and Sn-based TCOs 71

4.4.1 Reducing sub-bandgap absorption in a-ZTO thin films 72

4.4.2 SiZTO microstructure and composition 73

4.4.3 Addition of SiO_2 to SnO_2 78

4.4.4 $SiSnO_2$ microstructure and composition 79

4.4.5 A general process for Sn-based films 81

4.5 Si-modification to SnO_2 81

4.5.1 Oxygen vacancies 82

4.5.2 Addition of silicon 84

4.6 Conclusions 85

5 Zr-doped In_2O_3: Transport limiting mechanisms and application in silicon heterojunction solar cells. 87

5.1 Motivation and state of the art 88

5.2 Methods 90

5.3 Optoelectronic properties: effect of oxygen content and thermal annealing . . . 91

5.3.1 Optical bandgap 91

5.4 Microstructure of In_2O_3:Zr 93

5.5 Transparency of In_2O_3:Zr films of thickness < 100 nm 96

5.6 Mobility limiting mechanisms as a function of thickness for crystalline In_2O_3:Zr 99

5.7 Influence of annealing atmosphere on the optoelectronic properties of In_2O_3:Zr 102

5.8 In_2O_3:Zr films of thickness < 80 nm as front contact in silicon heterojunction solar cells 104

5.9 Conclusion 107

6 Weighted Average Figure of Merit and TCO comparison 109

6.1 Solar spectrum and TCOs 109

6.2 Weighted averaged figure of merit (FOM) 110

6.3 FOM for In_2O_3:Zr 111

6.4 FOM of SnO_2 -based TCOs 114

6.5 Comparison between TCOs 115

6.6 Conclusion 118

7 Conclusions and perspectives 119

7.1 General Conclusions 119

7.1.1 Chapter 3 119

7.1.2 Chapter 4 120

7.1.3 Chapter 5 121

7.1.4 Chapter 6 121

7.2 Perspectives 122

7.2.1 Alternative dopants for SnO_2 -based oxides 122

7.2.2 Sputtered indium-free transparent conductive oxides with perovskite structure 122

7.2.3 Effect of ZrO_2 on In_2O_3:Zr 123

7.2.4 In_2O_3:Zr in silicon heterojunction solar cells 123

A Co-sputtering In-based and Sn-based TCOs as electrodes in silicon heterojunction solar cells 125

A.1 Film fabrication 125

A.2 Optoelectronic properties 126

A.3 Microstructure and composition 128

A.4 Application in silicon heterojunction solar cells 128

A.5 Conclusions 129

Bibliography 150

Curriculum Vitae 151

List of Figures

1.1 Conduction-band formation (s-p orbital hybridization, where the s-orbitals are represented by the blue spheres and the p-orbitals by the red "dumbell" shape) for (a) a crystalline silicon, (b) an amorphous silicon, (c) a crystalline oxide and (d) an amorphous oxide. The amorphization reduces the conduction path for silicon since amorphous materials lack an efficient orbital overlap. In contrast, the overlap of the s-orbitals seems to be insensitive to amorphization. The Figure was taken and modified from reference [Kamiya et al., 2009b]. 4

1.2 Schematic representation of an (a) ideal crystal, a (b) crystal with a vacancy, (c) fully coordinated amorphous network and (d) an amorphous network with a deficiency. In crystalline or amorphous materials, a vacancy (or deficiency in the amorphous material), results in dangling bonds, i.e. undercoordinated atoms. 5

1.3 Fitting of the electron mobility limited by ionized impurities (μ_{ii}) as a function of free-carrier density for effective masses ranging from 0.25 m_e to 0.35 m_e. For this calculation, we assumed that one ionized defect per dopant, a κ of 4 and defects of charge +2. The green star in is the maximum μ_e for In_2O_3:Zr (chapter 5). 6

1.4 (Left) Schematic representation of Seto's grain boundary model. (Right) Schematic band-diagram corresponding to Seto's model. The trap density in the grain boundaries (N_{GB}) creates a potential barrier of height E_B. 9

1.5 μ_e as function of N_e for single crystal and polycrystalline ZnO, ZnO:Al and ZnO:Al,Ga deposited vapour chemical deposition, sputtering and pulsed lased deposition. The films were deposited onto glass and sapphire substrates. The thick black line corresponds to the fitting of Masetti's equation, while the other lines correspond to a combination of the BHD model and Seto's model. Figure taken from reference [Ellmer and Mientus, 2008]. 12

1.6 Representation of (a) the fundamental bandgap in an intrinsic direct semiconductor (E_g) and (b) the optical bandgap (E_{opt}) in a degenerate semiconductor. In degenerate semiconductors, the Fermi energy (E_F) is inside the conduction band, hence there is a shift of the optical bandgap to higher energy. This energy difference is known as the Burstein-Moss shift (ΔE_{BM}). 17

1.7 Illustration of the optical absorption of an amorphous semiconductor. The absorption is divided in three regions: Region A corresponds to the strong absorption edge, region B corresponds to the absorption involving transitions between band tails (known as Urbach region) and region C describes transitions within deep subgap states 18

1.8 Schematic of (a) the SnO_2 rutile structure and (b) the In_2O_3bixbyite structure. The O atoms are in red, the Sn atoms are in green and the In atoms are blue. . . 22

1.9 Calculated total and partial density of states of (a) SnO_2 and (b) In_2O_3(reproduced from [Mishra et al., 1995] and [Tanaka et al., 1997]) and band structure of (c) SnO_2 and (d) In_2O_3(taken from [Mishra et al., 1995] and [Mi et al., 1999] respectively) 23

1.10 Schematic representation of a monolithic tandem solar cell using ZnO:Al, In_2O_3:Sn and SnO_2 in the design. Adapted from [Albrecht et al., 2016]. 24

1.11 (a) Sketch of a silicon heterojunction (SHJ) solar cell with an n-type crystalline silicon wafer. (b) Diagram of current collection in the front TCO. 25

1.12 Calculated relative power loss of a SHJ solar cell resulting from Joule heat in the TCO. The power loss is shown as function of the distance between silver fingers for TCOs with different R_{sheet} . The dashed lines mark the power loss for the typical finger geometry, a reduction from 4% to 2% power loss is expected from a decrease in R_{sheet} from 100 Ω/sq to 50 Ω/sq. Note that this is an approximation that works as an upper boundary to the power loss in the TCO. 26

2.1 Schematic representation of a radio frequency magnetron sputtering system with two targets. 34

2.2 Schematic depiction of the Hall effect experiment. 35

2.3 Sample holder of the Hall effect experiment. 37

2.4 Schematic diagram of the spectrophotometer. The numbers indicate (1) The light source which is either a tungsten-halogen lamp or a deuterium lamp. (2) The monochromator which separates light into its spectral components, i.e. filters light in terms of wavelength. For the measurements in this work, the monochromator filtered every 10 nm. (3) A slit, (4) The transmittance and (5) reflectance apertures in the integrating sphere. (6) Semiconductor-based light detectors, which are either silicon-based or indium-gallium-arsenide (InGaAs) based. 38

2.5 Absorptance spectra as function of wavelength for a series of amorphous zinc tin oxide (a-ZTO) films modified with SiO_2 . For higher SiO_2 content, the films result in less absorptance in the visible and near-infrared regions of spectrum. 39

2.6 Scheme of the quadrupole mass detector (QMD) used for thermal desorption spectroscopy (TDS). 41

3.1 Hall mobility (μ_e) and free-carrier density (N_e) of as- deposited and annealed a-ZTO (a-$Zn_{0.05}Sn_{0.30}O_{0.65}$) thin films as a function of annealing temperature. The dashed line divides the two different regimes observed at low and high temperatures. 50

3.2 Total transmittance and absorptance of a-ZTO as-deposited and annealed at 150 °C (a) and at 500 °C (b) in air, N_2 and H_2 51

3.3 Photothermal deflection spectroscopy of as-deposited a- ZTO(black line) and samples annealed in (a) air, (b) nitrogen, and (c) hydrogen at 150 °C (dashed coloured lines) and 500 °C (solid coloured lines). A comparison between the films as-deposited and annealed at 500 °C is shown in (d) (blue for air, red for nitrogen, and green for hydrogen). 51

3.4 Tauc plot of a-ZTO annealed at 500 °C in air. The sub-bandgap absorption of the as-deposited a-ZTO and films annealed in other atmospheres, impede the bandgap estimation using this approach. For a-ZTO annealed at 500 °C optical bandgap of 3.7 eV was determined assuming direct allowed transitions 52

3.5 TEM analysis of the samples after deposition and after annealing at 500 °C in air. (a, b) TEM images of focused ion beam–prepared cross sections after deposition and annealing at 500 °C , respectively. (c, d) Selection of nanobeam electron diffraction patterns of the samples shown in (a) and (b), respectively. The last inset of each series shows the mean of 100 nanobeam diffraction patterns. (e, f) Rotationally averaged diffracted intensities of 1200 nanobeam diffraction patterns of the samples shown in (a) and (b), respectively, highlighting the absence of both crystallinity and significant restructuring upon annealing. ([Voyles and Muller, 2002] for further details.) 54

3.6 (a) Variance of the diffracted intensities of the samples after deposition (prepared either by FIB or by directly depositing a-ZTO onto Si_3N_4 thin supports) and after annealing at 500 °C in air. This data set was acquired using a probe size of 1.3 nm and a convergence semi-angle of 0.5 mrad. (b) Variable resolution variance data of the FIB-prepared sample annealed at 500 °C acquired using various probe sizes, ranging from 1.3 to 3 nm. 54

3.7 Thermal desorption of as-deposited a-ZTO and the films annealed at 500 °C in air, H_2 and N_2 atmospheres. The silicon substrate is shown for all films. We measured mass/charge (M/z) signal 64, 18, 32, 2 and 120, which correspond to effusion of Zn^{1+}, H_2O^{1+}, O_2^{1+}, H_2^{1+} and Sn^{1+}. The inset in Figure 3.7(c) shows the rate between the 32 and 64 signals. The desorption and the signal rate is in logarithmic scale. 56

3.8 Electron mobility (a) and free-carrier density (b) obtained by Hall effect measurements from -190 °C to 50 °C for as-deposited a-ZTO and films annealed at 150 °C and 500 °C in air, H_2 and N_2 atmospheres 58

3.9 Hall mobility plotted as function of free-carrier density for films annealed in air, H_2 , and N_2 atmospheres. Lines are simulations using the Brooks Herring Dingle model, considering ionized defects of charge $Z = +2$ and of defect density N_{ii} changing from 2×10^{19} cm^{-3} to 2×10^{20} cm^{-3} . Effective masses of 0.26 m_e and 0.3 m_e were used in the model, as calculated from Fourier transform infrared reflectance and Drude model fitting 59

3.10 Calculated densities of states of (top panel) the a-ZTO:$V_O^{\bullet\bullet}$ samples containing a local oxygen deficiency and (bottom panel) the a-ZTO:$V_O^{\bullet\bullet}$ +H samples with an additional H atom in the vicinity of the defect. The curves are aligned with respect to the main peak in the VB. Deep levels within the gap are mainly carried by one or two metal atoms (indicated in the top panel), while levels close to the VB stem from undercoordinated oxygen atoms (O_{uc}). The defect state of the a-ZTO:$V_O^{\bullet\bullet}$ +H sample s06 is related to a Sn-H bonding and neighbouring O atoms. 61

3.11 Supercells containing a local oxygen deficiency and a metal-metal defect: (a) a-ZTO:$V_O^{\bullet\bullet}$ sample s03, (b) a-ZTO:$V_O^{\bullet\bullet}$ sample s02, (c) a-ZTO:$V_O^{\bullet\bullet}$ +H sample s03, and (d) a-ZTO:$V_O^{\bullet\bullet}$ +H sample s06. Sn, Zn, O, and H atoms are depicted as grey, blue, red, and yellow spheres, respectively. The Sn, Zn, and O atoms contributing most to the defect levels are highlighted by dark grey, dark blue, and dark red, respectively. 62

3.12 Monolithic tandem cell structure with mesoscopic perovskite top cell and homojunction silicon bottom cell. The SEM images shows a cross-section of a typical perovskite top cell. TiO_2 is the electron transport layer which must be treated at 500 °C for proper functioning. 64

3.13 J-V curves of monolithic tandem cells with ITO or a-ZTO recombination layer. Dashed lines are for forward scans (Jsc to Voc) and solid lines are for reverse scan (Voc to Jsc) 65

4.1 (a) Hall mobility (μ_e) and free-carrier density (N_e) as a function of the oxygen flow ratio ($r(O_2)$). (b) Absorptance of a-ZTO films as a function of wavelength for depositions with different $r(O_2)$ during deposition. The inset in (b) shows the change in the overall electrical conductivity. All films were annealed at 200 °C for 30 minutes in air prior to the measurements. 71

4.2 (a) Plot of the simplified figure of merit (FOM) as a function of deposition parameters. The simplified FOM was calculated as the ratio of conductivity and average absorptance in the range 400 nm - 800 nm for SiZTO films deposited with different SiO_2 and O_2 content; (b) Hall mobility and free-carrier density of SiZTO as a function of power applied on the SiO_2 target, these films had a constant $r(O_2)$ of 1.00%. 72

4.3 (a) Broadband absorptance of annealed and as-deposited a-ZTO and SiZTO as a function of wavelength. The frame in (a) indicates the close-up region presented in (b). In addition, the inset in (b) shows the conductivity of the as-deposited and annealed films. While both films show virtually equal conductivities, SiZTO presents a lower absorptance below the bandgap and in the near infra-red part of spectrum when compared to the reference a-ZTO. The SiZTO and ZTO film corresponds to the depositions performed with $r(O_2)$ of 1.00% and 1.15% respectively. 73

4.4 (a) Nanobeam electron diffraction patterns taken along the growth direction of SiZTO thin films. The asymmetric speckles indicate an amorphous structure, unchanged with SiO_2 addition [Rucavado et al., 2017] and along the growth axis; (b) STEM HAADF image of the cross-section of the film (left panel) corresponding Si K edge EDX map (right panel); (c) at% line profiles (left to right) of the Si K, O K, Sn L and Zn K edges quantified using the FEI Velox software (assuming a sample thickness of 100 nm and a density of 6.5 $\mathrm{g\,cm^{-3}}$ for the absorption correction). 74

4.5 Thermal desorption spectroscopy (TDS) of SiZTO and a-ZTO for (a) M/z = 32 and, (b) M/z = 64. The signal of the silicon substrate is included for reference. . 75

4.6 Raw data (green), background subtracted data (blue) and pseudo-Voigt fit (red) of the XPS showing peaks corresponding to O 1s, Sn 3d and Zn 2p for as-deposited and annealed a-ZTO and SiZTO. The Pseudo-Voigt fitting of the XPS data was performed for O 1s, Sn 3d and Zn 2p. There is no signal for the Si 2p band, possibly due to the low concentration of Si atoms in the sample. Fitting shows virtually no change in the binding energy and in the FWHM between samples for each of these bands. 77

4.7 (a) Electron mobility and (b) free-carrier density for SnO_2 and $SiSnO_2$ as a function of oxygen flow ratio - $r(O_2)$ during deposition. All films were annealed at 200 °C for 30 minutes prior to Hall measurement. An optimal optoelectronic properties are achieved in $SiSnO_2$ for an $r(O_2)$ of 1.30%. 78

4.8 (a) Broadband absorptance of annealed and as-deposited a-$SiSnO_2$ and SnO_2 as a function of wavelength. The $r(O_2)$ for $SiSnO_2$ and SnO_2 are 1.30% and 1.45% respectively, which correspond to the optimized films. The frame in (a) shows a close-up of the absorptance in (b). In addition, the inset in (b) shows the conductivity of as-deposited and annealed SnO_2 and $SiSnO_2$. Just as for SiZTO, both films show similar conductivities, $SiSnO_2$ shows lower absorptance below the bandgap and in the near infra-red part of spectra when compared to the reference SnO_2 79

4.9 (a) Nanobeam electron diffraction taken along the growth direction of $SiSnO_2$, showing an increased crystallinity towards the end of the film (arrowheads); (b) STEM HAADF image of the cross-section of the film and Si EDX map; (c) at% line profiles (left to right) of the Si K, O K and Sn L edges quantified using the FEI Velox software (assuming a sample thickness of 100 nm and a density of 6.5 $\mathrm{g\,cm^{-3}}$ for the absorption correction 80

4.10 (a) STEM bright field image and (b) selected-area diffraction pattern of SnO_2. The microstructure of SnO_2 is amorphous near the glass substrate, and as the thickness increases it crystallizes to a polycrystalline structure. 81

4.11 (a) SnO_2 surrounding an oxygen vacancy defect. Sn atoms are shown as purple spheres, oxygen - red, Si - blue, the vacancy is indicated in green. Right panel: A and B number the two substitutional Si sites neighbouring the vacancy. Left panel: the distance between a substitutional Si_{Sn} far from V_O is indicated; (b) Formation energies (O-rich) of isolated defects and defect-clusters as a function of the Fermi level. $\epsilon(2/0)$ transitions are indicated by light grey lines. Δ marks the distance between $\epsilon(2/0)$ transition and the CBM. This distance, important in determining the ratio between different charge states, is shifted towards the CBM in the presence of Si. 83

4.12 Electronic densities of states for oxygen vacancy related defects in SnO_2. Results for the charge neutral (q = 0) and for doubly ionized (q = 2) supercells are shown. Coloured lines correspond to defect geometries described in detail in the main text. Defect induced states are highlighted by dashed circles. 84

5.1 N_e (a), μ_e (b), and absorptance (c) of as-deposited (empty triangles and dashed lines in c) and annealed (full squares and solid lines) of 100-nm-thick In_2O_3:Zr films sputtered with different r(O_2). A maximum for mobility of 105 $cm^2V^{-1}s^{-1}$ is obtained when sputtering with r(O_2) of 0.33%, while a maximum N_e is achieved for r(O_2) of 0.16%. A convenient trade-off between optical and electrical properties is obtained for films with mobility of 105 $cm^2V^{-1}s^{-1}$, since the average optical absorptance is 3.6%, while for the film sputtered with higher N_e show an average absorptance 6.2%. The film deposited with r(O_2), of 0.62% has a low average absorptance of 1.0% but its N_e and μ_e are reduced. Lines in figures (a) and (b) provide a guide to the eye. 92

5.2 (a) Absorption coefficient (α) of In_2O_3:Zr films deposited with r(O_2) from 0.08% mbar to 0.62%. As-deposited films are in dashed lines while annealed films are in solid lines. (b) Tauc plot of the films shown in (a). The Tauc plot shows that an optical bandgap of 3.6 eV to 3.7 eV are found for as-deposited samples, which increases to 3.9 eV to 4.0 eV after annealing. 93

5.3 Selected-area TEM diffraction patterns of (a) as-deposited and (c) annealed 100-nm-thick In_2O_3:Zr films and corresponding STEM bright-field images in (b) and (d). In (b), small (nanometric) crystallites, marked with red arrows, are visible in the amorphous matrix. The SAED and STEM imaging was performed on the optimized In_2O_3:Zr films (r(O_2) of 0.33%). The images and diffraction patterns confirm an amorphous-to-crystalline transition after thermal annealing at 200 °C 94

5.4 STEM bright field micrograph of annealed 50-nm-thick In_2O_3:Zr, the crystallites have an average size of ~ 400 nm. The EDX maps show an homogeneous composition of Zr, In and O. The EDX quantification resulted in averages of 2 at%, 39 at% and 59 at% of Zr, In and O. 95

5.5 ERDA measurements showing atomic-H depth profiles of the 9.5 at% mica standard (red), as-deposited (a) and annealed (b) In_2O_3:H, and as-deposited (c) and annealed (d) In_2O_3:Zr thin films. 95

5.6 Optoelectronic properties of as-deposited (empty symbols and dashed lines) and annealed (full symbols and solid lines) In_2O_3:Zr films deposited with r(O_2) = 0.33% for different thicknesses. The free-carrier density (a) and mobility (b) show an increase with thickness after annealing (lines in a and b are for eye guidance only). The optical absorptance decreases drastically for thinner films. The absorptance of the glass substrate is shown in black dotted lines in (c). As the thickness of the In_2O_3:Zr is reduced to 15 nm, the absorptance approaches that of the glass substrates, still with a conductivity of 400 S cm^{-1}. 97

5.7 STEM BF top view of films of (a) 15 nm, (c) 25 nm, (e) 50 nm and (g) 100 nm thickness and their corresponding electron diffraction patterns respectively in (b), (d), (f) and (h). All films were annealed in atmospheric pressure at 200 °C . 15-nm-thick films show a strained crystalline microstructure (grain boundaries are marked with the red arrows). Average crystallite sizes of 500 nm, 420 nm and 320 nm are found for 25 nm, 50 nm and 100-nm-thick films, respectively. The electron diffraction for (f) was performed in one single crystalline domain. . . . 98

5.8 N_e (a) and μ_e (b) as a function of temperature for In_2O_3:Zr films with a thicknesses from 100 nm to 15 nm. While N_e does not change in this temperature range, μ_e of the films changes with temperature. Thicker films exhibit larger temperature dependence, possibly due to a higher influence of optical phonon scattering compared to thinner films. 100

5.9 Room temperature inverse mobility (left axis) as a function of thickness. The contribution from phonon scattering (green) and ionized impurities (red) was calculated by fitting equation 5 at room temperature. The right axis shows the Hall mobility (black squares) as a function of film thickness. 101

5.10 STEM HAADF images of 50-nm-thick In_2O_3:Zr (a) as-deposited, (b) annealed in air, (c) annealed in H_2 and (d) N_2 atmospheres. The as-deposited films are amorphous with embedded nanometric-sized crystallites. The corresponding diffraction patterns confirm that the (e) as-deposited sample is mostly amorphous, (f) the sample annealed in air is crystalline and samples annealed in H_2 (c) and (g) and N_2 (d) and (h) have an amorphous microstructures with embedded crystallites of considerably higher grain size than those seen in the as-deposited film. 103

5.11 Electrical properties of optimized In_2O_3:Zr as-deposited (empty symbols) and films annealed in H_2 and N_2 atmospheres (blue, green and red full symbols respectively). Films were deposited with r(O_2) of 0.33% and for different thickness. (a) N_e and (b) μ_e are dependent of the annealing atmosphere. In (c) the conductivity for each film is shown as function of thickness, in addition we plotted lines for constant R_{sheet} 104

5.12 (a) Light IV characteristics of SHJ solar cells with 80 nm and 40-nm-thick In_2O_3:Zr (with and without MgF_2 as second antireflective coating. (b) External quantum efficiency (EQE) of the cells shown in (a) and the corresponding optical absorptance of the front TCOs. The absorptance of the 40-nm-thick In_2O_3:Zr does not change with MgF_2 and is not shown here. As reference, In_2O_3:Sn electrode was also used in the cells and in the absorptance measurement. 106

6.1 (Left axis) Spectral irradiance from the Sun at AM 1.5 G compared with the (right axis) absorptance of In_2O_3:Sn. Increasing N_e results in higher absorptance in the infrared part of spectra and blue-shift of the fundamental absorption due to higher values of E_{opt} 110

6.2 Weighted average absorptance ($A_{weighted}$) versus the logarithm of the sheet resistance (log(R_{sheet})) of In_2O_3:Zr films with thickness of 15 nm, 25 nm, 50 nm and 100 nm as-deposited and annealed in air, N_2 and H_2 atmospheres. The size of the markers is scaled linearly with the thickness of the samples. The FOM was calculated using Equation 6.1. The integration limits are from 390 nm to 1200 nm. In addition, the FOM for standard In_2O_3:Sn films are shown with green stripes. The solid lines mark constant FOM values of 2.0%, 1.0%, 0.2% and 0.1% 113

6.3 Weighted average absorptance ($A_{weighted}$) versus sheet resistance (R_{sheet}) of ZTO and SnO_2 films with thickness of 150 nm as-deposited and annealed in air, N_2 and H_2 atmospheres. In addition the as-deposited and annealed SiZTO and $SiSnO_2$ films are also shown. The FOM was calculated using Equation 6.1. The integration limits are from 390 nm to 1200 nm. 114

6.4 Averaged weighted absorptance as function of sheet resistance (in logarithmic scale) for SnO_2 -based oxides (red), In_2O_3:Zr (green) and In_2O_3:Sn (blue). The amorphous films (or a mixture amorphous/crystalline) have a thick border in the markers, while crystallized films have no border. Films modified with SiO_2 are half red and half black. The lines show constant FOM values. 115

A.1 Scheme of a-ZTO, In_2O_3:Zr and SiO_2 co-sputtering. The power in the In_2O_3:Zr and a-ZTO targets was of 80 W and 10 W in the SiO_2 target. The O_2 partial pressure in the deposition chamber was tuned to optimize the films. The rotating sample enabled an homogeneous composition. 126

A.2 (a) N_e and μ_e of co-sputtered In_2O_3:Zr, a-ZTO and SiO_2 as function of r(O_2) during deposition. The electrical properties of chosen annealed films is shown in empty symbols. (b) Electric conductivity of films in (a), as-deposited and after annealing (full and empty symbols respectively). 127

A.3 Optical absorptance of In_2O_3:Zr, In_2O_3:Sn, a-ZTO and the co-sputtered TCO (ZITO) deposited with an r(O_2) of 0.53%. The a-ZTO film and the co-sputtered film have a thickness of 150 nm, while In_2O_3:Zr and In_2O_3:Sn have a thickness of 100 nm. 127

A.4 Electron diffraction patterns of as-deposited and annealed co-sputtered films . 128

A.5 (a) IV-characteristics and (b) EQE as a function of wavelenght for the cells using the reference In_2O_3:Sn, a-ZTO and ZITO with two different oxygen contents, ZITO1 and ZITO2, with r(O_2) of 0.53% and 0.45% respectively. 129

List of Tables

1.1 Physical properties of In_2O_3, ZnO, SnO_2 and CdO. The table is adapted from references [Batzill and Diebold, 2005], [Ellmer, 2001], and extended with data from references [Madelung, 2012, Aldred and Pratt, 1963, Patnaik, 2003, Jefferson et al., 2008, Schleife et al., 2011] 21

1.2 Optoelectronic properties and process temperature of representative amorphous TCOs. The data from the TCOs was obtained in references [Orita et al., 2001, Hosono et al., 1996a, Yasukawa et al., 1995, Fortunato et al., 2006, Yaglioglu et al., 2006, Kumar et al., 2005, Utsumi et al., 2003, Minami et al., 1994] 22

3.1 Composition from RBS of as-deposited a-ZTO and a-ZTO annealed at 500 °C in different atmospheres 53

3.2 Compilation of the 38 supercell models generated by atomistic simulations, listing the number of samples (n_{samp}), the supercell composition, the total number of atoms per supercell, and the atomic percentage of elements (p_x). . . 60

5.1 Performance of SHJ solar cells using 80 nm and 40-nm-thick In_2O_3:Zr as front electrode. The 40-nm-thick In_2O_3:Zr also has a MgF_2 film as second antireflective coating (ARC). The standard In_2O_3:Sn was used as reference electrode. In addition the R_{sheet} and the weighted absorptance ($A_{weighted}$) of the films are shown. 105

6.1 Figure of merit (FOM), weighted absorptance ($A_{weighted}$) and sheet resistance (R_{sheet}) of annealed In_2O_3:Zr deposited with different r(O_2). 111

A.1 Performance parameters of SHJ solar cells (average values of 5 2 cm^2 × 2 cm^2 measured cells) using the co-sputtered TCO as front electrode. The results are compared with a reference cell with In_2O_3:Sn and a-ZTO front electrodes. The best-cell parameters are between parenthesis. 129

1 Introduction

The aim of this chapter is to construct a general scientific foundation, that will be useful to comprehend the full body of this thesis. It begins by explaining the general concepts of semiconductor materials that are directly applicable to transparent conductive oxides (TCOs). In addition it introduces the optical, electrical and structural characteristics of two important families of TCOs: tin-based and indium-based materials. Finally, this chapter describes the use of TCOs in photovoltaic solar cells, and explains how these devices could profit from improvements in TCO thin films.

1.1 What are transparent conductive oxides?

Given their universal usage, metals are the archetype of conducting materials. While silver is the metal with highest electric conductivity of 6.6×10^5 S cm^{-1} at 273 K [Neil Ashcroft, 1976], the room temperature conductivity of metals is typically on the order of 10^5 S cm^{-1}. The main reason for this high conductivity is metals' high free-carrier density (N_e), which is on the order of 10^{22} cm^{-3}. Their high free-carrier density explains the optical reflection properties of metals, as it will be described in detail in the next section. By contrast, transparent solids are not regarded as electrical conductors. For example, 3-mm-thick aluminium oxide (Al_2O_3) layer has a total transmittance higher than 80% in the wavelengths spanning from 200 nm to 6000 nm due to its wide bandgap of $\approx$ 7 eV, but it has an electric conductivity as low as 10^{-14} S cm^{-1} [Fox, 2010]. Hence there is a difference of 20 orders of magnitude between the typical conductivity of a metal and that of Al_2O_3, seemingly an irreconcilable difference. Nonetheless, TCOs find the middle ground. Having an optical bandgap ($E_{opt} \approx 3$ eV), TCOs are transparent in the visible and near-infrared part of spectrum. In addition TCOs are easily (n-type) doped, by intrinsic and/or extrinsic dopants, such as oxygen deficiencies or substitutional atoms. Doping the TCOs can trigger a N_e up to 10^{21} cm^{-3} , which results in relatively high electric conductivities (e.g. 10^4 S cm^{-1} for tin-doped indium oxide [Tuna et al., 2010]). The doping places the Fermi energy (E_F) of TCOs deep in the conduction band, making them degenerate semiconductor materials.

But doping compromises the optical properties, since the optical and electrical properties are intertwined. Increasing doping usually results in rising parasitic absorptance: a known trade-off between the optical and electrical properties of TCOs. This dissertation explores alternative routes to overcome this trade-off. The main objective is to improve the optical and electrical properties simultaneously and explore disordered indium-free TCOs which will be later compared to high-μ_e indium-based oxides. Our strategy is to understand the mechanisms limiting the optoelectronic properties in zinc-tin oxide as a case example of indium-free TCOs, and to overcome them by (i) controlling the deposition conditions, (ii) post-deposition treatments or (iii) co-depositing TCOs with other materials to decrease the influence of the limiting defects.

1.2 Fundamental properties of transparent conductive oxides

TCOs are degenerate semiconductors (mainly n-type), their electrical conductivity (σ, expressed in units of S cm^{-1}) is dominated by the flow of electrons and is described by

$$\sigma = e\mu_e N_e \tag{1.1}$$

where e is the charge of the electron, μ_e is the electron mobility (units of cm^{2}V^{-1}s^{-1}), and N_e is the free-carrier concentration (units of cm^{-3}). Free carriers are electrons that behave like a free electron gas propagating inside the conduction band. The resistivity (ρ) can be calculated as the inverse of σ. Furthermore, the sheet resistance of the films (R$_{sheet}$ in units of Ω/sq), is the resistivity averaged over the thickness of the film. For uniformly doped samples of constant thickness d, R$_{sheet}$ can be calculated by

$$R_{sheet} = \frac{\rho}{d} = \frac{1}{\sigma d} \tag{1.2}$$

where ρ is the resistivity.

Hence, the R$_{sheet}$ is controlled by N_e , μ_e and the thickness d. While N_e is linked to the doping of the films, μ_e is associated with electron transport in the TCO. μ_e describes how easily an electron propagates in the lattice of a material when an electric field is applied (or induced by other phenomena). From a microscopic perspective μ_e is linked to the average time between scattering events of the charge carriers ($\langle\tau\rangle$), and to the effective mass of the electrons in the TCO (m^*), following

$$\mu_e = \frac{e\langle\tau\rangle}{m^*} \tag{1.3}$$

where e is the electron charge. Increasing μ_e is one of the main interests in TCO design, since μ_e has a direct effect on σ, and increasing μ_e results in a decrease of the free-carrier absorptance in a first approximation. μ_e is limited by microscopic scattering mechanisms governing electron transport, and by the value of the effective mass. In a crystal, the effective mass is obtained by comparing the group velocity of electrons in the crystalline lattice [Neil Ashcroft, 1976], with the motion of free carriers in space when a force is applied. For an isotropic parabolic dispersion relation ($E \propto k^2$) the effective mass is defined as

$$m^* = \frac{\hbar^2}{\partial^2 E(k)/\partial k^2} \tag{1.4}$$

where $E(k)$ is the dispersion relation dependent on the wavenumber k. Equation 1.4 is a simplification for a two-dimensional crystal, since in fact the effective mass is a three-dimensional tensor. Nonetheless Equation 1.4 is useful to understand the effect of the conduction band in m^* and μ_e . An alternative strategy to increase μ_e is to increase $\langle\tau\rangle$, which can be boosted by reducing the point-defect density or by improving the film's microstructure as will be described bellow.

1.2.1 Electron transport in TCOs and mobility limiting mechanisms

Charge transport in TCOs is governed by free electrons in the conduction band. Given the degenerate character of semiconductors, the bottom of the conduction band is formed by the overlap of occupied spherical ns-orbitals of the metal cations (n is the main quantum number, $n = 5, 6$) [Kamiya and Hosono, 2010]. The spherical symmetry of the s orbitals results in a relative insensitivity of the electron transport to disorder (Figure 1.1) [Hosono, 2013, Orita et al., 2001, Hosono et al., 1996b]. As a consequence the electron mobility in amorphous TCOs (a-TCOs) is in the same order of magnitude as in their crystalline counterpart. In addition, the large spread of the metallic s orbitals also results in a low effective mass of electrons ($m^* =$ 0.25 m_e - 0.35 m_e, where m_e is the rest mass of the electron) [Kamiya et al., 2009b].

In addition to the m^*, Equation 1.3 shows that electron transport depends on $\langle\tau\rangle$. This section will discuss the main mechanisms decreasing $\langle\tau\rangle$, hence limiting μ_e . In addition, given that two or more types of scattering events could curb $\langle\tau\rangle$ simultaneously, the last subsection explains an empirical rule, which is useful to approximate the overall effect of the multiple scattering mechanisms. The dominant scattering mechanisms in TCOs vary according to their microstructure—single crystal, polycrystalline or amorphous.

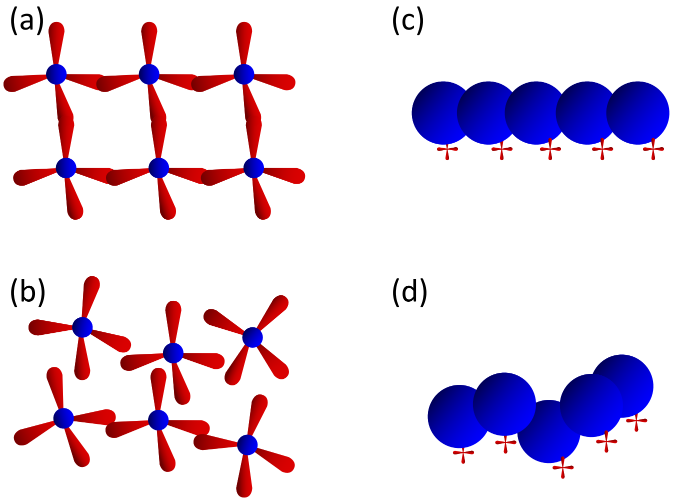

Figure 1.1 – Conduction-band formation (s-p orbital hybridization, where the s-orbitals are represented by the blue spheres and the p-orbitals by the red "dumbell" shape) for (a) a crystalline silicon, (b) an amorphous silicon, (c) a crystalline oxide and (d) an amorphous oxide. The amorphization reduces the conduction path for silicon since amorphous materials lack an efficient orbital overlap. In contrast, the overlap of the s-orbitals seems to be insensitive to amorphization. The Figure was taken and modified from reference [Kamiya et al., 2009b].

1.2.2 Defects in crystalline and amorphous materials

A crystal is a highly ordered, periodic array of atoms, which can be described by a crystal lattice [Neil Ashcroft, 1976]. The position of each atom is described by

$$\boldsymbol{R} = n_1 \boldsymbol{a_1} + n_2 \boldsymbol{a_2} + n_3 \boldsymbol{a_3} \tag{1.5}$$

Where $\boldsymbol{a_i}$ are the primitive vectors and n_i are integers (positive, negative and zero). Thus, in a crystal, the periodicity of the atomic structure results in short- and long-range order. Drastic deviations from an ideal crystal are known as defects, which can be point-like, line and surface defects. A whole variety of defects can be found in crystalline structures: vacancies, interstitials, dislocations, grain boundaries, stacking faults, voids, precipitates, etc. Defects in semiconductors alter the macroscopic properties of the material from its defect-free behaviour, e.g. its electrical conductivity or optical absorptance.

In contrast, amorphous semiconductors lack the long-range order present on crystalline materials. Nonetheless, their spatial atomic arrangement is not completely random, since atoms are constrained by local chemical properties such as bond-length, bond-angle and coordination. These local properties ultimately define the short-range order of the amorphous network. Ultimately, the short-range order is determined by the (i) number, (ii) the type and (iii) the spatial arrangement of immediate neighbours of a reference atom [Brodsky,

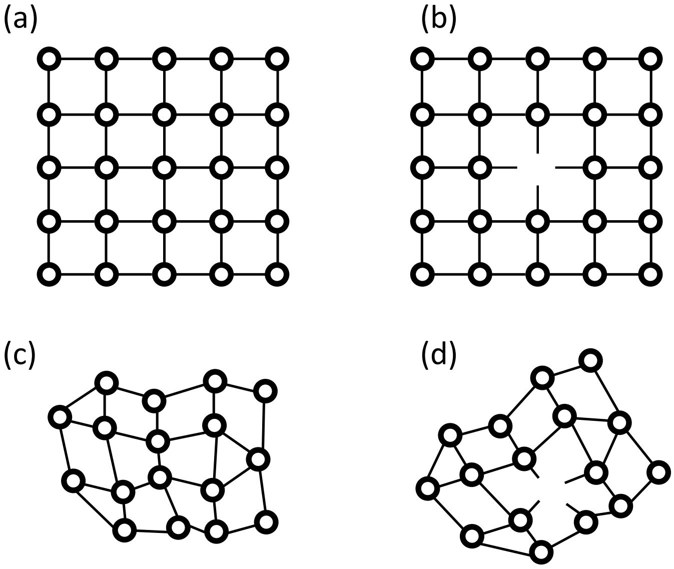

Figure 1.2 – Schematic representation of an (a) ideal crystal, a (b) crystal with a vacancy, (c) fully coordinated amorphous network and (d) an amorphous network with a deficiency. In crystalline or amorphous materials, a vacancy (or deficiency in the amorphous material), results in dangling bonds, i.e. undercoordinated atoms.

1979]. The average density of atoms at a given distance from a reference position results in a radial distribution function (RDF) that describes the short-range order. In amorphous semiconductors, "point-like" defects[1] could create an imbalance in the atomic network, disrupting the RDF and the coordination around a particular atomic species. In amorphous TCOs, the RDF serves as a structure-property, which can be correlated with the optoelectronic properties [Medvedeva et al., 2017, Proffit et al., 2012, Zhu et al., 2013, Zhu et al., 2014, Kamiya et al., 2009c].

Given the lack of grain boundaries in amorphous TCOs, the main scattering mechanisms are "point-like" defects: ionized and neutral impurities.

Ionized impurities

The Scattering of free carrier by ionized impurities is commonly described by the Brooks-Herring-Dingle (BHD) model [Dingle, 1955]. This model considers the effect of a screened Coulomb potential on the relaxation time between two different scattering events. This model results in an expression for mobility limited by ionized impurities, μ_{ii}

---

[1] Point-defects are, by definition, attributed to 0-dimensional deviations of a perfect lattice. Since here our aim is to describe defects in amorphous semiconductors, we use the term "point-like".

$$\mu_{ii} = \frac{3\pi\hbar^3(4\pi\epsilon_0\kappa)^2}{2Z^2e^3m^{*2}} \times \frac{N_e}{N_{ii}} \times \frac{1}{F(\xi)}$$

$$F(\xi) = ln(\xi+1) - \frac{\xi}{\xi+1} \tag{1.6}$$

$$\xi = 4\pi^3(\frac{3}{\pi})^{1/3}\frac{\epsilon_0\kappa\hbar^3N_e^{1/3}}{e^2m^*}$$

where $F(\xi)$ is the screening function, κ is the relative permittivity, ϵ_0 is the vacuum permittivity, N_{ii} is the concentration of ionized impurities, Z the charge of the impurity, m^* is the effective mass and $\hbar$ is the reduced Planck constant. Assuming that there are two free-electrons per defect-site, an m^* between $0.25m_e$ and $0.35m_e$, a κ of 4 and defects of charge +2, the change in μ_{ii} as a function of N_e can be plotted for defect densities from 5×10^{18} cm^{-3} to 10^{21} cm^{-3} as shown in Figure 1.3.

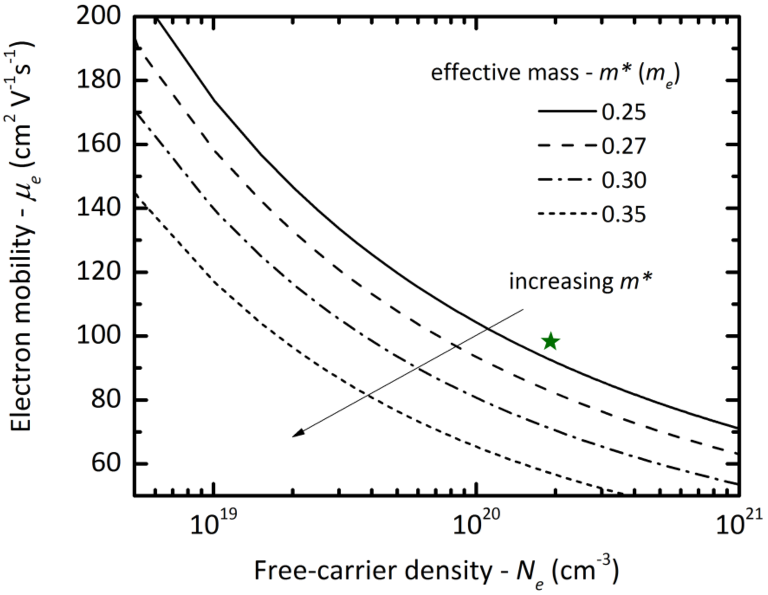

Figure 1.3 – Fitting of the electron mobility limited by ionized impurities (μ_{ii}) as a function of free-carrier density for effective masses ranging from 0.25 m_e to 0.35 m_e. For this calculation, we assumed that one ionized defect per dopant, a κ of 4 and defects of charge +2. The green star in is the maximum μ_e for In_2O_3:Zr (chapter 5).

In Figure 3.9, the experimental μ_e obtained of In_2O_3:Zr is shown as a function of N_e (see chapter 5). The experimental μ_e is higher than the fitting, possible due to a shift in the defect harge from +2 to +1 (due to hydrogen- or Zr-doping), or by the parabolic conduction-band approximation of the BHD model. Ionized impurity scattering is one of the most important mechanisms limiting the electron transport at high N_e .

Additionally, Pisarkiewicz [Pisarkiewicz et al., 1989] refined the BHD model by calculating the effect of non-parabolic conduction bands on the electron transport. The non-parabolicity influences the m^*, and the resulting μ_e of the refined model is

$$\mu_{ii,np} = \frac{3\pi\hbar^3(4\pi\epsilon_0\kappa)^2}{2Z^2e^3m^{*2}} \times \frac{N_e}{N_{ii}} \times \frac{1}{F(\xi_0,\xi_1)}$$

$$F(\xi_0,\xi_1) = \left(1+\frac{4\xi_1}{\xi_0}\left(1-\frac{\xi_1}{8}\right)\right) ln(\xi_0+1) - \frac{\xi_0}{\xi_0+1} - 2\xi_1\left(1-\frac{5\xi_1}{16}\right)$$

where (1.7)

$$\xi_0 = \pi^2(\frac{3}{\pi})^{1/3}\frac{\epsilon_0\kappa\hbar^2N_e^{1/3}}{e^2m^*}$$

$$\xi_1 = 1-\frac{m_0^*}{m^*}$$

using m^* as the effective mass dependent on the Fermi level, (i.e. it is doping dependent) and m_0^* is the effective mass at the bottom of the conduction band. Note that for $m^* = m_0^*$, the Equations 1.7 and 1.6 are equivalent.

Neutral impurities

Scattering from neutral impurities is described by [Erginsoy, 1950]

$$\mu_n = \frac{e^3m^*}{A4\pi\kappa\epsilon_0\hbar^3N_n} \tag{1.8}$$

where A is the cross section of the scattering process and N_n is the neutral defect density. Usually for TCOs the concentration and the scattering cross section of the neutral impurities are much smaller than those of ionized impurities, hence the effect of neutral impurities is often neglected [Zhang and Ma, 1996,Preissler et al., 2013,Macco et al., 2015]. As demonstrated by Frank and Kostling, in heavily doped In_2O_3:Sn, μ_e does not scale with N_e as expected from ionized impurity scattering, hence in this case the contribution of scattering from neutral impurities should be taken into account [Frank and Kostlin, 1982].

Phonon scattering

The motion of the atoms out of their equilibrium positions gives rise to a periodic dispersion relation with two possible solutions [Ibach and Luth, 2009, Neil Ashcroft, 1976] (or branches): optical and acoustical phonons. The optical phonons induce an oscillating dipole which propagates into the periodic lattice and interacts with the free carriers. The acoustic phonons describe the propagation of sound waves in a material. Preissler et al. [Preissler et al., 2013] used fitting of the different scattering mechanisms in a large set of In_2O_3 samples (with N_e from 7×10^{16} cm^{-3} to 10^{21} cm^{-3}), to suggest that scattering of polar phonons is important at low N_e, while acoustic phonons are not relevant regardless of the free-carrier density. Given the N_e values in a TCO, the electron-phonon interaction can be described as similar to that of a metal [Zhang and Ma, 1996, Dugdale, 1977]. Hence the electron mobility can be described by $\mu_e \propto T^{-p}$, where $p = 1$ if the measuring temperature is higher than the Debye temperature, and $2 < p < 4$ if the measuring temperature is lower than the Debye temperature. For our case, the Debye temperature of tin oxide and indium oxide are respectively 313 K [Collins et al., 1979] and 700 K [Preissler et al., 2013]. Hence, we describe the scattering from phonons using the expression

$$\frac{1}{\mu_{Ph}(T)} = \frac{1}{\mu_0}\left(\frac{T_0}{T}\right)^2 \tag{1.9}$$

where T is the temperature, and μ_0 is the electron mobility at T_0. A more refined description of the phonon-electron interactions (polar optical phonons, acoustic deformation potential, and piezoelectric potential) is summarized in reference [Ginley and Perkins, 2011].
In the case of a polycrystalline material, the scattering from grain boundaries should be considered as well.

Scattering by grain boundaries

Several thin film TCOs are polycrystalline, i.e. they are formed by crystalline domains separated by grain boundaries. Seto [Seto, 1975] developed a model to describe scattering from grain boundaries in polycrystalline silicon, which can be applied as a first approximation to TCOs (Figure 1.4).

This model views grain boundaries as electron traps, which reduce the total number of free carriers and creates a potential energy barrier (E_B) between grains. Seto's model also assumes that (i) the films are composed of equal grains of size L, (ii) the donors are totally ionized and uniformly distributed with a concentration of N_e (cm^{-3}), (iii) the thickness of the grain boundary is negligible compared with L, and (iv) the traps contain a defect density of N_{GB} (in

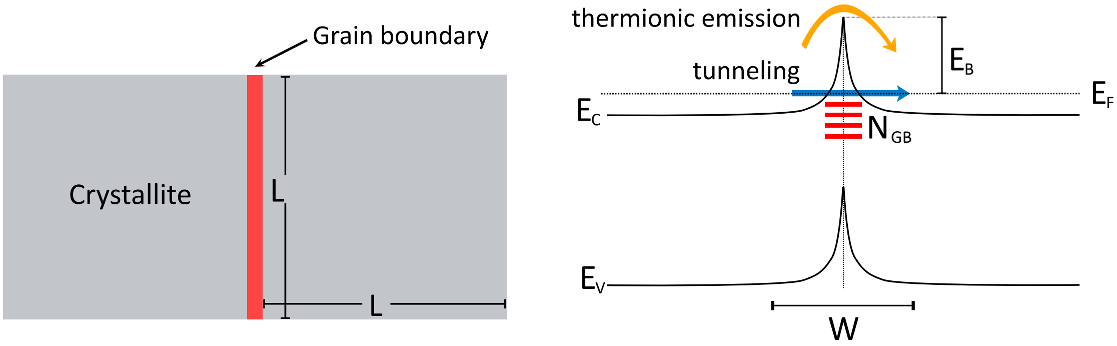

Figure 1.4 – (Left) Schematic representation of Seto's grain boundary model. (Right) Schematic band-diagram corresponding to Seto's model. The trap density in the grain boundaries (N_{GB}) creates a potential barrier of height E_B.

cm^{-2}). By solving Poisson's equation in one dimension, Seto found two possible values for E_B, one for in-grain free-carrier density larger than the trap density in the grain boundaries ($LN_e > N_{GB}$) and one for in-grain free-carrier density smaller than the trap density in the grain boundaries ($LN_e < N_{GB}$). This is,

$$\begin{aligned} E_B &= \frac{e^2 N_{GB}^2}{8\epsilon\epsilon_0 N_e} \quad \text{for} \quad LN_e > N_{GB} \quad \text{for non-depleted grains} \\ E_B &= \frac{e^2 L^2 N_e}{8\epsilon\epsilon_0} \quad \text{for} \quad LN_e < N_{GB} \quad \text{for depleted grains} \end{aligned} \tag{1.10}$$

In the context of this work, it is likely that $LN_e > N_{GB}$, given that the TCOs are highly-doped and in turn N_e is high compared with the defect density in the grains. This results in an E_B that depends directly on $1/N_e$, hence the boundary is lower for more highly doped films.

An electron can traverse the potential barrier by thermionic emission or by tunnelling. Electrons with high-enough energy are likely to contribute to the current via thermionic emission. Conversely, electrons with energy $< E_B$, are likely to tunnel through. Considering only thermionic emission, the electron mobility as a function of the energy barrier is given by

$$\mu_{thermionic} = \frac{eW}{\sqrt{2\pi m^* k_B T}} \exp\left(\frac{-E_B}{k_B T}\right) \tag{1.11}$$

where k_B is Boltzmann's constant, and T is the temperature. Conversely, μ_e of electrons tunnelling through an energy barrier E_B is expressed by

$$\mu_{tun} = \frac{el}{\hbar(3\pi^2 N_e)^{1/3}} \exp\left(\frac{-4\pi W\sqrt{2m^* E_B}}{\hbar}\right) \tag{1.12}$$

where l is the mean free path of the electron and W is the thickness of the grain boundary.

Steinhauser developed a model for the effective electron mobility in zinc oxide (ZnO) films [Steinhauser, 2009]. Considering $\mu_{intragrain}$, $\mu_{thermionic}$ and μ_{tun}, the effective electron mobility is described by

$$\frac{1}{\mu_{eff}} = \frac{L-W}{L}\left(\frac{1}{\mu_{intragrain}}\right) + \frac{W}{L}\left(\frac{1}{\mu_{thermionic} + \mu_{tun}}\right) \tag{1.13}$$

For non-depleted grains, the potential barrier decreases for increasing N_e , (Equation 1.10), hence for highly doped TCOs, intragrain scattering is likely to dominate electron transport. In addition, from Equation 1.13, the effective electron mobility for TCOs with grains of size much larger than the grain boundary thickness ($L >> W$) is also likely to be dominated by scattering from intragrain events. In the next sections, the main scattering mechanisms controlling $\mu_{intragrain}$ will be described.

Matthiessen's rule

The different scattering mechanisms limit μ_e of an electron, decreasing the overall conductivity in the TCOs. Suppose two types of scattering mechanisms (A and B) and a total collision rate (S). If we assume that A and B are independent, i.e. A has no influence on B, the total collision rate can be described as $S = S_A + S_B$.

If we assume the relaxation-time approximation[2], the contribution from A and B in τ and in

---

[2] The relaxation-time approximation asserts that (i) a scattering event "erases" the conditions of the scattered particles prior to the event and (ii) collisions maintain the thermodynamic equilibrium at whatever experimental temperature. For more details, see reference [Neil Ashcroft, 1976]

μ_e , can be expressed using Matthiessen's rule[3] [Neil Ashcroft, 1976]

$$\frac{1}{\langle\tau_{total}\rangle} = \frac{1}{\langle\tau\rangle_A} + \frac{1}{\langle\tau\rangle_B}$$

Using Equation 1.3 (1.14)

$$\frac{1}{\mu_{total}} = \frac{1}{\mu_A} + \frac{1}{\mu_B}$$

where μ_A is the electron mobility in the material if the only scattering mechanism present is A, and equivalently for μ_B. Thus, in polycrystalline materials, Equation 1.14 can be expressed as

$$\frac{1}{\mu_{total}} = \frac{1}{\mu_{intragrain}} + \frac{1}{\mu_{GB}} \tag{1.15}$$

where $\mu_{intragrain}$ is the electron mobility limited by scattering mechanisms in the bulk of the films[4], while μ_{GB} is the mobility limited just by the interaction between electrons and grain boundaries. Quantitatively, a simple evaluation of Equation 1.14 shows that given μ_A and μ_B, the smaller value is dominant. For example take μ_A = 10 cm^{2}V^{-1}s^{-1} and μ_B = 100 cm^{2}V^{-1}s^{-1} : the resulting μ_{total} from these two hypothetical scattering mechanisms is 9.1 cm^{2}V^{-1}s^{-1} .

An empirical rule to describe μ_e inside the grain of the materials is given by [Masetti et al., 1983]

$$\mu_{intragrain} \approx \mu_{Masetti} = \mu_{min} + \frac{\mu_{max} - \mu_{min}}{1 + (N_e/N_{ref1})^{\alpha_1}} - \frac{\mu_1}{1 + (N_{ref2}/N_e)^{\alpha_2}} \tag{1.16}$$

where μ_{min} is the mobility at high N_e, μ_{max} is the mobility at low N_e, $\mu_{min} - \mu_1$ is the cluster mobility (extremely high free-carrier density), and α_1, α_2, N_{ref1} and N_{ref2} are empirical coefficients. Ellmer and Mientus [Ellmer and Mientus, 2008] studied a large dataset of μ_e -N_e values of doped and undoped ZnO and fitted Masetti's model, and BHD model and Seto's model for electron mobility.

---

[3] It is also assumed that both scattering mechanisms are independent on the wavevector κ

[4] by using "bulk" we refer to the scattering mechanisms present inside the single-crystallite grain

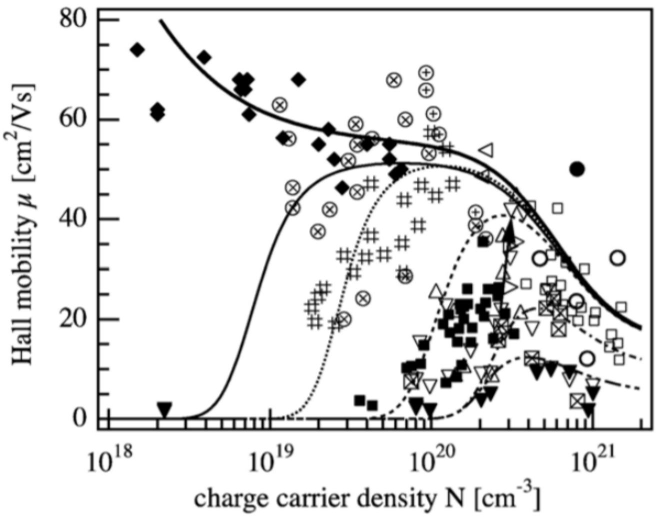

Figure 1.5 – μ_e as function of N_e for single crystal and polycrystalline ZnO, ZnO:Al and ZnO:Al,Ga deposited vapour chemical deposition, sputtering and pulsed lased deposition. The films were deposited onto glass and sapphire substrates. The thick black line corresponds to the fitting of Masetti's equation, while the other lines correspond to a combination of the BHD model and Seto's model. Figure taken from reference [Ellmer and Mientus, 2008].

While μ_e is dominated by ionized impurities at $N_e > 3 \times 10^{20}$, grain-boundary scattering limits the electron transport for lower N_e values. By fitting Seto's model. they found that the trap density in the grain boundaries (N_{GB}) can range between in 5×10^{12} cm^{-2} and 3×10^{13} cm^{-2}. Interestingly, the N_{GB} is highly dependent type of deposition system, e.g. deposition source- direct current or radio-frequency- or the orientation of the substrate with respect to the target [Ellmer and Mientus, 2008]. Fitting Masetti's equation it was found that for ZnO, μmax and $\mu min - \mu 1$ present values of 210 cm^{2}V^{-1}s^{-1} , 5 cm^{2}V^{-1}s^{-1} respectively.

1.2.3 Dopants in transparent conductive oxides

Intrinsic dopants

Defects are ubiquitous and unavoidable in semiconducting materials. In oxide materials, an oxygen vacancy (V_O) is the absence of an oxygen atom in the atomic network. In TCOs oxygen vacancies play a dual role: They can act as a source of free electrons i.e. as dopants, shifting the Fermi level deep in the conduction band and they can act as point defects that limit μ_e and might produce subgap states, which are detrimental for the optical properties [Bazzani et al., 2011, Calnan and Tiwari, 2010, Klein, 2013, Koida et al., 2012, Robertson et al., 2006]. In_2O_3, tin oxide (SnO_2) and ZnO can have free-carrier densities on the order of 10^{20} cm^{-3} without the need of extrinsic dopants due to V_O [Chopra et al., 1983]. If the defect level formed by V_O is shallow, the electrons occupy the conduction band minima. This defect chemistry is usually described in the Kroger-Vink notation[5] [Kröger and Vink, 1958] as

$$\frac{1}{2}O_2(g) + \mathrm{V}_{\mathrm{O}}^{\bullet\bullet} + 2e \Rightarrow O_0^x \tag{1.17}$$

where $\mathrm{V}_{\mathrm{O}}^{\bullet\bullet}$ is a vacancy with a double negative charge at the original position of the oxygen atom, O_0^x is an oxygen atom in the corresponding lattice position with no effective charge and $2e$ are two negatively charged electrons. Intrinsic defects that are not due to $\mathrm{V}_{\mathrm{O}}^{\bullet\bullet}$ also co-exist with $\mathrm{V}_{\mathrm{O}}^{\bullet\bullet}$ in TCOs. For example, charge-neutral V_{O} (or $\mathrm{V}_{\mathrm{O}}^{x}$) is found in SnO_2 at Fermi energies near mid-bandgap. Nevertheless, these defects are less likely to contribute as donors in degenerate TCOs due to their formation energies [Rucavado et al., 2018, Kılıç and Zunger, 2002]. Given that cation interstitials have low concentrations in TCOs —for example, Lany's calculations suggest 10^7 cm^{-3} and 10^{14} cm^{-3} for $In_2O_3$and ZnO respectively [Lany and Zunger, 2007]—and given that they have a formation energy much higher than that of V_{O} , it is less likely that In_i or Zn_i will form a stable defect in $In_2O_3$and ZnO as compared with V_{O} [Lany and Zunger, 2007].

Extrinsic dopants

Besides increasing the V_{O} density, substitutional atoms are effective dopants in TCOs [Chopra and Das, 1983]. Substitutional dopants can lead to enormous N_e values of up to 10^{21} cm^3. The dopants must have high solubility [Hall and Racette, 1964] in the undoped TCO to avoid dopant-clustering and compensation of defects [Agoston et al., 2010]. A common doping strategy is to use atoms from the group to the right of the cations in the periodic table, i.e. use an atom with one valence electron more than the metal cation of the oxide. For example, Sn^{4+} is used as a substitute for In^{3+} in In_2O_3, Al^{3+} is used as a substitute for Zn^{2+} in ZnO, and Sb^{3+} is used as a substitute for Sn^{4+} in SnO_2. In addition, oxygen substitution might also lead to TCO doping, e.g. F^{1-} substitutes O^{2-} in SnO_2 to form SnO_2 :F.

Nevertheless, dopants are not constrained to this rule of the thumb. For example, doping of SnO_2 with fluorine, lanthanum or molybdenum also leads to high N_e values on the order of 10^{20} cm^{-3} to 10^{21} cm^{-3} [Stjerna et al., 1994, Niedermeier et al., 2017, Dixon et al., 2016, Peng et al., 2016, Arai et al., 2017] and it is possible to achieve conductivities of 10^4 S cm^{-1} [Agashe et al., 1988]. Titanium, zirconium, molybdenum, tungsten and cerium have all beer reported as effective alternatives to Sn to dope In_2O_3 [Kobayashi et al., 2015, Delahoy and Guo, 2005, Koida and Kondo, 2006, Koida et al., 2018, Warmsingh et al., 2004].

Atomic hydrogen may be trapped in the film during deposition, and should be considered as a possible dopant [King et al., 2009, Limpijumnong et al., 2009, Bekisli et al., 2011, Hlaing Oo et al., 2010, Hanyu et al., 2013, Tang et al., 2015]. Computational and experimental evidence suggested that hydrogen, rather than $V_O^{\bullet\bullet}$, is the main source of free carriers in In_2O_3, SnO_2 , and ZnO [Limpijumnong et al., 2009, Singh et al., 2008, Van De Walle, 2000, King et al., 2009, Jiang et al., 2016, Hofmann et al., 2002, Mizokawa and Nakamura, 1974].

---

[5] Convention used to describe the electric charge and the lattice position of point defects in a crystal structure. For example $\mathrm{V}_{\mathrm{O}}^{\bullet\bullet}$ corresponds to a vacancy with double positive charge in the lattice site of oxygen. In case of interstitials, the subscript has an "i".

1.2.4 Effect of dopants on the optical properties of TCOs

The Drude model and free-carrier absorption

The Drude model applies the kinetic theory of gases to the electrons in metals. This seems an unlikely model since both physical systems are strikingly different, but to overcome these differences, the model makes certain assumptions:

1. Between collisions, the electron-electron and electron-ion interactions are neglected. Hence, in the absence of an electric or magnetic field, the electrons follow a straight line. If an electromagnetic field is applied, the electron follows Newton's laws of motion.
2. Collisions are considered to be instantaneous, and change the momentum of an electron.
3. The probability for an electron to experience a collision is $1/\tau$, where τ is known as the relaxation time[6].
4. Collisions are means for electrons to achieve thermodynamic equilibrium with the surrounding medium.

Therefore, if an external electric field is applied to a TCO, free electrons react following Newtons's laws of motion bounded to the atomic network of the solid. This is extremely useful, since we can use an optical experiment (the reaction to an electric field) to examine an electrical parameter (intragrain electron transport).

The reaction of electrons to an external electric field, can be described in terms of their complex dielectric function $\epsilon(\omega)$. $\epsilon(\omega)$ describes the physics of electrons in the TCO when excited by light with energy lower than the bandgap ($\hbar\omega << E_g$). This is achieved using a combination of Lorenz oscillators and the Drude model [Fujiwara and Kondo, 2005].

$$\epsilon(\omega) = (n - ik)^{1/2} = \epsilon_\infty \left(1 + \frac{\omega_p^2}{\omega^2 + i\omega\Gamma}\right) \tag{1.18}$$

where n is the refractive index, k is the extinction coefficient (the absorption coefficient is calculated using $\alpha = 4\pi k/\lambda$) , ϵ_∞ is the dielectric function at high frequency, $\Gamma = e/(\mu_{opt} m^*)$ or the inverse of the averaged relaxation time (τ^{-1}) and ω_p is the plasma frequency

---

[6] τ is also known as the collision time or the mean free time.

$$\omega_p = \left(\frac{e^2 N_{opt}}{\epsilon_0 \epsilon_\infty m^*} \right)^{1/2} \tag{1.19}$$

where m^* is the effective mass, N_{opt} is the optical free-carrier density and ϵ_0 is the vacuum permittivity (8.85×10^{-12} F m^{-1}).

Effective mass, optical mobility and optical free-carrier density

In Equations 1.18 and 1.19, the optical mobility (μ_{opt}) and optical free-carrier density (N_{opt}) and the effective mass (m^*) are required. These values can be extracted from fitting Fourier transform infrared (FTIR) reflectance measurements with the Drude model (See Section 2.3.2). If an electron absorbs the energy of an incoming photon (in the infrared regime), it is possible to approximate the mean free path of electrons using [Knoops et al., 2015]

$$l_{mfp} = \left(\frac{2E_p m^* \mu^2}{e^2} \right)^{1/2} \tag{1.20}$$

where E_p is the energy of the photon, μ is the electron mobility and e is the charge of the electron. For an μ of 100 cm^{2}V^{-1}s^{-1} , m^* of $0.3m_e$ and photon energies between 0.06 eV and 1.2 eV (typical energy range in FTIR), the mean free paths obtained are 20.6 nm and 4.5 nm, respectively. The l_{mfp} range is small compared to the grain sizes of a TCO with μ_e of 100 cm^{2}V^{-1}s^{-1} , e.g. typically 300 nm. Hence, it is possible to approximate μ_{opt} to as $\mu_{intragrain}$. Moreover, most of the TCOs explored in Chapters 3 and 4 are amorphous, and due to the absence of grain boundaries it is also possible to approximate μ_{opt} as μ_e . Finally, assuming that $N_{opt} = N_e$, it is possible to obtain the m^* if the plasma frequency is measured optically.

Plasma frequency and free-carrier absorption

The plasma frequency (Equation 1.19) describes the collective oscillation of free electrons in a conductive medium. The interaction of light with the electrons in the conduction band can be explained in terms of ω_p and its corresponding energy ($E_p = \hbar\omega_p$). If an incoming photon has energies considerably higher than the plasma energy (but still lower than the fundamental absorption of the TCO), the light does not interact with the electrons and is transmitted. If light has the same energy as the plasma wavelength, i.e. $\omega = \omega_p$, the photon is fully absorbed as the electron gas couples strongly with light. The photon's energy thermalizes due to the damped oscillation. On the other hand, if the photon has lower energy than the plasma energy, the electrons can oscillate easily at the same frequency as the light. As the energy decreases as compared with E_p, the free carriers oscillate in anti-phase to the exciting electric field, light cannot be transmitted in the solid, and the photons are reflected. The free-carrier absorption can be derived from Equation 1.18 by dividing the equation into the real and the complex part:

$$\begin{aligned}\epsilon_r &= \epsilon_\infty\left(1-\frac{\omega_p^2}{\omega^2+\Gamma^2}\right)\\ \epsilon_c &= \epsilon_\infty\left(\frac{\omega_p^2\Gamma/\omega}{\omega^2+\Gamma^2}\right)\end{aligned} \tag{1.21}$$

Typically, TCOs have $\tau \approx 10^{-14}$ s at room temperature, hence it is safe to make the approximation $\omega\tau >> 1$ at frequencies near the visible part of spectra. This leads to $\epsilon_r \approx \epsilon_\infty$ and $\epsilon_c << \epsilon_r$. Hence it is possible to find the solution to Equation 1.18 with $n = \sqrt{\epsilon_\infty}$ and $k = \epsilon_c/2n$. Replacing this into $\alpha = 4\pi k/\lambda$, we obtain an expression for free-carrier absorption

$$\alpha_{FCA} = \frac{\lambda^2 e^3 N_{opt} d}{4\pi^2 \epsilon_0 c^3 n m^{*2}\mu} \tag{1.22}$$

where c is the speed of light, λ is the wavelength ($\lambda\omega = c$) and d is the thickness of the film. Hence α_{FCA} is proportional to N_e/μ, which are the parameters controlling the conductivity in TCOs. Since metals have $N_e \approx 10^{22}$ cm^{-3} , the plasma energy lies in the ultraviolet part of the spectrum, light is reflected in the visible and this reflectance increases with wavelength at a rate of λ^2. TCOs have N_e between 10^{19} cm^{-3} and 10^{21} cm^{-3} and the plasma wavelength lies in the near infrared part of spectrum. For this reason TCOs are commonly used as windows which reflect infrared radiation. For example, heavy doping of In_2O_3:Sn can result in large-area films with average R$_{sheet}$ of 2 Ω/sq and total transmittance near 80% in the visible part of the spectrum and 80% reflectance in the infrared [Oyama et al., 1992, Granqvist, 2007].

1.2.5 Interband transitions, Burstein-Moss shift and optical bandgap in TCOs

In TCOs, the interactions between oxygen and metal orbitals create quantitatively similar electronic structures in the most common types of TCOs (SnO_2 , $In_2O_3$and ZnO, see Figure 1.6). While the valence band (E$_V$) of TCOs is formed by the bonding and non-bonding O 2p states, the conduction band (E$_C$) is formed by the anti-bonding metal s - oxygen p interactions. The energy difference between E$_C$ and E$_V$ generates the fundamental bandgap (E$_g$), which in hand determines the fundamental absorption o TCOs. An interband electronic transition occurs when electrons are excited from the maximum of the valence band (VBM) to the minimum of the conduction (MCB). For this process to be mediated by light, the photon's energy must be higher than that of the bandgap ($\hbar\omega > E_g = E_C - E_V$). If the CBM and the VBM share the same κ value, the transition is known as direct (Figure 1.6). Otherwise the transition is indirect and is usually mediated by a phonon [Pankove, 2012]. Calculated bandgaps for crystalline SnO_2 [Kılıç and Zunger, 2002], In_2O_3 [Mryasov and Freeman, 2001] and ZnO [Özgür et al., 2005] are found to be direct, nonetheless deviations from pristine crystalline structures could allow transitions otherwise forbidden [Fuchs and Bechstedt, 2008].

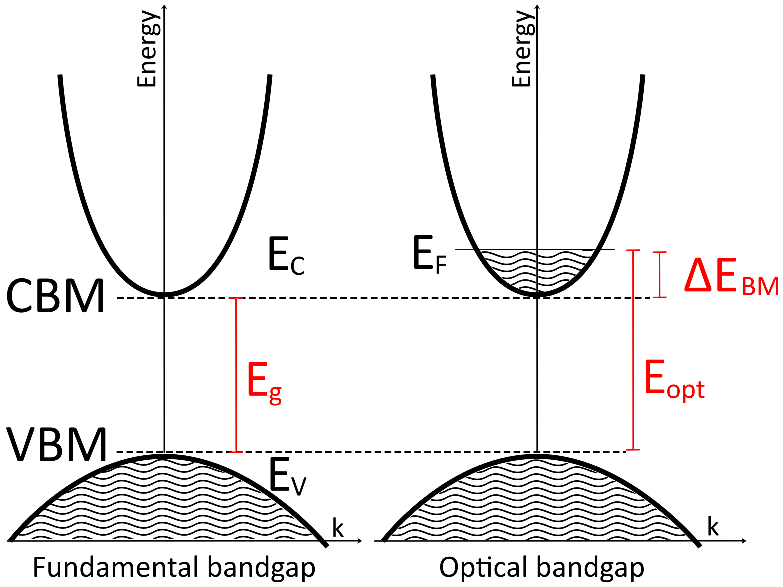

Figure 1.6 – Representation of (a) the fundamental bandgap in an intrinsic direct semiconductor (E_g) and (b) the optical bandgap (E_{opt}) in a degenerate semiconductor. In degenerate semiconductors, the Fermi energy (E_F) is inside the conduction band, hence there is a shift of the optical bandgap to higher energy. This energy difference is known as the Burstein-Moss shift (ΔE_{BM}).

Additionally, in degenerate semiconductors the Fermi energy (E_F) is inside the conduction band. Hence the lowest available energy state has higher energy than CBM. Therefore allowed optical transitions occur from VBM to the minimum empty state in the conduction band (represented in Figure 1.6(b)). Thus optical transitions in degenerate semiconductors have an energy of

$$E_{opt} = E_g + \Delta E_{BM} \tag{1.23}$$

where ΔE_{BM} is known as the Burstein-Moss shift [Burstein, 1954, Moss, 1954]. Since TCOs are mainly degenerate semiconductors, an absorption process occurs if the energy of photons is $\geq E_{opt}$. Therefore in this context, E_{opt} is known as the optical bandgap.

Parametrization of optical properties in amorphous transparent conductive oxides.

In crystalline semiconductors, the optical absorption is closely linked to the wave-vector (k) of a crystal. In amorphous semiconductors (and amorphous TCOs), the absence of long-range order makes impossible the application of Bloch's theorem and the crystal momentum ($\hbar k$), therefore a formalism alternative to the Drude Model is required to describe optical transitions. Even in the absence of a k-space, the density of states (DOS) is a meaningful concept in amorphous materials. In fact, optical absorption experiments have shown that in amorphous semiconductors, the density of states can be separated in a VB and a CB just as in crystalline materials [Pankove, 2012, Adachi, 2012]. In general, the DOS of amorphous semiconductors deviates from the crystalline counterpart in having (i) tail states attributed to the disorder of the atomic arrangement and (ii) localized deep subgap states which are usually attributed to dangling bonds. These results in an absorption coefficient as illustrated qualitatively in Figure 1.7. Regions A and B arise from fully coordinated amorphous network, while region C results from optical transitions involving the deep localized states.

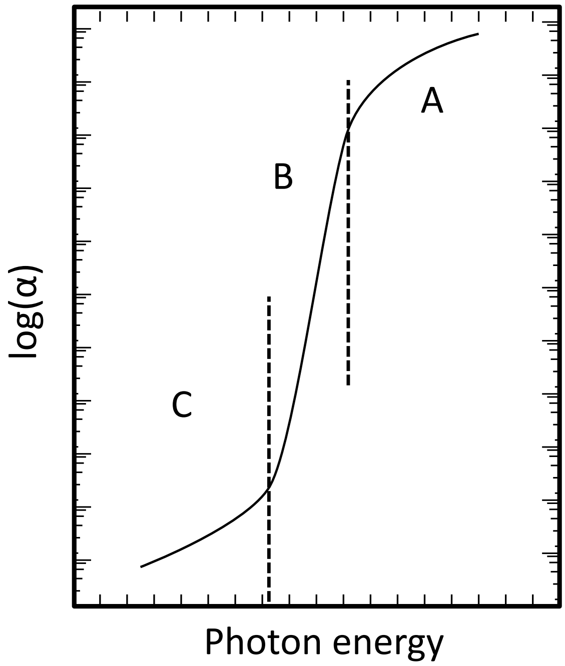

Figure 1.7 – Illustration of the optical absorption of an amorphous semiconductor. The absorption is divided in three regions: Region A corresponds to the strong absorption edge, region B corresponds to the absorption involving transitions between band tails (known as Urbach region) and region C describes transitions within deep subgap states

The strong absorption (region A) is usually attributed to band-to-band transitions, and α can be described by the relation

$$E\alpha \sim (E - E_{opt})^n \tag{1.24}$$

where n is a constant between 2 and 3 [Adachi, 2012]. At lower energies, transitions between band-tails result in an α which depends exponentially of the energy. This region is known as the Urbach region (region B) [Pankove, 2012]. The absorption coefficient in this spectral region is described by

$$\alpha \sim \exp(E/E_U) \tag{1.25}$$

where E_U is known as the Urbach energy, and it is the width of the exponential tail. The absorption from Region C corresponds to transitions within deep subgap states, usually attributed to dangling bonds. The absorption represented in region C is also described by an exponential equation

$$\alpha \sim \exp(E/E_t) \tag{1.26}$$

with E_t is always larger than E_U [Adachi, 2012]. Therefore, E_t is a measurement of the density of dangling bonds in the amorphous semiconductor [Sha et al., 2010].

Parametrization of optical properties of amorphous semiconductors was refined by Jellison and Modine [Jellison and Modine, 1996]. They combined the Tauc joint density of states and the Lorentz oscillator model to obtain the complex part of the dielectric function, $\epsilon_{c_{TL}}$. The real part of the dielectric function is obtained by the Kramers-Kronig relations. The resulting ϵ_c is described by

$$\begin{aligned} \epsilon_{c_{TL}}(E) &= \frac{AE_0C(E-E_g)^2}{(E^2-E_0^2)^2+C^2E^2}\frac{1}{E} \qquad \text{for} \qquad E > E_g \\ \epsilon_{c_{TL}} &= 0 \qquad \text{for} \qquad E \leq E_g \end{aligned} \tag{1.27}$$

while the real part of the dielectric function is obtained by solving the equation

$$\epsilon_{r_{TL}}(E) = \epsilon_r(\infty) + \frac{2}{\pi}P\int_{E_g}^{\infty}\frac{\xi\epsilon_{c_{TL}}(\xi)}{\xi^2-E^2}d\xi \tag{1.28}$$

where P is the Cauchy principal part of the integral. The solution of this integral can be found in reference [Jellison and Modine, 1996]. This parametrization has been used to described the origin of subgap states in a-IGZO, CdO, crystalline and amorphous $In_2O_3$and ZnO among others TCOs [Kamiya et al., 2009a, Liu et al., 2016, Koida et al., 2012, Sorar et al., 2011, Fujiwara and Kondo, 2005].

1.2.6 Summary of TCO properties

The most common TCOs are based on four different oxides: In_2O_3, SnO_2 , ZnO and cadmium oxide (CdO). Their physical properties, mineral nomenclature and dopants are summarized in Table 1.1.

Table 1.1 – Physical properties of In_2O_3, ZnO, SnO_2 and CdO. The table is adapted from references [Batzill and Diebold, 2005], [Ellmer, 2001], and extended with data from references [Madelung, 2012, Aldred and Pratt, 1963, Patnaik, 2003, Jefferson et al., 2008, Schleife et al., 2011]

Property	**In_2O_3**	**ZnO**	**SnO_2**	**CdO**
Mineral name	--	Zincite	Cassiterite	Monteponite
Abundance of the metal in the Earth's crust (ppm)	0.1	132	40	0.2
Crystal structure	cubic, bixbyite	hexagonal, wurtzite	tetragonal, rutile	cubic, rocksalt
Space group	$I2_13$	$P6_3mc$	$P4_2mnm$	Fm3m
Lattice constants (nm)	a = 1.012	a = 0.321 b = 0.5207	a = 0.474 b = 0.314	a = 0.469
Density (g cm^{-3})	7.12	5.67	6.5	8.15
Thermal expansion coefficient (RT) (10^{-6} °C^{-1})	6.7	∥c: 2.92 ⊥c: 4.75	∥c: 3.7 ⊥c: 4.0	14
Melting temperature (°C)	2190	2240	>1900	1426
Melting temperature of metal (°C)	157	420	232	321
Vapour pressure of metal at 500 °C (mbar)	1.3×10^{-6}	13.3	6.6×10^{-9}	0.01
Heat formation (eV)	9.7	3.6	6.0	2.67
Bandgap (eV)	3.75 (direct)	3.4 (direct)	3.6 (direct)	2.18 (direct)
Static dielectric constant	9	∥c: 8.75 ⊥c: 7.8	∥c: 9.6 ⊥c: 13.5	21.9
Single crystal electron mobility (cm^{2}V^{-1}s^{-1}) for a free-carrier density of (cm^3)	220 for (10^{17}) 60 for (1.1×10^{19})	205 for (10^{16}) 40 for (10^{20})	103 for (2.7×10^{17}) 15 for (8.0×10^{18})	180 for (10^{19}) 110 for (1.8×10^{19})
Experimental electron effective mass (m^*/m_0)	0.3	0.28	∥c: 0.23 ⊥c: 0.26	0.2
Common extrinsic dopants	Sn, Ti, Zr, F, Cl, Sb Ge, Zn, Pb, Si, Mo W, Ce	B, Al, Ga, In, Si Ge, Ge, Sn, Y, Sc, Ti, Zr, Hf, F, Cl	Sb, F, Cl, La, Nb Ta	Sn, In, Al, F

Amorphous TCOs and amorphous oxide semiconductors (AOS) can be processed at relatively low temperatures ($T < 350$ °C), yet they have optoelectronic properties similar to their crystalline counterparts. In Table 1.2 we listed the process temperature, the electrical and optical properties of representative amorphous TCOs. A comprehensive study of amorphous TCOs, AOS and their application in thin film transistors can be found in reference [Wager et al., 2008]

Table 1.2 – Optoelectronic properties and process temperature of representative amorphous TCOs. The data from the TCOs was obtained in references [Orita et al., 2001, Hosono et al., 1996a, Yasukawa et al., 1995, Fortunato et al., 2006, Yaglioglu et al., 2006, Kumar et al., 2005, Utsumi et al., 2003, Minami et al., 1994]

Amorphous TCO	**Optical properties**	**$N_e(10^{19}cm^{-3})$**	**μ ($cm^2V^{-1}s^{-1}$)**	**σ (Scm^{-1})**	**Process T (°C)**
$InGaO_3(ZnO)_m(m<4)$	E_g = 2.8 eV - 3 eV	1 - 10	12 - 20	170 - 400	RT
2 $CdO \cdot PbO_x$	E_g = 1.6 eV	10	9	180	250 °C
$AgSbO_3$	E_g = 2.3 eV	0.03	7	0.1	500 °C
In_2O_3 - ZnO 10 %	TT = 85 % (visible)	20 - 35	60	2000	200 °C
In_2O_3 - ZnO 10 %	--	20	52	1665	350 °C
In_2O_3 - ZnO 15 % - 48 %	E_g = 2.66 eV - 3.05 eV	12 - 35	60 - 70	2500	RT
In_2O_3 - SnO_2	70 % - 80 %	435	40	2800	RT - 300 °C
$ZnSnO_3$	TT = 80 % (visible)	1 - 10	10 - 20	250	RT - 300 °C

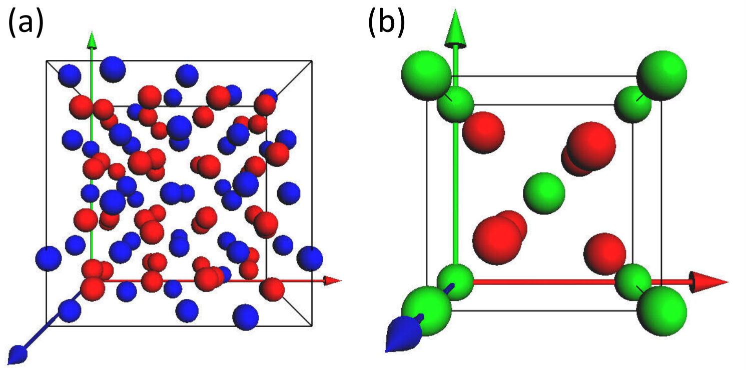

Figure 1.8 – Schematic of (a) the SnO_2 rutile structure and (b) the In_2O_3bixbyite structure. The O atoms are in red, the Sn atoms are in green and the In atoms are blue.

Given that this work is focused on the Sn- and In-based host-TCOs, we will show the crystal structure, band structure and typical density of states of these two materials. Figure 1.8(a) and (b) shows the crystal structures of SnO_2 and In_2O_3 respectively. SnO_2 crystallizes with a rutile structure with lattice parameters $a = b = 0.474$ nm and $c = 0.314$ nm [Baur and Khan, 1971]. The local structure around tin atoms corresponds to a octahedral coordination by 6 oxygen atoms. In_2O_3 crystallizes in the bixbyite structure with a lattice parameter of 1.012 nm [Marezio, 1966]. This structure is composed of 80 atoms in a conventional cell (16 units of In_2O_3) and 40 atoms in the primitive cell. It has two non-equivalent sites for indium cations, known as b-site and d-site. Locally, the oxygen anions are octahedral coordinated around indium atom, i.e.

every indium is surrounded by six oxygen atoms and two structural vacancies [Buchholz et al., 2014a].

The electronic density of states and band structures for the host InO$_x$ and SnO$_x$ TCOs are presented in Figure 1.9. The band structure of In$_2$O$_3$ was obtained using first principles-based density functional theory (DFT) calculations [Mi et al., 1999]. The density of states was calculated using a first-principles electronic-structure calculation using a discrete variational $\chi\alpha$ method [Tanaka et al., 1997]. The density of states of SnO$_2$ was calculated using a self-consistent-field scattered-wave molecular-orbital cluster approach, and its band structure was calculated using an augmented-spherical-wave supercell approach [Mishra et al., 1995].

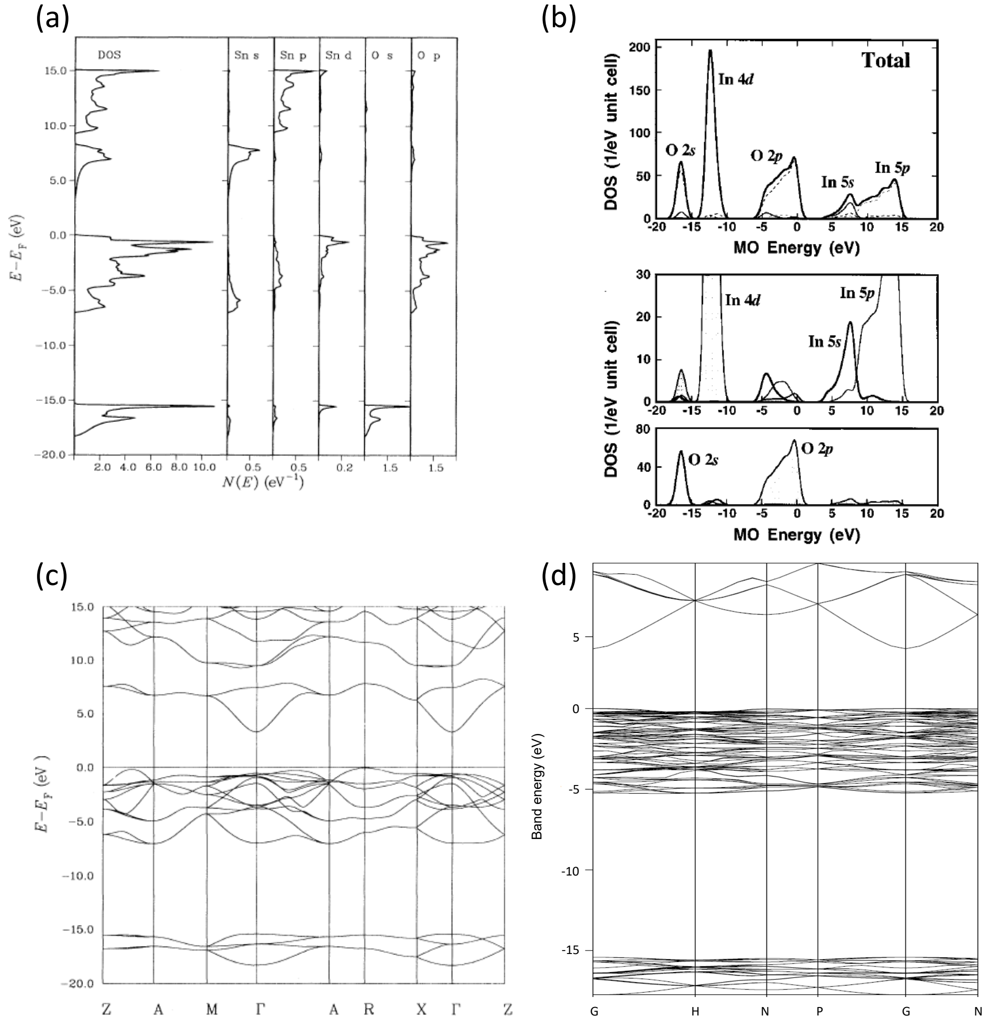

Figure 1.9 – Calculated total and partial density of states of (a) SnO$_2$ and (b) In$_2$O$_3$(reproduced from [Mishra et al., 1995] and [Tanaka et al., 1997]) and band structure of (c) SnO$_2$ and (d) In$_2$O$_3$(taken from [Mishra et al., 1995] and [Mi et al., 1999] respectively)

TCOs are widely used in industrial-scale applications, such as light-emitting diodes, thin-film transistors, infrared-reflecting coatings, electro-chromic or smart windows, gas sensors, flat-panel displays and electrodes in solar cells. Each of these applications has specific demands from the electrical and optical properties. In the context of this work, the application of TCOs in photovoltaic devices is crucial. Optimizing the optoelectronic properties of TCOs could result in higher conversion efficiencies in solar cells.

Given its chemical and thermal stability, F-doped SnO_2 has been widely used as a front electrode is several thin-film solar cells, and is currently playing a key role in the development of hybrid perovskite solar cells [Werner et al., 2018]. Furthermore, SnO_2 has been demonstrated as electron-selective contact in this same type of cells [Correa Baena et al., 2015]. A recent report by Albercht et al. [Albrecht et al., 2016] fabricated a silicon/perovskite tandem solar cell with three TCOs. At the back of the silicon wafer, aluminium-doped ZnO (ZnO:Al) was applied as an optical spacer and interfacial layer between the silver contact and the silicon. At the front of the silicon heterojunction cell, In_2O_3:Sn was deposited and SnO_2 was deposited via atomic layer deposition. The combination of SnO_2 and In_2O_3:Sn forms a recombination layer between the silicon and the perovskite cell. Furthermore, after the deposition of the perovskite solar cell, In_2O_3:Sn was deposited as the electrode facing the light (Figure 1.10). Tuning the optoelectronic properties of each of these TCOs is essential to achieve an optimal efficiency.

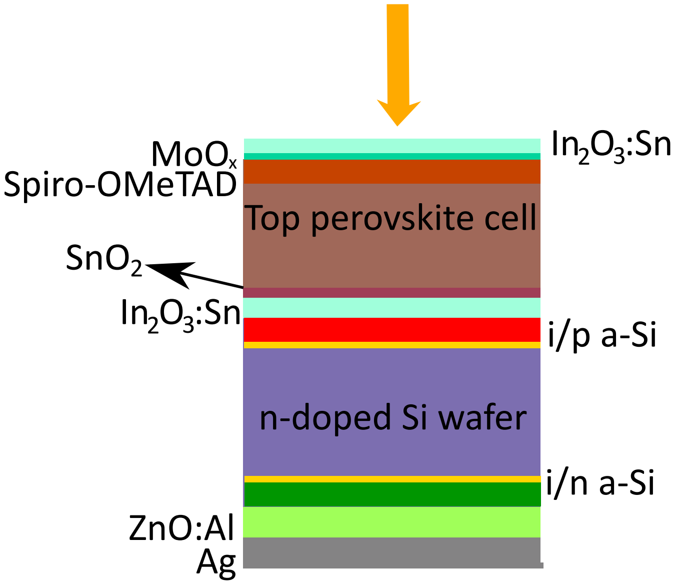

Figure 1.10 – Schematic representation of a monolithic tandem solar cell using ZnO:Al, In_2O_3:Sn and SnO_2 in the design. Adapted from [Albrecht et al., 2016].

In the top In_2O_3:Sn facing the light, low broadband optical absorptance and low R_{sheet} are required to maximize the light entering the tandem solar cell and to collect the charge. The recombination junction and the back ZnO:Al layer have more relaxed electrical constraints since lateral electron transport is not needed. Nonetheless the optimal optical coupling is required to avoid reflectance losses.

In the next section, the TCO requirements for silicon heterojunction solar cells are discussed in detail in terms of optical and electrical properties.

1.2.7 Transparent conductive oxide design for silicon heterojunction photovoltaics

Silicon heterojunction (SHJ) solar cells use a combination of intrinsic and doped hydrogenated amorphous silicon (a-Si:H(i) and a-Si:H(p^+/n^-)) for passivation and charge selection. This a-Si(i/p^+ or i/n^-) stack is not sufficiently conductive to transport the charge laterally to the silver fingers. Hence SHJ solar cells require a layer with electric conductivity for lateral charge transport with E_{opt} wide enough to allow the entrance of light to the active layers of the solar cell.

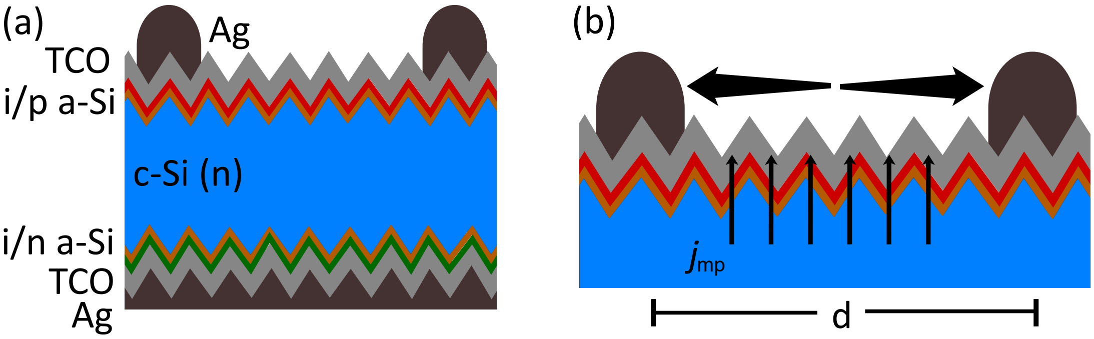

Figure 1.11 – (a) Sketch of a silicon heterojunction (SHJ) solar cell with an n-type crystalline silicon wafer. (b) Diagram of current collection in the front TCO.

Even though these requirements are fulfilled to a large extent by existing TCOs, optimizing these films is crucial to increase the efficiency of the solar cells. The transparency of the films allows incoming photons to enter the active layers of the solar cell, thus a highly transparent electrode can increase the photogenerated current. A highly conductive TCO can reduce the series resistance of the full solar cell, which ultimately leads to a high conversion efficiency. Nonetheless, given the entanglement between optical and electrical properties, it is very difficult to improve the one without affecting the other.

Electrical requirements for TCOs in SHJ solar cells

At the front (light-facing side for standard technology) of the SHJ solar cell, the TCO film acts as an electrical contact that transports charge laterally to the silver fingers. To ensure a negligible contribution of the sheet resistance of the TCO to the total series resistance losses, R_{sheet} of the front TCO should be $< 100\ \Omega/sq$ [De Wolf et al., 2012, Battaglia et al., 2016]. At the back of the cell, TCOs usually act as an interfacial layer to improve the contact resistance between the doped a-Si and the silver, while acting as an optical spacer between the semiconductor and the silver. Nonetheless the electrical requirements for the back TCO are more relaxed than for the front TCO [Holman et al., 2013, Bivour et al., 2014]. In the TCOs, Joule heating is responsible for a relative power loss of

$$\frac{\Delta P}{P} = \frac{j_{mp}(d/2)^2 R_{sheet}}{3V_{mp}} \tag{1.29}$$

where $\frac{\Delta P}{P}$ is the relative power loss, j_{mp} and V_{mp} are the current density and voltage at the maximum power point, d is the distance between silver fingers, and R$_{sheet}$ is the sheet resistance. This calculation is an approximation, valid only for vertical current collection from the wafer to the TCO (Figure 1.11(b)). The relative power loss (Figure 1.12) for a SHJ solar cell with j_{mp} = 38 mA cm^2 and V_{mp} = 620 mV decreases with R$_{sheet}$ and with d.

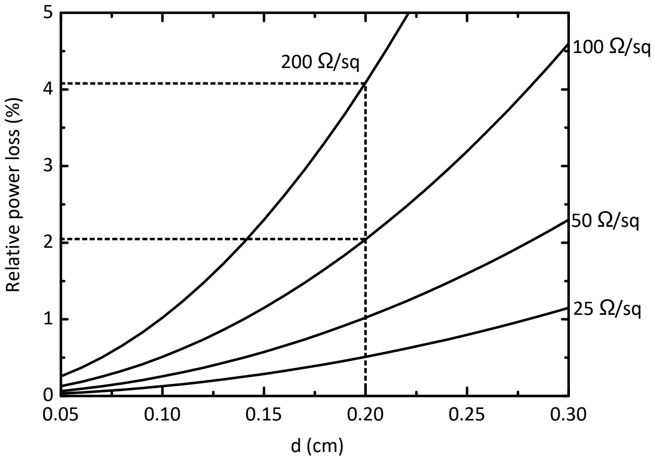

Figure 1.12 – Calculated relative power loss of a SHJ solar cell resulting from Joule heat in the TCO. The power loss is shown as function of the distance between silver fingers for TCOs with different R$_{sheet}$. The dashed lines mark the power loss for the typical finger geometry, a reduction from 4% to 2% power loss is expected from a decrease in R$_{sheet}$ from 100 Ω/sq to 50 Ω/sq. Note that this is an approximation that works as an upper boundary to the power loss in the TCO.

Thus, for a cell with d of 2 mm, and maintaining j_{mp} and V_{mp}, the relative power loss decreases from 4.1% to 2.0% when reducing the R$_{sheet}$ of the TCO from 100 Ω/sq to 50 Ω/sq. From Figure 1.12 the power loss decreases with d, but decreasing d in the cells results in increased shading from the silver fingers, which decreases the photogenerated current in the cell.

Optical requirements for TCOs in SHJ solar cells

Besides serving as a lateral transport medium, the front TCO layer in SHJ solar cells acts simultaneously as a window layer and as an anti-reflective coating. Optimally, we want the

TCO to be as transparent as possible in all spectral regimes and to decrease the reflectance of light out of the device, i.e. serve as antireflective coating. Reflection losses in a solar cell can result in a large fraction of the incident radiation being sent back to the incident medium without participating in carrier generation. Reflectance is determined by the difference between the refractive indices of the TCO and silicon. For normal incidence of light between two media with different refractive indices n_0 and n_1, reflectance is given by

$$R = \left(\frac{n_0 - n_1}{n_0 + n_1}\right)\left(\frac{n_0 - n_1}{n_0 + n_1}\right)^* \tag{1.30}$$

where the asterisk denotes the complex conjugate. In the case of incident light that is not normal, the polarization vector must be considered, but Equation 1.30 is a good approximation. For a TCO with refractive index n_{TCO} and thickness t, deposited over a substrate with refractive index n_s, destructive interference takes place if the condition

$$n_{TCO} \times t = \frac{(2m' + 1)}{4}\lambda_0 \tag{1.31}$$

where λ_0 is the wavelength of incoming light and m' is an integer. Hence for a TCO with a refractive index of 2, the reflectance for λ_0 = 600 nm is minimum for a TCO of thickness of ≈ 75 nm.

Considering just the absorption, TCO films can be tuned optically by changing N_e . An increase in N_e results in lower absorption in the ultraviolet part of spectrum due to a wider E_{opt} as predicted by the Burstein-Moss shift [Pankove, 2012]. However, as seen in Equation 1.22 increasing N_e also leads to higher absorption in the near-infrared part of spectrum due to free-carrier absorption as predicted by the Drude model. In addition, higher N_e also results in poor refractive index matching and additional reflectance of light [Holman et al., 2012]. A more quantitative description of the optical design rules for the front TCO can be found in reference [Holman et al., 2012].

The strategy: increasing electron mobility

The electrical and optical requirements for TCOs can be summarized as follows: a low R_{sheet} is needed to transport charge laterally (typical values of 50 Ω/sq to 100 Ω/sq [Battaglia et al., 2016]). In addition, given the absorption of silicon in the infrared, a more convenient trade-off for transparency is achieved by lowering N_e [Holman et al., 2012]. And, since the electric conductivity is defined as

$$\sigma = e\mu_e N_e \tag{1.32}$$

the most convenient way to increase conductivity of TCOs for SHJ solar cells is by increasing μ_e rather than N_e . Increasing μ_e results simultaneously in an increase in σ (therefore lowering R_{sheet}), and simultaneously a decrease in α_{FCA}, which decreases the parasitic absorptance and increases the photogenerated current in the solar cells.

1.3 This Thesis

This dissertation explores structure-property relations of tin-based and indium-based transparent conductive oxides with focus on a-ZTO and In_2O_3:Zr. It investigates electron transport and the optoelectronic properties of these materials and explains them in terms of the microstructure, atomic composition, and defects in the films. The main objective is to improve the optical and electrical properties simultaneously and explore multicompound disordered ZTO which will be later compared to high-μ_e indium-based oxides. Our strategy is to understand the mechanisms limiting the optoelectronic properties in disordered amorphous TCOs, and to overcome those limitations by (i) controlling the deposition conditions, (ii) post-deposition treatments or (iii) co-depositing TCOs with other materials to decrease the influence of the limiting defects.

1.3.1 Thesis outline

Chapter 1: Introduction. This chapter constructs a solid scientific foundation of transparent conductive oxides, reviewing concepts of semiconductor materials and presenting an overview of the properties of indium-based and tin-based TCOs. It also describes the importance of this research from a fundamental and a technical point of view with regards to solar cells.

Chapter 2: Thin-film fabrication and characterization techniques. This chapter describes the fundamental and technical aspects of the experimental techniques used for this thesis work.

Chapter 3: Defects and high-temperature passivation of amorphous zinc tin oxide. This chapter describes the defects governing the optoelectronic properties in amorphous zinc tin oxide. In addition we propose a high-temperature defect-passivation mechanism which results simultaneously in an increased of electron mobility and decreases optical absorptance.

Chapter 4: Alternative low-temperature passivation of tin-based oxides. This chapter describes an alternative passivation process for tin-based oxides through co-sputtering with

SiO_2 . A thorough explanation of the effects of silicon in tin-based TCOs is proposed, which complements the experimental results. In addition, the role of silicon and SiO_2 in the passivation of subgap defects is proposed based on material simulations and is supported by experimental results.

Chapter 5: Zirconium-doped indium oxide: transport mechanisms and applications in silicon heterojunction solar cells. This chapter describes the properties of high-mobility TCO materials based on indium oxide doped with zirconium. In addition, an explanation is given for the mechanisms limiting the electron transport in terms of the microstructure and the film's thickness. Finally the full potential of the material is exposed by comparing an optimized TCO film with the standard electrode in silicon heterojunction solar cells.

Chapter 6: Figure of merit TCO In previous chapters we have compared the optical and electrical properties of TCOs almost independently, using electron mobility to determine the optimal deposition conditions. In this chapter we introduce the figure of merit, which takes into account the electrical properties, and the optical properties weighted with the spectrum of the Sun in the wavelength range from 320 nm to 1200 nm. Using this figure of merit we compare the TCOs presented in this dissertation.

Chapter 7: Conclusions and perspectives Finally, in this chapter we summarize the main conclusions of the whole thesis, and we propose several research routes that could expand and complement the results from this dissertation.

Annex A. Co-sputtering of indium-based and indium-free TCOs for silicon heterojunction solar cells.

1.3.2 Contribution to the field

This thesis contributes to the field of TCOs based on SnO_2 and In_2O_3. Using our experimental results, correlated with density functional theory calculations, the following points are clarified:

- We identified V_O to be the cause of the sub-bandgap states in amorphous zinc tin oxide of specific composition $Zn_{0.05}Sn_{0.30}O_{0.65}$ (here labelled as a-ZTO). Conversely, we found that V_O are intrinsic donors in a-ZTO which increase the optical absorption and limit electron transport in the TCO.
- We demonstrate that passivation of V_O in a-ZTO can be performed by thermal treatments at temperatures between 400 °C and 500 °C in oxygen-rich atmospheres. We found that defect passivation decreases subgap absorption and increases electron mobility.

- We determined that the introduction of hydrogen into a-ZTO increases the free-carrier density but broadens the subgap absorptance. We propose that hydrogen atoms can influence the point-defects by: (i) introducing new defects in the bandgap of a-ZTO, (ii) shifting the existing defects deeper in the bandgap, and (iii) reducing the oxygen content in the films, therefore increasing the density of V_O .
- Using fluctuation electron microscopy and nanobeam electron diffraction, we demonstrate that thermal treatments up to temperatures of 500 °C do not significantly change the medium- or short-range order in a-ZTO.
- We demonstrate a new technique to passivate V_O in a-ZTO, which relies on co-sputtering of a-ZTO and SiO_2 . This method, performed completely at temperatures ≤ 200 °C , reduces subgap absorption in the TCO without significantly affecting the electrical properties.
- We show that, similar to a-ZTO, co-sputtering of SiO_2 and SnO_2 is equally effective at reducing the subgap absorption. Since SnO_2 and the co-sputtered films are polycrystalline, this demonstrates that the passivation route is useful in tin-based oxides regardless of their microstructure.
- Correlating our experimental results with density functional theory calculations, we propose that the effect of SiO_2 in tin-based TCOs is twofold: (i) oxygen from SiO_2 reduces the V_O , and (ii) a silicon atom near an undercoordinated tin atom promote the formation of doubly ionized V_O , which is a donor with energy close to the conduction band minimum.
- Annealing as-deposited In_2O_3:Zr films in oxygen-rich atmospheres results in an amorphous-to-crystalline transition. Conversely, we demonstrate that thermal treatments in reducing or neutral atmospheres results in nanometric-size crystallites embedded in an amorphous matrix.
- We demonstrate that ionized impurities and optical phonons limit electron transport in crystalline In_2O_3:Zr. In addition we show that depending on the film thickness, the dominant defects are either ionized impurities, or a combination of ionized point defects and optical phonons.
- We show that ionized impurity scattering originates from surface defects in In_2O_3:Zr films of thickness ≤ 50 nm.
- We demonstrate that, compared to thermal treatments in air, annealing in neutral or reducing atmospheres results in higher conductivity for films of thickness < 50 nm, as a high free-carrier concentration is maintained.

In summary, this thesis improves the understanding of the defects limiting the electron transport in a-ZTO and In_2O_3:Zr, and their effects on the optoelectronic properties. In addition we propose several routes to improve the optoelectronic properties in these TCOs either by defect tuning or structural transitions.

My doctoral work resulted in two peer-reviewed articles as main author ([Rucavado et al., 2017, Rucavado et al., 2018]) and one article in preparation and several peer-reviewed articles as co-author ([Werner et al., 2016, Nogay et al., 2017, Morales-Masis et al., 2018, Ingenito et al., 2018, Essig et al., 2018]).

2 Thin-film fabrication and characterization techniques

This chapter describes the basics of magnetron sputtering, the technique used in this work to deposit transparent conductive oxide (TCO) films. It also describes the characterization techniques used to study the electrical, optical and structural properties, as well as the composition of TCOs.

2.1 Radio frequency magnetron sputtering

Sputtering is a physical vapour deposition (PVD) technique. Formally, sputtering is the transfer of momentum from an incident energetic projectile to a solid target resulting in the ejection of surface atoms or molecules. The particles ejected from a target are deposited onto a previously chosen substrate. The basic steps for reactive radio frequency (RF) magnetron sputtering deposition are:

- The pressure in the process chamber is decreased using vacuum pumps. Note that the gaseous species in the process chamber might influence the final properties of the sputtered materials.
- A constant flow of an inert process gas is introduced into the chamber. In this work, argon (Ar) was used. In addition to argon, we introduced a constant flow of O_2, which tunes the intrinsic doping of the TCOs.
- An RF signal is applied using the target as the cathode. A plasma is formed of ionized argon atoms between the cathode and anode.
- The ionized argon atoms are accelerated towards the target by the potential difference between the plasma and the surface of the target (known as the plasma sheath).
- The collisions from the argon ions transfer kinetic energy to the target. This results in complex ion/solid interactions occurring simultaneously, among them the ejection of particles from the target (atoms and clusters of atoms) and the ejection of secondary electrons.

- The magnetic field from the magnetron confines the secondary electrons near the target, which increases the sputtering rate by increasing the number of collisions between the secondary electrons and the working gas. This confinement causes an erosion track (known as a "race track") in the sputtering targets.

- Due to the low pressure in the sputtering chamber, the particles ejected from the target can cross the length of the deposition system. Some of the particles arrive at the substrate and are deposited.

In this work, two sputtering systems were used: an Evatec Clusterline sputtering system for the films studied in Chapter 3 and a Leybold Univex sputtering system for the TCOs studied in Chapters 4 and 5. Both sputtering systems use Ar and O_2 as working gases and have planar target configurations. In addition, both deposition systems allow for the use of two targets simultaneously, which is ideal for co-sputtering and combinatorial material studies. The feasibility for co-sputtering was exploited to obtain the results of Chapter 4.

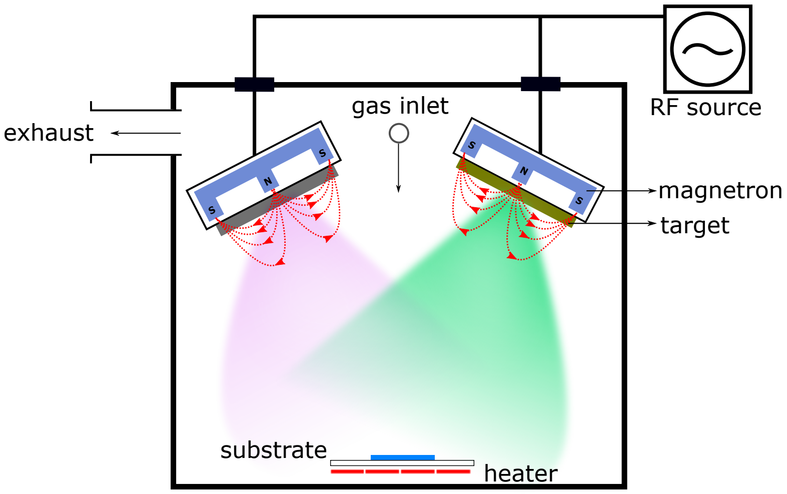

Figure 2.1 – Schematic representation of a radio frequency magnetron sputtering system with two targets.

2.1.1 Thin-film growth and co-sputtering

Ultimately, the structure of sputtered films is directly dependent on the formation of nucleation centres at the substrate's surface. The coalescence of these centres determines the final structure of the films. The film growth is determined by the flux of sputtered particles, the energy distribution of the ions, the adatom mobility, the adsorption probability, and the density of surface sites. Ultimately, these properties are controlled by the parameters during sputtering. In this regard, the Thornton model [Thornton, 1974] links the deposition parameters of a film with its structural properties. This model shows the link betwenn the microstructure of different metals (Mo, Cr, Ti, Fe, and Al-alloys) and the pressure during deposition, the deposition power and the ratio between the deposition temperature and the melting temperature. This model is applied to a full range of materials, e.g. in sputtered ZnO_2 [Kluth et al., 2003].

For this work, the pressure in the deposition chamber prior to sputtering was $< 10^{-6}$ mbar (base pressure). The working gas was a mixture of Ar and O_2. The flow ratio between these two gases is detailed in each chapter. The possibility to add O_2 to the working atmosphere is an advantage for the deposition of oxides, since the oxygen vacancies (V_O) can be tuned with the oxygen partial pressure. Depositions were done at either room temperature or temperature of 60 °C and 100 °C. The depositions discussed in Chapter 4 were performed using two targets simultaneously, a technique known as co-sputtering. By controlling the AC power in each target independently, i.e. the ion acceleration towards the target, it is possible to control the compositional ratio of the resulting films and design materials with target properties. Figure 2.1 shows a representation of a co-sputtering system with two different targets.

2.2 Electrical properties

2.2.1 Hall effect in the van der Pauw configuration

In 1879, while working on his doctoral thesis, Edwin Hall was trying to determine whether the force experienced by a current-carrying wire in a magnetic field was exerted in the whole wire or just upon the moving electrons on the wire. His experiment was based on the argument "if the electricity in a fixed conductor is itself attracted by a magnet, the current should be drawn to the side of the wire and therefore the resistance experienced should increase." Even though he did not measure this change in resistance, his efforts made it possible to measure a voltage transverse to the direction of the current, known today as the Hall voltage.

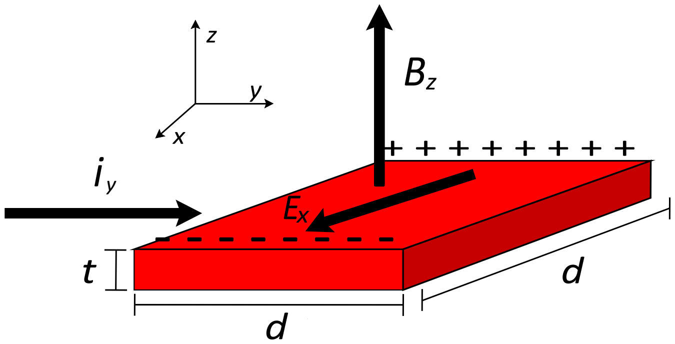

Figure 2.2 – Schematic depiction of the Hall effect experiment.

The Hall effect experiment is depicted in Figure 2.2. A current (i_y) is applied laterally to a conducting film of area d^2 and thickness t. A magnetic field ($\boldsymbol{B_z}$) is applied perpendicular to the film's surface (in teh z-direction). The magnetic field drives the electrons in the direction of x. However as soon the electrons encounter the border of the film they accumulate, charge builds up and creates the electric field E_x. This results in a charge difference between the edges of the film. The resulting Lorentz force is

$$\boldsymbol{F} = e\boldsymbol{E_x} + e\boldsymbol{v} \times \boldsymbol{B_z} \tag{2.1}$$

where $\boldsymbol{v}$ is the velocity of the electrons and e is the electron charge. In quasi-equilibrium, the forces are balanced, hence the force equation leads to

$$E_x = vB_z \tag{2.2}$$

which leads to a potential difference of

$$V_H = E_y d = vB_z d \tag{2.3}$$

where d is the length of the side of the film and V_H is the potential difference between the sides of the film, known as the Hall voltage.

As we know from the Drude theory for free electrons, the drift velocity of an electron is described by $\boldsymbol{v} = i_y / tdeN_{Hall}$, where N_{Hall} is the Hall free-carrier density hence the Hall voltage results in

$$V_H = \frac{i_y B_z}{N_{Hall} te} \tag{2.4}$$

Combining this result with the expression of mobility-dependent resistivity $\rho = \frac{1}{e\mu_{Hall} N_{Hall}}$ we obtain two expressions for the Hall mobility (μ_e) and free-carrier density (N_e)

$$\begin{gathered} N_{Hall} = \frac{i_y B_z}{V_H et} \\ \mu_e = \frac{1}{\rho N_{Hall} e} \end{gathered} \tag{2.5}$$

Since the thickness of the film is known, the only unknown parameter is the resistivity ρ. In this work, the Hall effect properties were measured with a HMS-5000 from Ecopia. This system measures the ρ using the van der Pauw configuration in which the contacts are placed in the corners of a square sample with vertices ABCD. Currents are applied between the non-adjacent corners of the sample while the voltage is measured in the other corners. The resistance can be calculated by solving numerically the Van der Pauw equation

$$\begin{gathered}\exp\left(\frac{-\pi R_1}{R_{sheet}}\right)+\exp\left(\frac{-\pi R_2}{R_{sheet}}\right)=1\\ \text{where}\\ R_1=\frac{1}{2}\left(\frac{V_{DC}}{I_{AB}}+\frac{V_{CD}}{I_{BA}}\right),\quad \text{and}\quad R_2=\frac{1}{2}\left(\frac{V_{AD}}{I_{BC}}+\frac{V_{DA}}{I_{CB}}\right)\end{gathered}\tag{2.6}$$

where R$_{sheet}$ is the sheet resistance. The voltages (V_{DC}, V_{CD}, V_{AD} and V_{DA}) and currents (I_{AB}, I_{BA}, I_{BC} and I_{CB}) are measured with the Hall setup and Equation 2.6 is solved numerically to obtain R$_{sheet}$. Using Equation 1.2, the resistivity (ρ) is obtained and can be used to solve Equation 2.5, therefore obtaining μ_e and N_e.

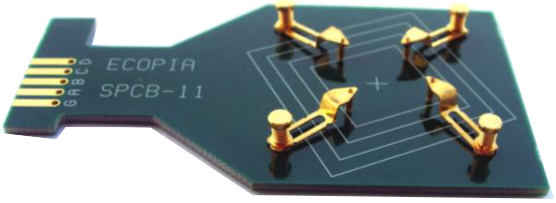

Figure 2.3 – Sample holder of the Hall effect experiment.

It is not intuitive that N_{Hall} and μ_{Hall} are equivalent to N_e and μ_e. In fact these properties differ from each other by a factor r such that [Orton and Powell, 1980]

$$\begin{aligned}N_e&=rN_{Hall}\\ \mu_e&=\frac{\mu_{Hall}}{r}\end{aligned}\tag{2.7}$$

where the coefficient r, known as the scattering factor, is a statistical parameter of the relaxation time of electrons dependent on the intensity of the magnetic field [Blood and Orton, 1978]. In the context of this thesis, we make the approximation of $r = 1$, since this value is normally used in degenerate semiconductors [Preissler et al., 2013].

To perform the Hall measurement, the HMS-5000 applies a field $\boldsymbol{B}$ with magnitude of 0.56 T. The outputs of the measurement are N_e, μ_e and the conductivity of the material. For the typical measurement, the sample should have a homogeneous thickness and be isotropic. The film and substrate should be positioned in the sample holder (Figure 2.3) and the contacts should be placed at the edges of the sample . The HMS-5000 is also able to perform temperature-dependent Hall effect measurements. For this, the measurement is performed in a dedicated sample holder. Usually, the sample holder is cooled to the temperature of liquid nitrogen temperature (-195 °C), and is then slowly heated to 75 °C . While heating, μ_e and N_e are measured at user-defined temperatures.

2.3 Optical properties

2.3.1 Ultraviolet-visible-near infrared spectrophotometry

An ultraviolet-visible-near infrared spectrophotometer with an integrating sphere was used to study the optical properties of the TCO films and the transparent glass substrate. This technique measures the intensity of light as a function of wavelength after transmitted and reflected from a TCO film, and it normalizes the results using between 100% and 0% transmittance and reflectance[1].

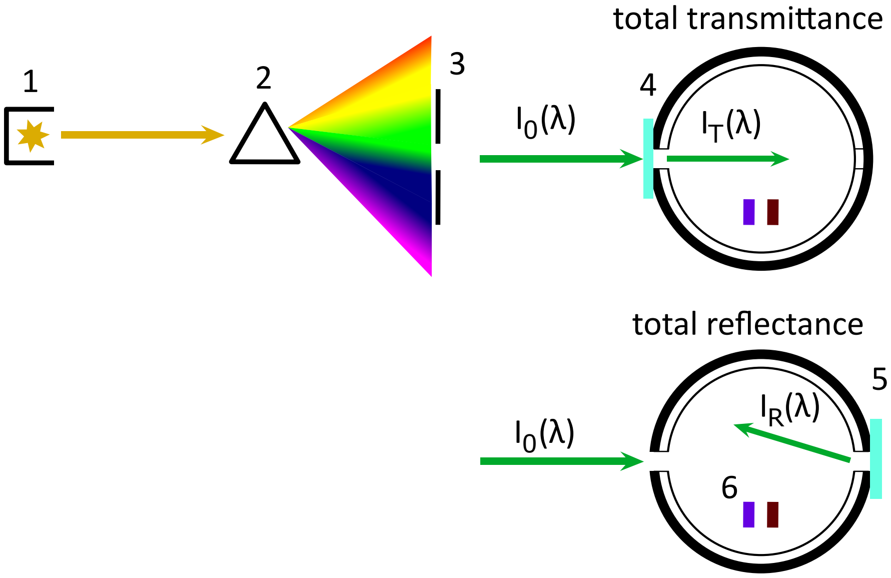

Figure 2.4 – Schematic diagram of the spectrophotometer. The numbers indicate (1) The light source which is either a tungsten-halogen lamp or a deuterium lamp. (2) The monochromator which separates light into its spectral components, i.e. filters light in terms of wavelength. For the measurements in this work, the monochromator filtered every 10 nm. (3) A slit, (4) The transmittance and (5) reflectance apertures in the integrating sphere. (6) Semiconductor-based light detectors, which are either silicon-based or indium-gallium-arsenide (InGaAs) based.

The spectrophotometer is composed of two light sources, a tungsten-halogen lamp which radiates light in the visible and near-infrared part of spectrum and a deuterium lamp which radiates in the ultraviolet (UV) part of spectrum. Furthermore the spectrophotometer has a monochromator, a slit, an integrating sphere made of sintered teflon (or Spectralon^{TM}), and a light detector (silicon-based for ultraviolet and visible and InGaAs-based for infrared).

---

[1] The 100% and 0% were spectra measured before each deposition. The 100% was measured by collecting all light with the integrating sphere, i.e. no sample, while the 0% was acquired by preventing light to arrive to the detector.

The total transmittance (TT) and total reflectance (TR) are collected as a function of wavelength. For the TT, the sample is placed in aperture (4), while for TR in aperture (5). For TCOs, the absorptance (A) as function of wavelength is calculated as $A(\lambda) = 1 - TT(\lambda) - TR(\lambda)$, which is a good approximation for highly transparent materials.

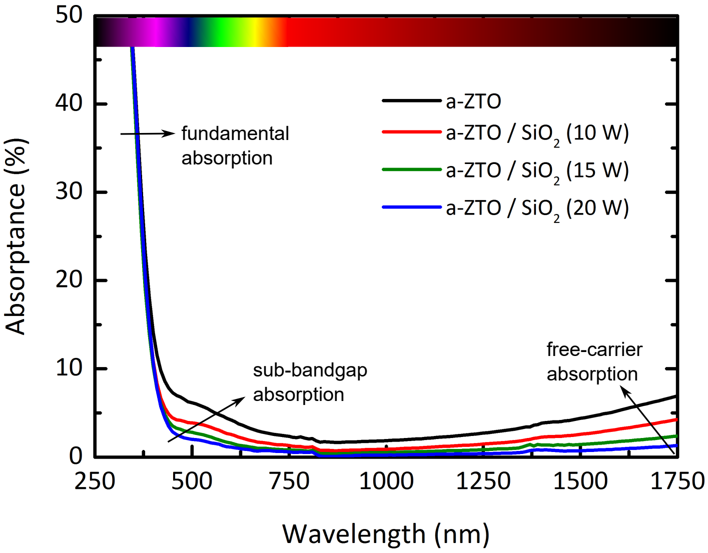

Figure 2.5 – Absorptance spectra as function of wavelength for a series of amorphous zinc tin oxide (a-ZTO) films modified with SiO_2 . For higher SiO_2 content, the films result in less absorptance in the visible and near-infrared regions of spectrum.

As light is transmitted (or reflected) in the sample, the light-solid interactions are wavelength-dependent. For TCOs, absorption in the UV reveals information about the optical bandgap of the material, while in the visible part of spectra the absorption unveils possible defects causing sub-bandgap absorption. Furthermore, the free-carrier absorption (α_{FCA}) is manifested as an increasing absorption in the near-infrared (Figure 2.5).

2.3.2 Fourier transform infrared spectrometer

The reflectance in the infrared part of the spectrum (from 1 μm to 25 μm) was measured with a Bruker Vertex 80 Fourier transform infrared spectrometer using a specular reflectance accessory. Given that the plasma wavelength (ω_p) of TCOs is in the infrared range, the interaction between TCOs and light in the infrared is dominated by reflectance (see Chapter 1). From the reflectance the optical properties and the effective mass were calculated by parametrizing using the Tauc-Lorentz model and the Drude Model for electric conductivity.

2.4 Structural and chemical properties

2.4.1 Transmission electron microscopy and energy dispersive X-ray spectroscopy

The TCO microstructure was investigated using transmission electron microscopy (TEM)[2] . The samples analysed by TEM were prepared by (i) extracting a lamella using the conventional focused-ion-beam lift-out technique in a Zeiss NVision 40 obtaining a cross section of the TCO film or by (ii) sputtering directly into a copper/carbon grid or a silicon nitride grid. The samples analysed in Chapters 3 and 4 were investigated using an FEI TITAN Themis (STEM EDX), while the films from Chapter 5 were studied using an FEI Tecnai Osiris operated at 200 kV. Energy dispersive X-rays (EDX) analysis was conducted using four silicon drift detectors [Schlossmacher et al., 2010].

2.4.2 Electron diffraction

Electron diffraction results from the inelastic scattering of electrons with the atomic lattice of the material. This technique is used widely in solid-state physics to determine the crystal structure (or the lack of) or the crystallographic orientation relationships between grains [Williams and Carter, 1996]. The structural results discussed in Chapter 3 were obtained with energy-filtered electron diffraction patterns, acquired in nanobeam conditions by scanning an electron probe in a raster over the thin sample with a FEI Titan S microscope operated at 300 kV. Information about the short-range order i.e. the first two coordination shells of a-ZTO, was obtained from radial profiles of diffraction patterns. Also in Chapter 3, information about the medium-range order of a-ZTO is discussed, i.e. from the third coordination shell to about 3 nm. This was assessed using fluctuation electron microscopy [Voyles and Muller, 2002] in the microscope by computing the normalized variance of 1200 diffraction radial profiles per sample and per probe size (1.5 nm for a convergence semi-angle of 0.5 mrad, 2 nm using 0.3 mrad, and 3 nm for 0.2 mrad). The fluctuation electron microscopy was performed in a probe Cs-corrected FEI TITAN microscope operated at 300 kV. The results of the nanobeam electron diffraction reported in Chapter 4, and of the selected area diffraction shown in Chapter 5 were obtained using an FEI Osiris microscope.

2.4.3 Thermal desorption spectroscopy

Thermal desorption spectroscopy (TDS) was performed using an ESCO (EMD-WA1000S) system equipped with a quadrupole mass spectrometer [3] (Figure 2.6). For the measurements, the base pressure of the chamber was set to 10^{-9} mbar and samples of 1×1 cm^2 were heated with a halogen lamp at a constant rate of 20 °C min^{-1} up to 700 °C . All of the films were deposited on substrates of undoped crystalline silicon. The background sample was measured for a (100-oriented) undoped c-Si wafer with an area of 1×1 cm^2.

---

[2] The TEM experiments were performed either in the Ernst Ruska-Centre for Microscopy and Spectroscopy with Electrons in Jülich, Germany, or in the Interdisciplinary Centre for Electron microscopy, Lausanne, Switzerland.

[3] TDS experiments were performed in the Compound Semiconductor Thin-Film Group at the National Institute of Advanced Industrial Science and Technology (AIST) in Tsukuba, Japan.

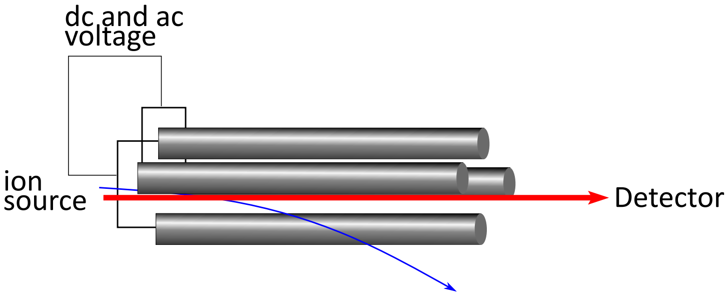

Figure 2.6 – Scheme of the quadrupole mass detector (QMD) used for thermal desorption spectroscopy (TDS).

The QMD is composed of four rods subjected to DC and AC voltages that filter the desorbed species based on their mass-to-charge ratio (M/z) and select them before detection. The TDS system has a detection limit of $\sim 10^{13}$ molecules.

2.4.4 Rutherford backscattering and elastic recoil detection analysis

The atomic composition of the films was obtained using Rutherford backscattering spectrometry (RBS) and elastic recoil detection analysis (ERDA)[4]. RBS was performed using 2 and 5 MeV He ions and a silicon PIN diode detector under 168 ° [Nastasi et al., 2014]. Hydrogen depth profiles were measured by ERDA with a 2 MeV He ion beam applying the absorber foil technique [Nastasi et al., 2014]. For ERDA, a mica substrate with a known hydrogen content was used as reference.

---

[4] Both techniques analyse the elastic collision between heavy ions and the films under study to obtain the chemical composition of the sample. The RBS measurements were performed either at EAG-laboratories, at the United States of America, or at the Laboratory of Ion Beam Physics at the Swiss Federal Institute of Technology Zurich (ETH).

3 Defects and high-temperature defect-passivation of amorphous zinc tin oxide

The results from Chapter 3 are based in the publications:

Rucavado, E., Jeangros, Q., Urban, D.F., Holovský, J., Remes, Z., Duchamp, M., Landucci, F., Dunin-Borokowski, R.E. Körner, W., Elsässer, C., Hessler-Wyser, A., Morales-Masis, M., Ballif, C. (2017). Enhancing the optoelectronic properties of amorphous zinc tin oxide by subgap defect passivation: A theoretical and experimental demonstration. *Physical Review B*, 245204:1-10

Werner, J., Walter, A., Rucavado, E.,Moon, S.-J., Sacchetto, D., Rienaecker, M., Peibst, R., Brendel, R., Niquille, X., De Wolf, S., Löper, P., Morales-Masis, M., Nicolay, S., Niesen, B., and Ballif, C. (2016). Zinc tin oxide as high-temperature stable recombination layer for mesoscopic perovskite/silicon monolithic tandem solar cells. *Applied Physics Letters*, 109(23):233902.

My original input and work in the manuscripts include: plan and execution of the sputtering and post-deposition thermal treatments of the a-ZTO films. All the electrical characterization, optical properties and thermal desorption spectroscopy measurements, as well corresponding data analysis. Interpretation of results and correlation with the computational calculations were discussed and planned with Dr. Morales-Masis and Dr. Urban for the PRB manuscript. Same experimental work (sputtering of a-ZTO and characterization of the films) were done for the APL article by myself as well. The data analysis and solar cell results were jointly discussed with Dr. Werner and co-authors.
I want to acknowledge Dr. Quentin Jeangros and Federica Landucci for the electron microscopy experiments and analysis, Dr. Daniel Urban and his collaborators for the density functional theory calculations, its interpretation and their correlation with the experimental results. I would also like to thank Dr. Takashi Koida for his support during the desorption spectroscopy and the following discussion, and Dr. Jérémie Werner for the development and characterization of the perovskite/silicon tandem solar cell

---

The text from reference [Rucavado et al., 2017] and reference [Werner et al., 2016] are reproduced and modified with permission from the publisher.

The link between sub-bandgap states and optoelectronic properties is investigated for amorphous zinc tin oxide (a-ZTO) thin films deposited by RF sputtering. a-ZTO samples were annealed up to 500 °C in oxidizing, neutral, and reducing atmospheres before characterizing their structural and optoelectronic properties by photothermal deflection spectroscopy, near-infrared-visible UV spectrophotometry, Hall effect, Rutherford backscattering, hydrogen forward scattering and transmission electron microscopy. By combining the experimental results with density functional theory calculations, oxygen deficiencies and resulting metal atoms clusters are identified as the source of sub-bandgap states, some of which act as electron donors but also as free-electron scattering centres. Hydrogen-atoms either create additional subgap states, or shift existing states, associated with oxygen deficiencies, deeper into the bandgap. Based on this detailed understanding of the different point defects present in a-ZTO, their impact on optoelectronic properties, and how they can be suppressed by post-deposition annealing treatments, an amorphous indium-free transparent conductive oxide,with a high thermal stability and an electron mobility up to 35 $\mathrm{cm^2V^{-1}s^{-1}}$, is demonstrated by defect passivation. Finally, given the high temperature stability of the microstructure and optoelectronic properties of a-ZTO thin films, the material was used as a recombination junction in a mesoscopic perovskite/silicon monolithic tandem solar which requires a high-temperature step during its processing.

3.1 Motivation and state of the art

As discussed in the introduction, in TCOs, point defects play an important role in the optoelectronic properties. A fine tuning of these defects is hence required to adjust the optoelectronic properties of TCOs depending on the desired application. In that regard, several research groups have used density functional theory (DFT) calculations to assess the structural origin of electronic states inside the bandgap. Körner et al. [Körner et al., 2012, Körner et al., 2014, Körner and Elsässer, 2014] developed a generic theory to explain the structural origin of sub-bandgap states in TCOs. It was demonstrated that uncoordinated oxygen generates deep states near the valence band, while oxygen deficiencies (or $\mathrm{V_O^{\bullet\bullet}}$ following the Kröger-Vink notation [Kroger and Vink, 1958]) and resulting metal atom clusters create shallow donor states near the conduction band edge. Experimentally, Jayaraj et al. demonstrated the interplay between oxygen concentration and localized sub-bandgap donors in pulsed-laser-deposited amorphous zinc tin oxide (Zn:Sn = 1:1 and 2:1) [Jayaraj et al., 2008]. Both low and high oxygen concentrations were found to result in low free-carrier concentration, as “free” electrons were numerous but trapped in localized states or low in number due to the small amount of donor states, respectively. Alternatively, Kamiya et al. [Kamiya et al., 2008a, Nomura et al., 2008] combined optical absorption measurements and DFT calculations to suggest that $\mathrm{V_O^{\bullet\bullet}}$ in amorphous $\mathrm{InGaZnO_2}$ may induce deep levels that could function as electron traps, instead of shallow donor states. In addition, they found that annealing in oxygen-rich atmospheres improved the electrical properties of the TCO by increasing the free-carrier concentration, an effect that was attributed to a reduction of localized sub-bandgap electron traps.

As mentioned in Section 1.2.3 , other studies have demonstrated that residual hydrogen, which may be trapped in the film during sputtering, and should be taken into account when between sources of subgap states in TCOs [King et al., 2009, Limpijumnong et al., 2009, Bekisli et al., 2011, Hlaing Oo et al., 2010, Hanyu et al., 2013, Tang et al., 2015]. Van de Walle and co-workers used DFT with the local density approximation and generalized gradient approximation (LDA and GGA, respectively) to suggest that hydrogen, rather than $V_O^{\bullet\bullet}$, is the main source of free-carriers by acting as a shallow donor in In_2O_3, SnO_2 , and ZnO [Limpijumnong et al., 2009, Singh et al., 2008, Van De Walle, 2000], in agreement with other reported experimental data [King et al., 2009, Jiang et al., 2016, Hofmann et al., 2002, Mizokawa and Nakamura, 1974].

Among the numerous TCO chemical compositions reported in literature [Ellmer, 2012, Morales-Masis et al., 2017b], amorphous zinc tin oxide has the following advantages: it is indium-free and hence low cost, and at a Zn/(Zn+Sn) composition of 0.1 has a stable microstructure at high temperature [Ko et al., 2007, Mereu et al., 2015, Zhu et al., 2014], presenting a total transmittance higher than 70% and an absorptance lower than 5% in the visible and near infrared [Minami, 1999, Frenzel et al., 2015, Morales-Masis et al., 2014], which makes it more transparent than commercially used indium tin oxide. Due to its amorphous microstructure, low surface roughness [Mereu et al., 2015], and low free-carrier density (i.e., restricted conductivity), it has been mainly applied in thin-film transistors as an active channel [Han and Lee, 2015, Lee et al., 2017, Sundholm et al., 2012]. Bikowski et al. [Bikowski et al., 2016] used combinatorial reactive sputtering to explain the optical absorption of SnO in terms of the Zn and O contents. It was found that the Zn-atoms modify the band-structure via isovalent alloying to SnO (structural disorder) and by local modification of the valence state of Sn. Zhu et al. [Zhu et al., 2014] examined amorphous zinc tin oxide thin films (of composition Zn/(Zn+Sn) = 0.1 and 0.3) by synchrotron x-ray scattering and x-ray absorption spectroscopy and found that the presence of zinc atoms induces strain in the atomic network, which enhances the thermal stability of amorphous zinc tin oxide and delays its crystallization.

Yet questions remain about the actual crystallography of the films after annealing at temperatures above 400 °C , the effect of hydrogen during annealing, as well as the source of free-carriers in amorphous zinc tin oxide [Koida et al., 2012, Körner et al., 2014, Körner et al., 2015, Singh et al., 2008, King and Veal, 2011, Sallis et al., 2014]. It was recently demonstrated that amorphous zinc tin oxide with the specific composition of $Zn_{0.05}Sn_{0.30}O_{0.65}$ (refered as a-ZTO for simplicity), could be successfully employed as a transparent electrode in flexible OLEDs [Morales-Masis et al., 2016, Dauzou et al., 2016]. To further improve the optical and electrical properties of a-ZTO, the nature of the sub-bandgap states is investigated here in detail, as well as their effect on the optoelectronic properties. Based on electrical, optical, microstructural, chemical characterization, and DFT calculations, the role of point defects is assessed.

3.2 Methods

A-ZTO was deposited on aluminoborosilicate glass using an Evatec Clusterline physical vapor sputtering system. This deposition chamber is equipped with planar circular targets with diameter of 10 cm. The composition of the zinc tin oxide target is 12% ZnO and 88% SnO_2 , i.e. 6 at% of Zn, 28 at% of Sn and 66 at% of O. The distance between the centre of the target and the substrate is of approximately 5 cm. The films were deposited using a power density of 1.01 W cm^{-2}, which resulted in a deposition rate of 2.7 nm min^{-1}. The substrate temperature was 60 °C while the deposition atmosphere was a combination of argon (Ar) and oxygen (O_2). Prior to deposition the base pressure was 2.5×10^{-7} mbar. Sputtering was done using a constant flow of 10 sccm of Ar and 2 sccm of Ar/O_2(the O_2 source is a mixture of 95% Ar and 5% O_2), resulting in a working pressure of 5.5×10^{-4} mbar, out of which the O_2 partial pressure was 6.7×10^{-6} mbar. More details on the development of the zinc tin oxide target with this particular composition are described in reference [Morales-Masis et al., 2016]. The films had a thickness of 150 nm and were systematically annealed from 150 °C to 500 °C in air, N_2, and H_2 atmospheres separately. Annealing experiments in air were performed at atmospheric pressure, while N_2 and H_2 treatments were done at a pressure of 0.5 mbar using a constant gas flow. The thermal treatments were performed by heating the material for 30 minutes from room temperature to the annealing temperature to avoid high thermal stress on the substrate. The a-ZTO samples were then kept for 30 min at the chosen temperature, before being cooled down passively to room temperature. The electron mobility (μ_e) and free-carrier concentration (N_e) of as-deposited and annealed films were obtained by Hall effect measurements in the Van der Pauw configuration using a HMS-5000 equipment. Temperature-dependent Hall effect measurements were performed from –190 °C to 45 °C using the same tool. The optical total transmittance (TT) and total reflectance (TR) of a-ZTO were determined using UV-vis near-infrared (NIR) spectrophotometry (Lambda-950 equipment from Perkin Elmer). The optical absorptance (A) was calculated from A = 100-TT-TR. Photothermal deflection spectroscopy (PDS) was used to measure the absorptance of a-ZTO layers deposited on fused silica. In this technique, the films are submerged in a temperature-sensitive liquid (Fluorinert FC-72) and illuminated by monochromatic light. Temperature gradients in the liquid, caused by light absorption in the film, induce a deflection of a probe laser. The direct relation between the laser deflection and the absorption of the films allows PDS to have higher sensitivity than spectrophotometry measurements. In addition, PDS measurements were performed on films deposited on fused silica substrates to decrease the absorpion contribution from the substrate. The details of PDS are described extensively in reference [Boccara et al., 1980]. This technique was performed using an in-house equipment based on a 150-W xenon lamp. The absorption coefficient was measured in the energy range of 0.7 – 4.96 eV.

The microstructure and crystallography of as-deposited and annealed a-ZTO was investigated using transmission electron microscopy (TEM). TEM 50-nm-thick cross-sectional samples were prepared using the conventional focused ion beam lift-out technique in a Zeiss Nvision

40. Given its spatial resolution in the 100 nm-range, standard selected-area electron diffraction (SAED) may fail to identify nanometric crystallites in an amorphous matrix. To surmount this issue, energy-filtered electron diffraction patterns were acquired in nanobeam conditions by scanning a 1-2 nm electron probe in a raster over the thin sample in an FEI Titan S microscope operated at 300 kV. This technique allows to acquire structural information of small material volumes. Information about short-range order (i.e., the first two coordination shells) in a-ZTO was obtained from radial profiles of diffraction patterns.

The presence of medium-range order (from the third coordination shell to about 3 nm) in a-ZTO as-deposited or annealed at 500 °C in air, was assessed using fluctuation electron microscopy [Voyles and Muller, 2002] by computing the normalized variance of 1200 diffraction radial profiles per sample and per probe size (1.5 nm for a convergence semiangle of 0.5 mrad, 2 nm using 0.3 mrad, and 3 nm for 0.2 mrad). The samples were thinned down using a Zeiss Nvision 40 until a thickness of 35 nm (as-deposited) and 45 nm (annealed at 500 °C). These thicknesses were reached using a final gallium beam voltage of 5 kV. To ensure that gallium irradiation during sample preparation did not result in surface amorphization, 40 nm of a-ZTO was deposited onto 30 nm Si_3N_4 thin films and observed in top view conditions for comparison. The nanobeam diffraction patterns were filtered in energy using a slit width of 10 eV. Following the methodology presented in reference [Voyles and Muller, 2002], a Mathematica code [Wolfram-Research-Inc, 2016] was developed to i) find the centre of each individual nanobeam electron diffraction pattern using a semi-automatic procedure (by maximizing the maximum intensity of the rotationally averaged diffraction intensities) to then ii) measure the corresponding rotationally averaged diffraction intensity, before iii) computing the normalized variance for groups of 100 nanobeam diffraction patterns. The mean signal of the 12 variance curves is then reported with one standard deviation to the mean error bars.

Rutherford backscattering (RBS) was done in a 6-MV HVEC Tandem accelerator using 2-MeV helium ions. Substrate signal and background arising from pileup events were subtracted. Hydrogen forward scattering (HFS) was performed by EAG Laboratories. These measurements were recorded using a detector 30° from the forward trajectory of an incident He^{2+} ion beam. The incident beam strikes the surface with an angle of 75° from the normal of the sample. Hydrogen concentrations were determined by comparing the number of hydrogen counts obtained from reference samples after normalizing the data by the stopping powers of the different materials.

3.2.1 Computational Methods.

The experimental investigations described in this chapter are supported by atomistic first-principles simulations based on density functional theory. The calculations are crucial to the understanding of our experimental results in terms of the atomic network and the electronic structure. These were calculated by Dr. Daniel Urban, Dr. Wolfgang Körner, and Prof. Dr Christian Elsässer from **The Fraunhofer Institute for Mechanics of Materials IWM**. A more detailed description about the simulations performed by this group can be found in references [Körner et al., 2012, Körner et al., 2014, Rucavado et al., 2017].

Generation of atomistic supercell models for a-ZTO

Amorphous structures were generated by performing classical molecular dynamics (MD) with the GULP code [Gale, 1997] and empirical Buckingham-type interatomic potentials. The heat-and-quench cycle was started at 5000 K and cooled down in steps of 10 K per 0.5 ps with time steps of 1 fs at constant temperature. Then the supercells were structurally optimized in volume, cell shape, and atomic positions by means of DFT calculations. The relaxations of interatomic forces and residual stresses were carried out with the Broyden-Fletcher-Goldfarb-Shanno algorithm using the projected augmented-wave (PAW) method [Blöchl, 1994] as implemented in the VASP code [Kresse and Furthmüller, 1996, Elsasser et al., 1990]. The LDA was used for the exchange-correlation functional and PAW pseudopotentials were used to describe Zn (3d,4s,4p), Sn (4d,5s,5p), and O (2s,2p) as valence electrons. For this study, we constructed a set of 38 amorphous structures.In the ZTO:$V_O^{\bullet\bullet}$ group of structures, the removal of the oxygen atom is done after the MD amorphization. In contrast, the structures of the "oxygen-poor" system are relaxed to an energy minimum already with the reduced oxygen concentration.

Electronic-structure calculations

The electronic-structure calculations on the basis of the SIC-LDA were performed using the computational mixed-basis pseudopotential (MBPP) method [Elsasser et al., 1990, Ho et al., 1992, Meyer et al., 1995, Lechermann et al., 2004]. For Zn, Sn, and O, optimally smooth norm-conserving pseudopotentials were constructed and a mixed basis of plane waves and nonoverlapping localized orbitals were used. Due to the localized orbitals, a plane-wave cut-off energy of 20 Ry (1 Ry = 13.606 eV) is sufficient to obtain well-converged results. For the k-point sampling of the Brillouin-zone integrals, a Monkhorst-Pack mesh of 3×3×3 and a Gaussian broadening of 0.2 eV were used. The DOS of the supercells were evaluated with the same mesh and a Gaussian broadening of 0.1 eV. The artificial self-interaction of the LDA is corrected by an incorporation of the SIC in the pseudopotentials [Vogel et al., 1996, Körner and Elsässer, 2010]. The SIC procedure uses weight factors $w = (w^{(s)}, w^{(p)}, w^{(d)})$ accounting for the occupations of the individual s, p, and d valence orbitals. The Zn 3d and Sn 4d semicore orbitals were corrected by 100%, i.e., $w_{Zn} = w_{Sn} = (0,0,1)$. The localized O–2s semicore orbitals are also corrected by 100%, while for the spatially more extended O-2p valence-band orbitals 90% was considered, which implies the weight factors $w_O = (1,0.9,0)$.The latter choice is a compromise between the optimal values of $w^{(p)}O = 0.8$ for ZnO and w(p)O = 0.93 for SnO_2 , which have

---

In Chapter 3 and Chapter 4 use two different computational approaches. Each Chapter has a short description of the computational methods used. The calculations in this Chapter were performed by Dr. Daniel Urban, in collaboration with The Fraunhofer Institute for Mechanics of Materials.

been found to reproduce the bandgaps of the binary crystalline compounds [Körner et al., 2014]. The main reason for the necessary adjustment of $w_O^{(p)}$ is the change from the fourfold (tetrahedral) coordination of ions in wurtzite ZnO to the sixfold (octahedral) coordination of ions in rutile SnO_2 . The choice of $w_O^{(p)} = 0.9$ for the SIC of oxygen in the calculations of all ternary Zn-Sn-O compounds leads to an electronic bandgap of 3.8 eV for crystalline $ZnSnO_3$, which is in very good agreement with experimental values [Körner et al., 2012]. For the adjustment of the atomic SIC to the crystal field in the solids, a scaling factor $\alpha = 0.8$ is applied.

3.3 Electrical properties: Hall mobility and free-carrier density

The as-deposited 150-nm-thick a-ZTO films have average μ_e of 21 $cm^2V^{-1}s^{-1}$ and N_e of 7 $\times 10^{19}$ cm^{-3} (from a total of 20 samples). Two different behaviours are then observed upon annealing depending on temperature (Figure 3.1). At low temperature (low-T, i.e. 150 °C , 200 °C and 300 °C), both N_e and μ_e increase with annealing temperature regardless of the treatment atmosphere. At higher temperatures (i.e. at 400 °C and 500 °C), N_e and μ_e are found to depend strongly on the annealing atmosphere. Thermal treatments in air result in an increase in μ_e from 20 $cm^2V^{-1}s^{-1}$ up to 35 $cm^2V^{-1}s^{-1}$, while N_e slightly decreases from 7.0×10^{19} cm^{-3} 6.0×10^{19} cm^{-3} . Similar changes in conductivity with annealing in air have been reported for amorphous zinc tin oxide with different atomic compositions as a-ZTO [Ko et al., 2007, Zhu et al., 2014, Mullings et al., 2014]. On the other hand, samples annealed in N_2 in the high-temperature range show a different behaviour, N_e increases up to 1.3×10^{20} cm^{-3} , while μ_e stabilizes at 26 $cm^2V^{-1}s^{-1}$. Films treated in H_2 at high temperatures exhibit the highest increase in N_e (up to 1.6×10^{20} cm^{-3} when annealing at 500 °C). On the other hand, μ_e decreases after an initial increase at low temperature and a final value 24 $cm^2V^{-1}s^{-1}$ is measured at 500 °C , which is slightly higher than the value obtained after deposition (of 21 $cm^2V^{-1}s^{-1}$).

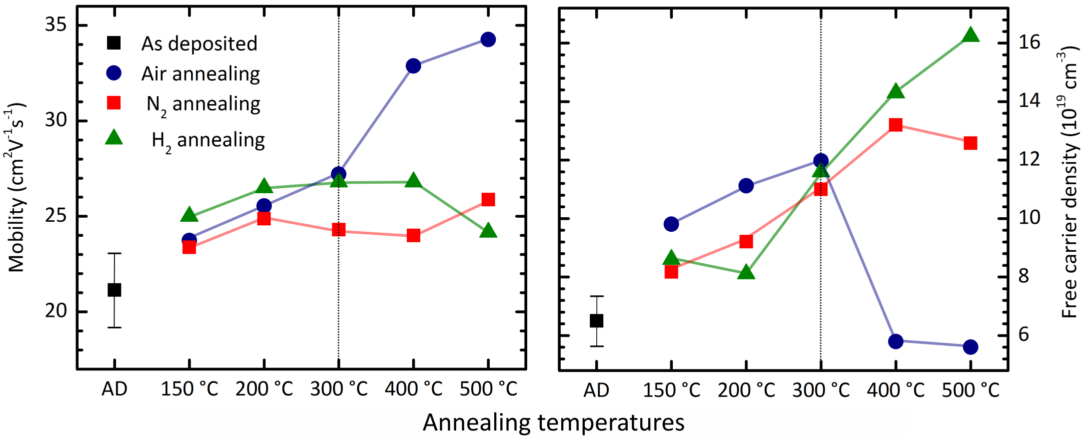

Figure 3.1 – Hall mobility (μ_e) and free-carrier density (N_e) of as- deposited and annealed a-ZTO (a-$Zn_{0.05}Sn_{0.30}O_{0.65}$) thin films as a function of annealing temperature. The dashed line divides the two different regimes observed at low and high temperatures.

3.4 Effect of thermal treatments on the optical properties of a-ZTO

Figure 3.2 shows the total transmittance TT and absorptance A of samples either as-deposited, annealed at 150 °C or 500 °C in different atmospheres. As-deposited a-ZTO exhibits a TT higher than 80% and an A as low as 2% in the visible and infrared. Samples annealed at 150 °C change only slightly compared to the as-deposited a-ZTO, regardless of the annealing atmosphere (Figure 3.2a). The slight increase in absorptance in the near IR region for samples annealed in air is assumed a consequence of free-carrier absorption (FCA), caused by the modest increase in N_e after such treatment. On the other hand, clear differences are observed after annealing at 500 °C (Figure 3.2b). The films annealed at 500 °C in H_2 absorb more in the near-infrared as a consequence of FCA which can be described by the Drude model [Chopra et al., 1983]. Alternatively, samples annealed in air show considerably lower FCA since N_e is lower in these films. In the visible part of the spectrum, as-deposited films present a slightly increased absorption approaching the bandgap edge (around 500 nm). This could be detrimental to the use of a-ZTO in optoelectronic devices with high spectral sensitivity in the visible range. Only the samples treated in air at 500 °C do not exhibit this absorption centre in the visible.

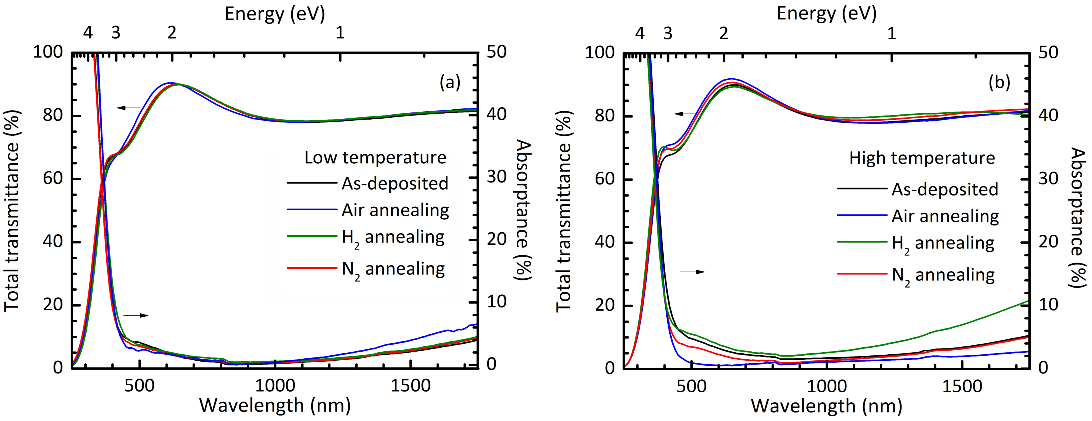

Figure 3.2 – Total transmittance and absorptance of a-ZTO as-deposited and annealed at 150 °C (a) and at 500 °C (b) in air, N_2 and H_2 .

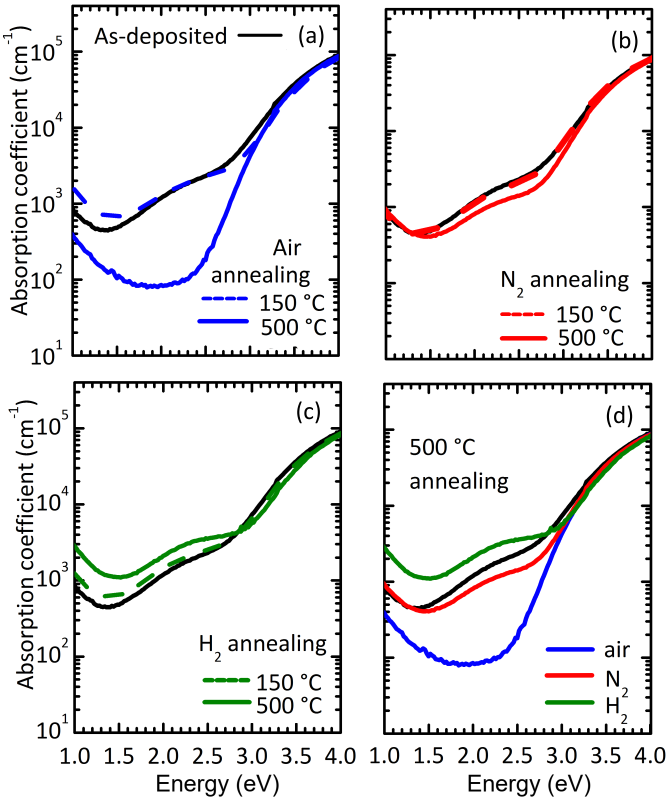

Figure 3.3 – Photothermal deflection spectroscopy of as-deposited a- ZTO(black line) and samples annealed in (a) air, (b) nitrogen, and (c) hydrogen at 150 °C (dashed coloured lines) and 500 °C (solid coloured lines). A comparison between the films as-deposited and annealed at 500 °C is shown in (d) (blue for air, red for nitrogen, and green for hydrogen).

A more detailed analysis of these absorption centres was performed by PDS measurements

(Figure 3.3). Figure 3.3(a) compares the absorption coefficient of as-deposited a-ZTO (black solid line), annealed in air at 150 °C (dashed blue) and at 500 °C (solid blue line). Films as-deposited and annealed at 150 °C show a broad sub-bandgap absorption at 2 eV, while samples treated in air at 500 °C exhibit a strong decrease in absorptance at this photon energy, confirming the observations of Figure 3.2. Alternatively, the absorption coefficients of the samples annealed in N_2 and H_2 (Figures 3.3(b) and 3.3(c)) change only slightly with temperature in this energy range. Figure 3.3(d) shows a comparison of films as-deposited and annealed at 500 °C in all three atmospheres. Using the absorption coefficient measured on the film annealed in air at 500 °C and the Tauc equation [Tauc, 1968], an optical bandgap of 3.7 eV was calculated. For this, it was assumed an allowed direct transition [Elangovan and Ramamurthi, 2005, Banyamin et al., 2014, Warner et al., 2015]. The bandgap of 3.7 eV (Figure 3.4) is in agreement with other reports in literature [Minami, 1999, Mullings et al., 2014]. It was not possible to measure the bandgap of the as-deposited films since the sub-bandgap absorption interfered with the Tauc plot.

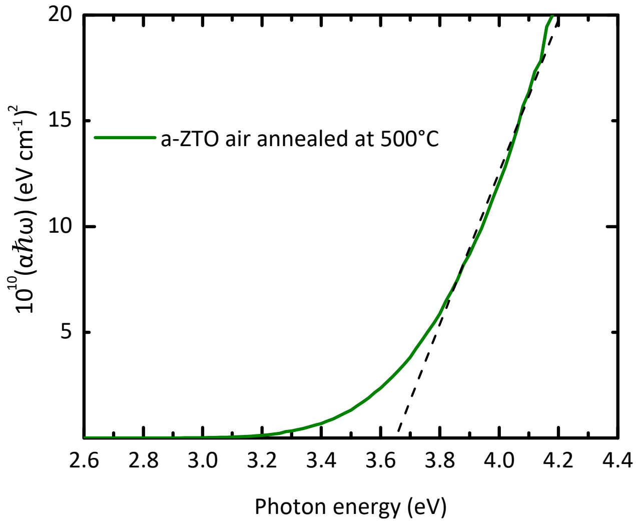

Figure 3.4 – Tauc plot of a-ZTO annealed at 500 °C in air. The sub-bandgap absorption of the as-deposited a-ZTO and films annealed in other atmospheres, impede the bandgap estimation using this approach. For a-ZTO annealed at 500 °C optical bandgap of 3.7 eV was determined assuming direct allowed transitions

3.5 Film Composition and Microstructure

3.5.1 Rutherford backscattering and electron recoil detection analysis

With respect to chemical composition, RBS measurements show that as-deposited and annealed films retain the atomic metallic molar fraction $Zn_{0.05}Sn_{0.30}O_x$, while the O content varies with the annealing atmosphere (Table 3.1). After annealing at T > 500 °C in air, the atomic concentration of oxygen increases by 1%, while thermal treatments in H_2 result in a decrease of 1% of the atomic ratio from the as-deposited material.

Table 3.1 – Composition from RBS of as-deposited a-ZTO and a-ZTO annealed at 500 °C in different atmospheres

Amorphous-ZTO	**Results from RBS**
As deposited	$Zn_{0.049}Sn_{0.299}O_{0.652}$
Annealed in air	$Zn_{0.047}Sn_{0.289}O_{0.664}$
Annealed in N_2	$Zn_{0.049}Sn_{0.304}O_{0.652}$
Annealed in H_2	$Zn_{0.051}Sn_{0.308}O_{0.641}$

This confirms the increase (decrease) of oxygen atoms in the amorphous network after annealing in O_2(H_2)- rich atmospheres, respectively. ERDA measurements indicate that the as-deposited a-ZTO films contain around 0.7 at% of hydrogen[2] . These results suggest that high temperature annealing in air reduces the content of hydrogen to less than 0.5 at% (under the detection limit of the ERDA technique), while annealing in H_2 at 500 °C results in an increase of hydrogen content up to 1.2 at%. The increased amount of H, together with the increase in N_e observed in Figure 3.1, suggests the role of hydrogen as a dopant [King et al., 2009, Hlaing Oo et al., 2010, Nomura et al., 2013, Janotti and Van de Walle, 2007]. In addition, H may also act as a reducing agent for oxygen [Morales-Masis et al., 2014], hence further increasing the $V_O^{\bullet\bullet}$ density and in turn sub-bandgap absorption, as observed in Figure 3.3.

3.5.2 Nanobeam diffraction and fluctuation electron microscopy

The changes observed in optoelectronic properties discussed previously do not appear to be linked to a change in microstructure of the samples. The nanobeam diffraction patterns acquired before and after annealing at 500 °C (Figures 3.5(c) and (d)) show diffuse rings broken into speckles due to the small number of atoms in the probe [Voyles and Muller, 2002]. This demonstrates the absence of nanometric crystallites in the samples before and after annealing at 500 °C in air. The presence of nanometric-sized crystallites would appear in

---

The TEM analysis and fluctuation electron microscopy (FEM) was done by Dr. Quentin Jeangros in Forschungszentrum Jülich. Dr. Jeangros design in addition the Mathematica code for the analysis of the FEM data

[2] ERDA measurements have an uncertainty of ±0.3

the nanobeam diffraction patterns as reflections symmetric with respect to the centre of the pattern. Moreover, both short- and medium-range order do not appear to evolve significantly, as both the radial profiles shown in Figures3.5(e) and 3.5(f) appear insensitive to annealing under these conditions.

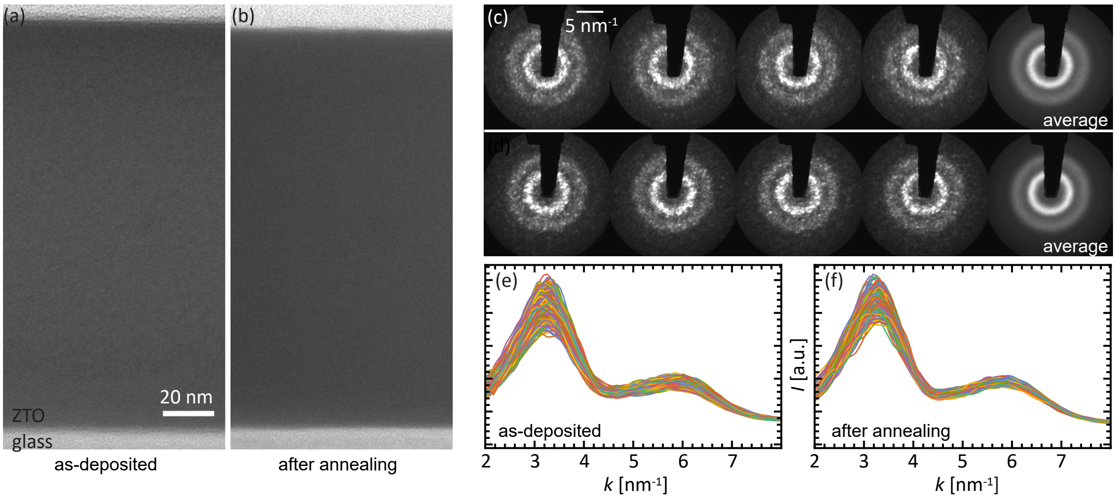

Figure 3.5 – TEM analysis of the samples after deposition and after annealing at 500 °C in air. (a, b) TEM images of focused ion beam–prepared cross sections after deposition and annealing at 500 °C , respectively. (c, d) Selection of nanobeam electron diffraction patterns of the samples shown in (a) and (b), respectively. The last inset of each series shows the mean of 100 nanobeam diffraction patterns. (e, f) Rotationally averaged diffracted intensities of 1200 nanobeam diffraction patterns of the samples shown in (a) and (b), respectively, highlighting the absence of both crystallinity and significant restructuring upon annealing. ([Voyles and Muller, 2002] for further details.)

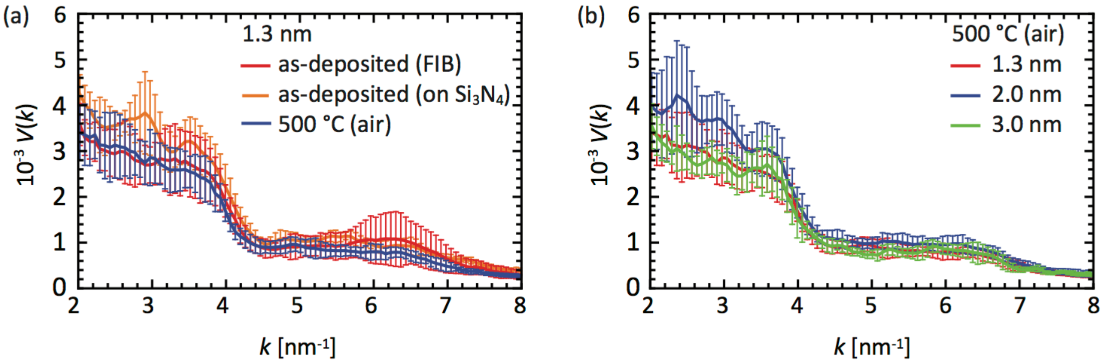

Figure 3.6 – (a) Variance of the diffracted intensities of the samples after deposition (prepared either by FIB or by directly depositing a-ZTO onto Si_3N_4 thin supports) and after annealing at 500 °C in air. This data set was acquired using a probe size of 1.3 nm and a convergence semi-angle of 0.5 mrad. (b) Variable resolution variance data of the FIB-prepared sample annealed at 500 °C acquired using various probe sizes, ranging from 1.3 to 3 nm.

The results of the fluctuation electron microscopy, shown in Figure 3.6, demonstrate the absence of well-defined peaks in the variance and hence the absence of significant medium range order after deposition and after annealing at 500 °C in air, at least within the detection limit of the technique. The FIB sample preparation does not appear to modify significantly the variance measurements, as a similar signal is obtained when depositing a-ZTO directly onto Si_3N_4.

The normalized variances of radial profiles of hundreds of nanobeam diffraction patterns appear insensitive to annealing at 500 °C in air. These results support the conjecture that the generation, modification, and annihilation of point defects during the different annealing procedures are responsible for the observed changes in the optical and electrical properties of the a-ZTO films.

3.5.3 Thermal Desorption Spectroscopy on a-ZTO

As seen in the Section3.5, the amorphous microstructure of a-ZTO withstands thermal treatments up to 500 °C without detectable variations. We therefore also studied the evolution of the film composition with temperature using thermal desorption spectroscopy (TDS; known also as temperature programmed desorption or TPD). In Figure 3.7 we show desorption spectra of the as-deposited and films annealed at 500 °C in the different atmospheres. The TDS spectra shows the effusion of species with mass to charge ratio (M/z) of 64, 18, 32, 2 and 120, which correspond to desorption of Zn^{1+}, H_2O^{1+} , O_2^{1+}, H_2^{1+} and Sn^{1+}.

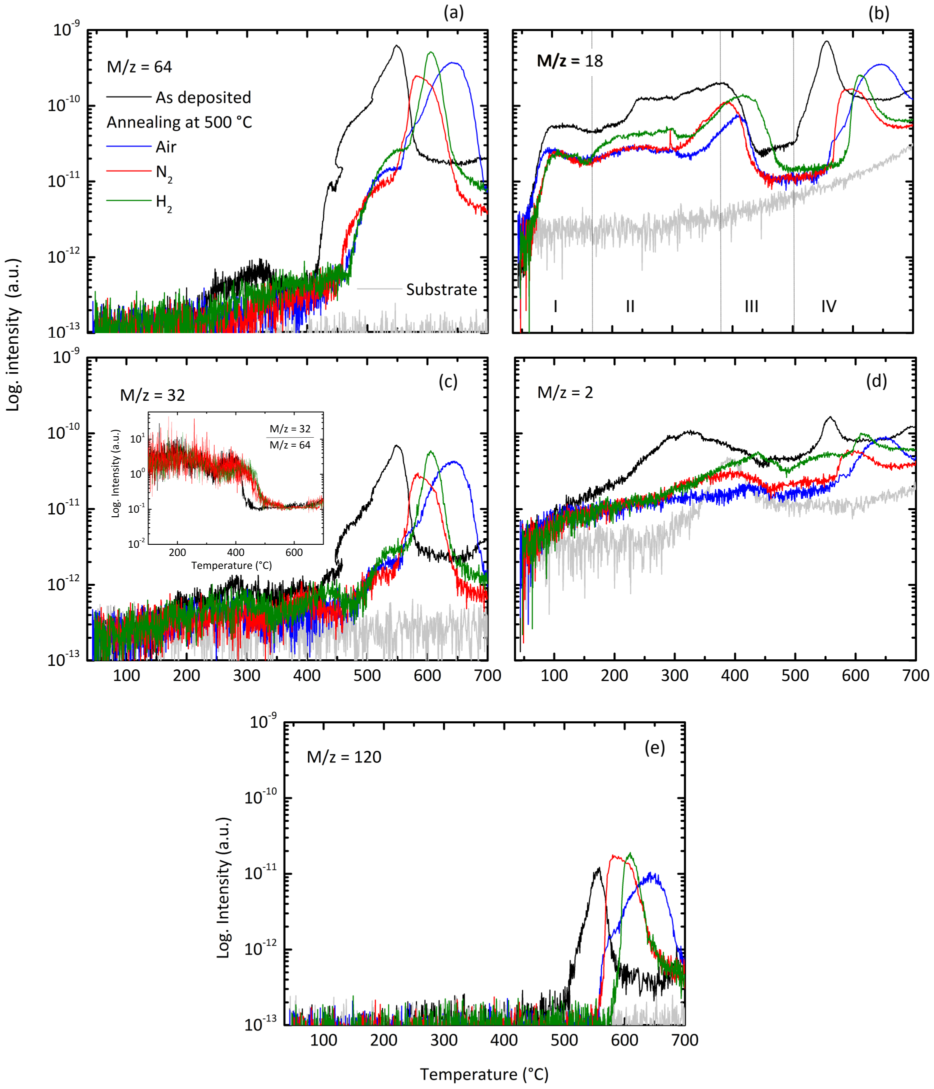

Figure 3.7 – Thermal desorption of as-deposited a-ZTO and the films annealed at 500 °C in air, H_2 and N_2 atmospheres. The silicon substrate is shown for all films. We measured mass/charge (M/z) signal 64, 18, 32, 2 and 120, which correspond to effusion of Zn^{1+}, H_2O^{1+}, O_2^{1+}, H_2^{1+} and Sn^{1+}. The inset in Figure 3.7(c) shows the rate between the 32 and 64 signals. The desorption and the signal rate is in logarithmic scale.

The M/z = 32 signal potentially includes the desorption of Zn^{2+} and O_2^{1+}, while M/z = 64 accounts solely for the desorption of Zn^{1+} [Koida et al., 2017]. From Figures3.7(a) and (c), we see a correlation between 32 and 64 signals since the effusion profile is similar for all cases. This is confirmed by the constant ratio between signals, as shown in the inset of Figure 3.7(b), and indicates that for temperatures > 450 °C the signal from 32 comes from Zn^{1+} rather than O_2^{1+}. At temperatures < 450 °C , the source of the M/z = 32 signal is ionized molecular oxygen.

We can divide the desorption profiles in four sections, marked for simplicity only on Figure

3.7(b). In Section I, from 45 °C to 175 °C , the effusion of adsorbed H and H-bonded H_2O molecules result in high signal from M/z = 18 and an increasing slope in signal from M/z = 2 [Kohl, 1989, Koida et al., 2010, Yamazoe et al., 1979]. The H_2O desorption at this range is considerably higher in the as-deposited films than in the annealed samples, which shows that thermal treatments at 500 °C result in films with less surface water and OH-groups, even if the films were exposed to environmental pressure after the thermal treatment. Section II, from 175 °C to 390 °C , the broad effusion of hydrogen from the as-deposited films (Figure 3.7(d) with its maximum at 322 °C) is remarkably higher than the annealed films. Nonetheless annealing a-ZTO in H_2 atmosphere, results in films with higher H-content than films thermal treated in N_2 or air, which partially confirms the results found in ERDA, i.e. there is a higher atomic-H content in the films annealed in H_2 than in the films annealed in N_2 or in air. Results from TDS and ERDA seem to conflict regarding the H-content in the as-deposited films, but in TDS we measure not only the bulk content of the films but also the surface H-atoms, and could potentially include fractions of water and OH-groups. A desorption peak of Zn^{2+} in as-deposited a-ZTO is present at T ≈ 280 °C (Figure 3.7(a)), which it is not detectable in the annealed films. This difference in Zn content was detected by RBS (≈ 1% Zn between annealed and as-deposited samples, See Table 3.1). This indicates that Zn atoms desorb from a-ZTO at temperatures lower than 500 °C . The desorption of Zn atoms from a-ZTO is studied in detail in reference [Landucci, 2019].

In region III, from 390 °C to 500 °C , there is a sharp decrease in the water effusion, simultaneously with an increase of signal O_2^{1+} and Zn^{1+}. This is linked to the onset of the decomposition of the material [Koida et al., 2017]. It is important to note that during TDS measurements the low pressure of the chamber (10^{-9} mbar) promotes the decomposition of the films at lower temperatures relative to atmospheric pressure [Lupis, 1983]. Finally the effusion signals from Sn^{1+} and Zn^{1+} ions at region IV (temperatures > 500 °C) mark the full decomposition of the films, as seen in Figure 3.7(c) and (d).

3.6 Electron scattering mechanisms

The dominating scattering mechanisms in TCOs are optical phonons, ionized impurities and grain boundary scattering. For a-ZTO, the absence of a crystalline structure (and of grain boundaries) simplifies the study of scattering. To pinpoint the scattering mechanisms for each of the films, temperature-dependent Hall effect measurements were performed from -190 °C to 50 °C . Resulting N_e and μ_e of the as-deposited and annealed films are independent of temperature (Figure 3.8(a) and (b)).

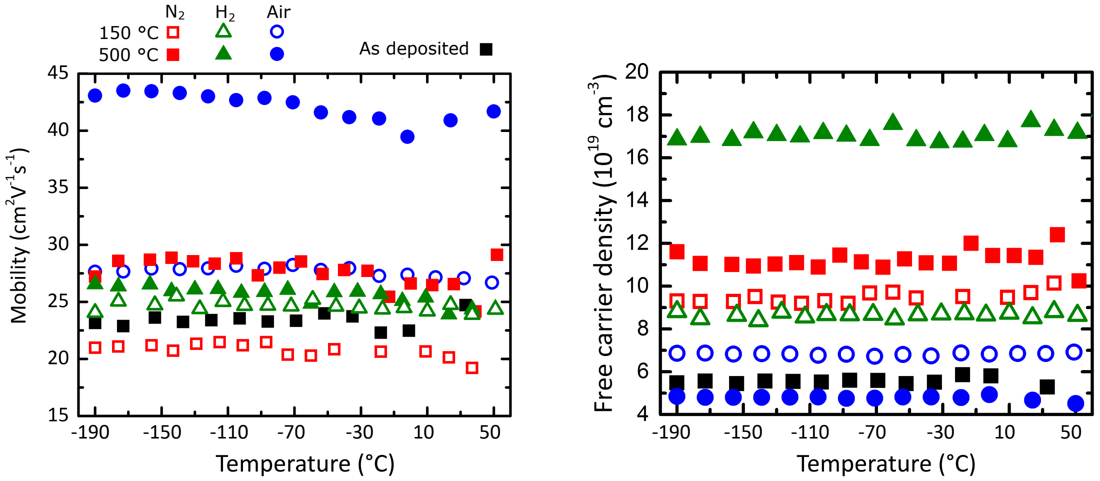

Figure 3.8 – Electron mobility (a) and free-carrier density (b) obtained by Hall effect measurements from -190 °C to 50 °C for as-deposited a-ZTO and films annealed at 150 °C and 500 °C in air, H$_2$ and N$_2$ atmospheres

Hence, for a-ZTO, only ionized defects limit the electron transport. Scattering of free-carriers by ionized impurities is commonly described by the Brooks-Herring-Dingle (BHD) model [Dingle, 1955]. This model considers the effect of a screened Coulomb potential on the relaxation time between two different scattering events that a charge carrier encounters, resulting in an equation for the mobility limited by ionized impurities, μ_{ii} ,

$$\begin{aligned}\mu_{ii} &= \frac{3\pi\hbar^3(4\pi\epsilon_0\kappa)^2}{2Z^2e^3m^{*2}} \times \frac{N_e}{N_{ii}} \times \frac{1}{F(\xi)}\\ F(\xi) &= ln(\xi+1) - \frac{\xi}{\xi+1}\\ \xi &= 4\pi^3(\frac{3}{\pi})^{1/3}\frac{\epsilon_0\kappa\hbar^3N_e^1/3}{e^2m^*}\end{aligned} \tag{3.1}$$

where F(ξ) is the screening function, κ is the relative permittivity, ϵ_0 is the vacuum permittivity, N_{ii} the concentration of ionized impurities, Z the charge of the impurity, m^* the effective mass, e the electron charge and $\hbar$ the reduced Planck constant. To apply this model to the experimental data, μ_e vs N_e was plotted in Figure 3.9, including the data shown Figure 3.1 and the result from the BHD model.

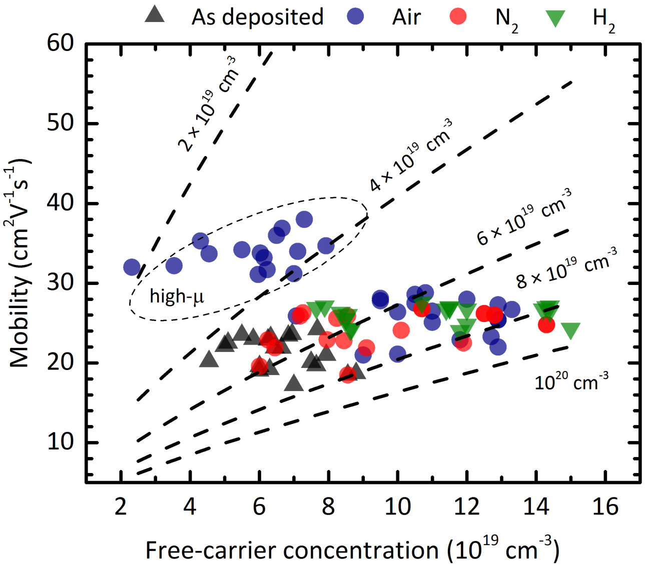

Figure 3.9 – Hall mobility plotted as function of free-carrier density for films annealed in air, H_2 , and N_2 atmospheres. Lines are simulations using the Brooks Herring Dingle model, considering ionized defects of charge $Z = +2$ and of defect density N_{ii} changing from 2×10^{19} cm^{-3} to 2×10^{20} cm^{-3} . Effective masses of 0.26 m_e and 0.3 m_e were used in the model, as calculated from Fourier transform infrared reflectance and Drude model fitting

The m^* values for the BHD-model were obtained from Fourier transform infrared spectroscopy reflectance measurements and Drude model fitting using the software WVASE®. Effective masses of 0.30 m_e and 0.26 m_e were obtained for the films as-deposited and annealed at 500 °C in air, respectively. Assuming that the majority of impurities in a-ZTO films have a charge Z of +2, the BHD model indicates that μ_e - N_e data of the samples as-deposited and annealed at temperatures lower or equal to 300 °C in H_2 and N_2 atmosphere are described by the model, assuming a N_{ii} value of $\approx 5\times10^{19}$ cm^{-3} to 1×10^{20} cm^{-3} [Kamp et al., 2005]. The group of data with higher mobility, i.e., between 30 $cm^2V^{-1}s^{-1}$ and 40 $cm^2V^{-1}s^{-1}$ (annealed in air at 500 °C), are described by a much lower N_{ii} , ranging from 2×10^{19} cm^{-3} to 4×10^{19} cm^{-3} . Even though the experimental data does not follow the trend set by the model when using constant N_{ii} values, these results suggest that annealing in air at temperatures above 300 °C reduces the density of ionized impurity defects, leading to the observed improvement in μ_e (Figure 3.1) and to the clear reduction of sub-bandgap defects observed in the PDS measurements (Figure 3.3).

3.7 Calculations and correlation with experimental results

For this study, we constructed a set of 38 amorphous structures, see Table 3.2. Initially, two subsets of samples were generated. To ensure valid statistical results, eight samples with composition $Zn_4Sn_{27}O_{58}$ were used to reflect the experimentally as-deposited a-ZTO films. These samples were labelled "stoichiometric," since their composition corresponds to an admixture of 4 ZnO units and 27 SnO_2 units.The second subset of eight samples with the composition $Zn_4Sn_{27}O_{57}$ is oxygen deficient and can be considered as systems with an annealed $V_O^{\bullet\bullet}$. From the stoichiometric set, we derived three further sets of samples by adding/removing some atoms and subsequently repeating the DFT procedure. (i) By removing an oxygen atom, we generated a local oxygen deficiency resembling an $V_O^{\bullet\bullet}$ of a crystal. (ii) Hydrogen-rich supercells were generated by adding a hydrogen atom (ZTO + H). (iii) Hydrogen atoms were added close to the oxygen deficiency sites of (i) to study the combined effect of $V_O^{\bullet\bullet}$ and H on the DOS ($V_O^{\bullet\bullet}$ +H). In the a-ZTO:$V_O^{\bullet\bullet}$ group of structures, the removal of the oxygen atom is done after an amorphization step. In contrast, the structures of the "oxygen-poor" system are relaxed to an energy minimum already with the reduced oxygen concentration.

Table 3.2 – Compilation of the 38 supercell models generated by atomistic simulations, listing the number of samples (n_{samp}), the supercell composition, the total number of atoms per supercell, and the atomic percentage of elements (p_x).

$Structure$	n_{samp}	Supercell	N_{at}	$p_{Zn}[at\%]$	$p_{Sn}[at\%]$	$p_O[at\%]$	$p_H[at\%]$
a-ZTO "stoichiometric"	8	$Zn_4Sn_{27}O_{58}$	89	4.50	30.3	65.2	0
ZTO "oxygen poor"	8	$Zn_4Sn_{27}O_{57}$	88	4.55	30.7	64.8	0
ZTO:$V_O^{\bullet\bullet}$	7	$Zn_4Sn_{27}O_{57}$	88	4.55	30.7	64.8	0
ZTO:$V_O^{\bullet\bullet}$ + H	8	$Zn_4Sn_{27}O_{57}H$	89	4.50	30.3	64.0	1.12
ZTO+H	7	$Zn_4Sn_{27}O_{58}H$	90	4.44	30.0	64.4	1.11

We considered a-ZTO:$V_O^{\bullet\bullet}$ samples, i.e. samples which contain a local atomic environment similar to an oxygen vacancy in a crystal (local oxygen deficiency). These structures are generated by removing an oxygen atom from the stoichiometric samples (followed by the DFT structural optimization). The DOS of these samples are shown in Figure 3.10(a). Distinct localized defect levels appear in the upper half of the bandgap for the majority of samples.

In recent studies on IGZO, In_2O_3:Sn, and IZO, metal-metal clustering (two metal atoms without a separating oxygen) was identified to be the common origin of the deep levels in the upper part of the bandgap [Körner et al., 2013]. The same interpretation was recently shown to hold for amorphous SnO_2 and SnO by [Wahila et al., 2016]. The energetic positions of the metal-metal defect levels depend on the whole neighbourhood (e.g., the number and distance of oxygen atoms that attract electrons from the metal atoms). In order to study the effect of hydrogen in amorphous samples and on the deep levels, individual hydrogen atoms were inserted into the amorphous samples in the vicinity of the atoms. In most cases, the defect level is shifted deeper into the bandgap by approximately - 0.2 eV to - 0.4 eV. For two samples the addition of hydrogen resulted in the elimination of the level after structural optimization. An interesting result was found for sample s06 of a-ZTO:$V_O^{\bullet\bullet}$. Here, the local $V_O^{\bullet\bullet}$ alone did not result in a deep level. However, when a H atom was added in close vicinity of the respective atomic environment, a deep level appeared with a strong contribution of the H atom, which is

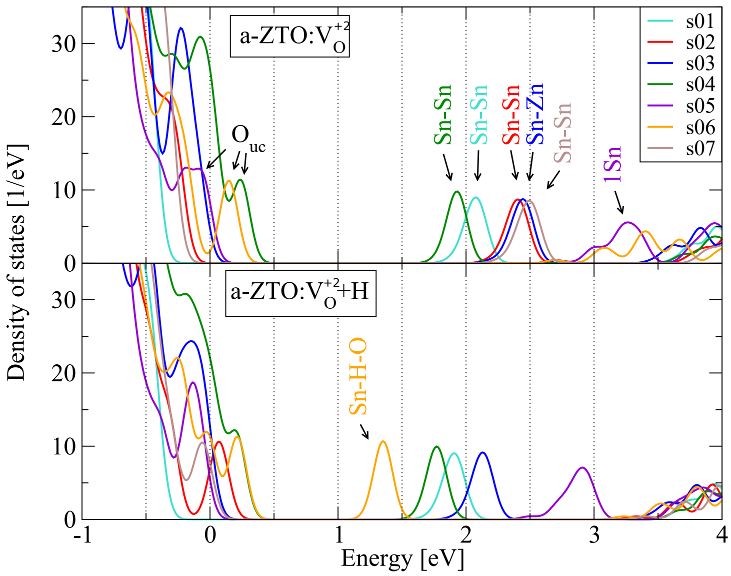

Figure 3.10 – Calculated densities of states of (top panel) the a-ZTO:$\mathrm{V}_\mathrm{O}^{\bullet\bullet}$ samples containing a local oxygen deficiency and (bottom panel) the a-ZTO:$\mathrm{V}_\mathrm{O}^{\bullet\bullet}$ +H samples with an additional H atom in the vicinity of the defect. The curves are aligned with respect to the main peak in the VB. Deep levels within the gap are mainly carried by one or two metal atoms (indicated in the top panel), while levels close to the VB stem from undercoordinated oxygen atoms (O_{uc}). The defect state of the a-ZTO:$\mathrm{V}_\mathrm{O}^{\bullet\bullet}$ +H sample s06 is related to a Sn-H bonding and neighbouring O atoms.

found to form a Sn-H bond with the previously undercoordinated Sn atom Figure 3.11(d). The effect of hydrogen on the annealed stoichiometric samples was also investigated. Here, no deep levels were generated.

3.7.1 Correlation with optoelectronic properties

For annealing temperatures < 300 °C , the increase in N_e occurs together with an increase in μ_e and is independent of the annealing atmosphere, as seen in Figure 3.1. In this temperature range, the amorphous network does not appear to interact significantly with the chemical species coming from the annealing atmosphere and the changes are induced mostly by the temperature alone. Similar effects have been described in literature and their origin is still under debate. For example, μ_e and N_e increase in zinc tin oxide (for layers with composition Sn/(Sn+Zn) of 0.11 and 0.45) has been explained by a structural relaxation around Sn atoms, which may form $\mathrm{V}_\mathrm{O}^{\bullet\bullet}$ donors instead of V_O^X [Zhu et al., 2014]. Moreover, structural relaxations could result in the activation of H dopants [Janotti and Van de Walle, 2007] or charged metal ions [Kim et al., 2006] that act as dopants in a-ZTO. Furthermore, low temperature annealing could cause the reduction of non dominating scattering defects such as neutral impurities [Ito et al., 2006] or electron traps [Hanyu et al., 2013], which contribute to increase μ_e . Overall, even if the electric properties of a-ZTO improved, it should be mentioned that these thermally

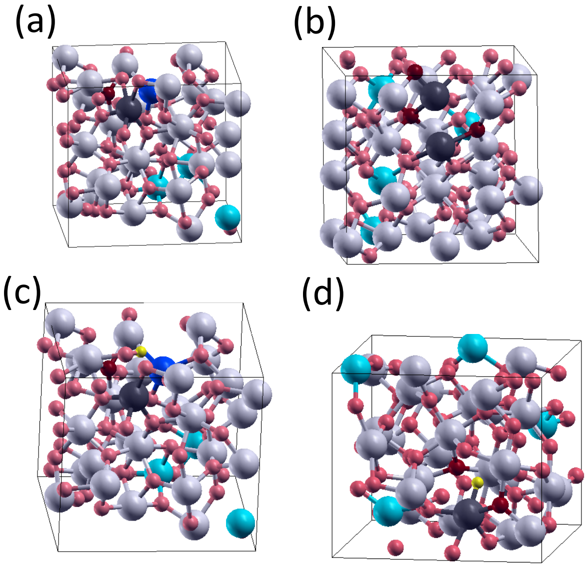

Figure 3.11 – Supercells containing a local oxygen deficiency and a metal-metal defect: (a) a-ZTO:$V_O^{\bullet\bullet}$ sample s03, (b) a-ZTO:$V_O^{\bullet\bullet}$ sample s02, (c) a-ZTO:$V_O^{\bullet\bullet}$ +H sample s03, and (d) a-ZTO:$V_O^{\bullet\bullet}$ +H sample s06. Sn, Zn, O, and H atoms are depicted as grey, blue, red, and yellow spheres, respectively. The Sn, Zn, and O atoms contributing most to the defect levels are highlighted by dark grey, dark blue, and dark red, respectively.

induced structural relaxation processes are not easily detectable, as confirmed by the TEM nanobeam diffraction experiments, which assess that both short- and medium-range order do not appear to change significantly with temperature (Figure 3.5). In addition, the effect of the thermally induced local structural changes on the defect states, e.g. originating from undercoordinated oxygen, modestly increases with increasing temperature. As an example, only a modest reduction of defect states can be observed for samples annealed under nitrogen atmosphere at 500 °C (Figure 3.3). In contrast, a clear reduction in the density of sub-bandgap defects is observed when annealing in air at temperatures >300 °C (Figures 3.1 3.3, and 3.2). The electron mobility also increases significantly when annealing in air at these temperatures (up to 35 $cm^2V^{-1}s^{-1}$, Figure 3.1). The RBS data (cf. Table3.1) and the changes in optoelectronic properties when annealing in oxygen-rich atmospheres (Figures 3.1, 3.2 and 3.3) indicate that this effect mainly originates from the introduction of oxygen in the films. A reduction of the number of sub-bandgap defects with increased oxygen content, as observed when annealing in air, is in agreement with the atomistic calculations. The source of sub-bandgap states in the upper half of the bandgap are local oxygen deficiencies, which lead to undercoordinated Sn or Zn atoms (Figure 3.11). These oxygen-deficient states are known to act as donors [Klein, 2013, Koida et al., 2012, King and Veal, 2011, Narushima et al., 2002]. At T > 300 °C , $O_2$from the atmosphere absorbs, dissociates, and eventually passivates these metallic dangling bonds, hence reducing the number of sub-bandgap defects and as a result N_e . Indeed, the decrease in N_e with an increased oxygen concentration in the film can be explained by $\frac{1}{2}O_2(g)+V_O^{\bullet\bullet}$

$+2e^{-}$ -> O_{O}^{x} .

In other words, the formation of O_{O}^{x} (or passivation of $V_{O}^{\bullet\bullet}$) comes at the expense of charge carriers. While these defects act as dopants, they are also scattering centres, limiting the mobility. By reducing the number of such charged defects by annealing in air at high temperature, μ_e increases by 70% with respect to its original value, as shown in Figure 3.1. Alternatively, several effects can explain the higher absorption of a-ZTO films annealed at high temperature in H_2 (Figure 3.3), as well as the drastic increase in N_e (see Figure 3.1). First, the energy shift of sub-bandgap states (- 0.2 to - 0.4 eV) deeper in the bandgap (Figure 3.10) when introducing hydrogen near oxygen deficiencies corresponds to the measured broadening of the absorption energy range seen in Figure 3.3. Second, the addition of hydrogen, might introduce new defect levels within the bandgap. These defects may act as donors. And third, hydrogen may also create more oxygen deficiencies by removing oxygen from the sample close to the surface, which also increases sub-bandgap absorption as the $V_{O}^{\bullet\bullet}$ density increases. While hydrogen allows an improved conductivity up to 577 S cm^{-1} by increasing N_e , it also results in more absorbing films. On the other hand, a remarkable μ_e of 35 $cm^2V^{-1}s^{-1}$ for a full amorphous indium-free electrode has been obtained by high-temperature annealing in oxygen-rich atmospheres. This results in the passivation of defects, specifically, undercoordinated Sn and Zn bonds, by introducing atomic oxygen to the amorphous network. This allows the formation of Sn-O-Sn (or Zn-O-Zn, Zn-O-Sn) bonds, reducing the density of sub-bandgap defects (and hence the number of scattering centres), and with it reaching excellent optical properties with a conductivity of 445 S cm^{-1}.

3.8 A-ZTO as recombination junction for perovskite/Silicon monolithic tandem solar cells

Combining a high-bandgap perovskite absorber with a crystalline silicon solar cell results in the reduction of losses due to thermalization of photons of energy higher than the silicon bandgap. Therefore perovskite/crystalline silicon tandem solar cells have the potential to reach efficiencies higher than those of silicon single-junction record devices. Monolithic tandem cells require a recombination junction with appropriate band structure to guarantee charge transfer between the bottom silicon cell and the top perovskite cell, optical transparency (from 600 nm to 1200 nm) and chemical stability. However, for some mesoscopic perovskite solar cells, a required high-temperature process could limit their implementation in tandem devices due to the thermal load in the recombination junction.

This section describes the application of a-ZTO in perovskite/Silicon tandem solar cells. It should be noted that the work for the publications [Werner et al., 2016] and [Rucavado et al., 2017] were done in parallel, nonetheless, reference [Werner et al., 2016] was published first. The results shown in this section are based on the work performed by Dr. Jérémie Werner, as he is responsible of the fabrication and characterization of the perovskite/silicon tandem solar cell. More detailed description of the cell process can be found in reference [Werner et al., 2016].

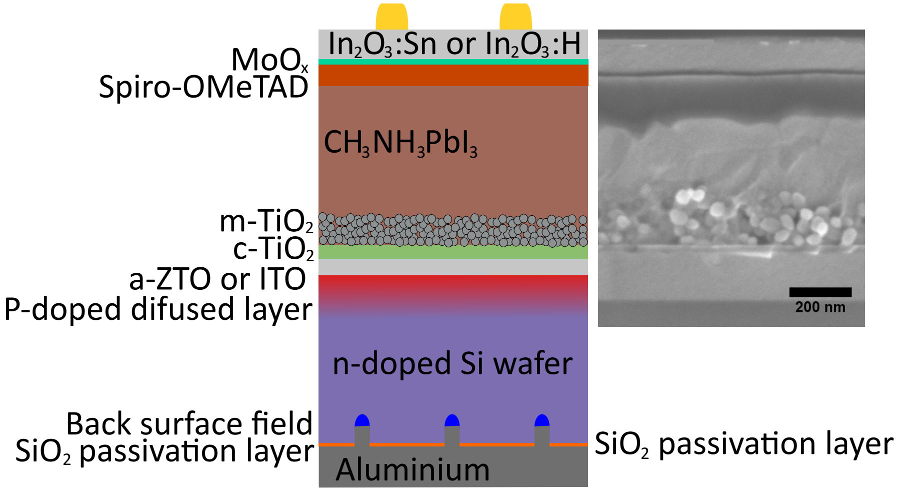

Figure 3.12 – Monolithic tandem cell structure with mesoscopic perovskite top cell and homojunction silicon bottom cell. The SEM images shows a cross-section of a typical perovskite top cell. TiO_2 is the electron transport layer which must be treated at 500 °C for proper functioning.

Bottom silicon solar cell fabrication started with electrical junction formation in n-type silicon wafers. For this, silicon oxide layers were thermally grown on both wafer surfaces. The active device area was then defined by removing the oxide on the front side of the Si wafers, followed by boron implantation, thus forming a hole-collecting contact. On the rear side, the surface-passivating silicon oxide layer was laser-patterned and phosphorus implanted for local contact and back surface field formation. We remark that the used wafers featured mirror-polished front sides (and a lapped back side), to avoid shunting of the solution processed top cell. To ensure the absence of a native SiO_2 layer, we performed a HF dip before the TCO (In_2O_3:Sn or a-ZTO) was directly sputtered onto the boron-implanted silicon surface, followed by the perovskite top cell deposition. The perovskite cell was composed of a sputtered compact TiO_2 layer, a spin-coated TiO_2 scaffold layer which needs an annealed step at 500 °C , a $CH_3NH_3PbI_3$ perovskite layer, and a spiro-OMeTAD/MoO_x/IO:H/In_2O_3:Sn top electrode. More details of the solar cell fabrication are found in reference [Werner et al., 2016].

In Figure 3.12 we see a simple schematics of the monolithic tandem solar cell and an microscopy image of the perovskite cell. As bottom cell, an homojunction silicon solar cell with locally passivated rear contact was used.

Amorphous-ZTO as recombination junction

Since In_2O_3:Sn (known as indium tin oxide or ITO) is one of the most commonly used TCOs in photovoltaics, it was naturally the initial choice for the intermediate recombination layer. However, strong degradation could be observed on finished monolithic tandem cells with poor current-voltage characteristics, similar to the example shown in Figure 3.13(a). Electrical characterization of the In_2O_3:Sn layers on glass before and after annealing at 500 °C showed a strong reduction of conductivity, which is attributed to an excess of oxygen in the films from the air or from the capping TiO_2. Consequently, the electrical properties of In_2O_3:Sn before the thermal treatment (μ_e of 36.8 $cm^2V^{-1}s^{-1}$ of and N_e of 3.7×10^{20} cm^{-3}) decreased drastically, making the films non-measurable with our Hall-effect setup after the complete annealing sequence. We believe that the strongly increased resistance in this recombination layer is responsible for the non-functional tandem devices.

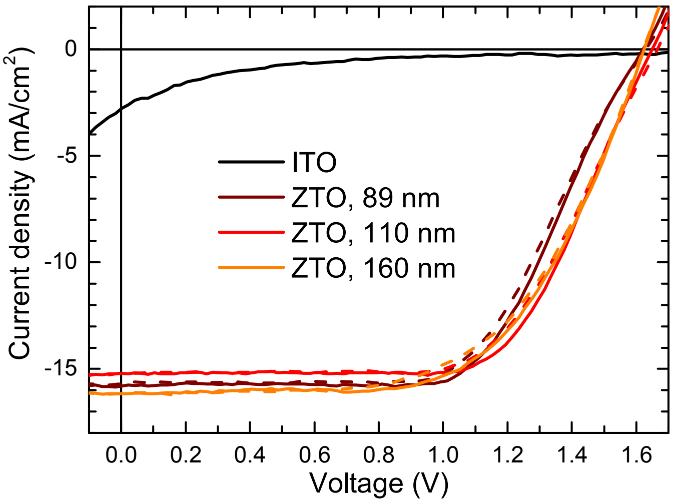

Figure 3.13 – J-V curves of monolithic tandem cells with ITO or a-ZTO recombination layer. Dashed lines are for forward scans (Jsc to Voc) and solid lines are for reverse scan (Voc to Jsc)

As seen in Sections 3.3 and 3.4, the optoelectronic properties of a-ZTO improve with temperature treatments at 500 °C in air, this ensures good transverse charge transport as recombination junction . We applied a-ZTO as intermediate recombination layer and investigated the effect of thickness variation from 20 nm to 160 nm. The resulting current-voltage (J-V) characteristics is seen in Figure 3.13, showing rectifying diode-like curves, in contrast to the series resistance limited In_2O_3:Sn-based tandem cells. The J-V curves with thinner a-ZTO layers were slightly s-shaped around the open-circuit voltage (Voc) (89 nm of a-ZTO as recombination junction), suggesting deficient electron transport in the film. However, this problem disappeared with thicker layers, as shown in Figure 3.13.

In this study, the best monolithic tandem cell with an aperture area of 1.43 cm^2 showed a Voc of 1643 mV and an initial efficiency of 16.3%, as obtained from J-V characteristics. During maximum power point tracking, a steady efficiency of 16% was reached. In addition, a smaller cell of 0.25 cm^2 reached a conversion efficiency of 17.4% (16.4% in steady-state).

3.9 Conclusion

Using a combination of experimental techniques and atomistic calculations, the relation between sub-bandgap states and optoelectronic properties was clarified for sputtered a-ZTO thin films. The effects of annealing temperature and atmosphere on the optoelectronic properties of the films were investigated. Annealing at low temperatures (T < 300 °C) induced a increase in μ_e and N_e (from 20 $\text{cm}^2\text{V}^{-1}\text{s}^{-1}$ and $\approx 6.5 \times 10^{19}$ cm^{-3} to 25 $\text{cm}^2\text{V}^{-1}\text{s}^{-1}$ and $\approx 1 \times 10^{20}$ cm^{-3}), independently of the annealing atmosphere. These changes occur presumably due to structural relaxations of the atomic network, or the activation of hydrogen dopants with temperature. At higher temperatures (300 °C < T < 500 °C), the optoelectronic properties of the films were strongly modified, with the final effect on μ_e and N_e depending on the annealing atmosphere. Indeed, air treatments resulted in films with low absorptance (as low as 0.3% at a wavelength of 1000 nm), an increase in μ_e (up to 35 $\text{cm}^2\text{V}^{-1}\text{s}^{-1}$) and low free-carrier concentration. Hydrogen-annealed films have high free-carrier density but lower mobility and high absorptance. As the films remained amorphous, these results are explained by the generation or passivation of point defects and by an increase of the film's density after thermal annealing as suggested by TDS measurements. Indeed, DFT simulations identified local oxygen deficiencies and resulting metal atom clusters as the source of energy levels in the upper half of the bandgap. These states act as the source of free-carriers but also as scattering centres, hence limiting the mobility and deteriorating the optical properties. These defects are present in the film after deposition and can be modulated at high temperatures (higher than 300 °C) by the annealing atmosphere. The strong increase in both free-carrier concentration and absorption within the bandgap when annealing in H_2 is linked to both the formation of additional metal-hydrogen states within the bandgap and the shift of the existing oxygen deficiency levels deeper into the bandgap. On the other hand, the introduction of oxygen into the amorphous network during annealing in air at 500 °C passivates the oxygen deficiencies and results in the films with the best optoelectronic properties (μ_e of 35 $\text{cm}^2\text{V}^{-1}\text{s}^{-1}$ when compared to 21 $\text{cm}^2\text{V}^{-1}\text{s}^{-1}$ after deposition). Overall, these results indicate that a fine control of the oxygen and hydrogen contents is essential to optimize the optoelectronic properties of a-ZTO. Several strategies may be envisaged to further improve the properties of these films, e.g., by depositing other oxides together with a-ZTO to passivate these oxygen deficiencies in a controlled manner. Considering that the a-ZTO films presented here are free of macroscopic defects, the tradeoff between optoelectronic properties suggests that a carrier transport optimum, i.e. a maximum μ_e , has been reached for zinc tin oxide with this specific composition. Finally, given the high-temperature structural stability of a-ZTO, we have demonstrated the applicability of the film as a recombination layer by optoelectronic characterization and integration to fully functional devices. By using a-ZTO as recombination layer allowed us to fabricate mesoscopic perovskite/silicon homojunction monolithic tandem solar cells with >16% efficiency.

4 Alternative low-temperature passivation route for Sn-based oxides

Chapter 4 is based on the publication:

Rucavado, E., Graužinytė, M., Flores-Livas, J. A., Jeangros, Q., Landucci, F., Lee, Y., Koida, T., Goedecker, S., Hessler-Wyser, A., Ballif, C., and Morales-Masis, M. (2018). New route for "cold-passivation" of defects in tin-based oxides. The Journal of Physical Chemistry C, 122(31):17612–17620.

My original input and work in the manuscripts include: plan and execution of the sputtering and post-deposition thermal treatments of the a-ZTO, SiZTO, SnO_2 and $SiSnO_2$ films. All the electrical characterization, optical properties and thermal desorption spectroscopy measurements, as well corresponding data analysis. Interpretation of results and correlation with the computational calculations were discussed and planned with Dr. Morales-Masis, Dr. Jeangros, Dr. Flores-Livas, Dr. Graužnytė for the JPCC manuscript.
I want to acknowledge Dr. Quentin Jeangros for the electron microscopy experiments and analysis, Dr. José A. Flores-Livas and Dr. Graužinytė for the density functional theory calculations and interpretation. Also I want to thank Dr. Takashi Koida for his support during the desorption spectroscopy, Dr. Pierre Mettraux for the XPS measurements and the following discussion and Dr. Max Döbeli for the RBS experiments and discussion.

In Sn-based oxides oxygen deficiencies and undercoordinated Sn atoms result in an extended density of states below the conduction band edge. Although shallow states provide free-carriers necessary for electrical conductivity, deeper states inside the bandgap are detrimental to transparency. In amorphous zinc tin oxide (a-ZTO), the overall optoelectronic properties can be improved by defect passivation via annealing at high temperatures. Yet, the high thermal budget associated with such treatment is incompatible with many applications (e.g. silicon heterojunction solar cells). Here, we demonstrate an alternative, low-temperature

---

Results from reference [Rucavado et al., 2018] are reproduced and modified with permission from the publisher.

passivation method, which relies on co-sputtering deposition of Sn-based TCOs with silicon dioxide (SiO_2). Using a-ZTO and amorphous/polycrystalline tin dioxide (SnO_2) as representative cases, we demonstrate through optoelectronic characterization and density functional theory simulations that the effect of SiO_2 is twofold. First, oxygen from SiO_2 passivates the oxygen deficiencies that form deep defects in SnO_2 and a-ZTO. Second, the ionization energy of the remaining deep defect centers is lowered by the presence of silicon atoms. Remarkably, we find that these ionized states do not contribute to sub-bandgap absorptance. This simple passivation scheme significantly improves the optical properties without affecting the electrical conductivity, hence overcoming the known transparency-conductivity trade-off in Sn-based TCOs.

4.1 Motivation and state of the art

As discussed in Chapter 3, in a-ZTO oxygen defficiencies (V_O) can be passivated by post-deposition treatments in air at temperatures > 400 °C , annealing in these conditions is thermally costly and/or not convenient for devices with low thermal budgets, such as solar cells based on thin hydrogenated amorphous silicon layers or hybrid organic-inorganic perovskite materials [De Wolf et al., 2012, Morales-Masis et al., 2017a, Werner et al., 2018].

Alternatively, previous investigations have shown that the co-deposition of silicon dioxide (SiO_2) with different TCOs, mainly with zinc oxide, may decrease the density of V_O defects [Dabirian et al., 2016, Kizu et al., 2016, Mitoma et al., 2014, Kang et al., 2012], but also lower the refractive index [Dabirian et al., 2016, Minami et al., 1986], decrease the resistivity [Minami et al., 1986, Faure et al., 2012, Rashidi et al., 2013] and amorphize the TCO [Faure et al., 2012, Clatot et al., 2011, Sorar et al., 2011]. For the case of Si in Sn-based TCOs, Kang and co-workers [Kang et al., 2012] used first-principle calculations to suggest that silicon atoms alter the coordination number of Sn in amorphous Zn_2SnO_4. This leads to an increase in the formation energy of oxygen deficiencies. Yet, this passivation mechanism leads to a strong decrease in electrical conductivity as these deficiencies are the source of free-carriers. Furthermore, it was recently proposed that Si modifies the bandgap of zinc tin oxide, resulting in improved thin-film transistor performance [Choi et al., 2016]. However, the role of Si in the sub-bandgap structure of zinc tin oxide was not fully clarified at the atomistic level in this study.

In contrast to previous reports, here we combine experimental and computational techniques to explain the effect of Si on the optoelectronic properties of SnO_2-based materials. We demonstrate that adding SiO_2 during deposition of Sn-based TCOs (using a-ZTO and SnO_2, as case examples) results in a decrease in the sub-gap absorption while keeping electrical properties unchanged. By combining these experimental results with density functional theory (DFT) calculations, we find that, while the oxygen from SiO_2 passivates deep sub-bandgap defects, the addition of Si decreases the ionization energy of oxygen deficiencies and shifts the corresponding sub-bandgap defect states close to the conduction band minimum

(CBM). Thanks to this effect, the defect no longer contributes to the formation of detrimental sub-bandgap absorption centers and provides free-carriers.

4.2 Methods

4.2.1 Experimental details

150 nm-thin films of a-ZTO, SnO_2 , SiZTO and $SiSnO_2$ were deposited onto aluminoborosilicate glass. While the TCO films described in Chapter 3 were sputtered using a Clusterline deposition system, the films described in this Chapter were deposited using a Leybold Univex sputtering system. Modifications of the deposition parameters were required to obtain a-ZTO films with the same optoelectronic properties and microstructure as the ones described in Chapter 3. While the deposition power and the sputtering targets were unchanged, i.e. 80 W for a 10 cm-diameter target (power density of 1.01 W cm^2 in both deposition systems), the substrate temperature was changed from 60 °C to 100 °C . In addition, the base pressure prior to deposition was $\approx 6 \times 10^{-7}$ mbar and the working pressure for a-ZTO was $\approx 8.5 \times 10^{-4}$ mbar. During the deposition of a-ZTO, a constant flow of Ar and Ar/O_2 were set to 10 sccm and 3.5 sccm respectively. Since the source of O_2 is a combination of Ar and O_2 (95% of Ar and 5% of O_2), the oxygen flow ratio ($r(O_2)$) is calculated by the ratio of the oxygen flow and the total flow, i.e. $r(O_2) = 100 \#times O_2/(Ar+O_2)$. During deposition the Ar/O_2flow was changed between 1.0 sccm and 3.5 sccm, which resulted in $r(O_2)$ between 0.45% and 1.3%. Using these deposition conditions, a-ZTO films presented an amorphous microstructure, μ_e of ≈ 20 $cm^2V^{-1}s^{-1}$, N_e of $\approx 7 \times 10^{19}$ cm^{-3} and optical properties similar to those seen in Figure 3.2 in Chapter 3.

SiZTO and $SiSnO_2$ were deposited from separate targets of SnO_2 , zinc tin oxide (target composition of 6 at% Zn and 28 at% Sn and 66 at% of O) and SiO_2 . Co-depositions were performed using two targets simultaneously, i.e. zinc tin oxide and SiO_2 targets to deposit SiZTO or SnO_2 and SiO_2 targets to deposit $SiSnO_2$. The power applied to the zinc tin oxide and SnO_2 targets was fixed to 80 W and the power on the SiO_2 target was varied between 0 W and 20 W (all targets are 10 cm-diameter, hence the power density in the SiO_2 target was varied between 0 W cm^{-2} and 0.25 W cm^{-2}). Substrate temperatures of 100 °C was used for the deposition of SiZTO, while for the deposition of SnO_2 and $SiSnO_2$ the substrate was not intentionally heated, as these conditions yielded high-quality films. For the co-sputtering, a constant flow of 10 sccm of Ar was used, while the Ar/O_2 flow was varied from 1.0 sccm to 3.5 sccm to optimize the optoelectronic properties. This resulted in $r(O_2)$ that variates from 0.45% to 1.3% and resulting in working pressures between 4×10^{-4} mbar and 10×10^{-4} mbar. Following depositions, the films were subjected to a thermal treatment at 200 °C for 30 minutes in air using a hot plate. The free-carrier density and Hall mobility of the films were obtained with a Hall effect HMS-5000 system in the Van der Pauw configuration. Their optical properties were measured using a Perkin-Elmer Lambda 900 spectrophotometer equipped with an integrating sphere. The absorptance of the films was calculated using the total transmittance and the total reflectance (A = 100 - TT - TR). To assess the microstructure and composition of the films, transmission electron microscopy (TEM) was performed in a FEI Tecnai Osiris operated at 200 kV and equipped with four silicon-drift energy-dispersive X-ray spectroscopy (EDX) detectors. Samples were characterized either in plane-view or in cross-section. In the former case, films were sputtered directly onto copper grids coated with a thin carbon film. In the latter case, a thin lamella was extracted using the conventional focused ion beam lift-out method in a Zeiss NVision 40. Rutherford backscattering spectrometry was used to assess the atomic concentration of the different atomic species in SiZTO and a-ZTO. During RBS measurements, high-energy He^{2+} ions are directed onto the samples and the energy distribution and yield of the backscattered He^{2+} ions is measured. Thermal desorption spectroscopy (TDS) was performed using an ESCO spectrometer equipped with a quadrupole mass spectrometer and a halogen lamp at a base pressure of 10^{-9} mbar. By comparing the total effusion and desorption rates from TDS, it was possible to compare total oxygen, tin and zinc desorption for a-ZTO and SiZTO, while heating the samples at a constant rate of 20 °C /minute up to 700 °C . X-Ray photoelectron Spectroscopy (XPS) measurements were carried out using a PHI VersaProbe II scanning XPS microprobe. The analysis was performed using a monochromatic Al Kα X-ray source of 24.8 W power with a beam size of 100 μm. The spherical capacitor analyser was set at a 45° take-off angle with respect to the sample surface. The pass energy was 46.95 eV, yielding a full width at half maximum of 0.91 eV for the Ag 3d 5/2 peak. The background subtraction, data fitting, and calculation of binding energy and FWHM was performed using the Mathematica software.

4.2.2 Computational methods

Similarly to Chapter 3, the experimental investigations described in this Chapter are supported by atomistic first-principle calculations based on density functional theory (DFT). These calculations are essential to understand the effect of Si in in the electronic structure of Sn-based TCOs. The DFT calculations were performed by Dr. Graužinytė and Dr. Flores-Livas, supervised by Prof. Goedecker in the University of Basel.

All density functional theory calculations were performed using the PBE0 hybrid functional as implemented in the VASP electronic structure code [Kresse and Furthmüller, 1996, Paier et al., 2006, Adamo and Barone, 1999]. Si 3s and 3p (4), O 2s and 2p (6) and Sn 5s, 5p and 4d (14) electrons were included in the valence. All defects were introduced into a 2×2×3 (72 atom) supercell of rutile SnO_2 phase. The atomic positions were relaxed using a 2×2×2 MP kpoint mesh until the forces were below 0.02 eV/Å. Final densities of states were obtained using a 3×3×3 Γ-centered kpoint mesh. The volume of the supercell was fixed to that of the (expanded) perfect crystal calculated via fitting the Birch-Murnaghan [Birch, 1947] equation of state. A 3×3×4 (216 atoms) supercell was tested to verify convergence with respect to supercell size and good qualitative agreement was found.

4.3 Trade-off in optoelectronic properties of a-ZTO

Before optimizing a-ZTO by co-sputtering with SiO_2, the properties of a-ZTO films were studied as a function of r(O_2) during deposition. As seen in Figure 4.1, a-ZTO films sputtered with a low r(O_2) during deposition (0.65%) present low conductivity, mainly caused by low μ_e of $\approx 5\ \mathrm{cm^2V^{-1}s^{-1}}$, and high optical absorption from 400 nm to 900 nm. Initially, increasing the r(O_2) improves the film transparency and its conductivity reaches a maximum of 456 $\mathrm{S\ cm^{-1}}$ with μ_e and N_e of 25 $\mathrm{cm^2V^{-1}s^{-1}}$ and $1.12 \times 10^{20}\ \mathrm{cm^{-3}}$ respectively (Figure 4.1(a)). Increasing the r(O_2), above 1.15% reduces the optical absorptance but at the expense of conductivity, which drops by 62% due to a decrease in both μ_e and N_e . A trade-off often observed in TCOs is reached: improving the optical properties worsens the electrical ones and vice-versa. As observed in Figure 4.1, optimizing the oxygen flow during deposition does not yield a film that combines electrical conductivity above 400 $\mathrm{S\ cm^{-1}}$ and a low absorptance in the visible and near infra-red part of the spectra. Hence, alternative approaches are required to control the amount of oxygen in the films and to ensure both high conductivity and transparency.

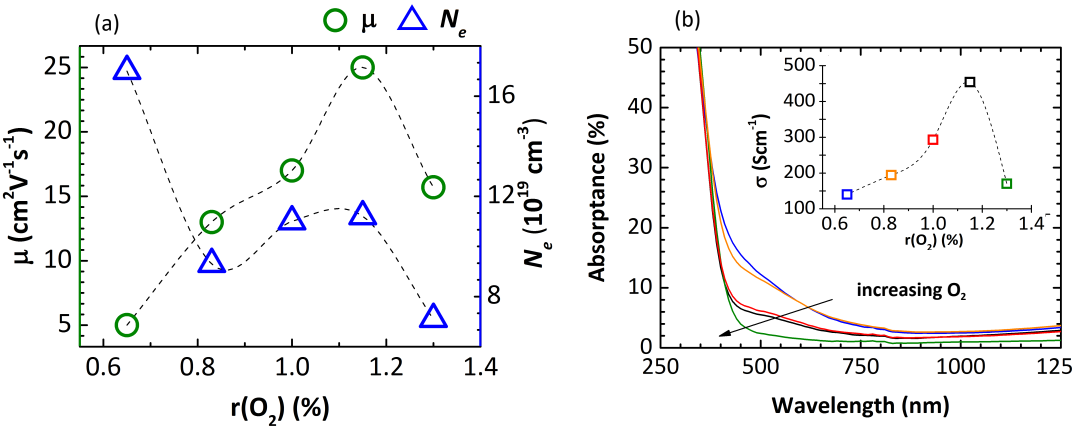

Figure 4.1 – (a) Hall mobility (μ_e) and free-carrier density (N_e) as a function of the oxygen flow ratio (r(O_2)). (b) Absorptance of a-ZTO films as a function of wavelength for depositions with different r(O_2) during deposition. The inset in (b) shows the change in the overall electrical conductivity. All films were annealed at 200 °C for 30 minutes in air prior to the measurements.

4.4 Co-deposition of SiO_2 and Sn-based TCOs

To introduce oxygen into Sn-based TCOs in a precise manner, while avoiding high temperature steps [Rucavado et al., 2017], a-ZTO or SnO_2 were co-sputtered with SiO_2 . In the following subsections we describe in detail the optimization and characterization of a-ZTO with SiO_2 (referred to as SiZTO). The a-ZTO film with highest conductivity (a composition reported in references [Rucavado et al., 2017, Morales-Masis et al., 2016]) will be used as a reference to assess the effectiveness of co-sputtering deposition with SiO_2 . In addition, we will discuss the optimization and following characterization of SnO_2 and $SiSnO_2$.

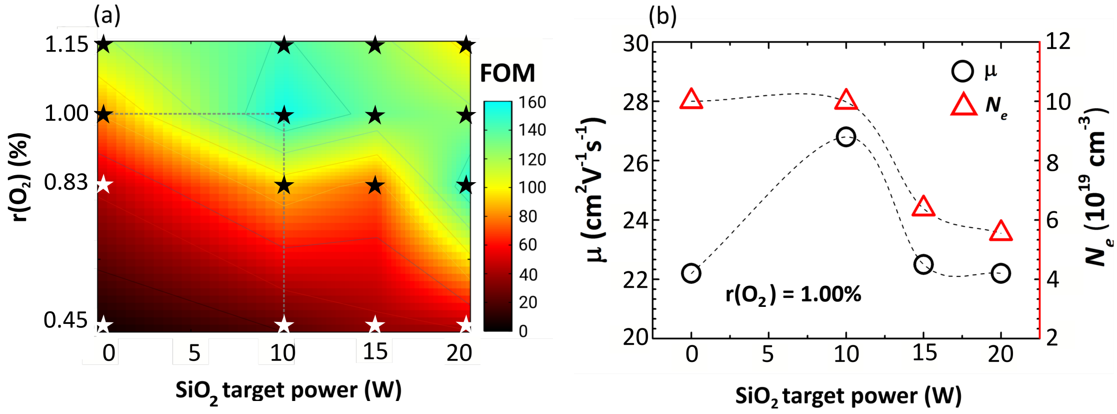

Figure 4.2 – (a) Plot of the simplified figure of merit (FOM) as a function of deposition parameters. The simplified FOM was calculated as the ratio of conductivity and average absorptance in the range 400 nm - 800 nm for SiZTO films deposited with different SiO_2 and O_2 content; (b) Hall mobility and free-carrier density of SiZTO as a function of power applied on the SiO_2 target, these films had a constant r(O_2) of 1.00%.

4.4.1 Reducing sub-bandgap absorption in a-ZTO thin films

We determined the optimal deposition conditions (regarding SiO_2 content and r(O_2)), by comparing a simplified figure of merit (simplified-FOM) of films sputtered under different conditions. The simplified-FOM was calculated as: simplified-FOM = $\frac{\sigma}{A_{400\text{-}800}}$, where σ is the electrical conductivity and $A_{400\text{-}800}$ is the average absorptance from 400 nm to 800 nm. Therefore, a high simplified-FOM is indicative of films with high electrical conductivity and/or low absorptance in the visible spectral range. The SiZTO films with the highest simplified-FOM were deposited using 10 W (with a power density of 0.13 W cm^{-2}) in the SiO_2 target and an r(O_2), of 1.00% (marked with dashed lines in Figure 4.2(a)). The evolution of the electrical properties of SiZTO with SiO_2 content is shown in Figure 4.2(b) (all films deposited with a r(O_2) of 1.00%). The electron mobility increases from 22.2 cm^{2}V^{-1}s^{-1} up to a maximum of 26.8 cm^{2}V^{-1}s^{-1} when the power applied to the SiO_2 target is increased from 0 to 10 W. For these powers, N_e remains constant at 1×10^{20} cm^{-3}. Further increasing the SiO_2 content makes the films less absorbing, but it also results in a decrease of free-carrier density and mobility. The addition of SiO_2 to a-ZTO has an effect in the electrical properties very similar to the increase of oxygen during deposition. As seen in Figure 4.1, the increase in O_2 during deposition initially increases the electrical conductivity, but after a certain threshold is achieved, the conductivity decreases drastically. For SiZTO this threshold is when the power in the SiO_2 target is 10 W, since at 15 W both μ_e and N_e decrease simultaneously.

To highlight the effect of adding SiO_2 in the optoelectronic properties of a-ZTO, the conductivity and absorptance of the optimized SiZTO and the a-ZTO reference are compared in

---

In Chapter 6, a different definition of FOM is used. Here we used a simplified-FOM to compare only Sn-based TCOs, only for their sheet resistance and transparency. In Chapter 6 we compare the TCOs based in their sheet resistance and the absorptance weighted with the solar irradiance spectrum

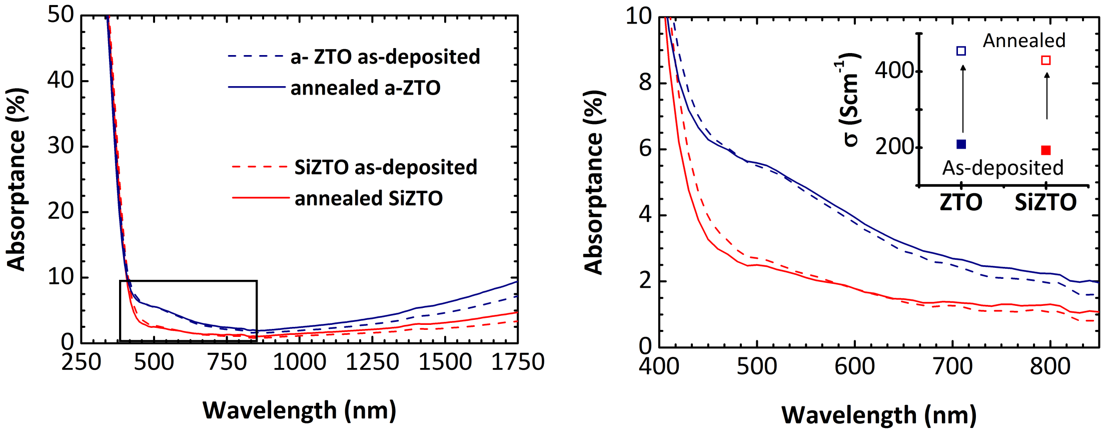

Figure 4.3 – (a) Broadband absorptance of annealed and as-deposited a-ZTO and SiZTO as a function of wavelength. The frame in (a) indicates the close-up region presented in (b). In addition, the inset in (b) shows the conductivity of the as-deposited and annealed films. While both films show virtually equal conductivities, SiZTO presents a lower absorptance below the bandgap and in the near infra-red part of spectrum when compared to the reference a-ZTO. The SiZTO and ZTO film corresponds to the depositions performed with r(O_2) of 1.00% and 1.15% respectively.

Figure 4.3. In Figure 4.3(a) we see the optical absorptance of as-deposited and annealed a-ZTO and SiZTO. Annealing both films result in a slight decrease of absorptance in the near infrared part of the spectra, but the thermal treatment has virtually no effect on the sugbap optical region. On the other hand the addition of SiO_2 to a-ZTO decreases the optical absorptance in the near infrared and the sub-bandgap part of the spectra. To stress the effect of SiO_2 in the sub-bandgap absorptance of a-ZTO and on the electrical conductivity, Figure 4.3(b) compares the annealed and un-annealed materials. It is worth noting that only a slight difference in conductivity between a-ZTO and SiZTO is observed (208 S cm^{-1} and 192 S cm^{-1} in the as-deposited films and 454 S cm^{-1} vs. 429 S cm^{-1} after a mild annealing at 200 °C), with the clear advantage of SiZTO presenting less absorptance than a-ZTO. Indeed, at a wavelength of 500 nm, a-ZTO has a 5.5% absorptance, while SiZTO has an absorptance of only 2.5%. At wavelengths above 1000 nm, SiZTO exhibits an absorptance below 5%.

At this point, it is worth noting that the decrease in optical absorptance is very similar to the one shown for a-ZTO in Chapter 3. Nonetheless the absorptance decrease was obtained by annealing at temperatures > 400 °C , while in this Chapter the improved absorptance results from the addition of SiO_2. Annealing at 200 °C resulted in an increase in the electrical conductivity.

4.4.2 SiZTO microstructure and composition

The asymmetric speckles in the nanobeam diffraction patterns of SiZTO films (optimized material i.e. using 10 W in the SiO_2 target and r(O_2) of 1% indicate an amorphous microstructure

(Figure 4.4a), analogous to that of a-ZTO [Rucavado et al., 2017]. A scanning transmission electron microscopy (STEM) high-angle annular dark-field (HAADF) image and an energy dispersive X-ray spectroscopy analysis (EDX) of the cross-section of SiZTO film (deposited on sapphire) are shown in Figure 4.4b-c respectively. The HAADF image of the cross-section of the sample indicates a dense (voidless) and homogeneous microstructure, while the EDX line profiles (Figure 4.4c) demonstrate that the distribution of elements is uniform within the amorphous film. A slight Si accumulation is measured at the top of the film since the SiO_2 target shutter was closed slightly after the one of the a-ZTO.

The composition of the optimized SiZTO film determined by Rutherford backscattering (RBS) is $Si_{0.02}Zn_{0.04}Sn_{0.27}O_{0.67}$, indicating an absolute increase in oxygen concentration of 2 at% when compared to the reference a-ZTO ($Zn_{0.05}Sn_{0.30}O_{0.65}$). EDX and RBS yield a similar atomic composition.

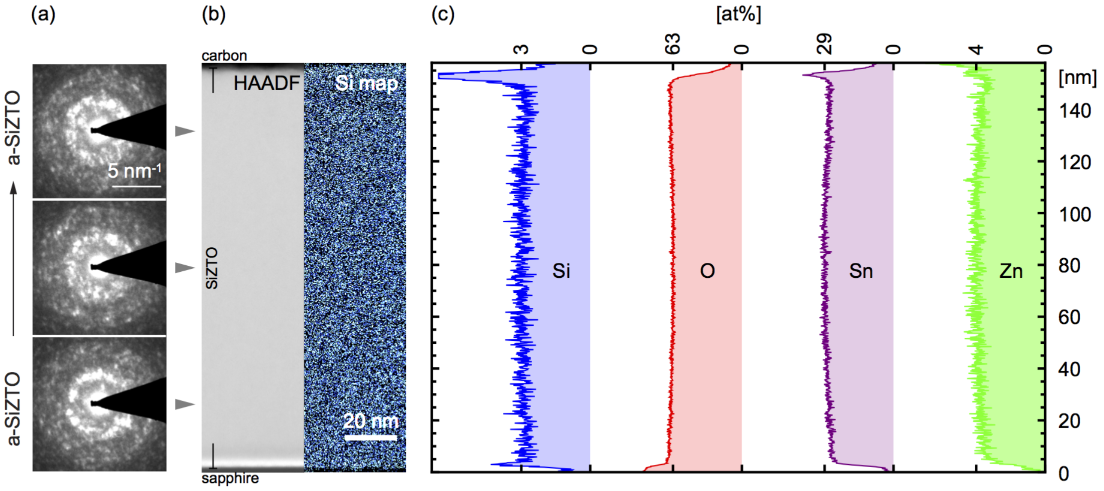

Figure 4.4 – (a) Nanobeam electron diffraction patterns taken along the growth direction of SiZTO thin films. The asymmetric speckles indicate an amorphous structure, unchanged with SiO_2 addition [Rucavado et al., 2017] and along the growth axis; (b) STEM HAADF image of the cross-section of the film (left panel) corresponding Si K edge EDX map (right panel); (c) at% line profiles (left to right) of the Si K, O K, Sn L and Zn K edges quantified using the FEI Velox software (assuming a sample thickness of 100 nm and a density of 6.5 $\mathrm{g\,cm^{-3}}$ for the absorption correction).

Thermal desorption spectroscopy

Thermal desorption spectroscopy measurements were performed on the optimized SiZTO and a-ZTO films. The measurements show the effusion of species with mass to charge ratios (M/z) of 32 and 64. The $M/z = 32$ signal potentially includes the desorption of Zn^+ and O_2^+, while $M/z = 64$ accounts solely for the desorption of Zn^+ [Koida et al., 2017]. At temperatures < 400 °C there is no significant effusion of $M/z = 64$ (Zn^+) species (Figure 4.5b), while for the case of $M/z = 32$ (Zn^+ or O_2^+) a high effusion signal is observed in SiZTO (red curve, Figure 4.5a). The very low effusion of M/z = 64 (Zn^+) for SiZTO at T < 400 °C indicates that the origin of the M/z = 32 signal is solely O_2^+ desorbing from the SiZTO film. The high oxygen signal from SiZTO, when compared to that of a-ZTO, supports the role of SiO_2 as a source of additional oxygen in a-ZTO. At temperatures above 400 °C , the M/z = 64 (Zn^+) signal (Figure 4.5b) increases drastically (by three orders of magnitude) for a-ZTO, while it only increases by one order of magnitude in SiZTO. For a-ZTO, there is a clear correlation between both signals (M/z = 32 and 64), confirmed by the constant ratio between the signals. This indicates that Zn^{2+} desorbs with O^{2+} in a-ZTO at temperatures above 450 °C . In contrast, Zn desorption is shifted to higher temperatures in SiZTO and occurs at a lower rate than in a-ZTO. Interestingly, these results indicate that the addition of SiO_2 to the a-ZTO also result in a material with higher resistance to thermal decomposition. The Zn effusion peak at T > 450 °C has been observed in ZnO and ZnO:Al films previously [Koida et al., 2017], which has been attributed to film decomposition.

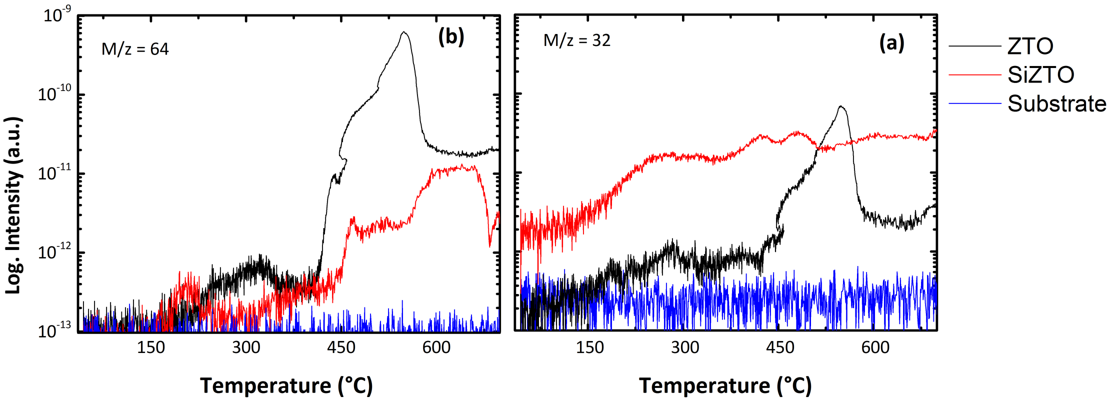

Figure 4.5 – Thermal desorption spectroscopy (TDS) of SiZTO and a-ZTO for (a) M/z = 32 and, (b) M/z = 64. The signal of the silicon substrate is included for reference.

Note that the low chamber pressure during TDS experiments promotes the decomposition of the films at lower temperatures (when compared to atmospheric pressure) [Lupis, 1983]. Desorption of Sn^+ shows the same trend as Zn^+, but at a slightly higher temperature since the bonding energy of Sn-O bonds is higher than that of Zn-O bonds [Gardner, 1940].

X-Ray photoelectron spectroscopy

X-ray photoelectron spectroscopy (XPS) was performed in the a-ZTO and SiZTO films (before and after annealing) to evaluate possible changes in the oxidation state of the elements present with addition of SiO_2 and/or with annealing. To obtain the spectra from the surface and the bulk of the films, the films were etched with Ar-ions before each measurement in steps of 12 nm. Every 12 nm a XP-spectra was obtained from the surface to the interface with the substrate.

A background subtraction was performed using a Top-Hat transform[1]. A pseudo-Voigt fitting was done on the background-subtracted data to calculate the binding energies and the FWHM for peaks corresponding to Sn 3d, O 1s and Zn 2p. In Figure 4.6, the signals corresponding to the ~ 100 nm inside the sample are shown. Only slights differences between the measured samples were found. The absence of the Si 2p signal (Figure 4.6) suggests that the Si concentration was too low to be detected with this setup and acquisition parameters [Shard, 2014, Watts and Wolstenholme, 2003]. Nonetheless, the presence of silicon was confirmed by RBS and EDX separately. The contradiction between techniques (RBS and EDX suggesting ~ 3 at% Si and XPS showing no silicon) is not possible to explain using the existing data. To answer this, further investigations in XPS are required, e.g. repeat the XPS experiments or use higher concentrations of Si in ZTO.

---

[1] The Top-Hat transform is a digital image algorith that substracts small elements from a specific image

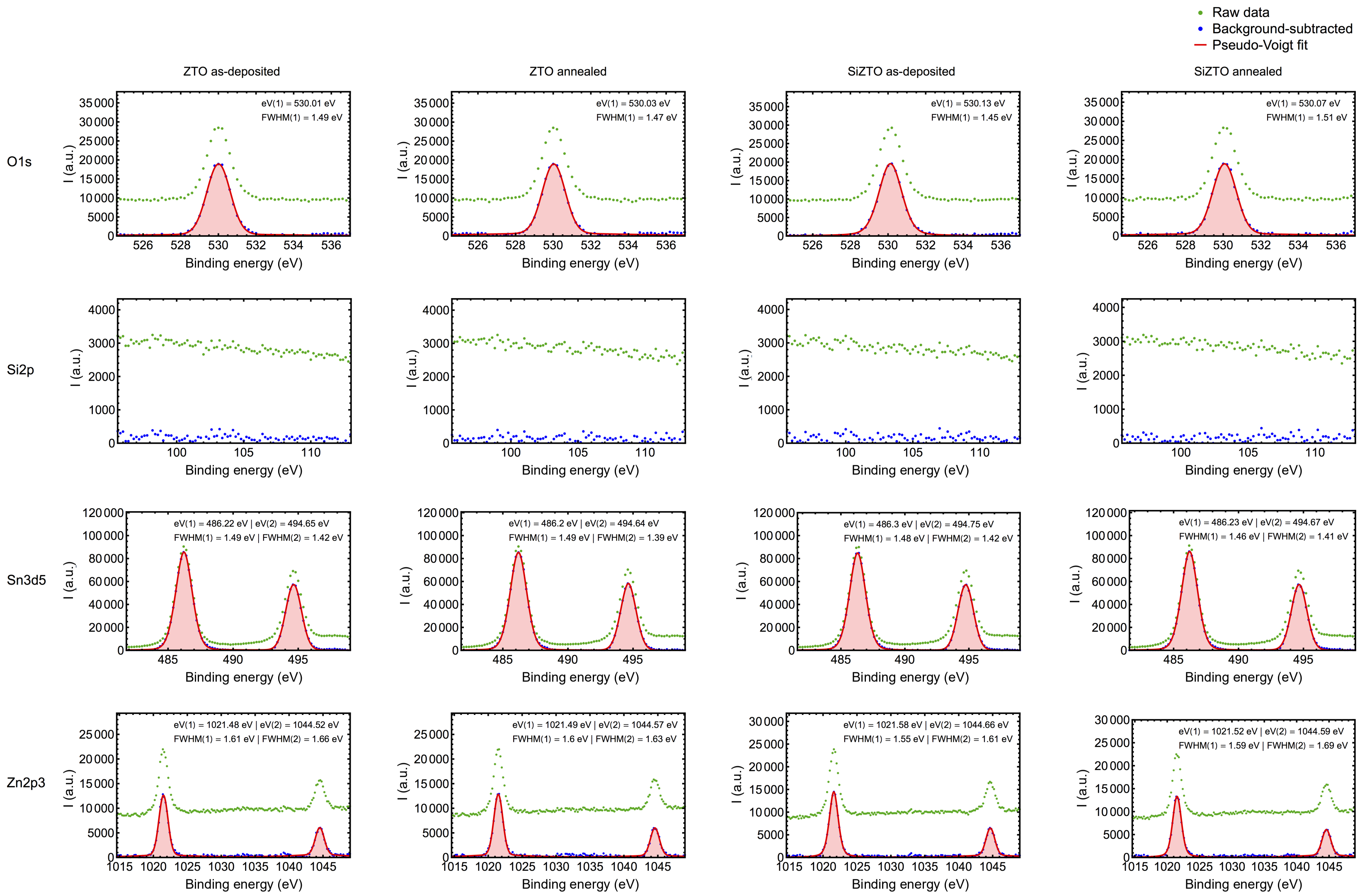

Figure 4.6 – Raw data (green), background subtracted data (blue) and pseudo-Voigt fit (red) of the XPS showing peaks corresponding to O 1s, Sn 3d and Zn 2p for as-deposited and annealed a-ZTO and SiZTO. The Pseudo-Voigt fitting of the XPS data was performed for O 1s, Sn 3d and Zn 2p. There is no signal for the Si 2p band, possibly due to the low concentration of Si atoms in the sample. Fitting shows virtually no change in the binding energy and in the FWHM between samples for each of these bands.

4.4.3 Addition of SiO_2 to SnO_2

To test the universality of adding SiO_2 in Sn-based films to improve the optoelectronic properties of Sn-based TCOs, SiO_2 was co-sputtered this time with pure SnO_2 . To optimize the deposition properties, co-sputtered of SiO_2 and SnO_2 was performed using similar conditions to the ones obtained with SiZTO, i.e. 80 W and 10 W in the SnO_2 and SiO_2 targets respectively. Variating the oxygen during deposition resulted in a very similar result as with a-ZTO, less optical absorptance without any detrimental effect on μ_e nor N_e.

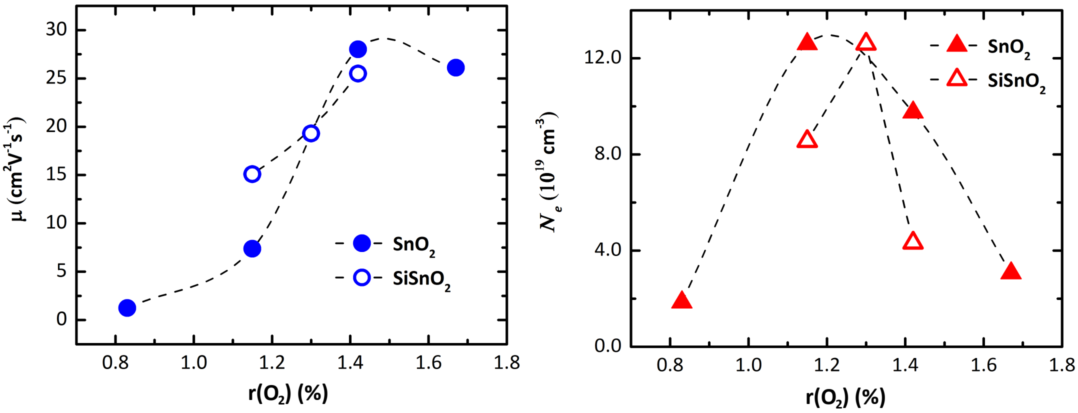

Figure 4.7 – (a) Electron mobility and (b) free-carrier density for SnO_2 and $SiSnO_2$ as a function of oxygen flow ratio - r(O_2) during deposition. All films were annealed at 200 °C for 30 minutes prior to Hall measurement. An optimal optoelectronic properties are achieved in $SiSnO_2$ for an r(O_2) of 1.30%.

μ_e and N_e dependence of oxygen flow is shown in Figure 4.7. For all films, free-carrier density and mobility increase after annealing at 200 °C under atmospheric pressure. This could be attributed to structural relaxations and slightly denser films. For simplicity, only annealed samples will be discussed. As seen in Figure 4.7, a trade-off with the addition of oxygen is seen: for all films mobility increases with O_2 content during deposition, but free-carrier density decreases drastically after a given threshold in O_2 partial pressure. The threshold changes when Si-atoms are present in the material. For SnO_2 , the optimal r(O_2) is 1.45%, while for $SiSnO_2$ is 1.30%. To compare with the effect of SiO_2 in a-ZTO (Figure 4.3), the optical absorptance of SnO_2 and $siSnO_2$ are shown from 250 nm to 1750 nm and from 400 nm to 850 nm (Figure 4.8(a) and (b) respectively). For both materials, the optimized films show a drastic change with the addition of SiO_2 in the visible and near infrared part of the spectra, while preserving similar electric conductivities.

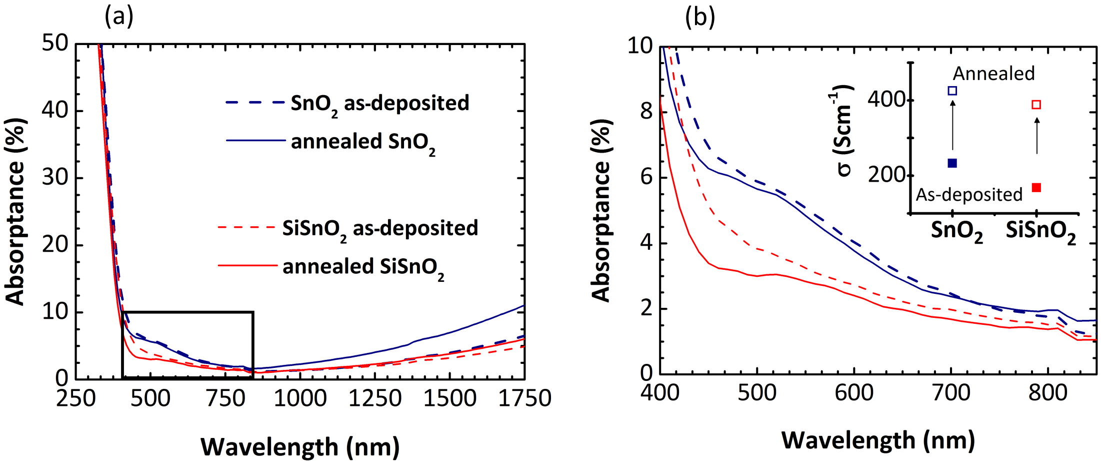

Figure 4.8 – (a) Broadband absorptance of annealed and as-deposited a-$SiSnO_2$ and SnO_2 as a function of wavelength. The r(O_2) for $SiSnO_2$ and SnO_2 are 1.30% and 1.45% respectively, which correspond to the optimized films. The frame in (a) shows a close-up of the absorptance in (b). In addition, the inset in (b) shows the conductivity of as-deposited and annealed SnO_2 and $SiSnO_2$. Just as for SiZTO, both films show similar conductivities, $SiSnO_2$ shows lower absorptance below the bandgap and in the near infra-red part of spectra when compared to the reference SnO_2

4.4.4 $SiSnO_2$ microstructure and composition

A detailed overview of the microstructure of $SiSnO_2$, described by transmission electron microscopy, is shown in Figure 4.9. The section of the $SiSnO_2$ film in contact with the substrate is amorphous, however, as the material thickens, it crystallizes into rutile c-SnO_2 structure. Nanocrystallites are formed halfway through the 150-nm-thick film. A composition of $Sn_{0.38}O_{0.62}$ is obtained by EDX before the addition of SiO_2. For SiZTO, EDX indicates that Si is homogeneously distributed at an average value of 3 at% within the films, while the oxygen content increases slightly to 63 at%. Furthermore, Si atoms do not accumulate at grain boundaries or inside the bulk (amorphous or crystalline) of $SiSnO_2$ (see Si map in Figure 4.4(e)). No Si-rich clusters are observed, particularly towards the top of the film, where the film is composed of small crystallites (Figure 4.4(d)).

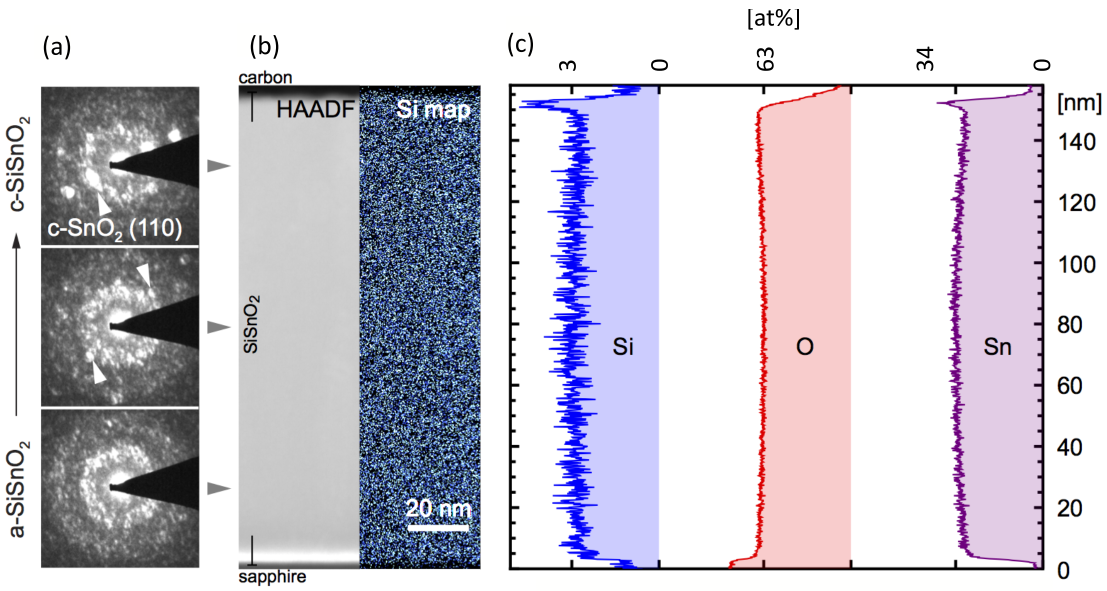

Figure 4.9 – (a) Nanobeam electron diffraction taken along the growth direction of $SiSnO_2$, showing an increased crystallinity towards the end of the film (arrowheads); (b) STEM HAADF image of the cross-section of the film and Si EDX map; (c) at% line profiles (left to right) of the Si K, O K and Sn L edges quantified using the FEI Velox software (assuming a sample thickness of 100 nm and a density of 6.5 g cm^{-3} for the absorption correction

As seen in Figure 4.9, the conductivity of the as-deposited and annealed SnO_2 drops slightly when adding 3 at% of Si, while the absorptance in the visible and near infra-red decreases simultaneously (from 6% to 3% at 500 nm). Hall effect measurements indicate a free-carrier density of 1.75×10^{20} cm^{-3} for SnO_2 and 1.26×10^{20} cm^{-3} for $SiSnO_2$, and mobilities of 28.2 cm^2 V^{-1} s^{-1} and 25.5 cm^2 V^{-1} s^{-1} for SnO_2 and $SiSnO_2$, respectively. Notably, the SnO_2 film contains both amorphous and polycrystalline regions (Figure 4.10(a)), demonstrating that the addition of SiO_2 passivates sub-bandgap defects in amorphous and mixed-phase amorphous/polycrystalline thin films. In addition, the presence of Si-atoms in SnO_2 retards the onset of crystallization of the films: grains start to appear closer to the top surface in $SiSnO_2$ when compared to SnO_2 . A similar effect has been previously reported for Zn-modification of SnO_2 [Zhu et al., 2014]. An extensive study of the amorphous-to-crystalline transition of SnO_2 and a-ZTO using XRD is found in reference [Landucci, 2019]. Finally, the presence/lack of Zn does not appear to modify the passivation mechanism.

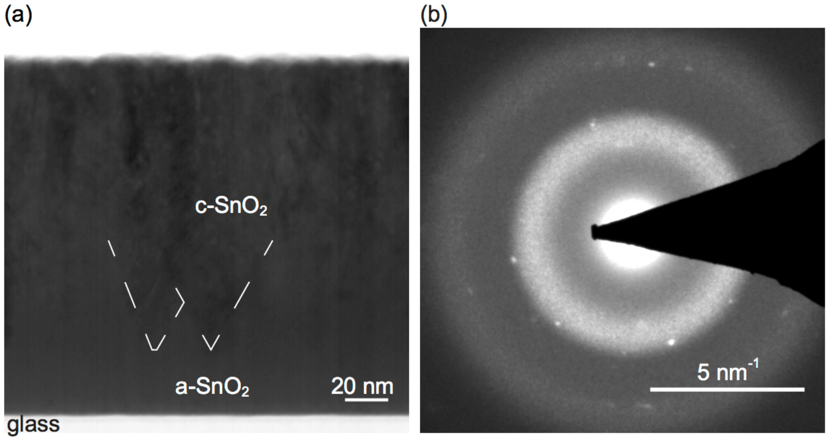

Figure 4.10 – (a) STEM bright field image and (b) selected-area diffraction pattern of SnO_2. The microstructure of SnO_2 is amorphous near the glass substrate, and as the thickness increases it crystallizes to a polycrystalline structure.

4.4.5 A general process for Sn-based films

Experimentally, we have demonstrated that the addition of ≈ 2% of SiO_2 to Sn-based oxides results in a decrease of the optical absorptance in the sub-bandgap region. The decrease in absorptance is similar to the effect of thermal annealing in oxidizing atmospheres at 500 °C seen in a-ZTO (3.2 in Chapter 3). Also, similar changes in the optical properties were seen if the r(O_2) was increased during deposition (Figure 4.1), but this resulted in a poor electrical properties. In contrast, the addition of SiO_2 to SnO_2 and a-ZTO resulted in a reduction of absorptance without important changes in either μ_e nor N_e . In addition, the effect of SiO_2 in SnO_2 and a-ZTO is the same regardless of the microsctructure. From this, we conclude that the addition of SiO_2 is a different passivation mechanism to the introduction of oxygen atoms in the films. The following sections aim to understand and explain the effect of Si in Sn-based oxides.

4.5 Si-modification to SnO_2

The effect of point defects in the optoelectronic properties of Sn-based materials is described qualitatively using Figure4.1. TCO deposition with low r(O_2) results films with high V_O density, with deficient optical and electrical properties. As the number of V_O decreases, there is an improvement in the optoelectronic properties. This effect is described in detail quantitatively for a-ZTO in Chapter 3. As shown in previous sections, it is possible to improve the properties of Sn-based TCOs by adding a small quantity of Si-atoms in the atomic network. The gain in optical properties occurs irrespective of whether the microstructure is fully amorphous (SiZTO) or an amorphous/polycrystalline mixture ($SiSnO_2$). Moreover, both Si and O are found by EDX to be homogeneously distributed within the thin films and show no segregation (e.g.

Si does not accumulate at the grain boundaries of the polycrystalline SnO_2 structure as shown in Figure 4.4d-f). These observations indicate that the addition of SiO_2 is modifying the nature of point defects present within the films, defects that are present in both amorphous and crystalline structures. To understand in detail the nature of these defects and their passivation mechanism by Si addition, density functional theory calculations were performed. For these calculations, the rutile crystal structure of SnO_2 was used as a starting point, since: i) the same effect was observed for amorphous and polycrystalline structures, ii) a-ZTO crystallizes into rutile SnO_2 and has first coordination shells very close to this atomic structure [Zhu et al., 2014], iii) Zn does not appear to modify the Si-passivation mechanism and iv) in a crystalline structure the effects induced by point defects can be isolated and only a limited number of defect sites needs to be considered compared to an amorphous environment, thus preventing the convolution of different effects (i.e. induced by the aperiodic structure and/or locally missing atoms) that may blur the contribution of individual point defects in an amorphous material.

The stoichiometric phase of crystalline SnO_2 has a defect-free bandgap of 3.6 eV with no parasitic absorption in the visible range [Summitt et al., 1964]. One possible cause for the optical absorption feature shown in Figure 4.8(b) is deep defect states arising from charge neutral oxygen vacancies (V_O^x). These defects have been predicted by theoretical models [Körner et al., 2014, Körner et al., 2012]. A similar role of oxygen deficiency related defects in sub-bandgap absorptance was demonstrated for the a-ZTO films, as shown in Chapter 3. The link between V_O -related defects and the absorptance features at 600 nm observed in Figure 4.3 is further supported by the observation that increasing $r(O_2)$ during deposition suppresses the absorption (Figure 4.1). The central role of oxygen deficiencies in sub-bandgap absorption and its reduction in the presence of silicon suggests an indirect or direct passivation mechanism of the vacancies upon SiO_2 addition. In this section, one such possible mechanism is discussed by considering a direct interaction between Si and oxygen vacancies. First, the contribution of oxygen vacancies to the parasitic absorption in SnO_2 is described in detail and then the impact of Si addition is elucidated.

4.5.1 Oxygen vacancies

The structure of the SnO_2 crystal containing an oxygen vacancy is shown in Figure 4.11a. Local relaxations of the three-neighbouring tin atoms following the creation of an oxygen vacancy result in two symmetry inequivalent Sn-sites labelled site (A) and site (B) in the inset of Figure 4.11a. An isolated V_O is seen to be stable in two charge states in the crystalline SnO_2 film (see Figure 4.11b): an ionized q = +2 charge state when the Fermi level is below 2.77 eV and in a charge neutral q = 0 state when the Fermi level is approaching the conduction band. In agreement with previous studies [Kılıç and Zunger, 2002, Guo and Hu, 2012, Graužinytė et al., 2017], we observe electronic defect states in the mid-gap region for a charge neutral vacancy (V_O^x) (Figure 4.12a), which would contribute to parasitic absorption. In contrast, a doubly ionized vacancy ($V_O^{\bullet\bullet}$) (Figure 4.12b) results in electronic states at the edge of the

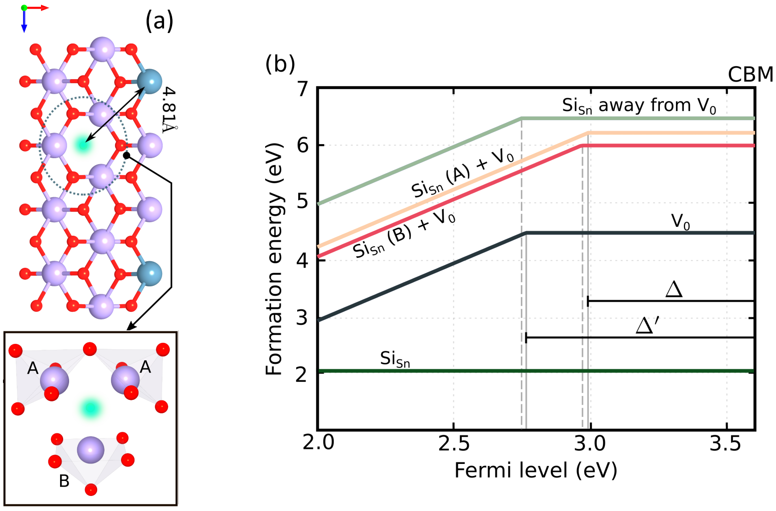

Figure 4.11 – (a) SnO_2 surrounding an oxygen vacancy defect. Sn atoms are shown as purple spheres, oxygen - red, Si - blue, the vacancy is indicated in green. Right panel: A and B number the two substitutional Si sites neighbouring the vacancy. Left panel: the distance between a substitutional Si_{Sn} far from V_O is indicated; (b) Formation energies (O-rich) of isolated defects and defect-clusters as a function of the Fermi level. $\epsilon(2/0)$ transitions are indicated by light grey lines. Δ marks the distance between $\epsilon(2/0)$ transition and the CBM. This distance, important in determining the ratio between different charge states, is shifted towards the CBM in the presence of Si.

conduction band minimum (CBM) of stoichiometric SnO_2 , which would not detrimentally affect the optical properties of the TCO. This transition of electronic defect states from deep to shallow is a result of local atomic relaxations that follow the ionization of the vacancy. Similar metastable shallow donor state formation via ionization has also been reported for other TCOs, namely ZnO and In_2O_3 [Lany and Zunger, 2007, Lany and Zunger, 2005].

Whether an oxygen vacancy contributes to parasitic absorption or not is, therefore, determined by the position of the Fermi level, ϵ_F. The Fermi energy at which two different charge states of a given defect have the same formation energy (i.e. form in equal concentrations) is known as the thermodynamic transition level. The calculated thermodynamic transition levels, $\epsilon(2/0)$, are indicated by grey lines in Figure 4.11. In the case of an isolated oxygen vacancy the $\epsilon(2/0)$ transition was found to occur at a Fermi level of 2.77 eV above the valence band. However, in an n-type TCO material ϵ_F is expected to lie at or above the conduction band minimum. The energy between the CBM and the thermodynamic transition level is (Δ) therefore, the quantity that determines the ratio between the concentrations, C_q, in which the different charge states, q, will form

$$\frac{C_0}{C_2} = exp\left(\frac{2\Delta}{k_B T}\right) \tag{4.1}$$

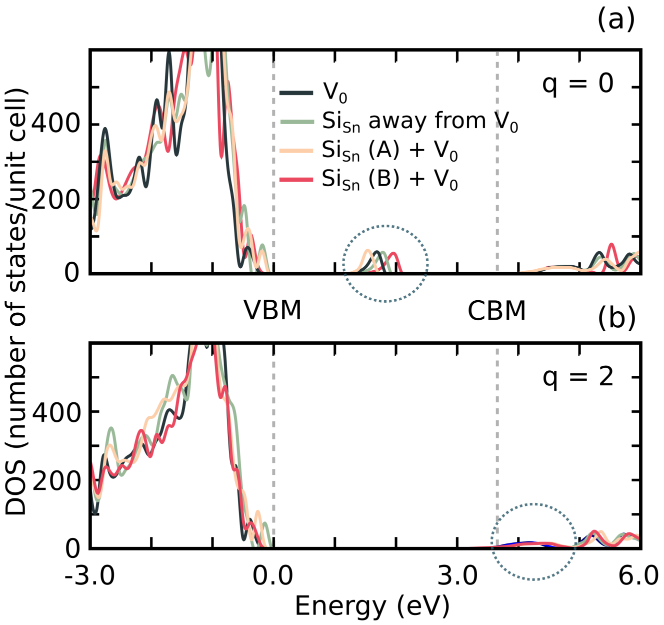

Figure 4.12 – Electronic densities of states for oxygen vacancy related defects in SnO_2. Results for the charge neutral (q = 0) and for doubly ionized (q = 2) supercells are shown. Coloured lines correspond to defect geometries described in detail in the main text. Defect induced states are highlighted by dashed circles.

In the case of an isolated V_O a value of 0.855 eV for Δ was obtained. As a consequence, in an n-type SnO_2 the majority of oxygen vacancies are expected to be charge neutral and likely to lead to parasitic absorption. On the other hand, the presence of silicon in the atomic structure of SnO_2 shifts the C_0/C_2 ratio as we shall see in the next section.

4.5.2 Addition of silicon

The EDX measurements reveal a uniform distribution of Si atoms in the SnO_2 and a-ZTO atomic networks, hence Si clustering was not considered in the modelling process of the materials. The rutile structure of SnO_2 offers two obvious substitutional sites for Si incorporation: the oxygen, Si_O, or the tin, Si_{Sn}, site. We found that silicon preferentially substitutes Sn with a formation energy of 2.04 eV and remains electrically inactive for Fermi levels across the bandgap, as demonstrated in Figure 4.11b. O-site substitution, on the other hand, results in a formation energy over 10 eV higher than that of a Sn-site (not-shown in Figure 4.11), which suggests this defect-type is unlikely to occur.

We then consider the formation of Si_{Sn}-V_O defect clusters, where the Si atom takes one of the two symmetry inequivalent Sn sites neighbouring the oxygen vacancy, marked by A and B on the right panel of Figure 4.11a. The calculated binding energies of the ionized Si_{Sn}-V_O clusters were found to be 0.757 eV on site A and 0.927 eV on site B. The positive binding energy suggests that substitutional Si prefers to incorporate nearby undercoordinated Sn atoms.

As seen in Figure 4.12, in all cases, the electronic defect states associated with a $\mathrm{V_O}$ formation are not strongly affected by the presence of a neighbouring Si atom. However, Figure 4.11b reveals that when the $\mathrm{Si_{Sn}}$-$\mathrm{V_O}$ pair is formed the thermodynamic transition energies $\epsilon(2/0)$ are shifted closer to the conduction band and values of Δ equal to 0.635 eV (site B) and 0.655 eV (site A) are obtained. The exponential dependence on the value of Δ suggests that a 25% shift observed in the presence of Si, could significantly affect the ratio between the different charge states of oxygen vacancies present in the TCO. The presence of silicon is, accordingly, seen to promote the formation of ionized oxygen vacancies, i.e. charge states that do not contribute to the parasitic absorption.

Finally, we validate our results by placing the $\mathrm{Si_{Sn}}$ and the $\mathrm{V_O}$ defects inside the same cell, but as far away from each other as the cell size allows. This defect geometry is shown in the left panel of Figure 4.11a. In the limit of an infinite cell, one should recover the exact sum of the behaviours of the two defects in isolation. Instead, Figure 4.11b reveals a small shift of 20 meV in the thermodynamic transition level $\epsilon(2/0)$, when compared to isolated $\mathrm{V_O}$. Changes of similar magnitude are seen in the electronic defect states shown in Figure 4.12. These shifts reflect the size of the error that results from the choice of the supercell and demonstrate the validity of the $\mathrm{Si_{Sn}}$-$\mathrm{V_O}$ cluster calculations.

4.6 Conclusions

In this chapter we show that combining SiO_2 and Sn-based oxides (namely a-ZTO or SnO_2) by co-sputtering from separate targets results in a material with similar electrical properties as the Sn-based materials ($\mu_e \approx 25$ cm^{2}V^{-1}s^{-1} and $N_e \approx 10^{20}$ cm^{-3}) but less optical absorption in the visible and infra-red part of spectrum. The introduction of over 2.6 wt% of SiO_2 in the Sn-based oxides results in a reduction of average optical absorptance from 4.2% to 2.3% in SiZTO and from 4.0% to 3.2% in $SiSnO_2$ (in the spectral range from 400 nm to 850 nm). The reduction of optical absorptance in not restrictive to the visible part of spectra, overall broadband absorption (from 400 nm to 2000 nm) is also reduced from 5.6% to 2.9% in SiZTO and from 6.2% to 3.3% in $SiSnO_2$. This method prove to be equally effective in amorphous and mixed phase amorphous/polycrystalline microstructures. While for a-ZTO there is no effect on its amorphous microstructure, co-sputtering of SiO_2 postpones the amorphization of SnO_2 , since crystalline domains appear earlier in SnO_2 than in $SiSnO_2$, which suggest that SiO_2 amorphizes the TCOs. In addition, this "cold passivation" technique has low thermal budget (temperatures < 200 °C), which enables its usage in temperature-sensitive substrates and devices.

We used density functional theory calculations of SnO_2 with rutile structure, to provide a quantitative explanation for the mechanisms governing the defect passivation of the materials with SiO_2 . We found that the effect of SiO_2 is two-fold, on one hand the oxygen atoms from SiO_2 passivates the oxygen ubiquitous oxygen deficiencies in Sn-based oxides. On the other hand, DFT calculations suggest that Si-atoms promote the formation of ionized defects which do not contribute to the detrimental sub-bandgap absorption.

Finally, this low-temperature technique could in principle be scalable to industrial volumes; and should serve as an inspiration to design and discover oxides that could potentially play a similar role in other TCOs as SiO_2 does in SnO_2 and a-ZTO.

5 Zr-doped In_2O_3: Transport limiting mechanisms and application in silicon heterojunction solar cells.

My original input and work for the results presented in this chapter include: the plan and execution of the sputtering and post-deposition thermal treatments of In_2O_3*:Zr, all the electrical characterization, the optical characterization with the spectrophotometer and the coordination of the RBS and TEM experiments.*
I want to acknowledge Federica Landucci for the electron microscopy analysis, Dr. Max Döbeli for the RBS and ERDA experiments and discussion, Raphäel Monnard and Dr. Mathieu Boccard for the solar cell development and discussion, Dr. Jakub Holovský for the photothermal deflection spectroscopy measurements and Dr. Jeremie Werner for the useful discussion.

To benchmark our indium-free TCOs, here we study an indium-based material in both the amorphous and the crystalline phase. Due to its high conductivity and broadband transmittance, Zr-doped In_2O_3(In_2O_3:Zr) is chosen for this study. Films with thickness from 15 nm to 100 nm were sputtered in the amorphous state and annealed in different atmospheres to investigate the links between defects, microstructure and optoelectronic properties. Annealing in air yields fully crystalline films with low free-carrier concentration, high transparency and a high electron mobility limited by scattering from optical phonons and ionized impurities. 15-nm-thick films exhibit an average absorptance of $< 0.5\%$ in the wavelength range 390 to 2000 nm and an electron mobility of 50 $cm^2V^{-1}s^{-1}$, increasing to 105 $cm^2V^{-1}s^{-1}$ for 100 nm films. Alternatively, thermal treatments in a neutral or reducing atmospheres result in a higher conductivity for films thinner than 50 nm as a high free-carrier concentration is maintained. The possibility of thinning down the In_2O_3:Zr to a few tens of nm while keeping high lateral conductivity makes this material a promising candidate for a wide range of applications, including flexible touch-screens, solar cells and light emitting diodes. Finally, as a proof of concept we used 40-nm-thick In_2O_3:Zr as a transparent front electrode in silicon heterojunction (SHJ) solar cells. To minimize optical losses, a MgF_2 secondary antireflective coating was applied on top of the 40-nm-thick In_2O_3:Zr. The thickness reduction and the MgF_2 results in solar cells with higher photo-generated current than the cells with 80-nm-thick In_2O_3:Sn (standard electrode in SHJ solar cells). This results in increasing the short circuit current and decreasing the usage of indium oxide in the solar cells.

5.1 Motivation and state of the art

As discussed in Chapter 1, tin-doped indium oxide (In_2O_3:Sn known commonly as ITO) is the mainstream material in industry [Ginley and Perkins, 2011]. Nonetheless its optoelectronic properties have limitations: a high N_e (typically from 10^{20} cm^{-3} to 10^{21} cm^{-3}) is necessary to achieve a high conductivity but this results in relatively low electron mobility (typically $\mu_e < 40$ $cm^2V^{-1}s^{-1}$) [Yamada et al., 2000], which leads to high free-carrier absorption. In contrast, hydrogenated indium oxide (In_2O_3:H) has excellent optoelectronic properties due to its high mobility ($\mu_e \approx 100$ $cm^2V^{-1}s^{-1}$), and has relatively low free-carrier density ($\approx 10^{20}$ cm^{-3}) leading to a low free-carrier absorption [Koida and Kondo, 2007b, Koida et al., 2010]. During deposition of In_2O_3:H, the introduction of water leads to the formation of an amorphous microstructure [Wardenga et al., 2015]. A post-deposition thermal annealing at temperatures from 150 °C to 200 °C crystallize the film and improves its μ_e and its optical properties. Deposition without intentional introduction of water, results in films that are already crystalline but with low electron mobility (≈ 10 $cm^2V^{-1}s^{-1}$) , which does not increase drastically after the subsequent thermal treatment (≈ 30 $cm^2V^{-1}s^{-1}$) [Jost et al., 2016]. Experimental and computational studies have described extensively the doping, transport and crystallization mechanisms of In_2O_3:H. Experimental results [Koida and Kondo, 2007b, Koida et al., 2010, Mizuno et al., 1997] suggest that hydrogen plays a key role in reducing the number of defects in the films, since during crystallization H-atoms seem to passivate doubly charged oxygen vacancies ($V_O^{\bullet\bullet}$) by substituting them with singly charged H-atoms ($H_O^{\bullet}$). This effect simultaneously provides passivation of doubly-charged defects while generating one free-carrier per defect-site, which contributes to the high conductivity of the material. This passivation, combined with the reduction of structural disorder by crystallizing the films, increases μ_e . By carefully analysing Hall effect results and optical mobility calculations, the authors found that, for 70-nm-thick In_2O_3:H, the dominant scattering mechanisms in their films were ionized impurities and phonon scattering [Koida and Kondo, 2007b, Koida et al., 2010, Mizuno et al., 1997]. In this regard, previous experimental evidences [Macco et al., 2016] and scattering calculations [Preissler et al., 2013] have shown that, for In_2O_3:H, polar optical phonons are dominant over acoustic phonons. In addition, first-principle studies using density functional theory (DFT) have shown the formation energy of H-related defects [Limpijumnong et al., 2009] and it was found that substitutional and interstitial hydrogen atoms ($H_O^{\bullet}$ and $H_i^{\bullet}$) act as shallow donors in In_2O_3:H. A complementary study performed by Macco et al. [Macco et al., 2016] supports these results for 75-nm-thick In_2O_3:H deposited by atomic layer deposition, and, in addition, describes that nanometric-sized crystallites trigger crystallization of the films. In addition, using a combination of X-ray absorption fine structure and molecular dynamics simulations, Medvedeva et al. studied the amorphous-to-crystalline transition of $In_2O_3$and its effect on μ_e [Medvedeva et al., 2017, Buchholz et al., 2014a]. Simulated InO_x polyhedra were modified in terms of bond-angle, bond length and atom deficiency to describe amorphous and crystalline microstructures. Amorphous structures with decreased bond-length form polyhedral chains that enable higher mobility compared with other amorphous structures. The chains are formed prior to the In_2O_3crystallization. In the onset of crystallization μ_e decreases due to a combination of amorphous and crystalline microstructures which produces incoherent inter-face boundaries that act as scattering centres. Fully crystallized films exhibit a higher mobility due to spatially spread polyhedral chains, a large In-O-In angle, which facilitates higher symmetry of the oxygen p-orbitals and enables an efficient overlap between the indium s-orbitals.

Experimentally, after the demonstrated high-μ_e of In_2O_3:H, a plethora of In-based TCOs have been investigated featuring other extrinsic dopants deposited introducing water during deposition, a source of molecular hydrogen [Jost et al., 2016, Boccard et al., 2016b] or by carefully controlling the deposition base pressure [Boccard et al., 2016a]. As an example of these materials, W-doped, Ce-doped and Mo-doped In_2O_3 [Warmsingh et al., 2004, Koida et al., 2018, Kobayashi et al., 2015, Newhouse et al., 2005, Meng et al., 2001] have high electron mobilities and free-carrier densities (N_e of 1.9×10^{20} cm^{-3} , 1.1×10^{20} cm^{-3} , and 1.9×10^{20} cm^{-3} and μ_e of 104 cm^{2}V^{-1}s^{-1} , 110 cm^{2}V^{-1}s^{-1} and 95 cm^{2}V^{-1}s^{-1} for W-doped, Ce-doped and Mo-doped In_2O_3 respectively). Another metal-doped In_2O_3 with promising optoelectronic properties is Zr-doped indium oxide (In_2O_3:Zr). Koida et al. demonstrated that epitaxial grown films of 250 nm of In_2O_3:Zr show μ_e of 110 cm^{2}V^{-1}s^{-1} and N_e of 10^{20} cm^{-3} for 250-nm-thick films [Koida and Kondo, 2006]. Additionally, the same group demonstrated the feasibility to sputter 270-nm-thick In_2O_3:Zr films with a $\mu_e > 80$ cm^{2}V^{-1}s^{-1} and a N_e of 3×10^{20} cm^{-3} at a substrate temperature of 450 °C [Koida and Kondo, 2007b]. For these films, Zr-doping increases the electrical conductivity, since in concentrations ≤ 2 at%, the Zr-atoms act as efficient substitutional dopants for In ($\mathrm{Zr}_{\mathrm{In}}^{\bullet}$), while reducing the detrimental effect of $\mathrm{V}_{\mathrm{O}}^{\bullet\bullet}$ [Koida and Kondo, 2006, Koida and Kondo, 2007a, Kanai, 1984]. In addition Zr^{4+} and In^{3+} have similar ionic radii (72 p.m. and 80 p.m. respectively [Shannon, 1976]), indicating that Zr is not expected to affect the lattice constant and will not induce lattice strain.

Recently, we demonstrated the fabrication of In_2O_3:Zr with $\mu_e > 100$ cm^{2}V^{-1}s^{-1} and $N_e >$ 2.5×10^{20} cm^{-3} and an average absorptance of 3.6% (between 390 nm and 2000 nm) for 100-nm-thick films [Morales-Masis et al., 2018]. These properties clearly place In_2O_3:Zr as an ideal choice for broadband transparent electrodes, showing a high lateral conductivity of 4200 S cm^{-1}, a bandgap of 3.9 eV and a low free-carrier absorption. In this Chapter, we further investigate the properties of this material at thicknesses from 100 nm down to 15 nm, annealed the films in reducing and neutral atmospheres, and present an analysis of the scattering mechanisms and their relation to the microstructure and thickness of the films. Finally, we implement 40-nm-thick In_2O_3:Zr films as front electrode in SHJ solar cells. As compared with In_2O_3:Sn front electrodes, cells using In_2O_3:Zr thin films present an enhanced current density (J_{sc}), which results in high-efficiency devices, which place the material as a promising candidate to replace In_2O_3:Sn and reduce the usage of indium by reducing the electrode thickenss.

5.2 Methods

In_2O_3:Zr films were sputtered at room temperature onto alumino-borosilicate glass using a Leybold Univex system from a target with a 98/2 wt% composition ratio of In_2O_3/ZrO_2. The RF power density was fixed to 0.95 W cm^{-2} (i.e. 75 W in a target with a diameter of 10 cm) and the deposition atmosphere was a mixture of Ar and O_2. To modify the oxygen content in the films, the O_2 the oxygen flow ratio ($r(O_2) = O_2/(Ar+O_2)$) was varied between 0.0% and 0.61%, while the working pressure changed from 2.05×10^{-3} mbar to 2.32×10^{-3} mbar. The initial base pressure was ~ 10^{-6} mbar. After deposition, the films were annealed at 200 °C for 30 minutes under atmospheric pressure or under a pressure of 0.5 mbar of H_2 or N_2 . The film's thickness was measured using an Ambios XP-2 contact profilometer. The electron mobility (μ_e) and free-carrier density (N_e) of the films were measured using a HMS-3000 Hall effect system in the Van der Pauw configuration. Total reflectance (TR) and total transmittance (TT) were measured with a PerkinElmer Lambda 900 spectrophotometer. The absorptance (A) of the films was calculated using: A = 100 - TT – TR, which is a good approximation for highly transparent regions. Effective masses (m^*) were estimated using the Drude model by fitting the reflectance of Fourier transform infrared spectroscopy measurements, performed in a Bruker Vertex 80-system. Photothermal deflection spectroscopy (PDS) was performed by an in-house developed system based on a 150W Xenon lamp. Fluorinert FC-72 was used as a temperature sensitive liquid. The absorption coefficient and refractive index were evaluated as described in [Morales-Masis et al., 2015]. The microstructure of the films was analysed by transmission electron microscopy (TEM) using an FEI Tecnai Osiris operated at 200 kV. For that purpose, films were deposited on SiN grids. Scanning TEM (STEM) images and selected-area diffraction patterns (SAED) were acquired in a top view configuration. Energy dispersive X-rays spectroscopy (EDX) was conducted in the same microscope using 4 silicon drift detectors [Schlossmacher et al., 2010]. The composition of the films was obtained using Rutherford backscattering spectrometry (RBS) using 2 and 5 MeV He ions and a silicon PIN diode detector under 168° [Nastasi et al., 2014]. Hydrogen depth profiles were measured by elastic recoil detection analysis (ERDA) with a 2 MeV He ion beam applying the absorber foil technique [Nastasi et al., 2014].

SHJ solar cells were fabricated on a 240 μm-thick, 4-in-diameter, 3-Ωcm, float-zone wafer, which was textured in a KOH-based solution, cleaned and dipped in 5% HF for one minute prior to loading for layer depositions. Plasma-enhanced chemical vapour deposition (PECVD) was used to deposit the intrinsic (i) and doped (p and n) amorphous silicon (a-Si:H) layers on each side. For front (back) emitter cells, the p-type (n-type) layer was deposited on the front (light-incoming) side of the wafer. The front TCO was then sputtered using a shadow mask to define a 2 cm × 2 cm cell areas, and on the rear side, In_2O_3:Sn and Ag were subsequently sputtered. Screen printing was used for the front Ag grid, and the device was finally cured at 210 °C for 20 minutes.

5.3 Optoelectronic properties: effect of oxygen content and thermal annealing

For 100-nm-thick In_2O_3:Zr, the evolution of N_e and μ_e as a function of r(O_2), is shown in Figure 5.1 (a) and (b). Figure 5.1(c) shows the optical absorptance for these films as a function of wavelength. μ_e of the as-deposited films increases with r(O_2), while N_e is maximum at an r(O_2), of 0.16%. Films deposited without O_2 during deposition present a high absorption in all the measured wavelengths, additionally these films show sub-bandgap absorption (from 380 nm to 630 nm) in the as-deposited state which decrease after the thermal treatment. Increasing the oxygen content during deposition results in an overall decrease in absorptance of the films. When annealed in air, all films show an increase in μ_e and a decrease in N_e , accompanied by a decrease in optical absorptance at a wavelength ranging from the conduction band edge to the near infrared. After thermal annealing, μ_e shows a maximum at r(O_2) of 0.33%, which decreases for higher r(O_2). Given the outstanding μ_e of the film deposited with an r(O_2) of 0.33% (105 $cm^2V^{-1}s^{-1}$), this film considered as the optimized In_2O_3:Zr.

5.3.1 Optical bandgap

To measure accurately the optical bandgap of In_2O_3:Zr, photothermal deflection spectroscopy (PDS) with an UV source to achieve high sensitivity in the visible range is desired. Due to its high sensitivity in the ultraviolet and visible spectral regions, PDS was employed to measure the absorption coefficient (α) of the films and to extract the optical bandgap (Figures 5.2 (a) and (b) respectively). On one hand, higher r(O_2) leads to a decrease in α in all the measured energy range, which confirms the observations made in Figure 5.1(c). In addition, thermal treatment in air results in considerable reduction in α for samples deposited with r(O_2) in the range 0.16% to 0.62% . The film deposited with r(O_2) of 0.08% does not show a reduction in the optical absorptance in the bandgap range, possibly due to a high density of undercoordinated metallic defects (similar to the ones described in Chapter 3 and reference [Rucavado et al., 2017]), which possibly did not decreased drastically after thermal annealing. Assuming direct optical transitions, i.e., n = 2 in the Tauc relation $\alpha \propto (h\nu - E_g)^{1/n}$, an optical bandgap ranging from 3.6 eV to 3.7 eV are found for as-deposited samples, which increased to 3.9 eV to 4.0 eV for the annealed samples (see Figure 5.2(b)). These correspond to values reported in the literature for polycrystalline In_2O_3:Zr films [Kim et al., 2001]. The origin of this shift is the crystallization of the film, and it will be further explained in section5.4. As observed in Figure 5.2(b), for both, as-deposited and annealed samples, a slight blue shift with decreasing r(O_2) is measured, which could be mainly attributed to the Burnstein–Moss shift [Pankove, 2012].

Photothermal deflection spectroscopy was not performed for films sputtered with r(O_2) = 0.0. Nonetheless, films with r(O_2) = 0.08% were measured, and can be used to compare with less absorbing In_2O_3:Zr films.

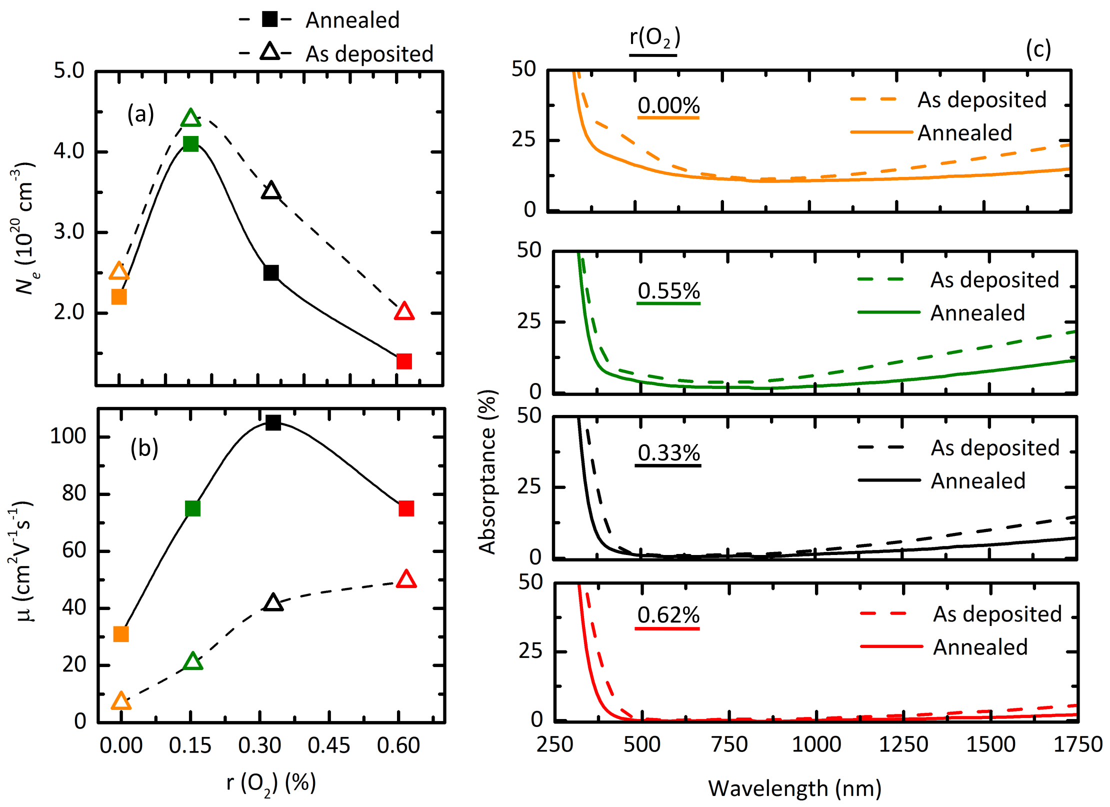

Figure 5.1 – N_e (a), μ_e (b), and absorptance (c) of as-deposited (empty triangles and dashed lines in c) and annealed (full squares and solid lines) of 100-nm-thick In_2O_3:Zr films sputtered with different r(O_2). A maximum for mobility of 105 $cm^2V^{-1}s^{-1}$ is obtained when sputtering with r(O_2) of 0.33%, while a maximum N_e is achieved for r(O_2) of 0.16%. A convenient trade-off between optical and electrical properties is obtained for films with mobility of 105 $cm^2V^{-1}s^{-1}$, since the average optical absorptance is 3.6%, while for the film sputtered with higher N_e show an average absorptance 6.2%. The film deposited with r(O_2), of 0.62% has a low average absorptance of 1.0% but its N_e and μ_e are reduced. Lines in figures (a) and (b) provide a guide to the eye.

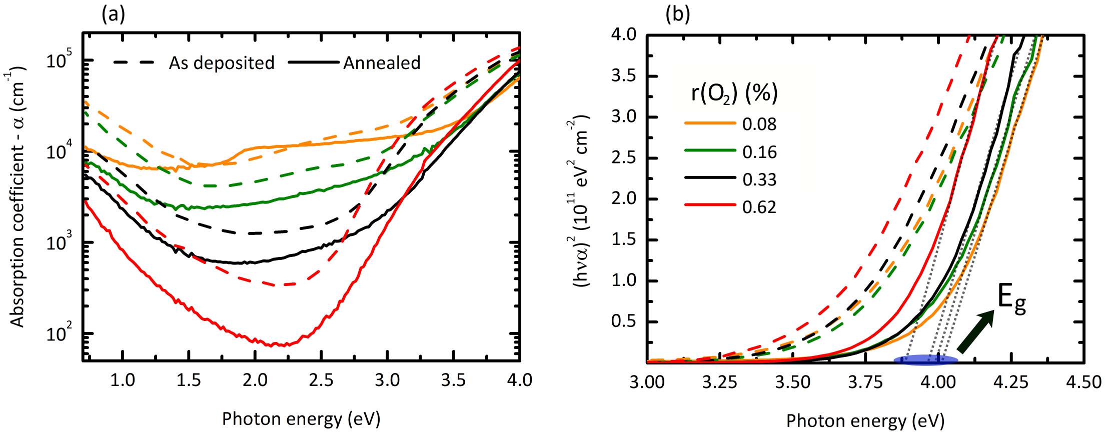

Figure 5.2 – (a) Absorption coefficient (α) of In_2O_3:Zr films deposited with r(O_2) from 0.08% mbar to 0.62%. As-deposited films are in dashed lines while annealed films are in solid lines. (b) Tauc plot of the films shown in (a). The Tauc plot shows that an optical bandgap of 3.6 eV to 3.7 eV are found for as-deposited samples, which increases to 3.9 eV to 4.0 eV after annealing.

5.4 Microstructure of In_2O_3:Zr

To study the microstructure of the optimized films, scanning TEM (STEM) bright-field (BF) micrographs, selected-area electron diffraction patterns and energy-dispersive X-ray (EDX) spectra were acquired. The as-deposited film presents a microstructure that is predominantly amorphous, as confirmed by the diffuse rings in the diffraction pattern in Figure 5.3(a). Small (nanometric) randomly distributed nanocrystals (white and black spots marked by red arrows) are embedded in the amorphous matrix. The crystallites have an average size of 2 nm and their density is ≈ 5 μm^{-2}. Similar microstructures have been reported elsewhere [Koida et al., 2010]. The films undergo an amorphous to crystalline transition during thermal annealing at 200 °C in air (Figure 5.3(c) and (d)). The annealed films show crystalline domains of an average size of 320 nm, with body-centered cubic structure (bixbyite-like structure [Buchholz et al., 2014a]) (Figure 5.3(c) and (d)). Additionally, EDX results show that zirconium, oxygen and indium-atoms are distributed homogeneously within the films, and that the atomic composition is 59 at%, 2 at% and 39 at% of oxygen, zirconium and indium respectively (Figure 5.4).

RBS data of the optimized as-deposited In_2O_3:Zr films[1] indicates a composition of $Zr_{0.01}In_{0.40}O_{0.59}$, which changes after thermal treatment to $Zr_{0.01}In_{0.38}O_{0.61}$. From electron recoil detection analysis (ERDA)[2], we estimate the H-content in our films by comparing with measurements of a mica reference (9.5 at% of atomic-H). Hence, for a constant H-concentration, the signal should decrease monotonically as the mica standard. Thermal annealing of In_2O_3:Zr leads to an average atomic-H content changing from 2.3 ± 0.3 at% to 1.8 ± 0.3 at%. Note that given the uncertainty of ERDA measurements, the results show a tendency of H-content in the films. In

---

[1] The optimized films were deposited with r(O_2) of 0.33% and μ_e of 105 cm^{2}V^{-1}s^{-1} .

[2] ERDA and RBS measurements were performed in the optimized In_2O_3:Zr films, i.e. sputtered with r(O_2) = 0.33% before and after annealing.

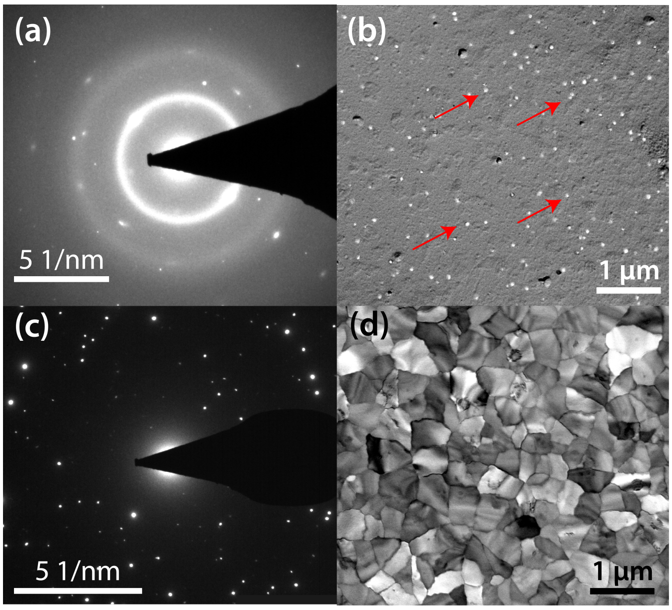

Figure 5.3 – Selected-area TEM diffraction patterns of (a) as-deposited and (c) annealed 100-nm-thick In_2O_3:Zr films and corresponding STEM bright-field images in (b) and (d). In (b), small (nanometric) crystallites, marked with red arrows, are visible in the amorphous matrix. The SAED and STEM imaging was performed on the optimized In_2O_3:Zr films (r(O_2) of 0.33%). The images and diffraction patterns confirm an amorphous-to-crystalline transition after thermal annealing at 200 °C .

addition, the ERDA results suggest that an accumulation of H-atoms is present in the surface of the annealed film compared with the as-deposited In_2O_3:Zr (Figures 5.5(c) and (d)).

The presence of H-atoms in the films is expected as these are ubiquitous in deposition systems at a base pressure of 10^{-6} mbar. To compare with other high-μ_e TCOs, ERDA measurements show that In_2O_3:H has an H-content of 2.7± 0.3 at% is found in the as-deposited films. Annealing In_2O_3:H in the same conditions as In_2O_3:Zr, resulted in an unchanged average H-content in the films nonetheless, just as for In_2O_3:Zr, H-atoms are found accumulated in the film's surface after thermal treatments (Figure 5.5(a) and (b)). Other studies also report an unchanged H-content after thermal treatments in In_2O_3;H grown under with similar conditions and annealed correspondingly [Koida et al., 2010, Macco et al., 2015].

The μ_e increase after annealing (41.4 $cm^2V^{-1}s^{-1}$ to 105 $cm^2V^{-1}s^{-1}$) is intrinsically linked to the crystallization of the film, as shown experimentally in In_2O_3:H by [Koida et al., 2007, Macco et al., 2014] and explained by [Medvedeva et al., 2017]. Crystallization provokes an increase the In-O and the In-In bond distance. This is caused by a high rate of shared O-atoms by In-cations and results in increased symmetry of the O-p orbitals, which enables an effective overlap between the In-s orbitals. In addition, the crystalline phase is composed of InO_x polyhedral chains that allow efficient electron transport [Medvedeva et al., 2017]. Finally,

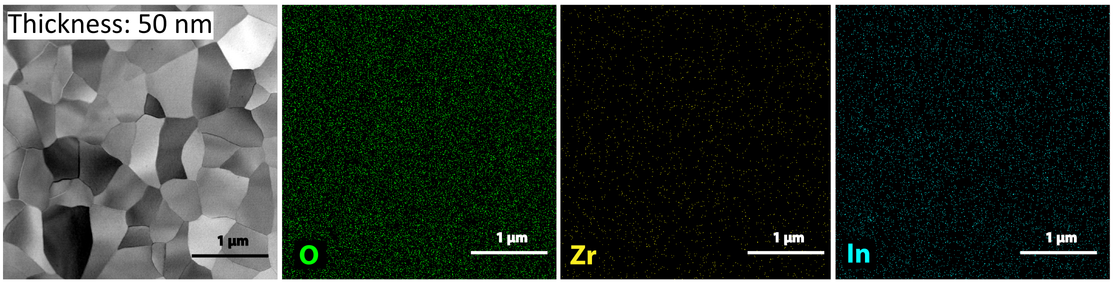

Figure 5.4 – STEM bright field micrograph of annealed 50-nm-thick In_2O_3:Zr, the crystallites have an average size of ~ 400 nm. The EDX maps show an homogeneous composition of Zr, In and O. The EDX quantification resulted in averages of 2 at%, 39 at% and 59 at% of Zr, In and O.

the crystalline transition is also accountable for the bandgap shift after thermal annealing (Figure 5.1(c)) [Wardenga et al., 2015, Koida et al., 2010]. The amorphous microstructure of In_2O_3 allows optical direct transitions that are forbidden in its crystalline counterpart, hence the optical bandgap in the amorphous films is reduced as compared with the crystalline films [Walsh et al., 2008, Koida et al., 2018, Fuchs and Bechstedt, 2008].

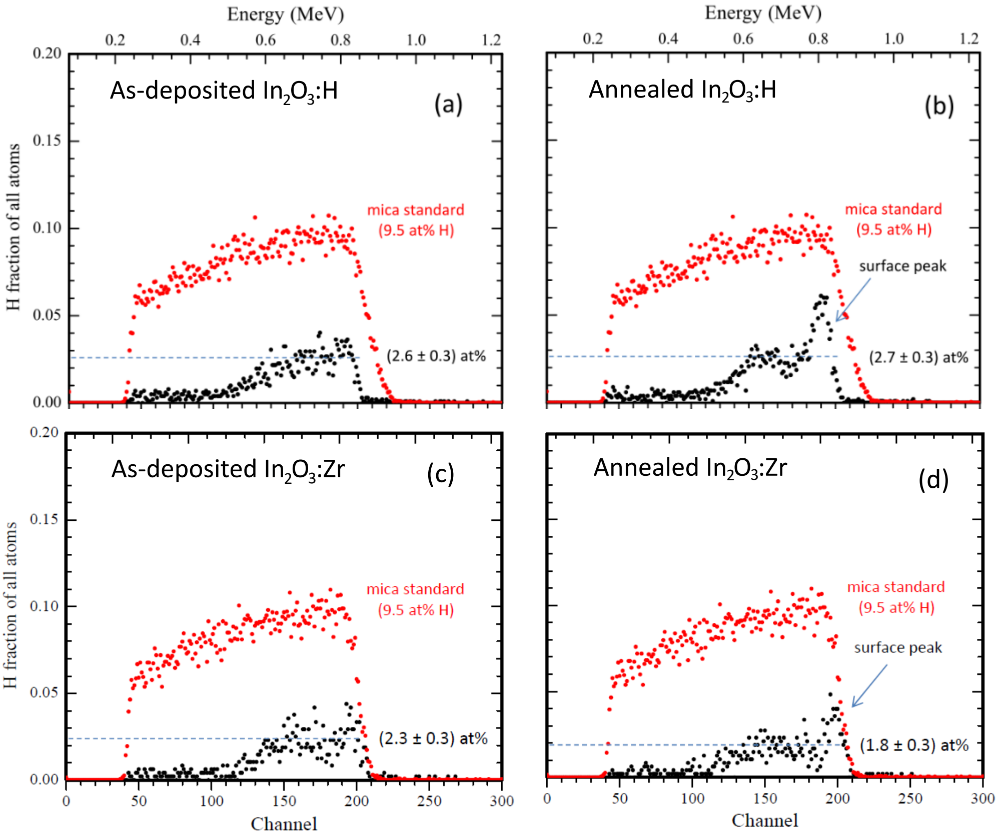

Figure 5.5 – ERDA measurements showing atomic-H depth profiles of the 9.5 at% mica standard (red), as-deposited (a) and annealed (b) In_2O_3:H, and as-deposited (c) and annealed (d) In_2O_3:Zr thin films.

The 2% absolute increase in O-content measured by RBS after crystallization suggests a passivation of $V_O^{\bullet\bullet}$, which has two possible consequences. N_e decreases as seen in 5.1(a), which results in a further increase in μ_e due to a decrease in scattering centres. Furthermore, the increase in μ_e and decrease in N_e result in a reduction of free-carrier absorption as observed in 5.1(c) for all films after crystallization. The interplay between three possible dopants could explain N_e of In_2O_3:Zr: atomic hydrogen ($H_i^{\bullet}$ and $H_O^{\bullet}$), Zr-dopants, and $V_O^{\bullet\bullet}$. On one hand, Zr^{4+} could substitute In^{3+} and generate single-charged defects ($Zr_{In}^{\bullet}$), which contributes to one conduction electron per site [Koida and Kondo, 2006]. Hydrogen atoms are considered to be beneficial for In-based TCOs when acting as substitutional of oxygen atoms ($H_O^{\bullet}$), decreasing the $V_O^{\bullet\bullet}$ density and donating one electron per defect [Koida et al., 2010]. ERDA indicates that annealing reduced the H-content from 2.3 at% to 1.8 at%, in parallel the thermal treatment reduced N_e from 3.5×10^{20} cm^{-3} to 2.5×10^{20} cm^{-3} . The reduction of N_e could be linked to the H-concentration in two ways: (i) Structural rearrangements could promote H-atoms to replace $V_O^{\bullet\bullet}$ (to form $H_O^{\bullet}$), decreasing the overall free-carrier density [Koida et al., 2010], and (ii) at 200 °C hydrogen effusion reduces the $H_i^{\bullet}$, which could decrease the doping [Koida et al., 2018, Limpijumnong et al., 2009]. In addition, just as in In_2O_3:H, H-atoms could passivate the surfaces in the grains of In_2O_3:Zr therefore decreasing the scattering from grain boundaries in In_2O_3:Zr [Wardenga et al., 2015, Macco et al., 2015].

5.5 Transparency of In_2O_3:Zr films of thickness < 100 nm

The optoelectronic properties of the films when reducing the thickness from 100 nm down to 15 nm was furthermore studied using the optimized conditions r(O_2) of 0.33%). In Figure 5.6(a) and (b), μ_e and N_e are shown as a function of thickness for as-deposited (empty symbols) and annealed films (full symbols).

Annealing the samples results in a similar behaviour as observed in Figure 5.1, an increase in μ_e and a decrease in N_e . Reducing the thickness from 100 to 15 nm results in a decrease in both, N_e and μ_e , leading to a conductivity drop from 4200 S cm^{-1} to 400 S cm^{-1}. The optical absorptance is also reduced when decreasing the thickness (Figure 5.6(c)). For wavelengths between 390 nm and 2000 nm, the 100-nm-thick films annealed in air present an average absorptance of 3.6%. The absorptance decreases to 1.3%, 0.7% and 0.4% for the 50 nm, 25 nm and 15-nm-thick In_2O_3:Zr respectively. This is expected since $I(d) = I_0 Exp(-\alpha \times d)$, where I_0 is the intensity of the incident light, d is the thickness and α is the absorption coefficient [Pankove, 2012]. For the 15 nm film, the absorptance is virtually equal to that of the glass for wavelengths above 460 nm, nonetheless the film has a μ_e of 50 $cm^2V^{-1}s^{-1}$ and a N_e of 5.0×10^{19} cm^{-3} . To highlight the films transparency, we plotted the absorptance of the bare glass substrate for comparison.

Top view STEM BF micrographs of the annealed In_2O_3:Zr films are shown in Figure 5.7 for each thickness. The 15-nm-thick films show a strained polycrystalline microstructure, as highlighted by the presence of bend contours [Williams and Carter, 1996], which gives rise to contrast in the images and makes a reliable grain size assessment more difficult. Increasing

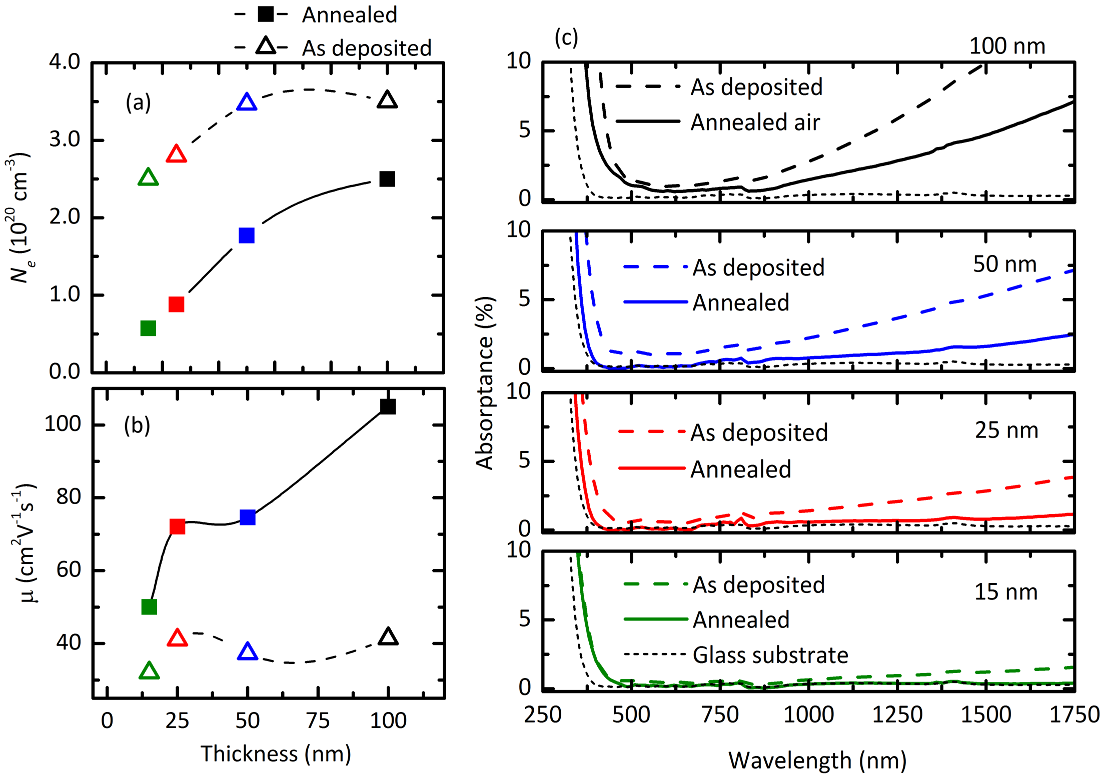

Figure 5.6 – Optoelectronic properties of as-deposited (empty symbols and dashed lines) and annealed (full symbols and solid lines) In_2O_3:Zr films deposited with r(O_2) = 0.33% for different thicknesses. The free-carrier density (a) and mobility (b) show an increase with thickness after annealing (lines in a and b are for eye guidance only). The optical absorptance decreases drastically for thinner films. The absorptance of the glass substrate is shown in black dotted lines in (c). As the thickness of the In_2O_3:Zr is reduced to 15 nm, the absorptance approaches that of the glass substrates, still with a conductivity of 400 S cm^{-1}.

the thickness of the films up to 25 nm and 50 nm results in the formation of large crystalline grains with average sizes of 500 nm and 420 nm, respectively. The grains are large along the specimen plane when compared with the film's thickness. Doubling the thickness up to 100 nm results in smaller grain sizes, with an average size of 320 nm. Grain sizes were calculated using the average grain intercept method, in which lines (of length L) are drawn across the top view micrographs and the number of intercepts are summed up (N), the grain size is calculated by dividing L by N.

A crystallization model proposed by Macco et al. for In_2O_3:H films pepared by atomic layer deposition suggests that the as-deposited films are mostly amorphous, but have a low density of embedded crystallites. Upon annealing, the In_2O_3:H crystallites grow until a full conversion to a crystalline phase [Macco et al., 2016]. A similar scenario could explain the crystallization of In_2O_3:Zr films, since, as highlighted in Figure 5.3(b), small crystallites are dispersed across the volume of the amorphous film. The final grain size is directly linked to the two-dimensional

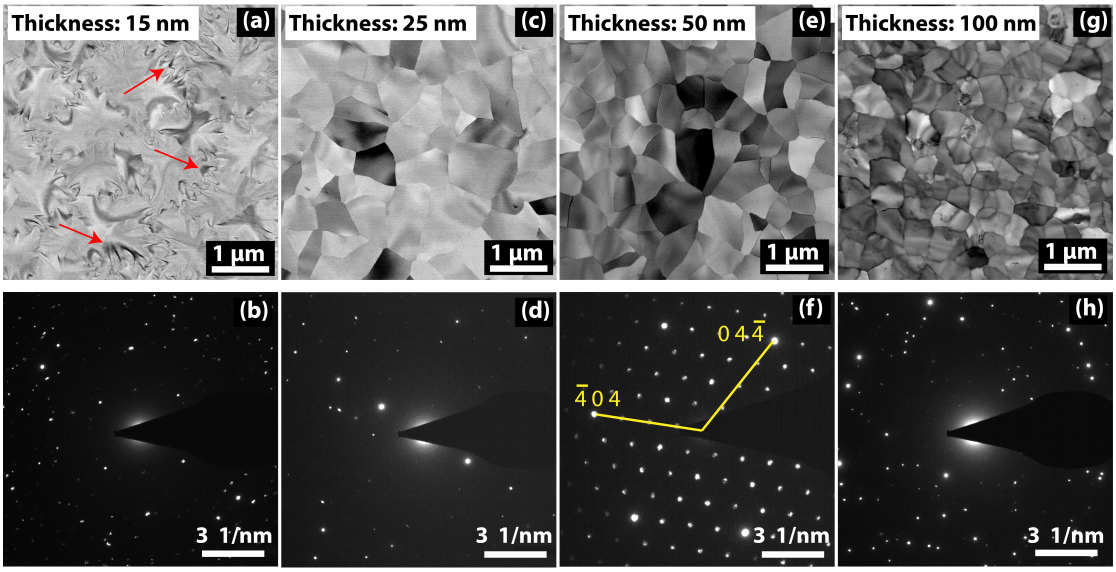

Figure 5.7 – STEM BF top view of films of (a) 15 nm, (c) 25 nm, (e) 50 nm and (g) 100 nm thickness and their corresponding electron diffraction patterns respectively in (b), (d), (f) and (h). All films were annealed in atmospheric pressure at 200 °C . 15-nm-thick films show a strained crystalline microstructure (grain boundaries are marked with the red arrows). Average crystallite sizes of 500 nm, 420 nm and 320 nm are found for 25 nm, 50 nm and 100-nm-thick films, respectively. The electron diffraction for (f) was performed in one single crystalline domain.

density of these crystalline seeds (density projected on the specimen plane, in nm^{-2}). Assuming that the volumetric density (in nm^{-3}) of these crystal seeds is the same in each film, thinner films feature overall less seeds (as they are thinner). And so, these crystals may extend further until impinging a neighbouring seed in thinner films, leading to a larger grain size. The results from Figure 5.6 and Figure 5.7 indicate that while a clear change in the optoelectronic properties is observed with decreasing thickness, all annealed films show the formation of large crystalline grains with bixbyite structure. In addition the diffraction patterns shown in Figure 5.7 (b), (d), (f) and (h) where indexed. The SAED in Figure 5.7(f) corresponds to a single grain oriented to [111]. The rest of the SAED are not oriented and include more than one crystalline domain, but all reflections can be indexed by the In_2O_3 bixbyite atomic structure. Surprisingly, from Figure 5.6 and Figure 5.7 we see that for films thicker than 25 nm, there is a negative correlation between the grain size and μ_e of the films, i.e. larger crystalline domains result in lower μ_e .

To understand what influences the transport of the carriers in In_2O_3:Zr we have furthermore performed temperature-dependent Hall effect measurements and estimated the optical mobility and effective mass by FTIR and Drude model fitting.

5.6 Mobility limiting mechanisms as a function of thickness for crystalline In_2O_3:Zr

Grain boundary scattering, optical phonons and ionized impurities are the most common mechanisms limiting the electron transport in crystalline TCOs. The contribution of each mechanism to the total mobility can be expressed by applying Matthiessen's rule:

$$\frac{1}{\mu_T} = \frac{1}{\mu_{GB}} + \frac{1}{\mu_{Ph}} + \frac{1}{\mu_{ii}} \tag{5.1}$$

where μ_T is the total mobility, μ_{GB} the mobility limited by grain boundaries, μ_{Ph} the mobility limited by optical phonons and μ_{ii} the mobility limited by ionized impurities. To estimate the effect of grain boundaries in crystallized In_2O_3:Zr, we compared μ_e , with the optical mobility obtained from a fitting of the Drude model on FTIR reflectance measurements [Fujiwara and Kondo, 2005]. If an electron absorbs all the energy of an incoming photon, its mean free path can be calculated using [Knoops et al., 2015]

$$l_e = v_e \times \tau = \sqrt{\frac{2E_{IR}m^*\mu^2}{e^2}} \tag{5.2}$$

Where v_e is the kinetic energy transferred by the photon, τ is the time between two scattering events, E_{IR} is the energy of the photon, m^* is the effective mass of the electron and e its charge. For E_{IR} in the regime (0.05 eV – 0.7 eV), and assuming an effective mass of 0.3 m_e [Koida et al., 2010], l_e is < 15 nm, i.e. excited by the IR photons, the electrons do not cross a grain boundary and they are confined inside one crystalline domain. Fittings of the optical conductivity, suggest that the intra-grain mobility is not higher than μ_e since the values obtained for the optical mobility are similar to those measured by Hall effect (75 $cm^2V^{-1}s^{-1}$ < μ_{opt} < 105 $cm^2V^{-1}s^{-1}$ for the 100-nm-thick film). This suggests that grain boundaries are not a dominant mechanism limiting electron transport. This was previously suggested by the relation between grain size and μ_e (Figure 5.6 and Figure 5.7) and literature reports of other high-μ_e In-based oxides [Koida et al., 2010, Wardenga et al., 2015, Macco et al., 2015, Preissler et al., 2013]. In addition, the fitting indicates that the effective mass is low (< 0.3 m_e). To pinpoint the dominating scattering mechanism for each thickness, temperature dependent Hall effect measurements were performed from -200 °C to 70 °C . As shown in Figure 5.8, N_e of the films does not change significantly with temperature in this range, which indicates that all films are degenerately doped. Nonetheless, μ_e decreases differently with temperature for each film thickness. The strongest change is seen for the 100-nm-thick films whereas 15 nm films shows almost unchanged mobility for all temperatures.

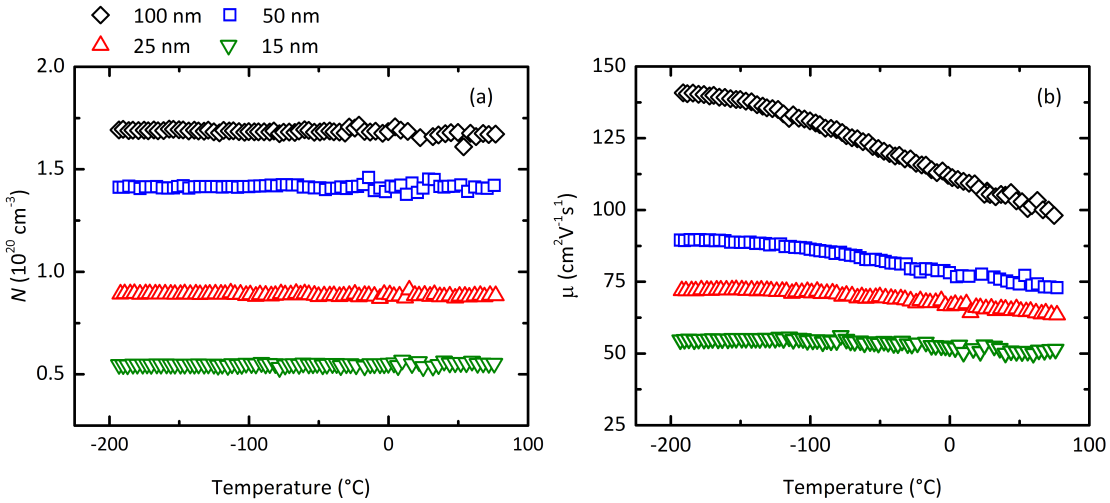

Figure 5.8 – N_e (a) and μ_e (b) as a function of temperature for In$_2$O$_3$:Zr films with a thicknesses from 100 nm to 15 nm. While N_e does not change in this temperature range, μ_e of the films changes with temperature. Thicker films exhibit larger temperature dependence, possibly due to a higher influence of optical phonon scattering compared to thinner films.

To deconvolve the different contributions to the mobility based on their temperature dependence, we used a simple model [Dugdale, 1977, Zhang and Ma, 1996] with one temperature independent component (μ_{ii} , which includes bulk ionized impurities and scattering from surfaces) and a temperature dependent component (μ_{Ph}), which approximates the scattering from polar optical phonons. The expression for Matthiessen's rule then becomes:

$$\frac{1}{\mu(d,T)} = \frac{1}{\mu_0}\left(\frac{T_0}{T}\right)^2 + \frac{1}{\mu_{ii}(d)} \tag{5.3}$$

where $\frac{1}{\mu_0}\left(\frac{T_0}{T}\right)^2$ is the mobility limited by phonon scattering, i.e. μ_{Ph}, μ_0 is the mobility at temperature T$_0$ and T is the temperature. By fitting the temperature dependence of the mobility for each thickness, μ_{Ph} and μ_{ii} were calculated using Equation 5.3. At room temperature, we calculated the inverse of μ_{Ph} and μ_{ii} as a function of thickness. Figure 5.9 shows the inverse of μ_{Ph}, and μ_{ii} for each thickness. The limiting scattering mechanism is the one showing larger inverse-μ_e . The influence of ionized impurity scattering is dominant for thinner films, while for the 100-nm-thick films ionized impurities and phonon scattering have a comparable effect on μ_e . The influence of ionized impurities for thinner films likely results from surface defects. The abrupt rupture of the crystal structure at the surface creates a local deviation of the Fermi level position relative to the band-edges [Sze, 1981]. The causes for the band-bending are intrinsic and extrinsic. Intrinsic band bending is two fold [Butler et al., 2014]; on one side, the penetration of the electron wave-function into vacuum results in lower electron density of states in the surface region. Conversely, the difference in the coordination number in the surface atoms also contributes to band-bending.

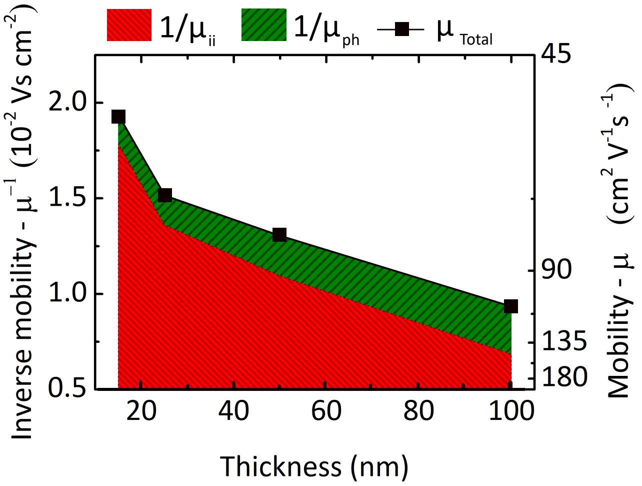

Figure 5.9 – Room temperature inverse mobility (left axis) as a function of thickness. The contribution from phonon scattering (green) and ionized impurities (red) was calculated by fitting equation 5 at room temperature. The right axis shows the Hall mobility (black squares) as a function of film thickness.

Additionally, external adsorbed impurities give rise to band bending as well. In this regard, bixbyite-type lattices show a high mobility of atomic oxygen [Agoston et al., 2010] and a higher number of interstitial and substitutional sites for oxygen than other n-type structures [Harvey et al., 2006]. The mobile O-atoms lead to the passivation of $V_O^{\bullet\bullet}$ and to the formation of other oxygen related ionized impurities such as oxygen interstitial and substitutional oxygen (O_i'' and O_{In}'') [Ágoston et al., 2009] near the surface of the films. These defect species affect the overall electrical properties of thinner films (thickness < 100 nm), since the passivation of $V_O^{\bullet\bullet}$ by excess-O is reflected in a decrease of N_e (Figure 5.6(a)). Conversely, the ionic nature of adsorbed O_i'' and O_{In}'' further limits μ_e for thin-films, since they increase the scattering events of the free electrons.

To gain further insights into scattering at the surface, we used a phenomenological model proposed by Look et al. to describe the thickness dependence of μ_e [Look et al., 2013]. This model proposes that the boundary-scattering-limited mean free path is proportional to the thickness of the film and to the Fermi-velocity. In contrast the scattering from the bulk is proportional to the quality factor of the surfaces, d*. The thickness-dependent mobility then is given by

$$\mu(d) = \frac{\mu(\infty)}{1 + \frac{d^*}{d+\delta d}} \tag{5.4}$$

Where $\mu(\infty)$ is mobility of electrons in the bulk of the material (absent of surface defects), d is the thickness of the films, δ d is the thickness of the depletion layer, d* is a fitting parameter which describes the quality of the interface, defined as $\mu(d^* - \delta d) = \mu(\infty)/2$. Fitting Equation 5.4 to the mobility values from Figure 5.6(b), we found that In_2O_3:Zr sputtered on glass has a δd of 7.6 nm, $\mu(\infty)$ of 126 $cm^2V^{-1}s^{-1}$, and d* of 31 nm. The δd is an estimation of the thickness of a superficial, low-μ_e section the film, affected by the surface defects. For the 15-nm-thick film, δd represents half of its thickness, which influences the electron transport in the films, limit μ_e to 50 $cm^2V^{-1}s^{-1}$. As the film thickens (25 nm and 50-nm-thick films), the influence of δd is reduced since the high-μ_e region becomes more important in the overall electron transport of the film. Finally, for 100-nm-thick films, 7.6 nm represents a less important proportion of the conduction path, therefore less defects per volume are expected, which results in the overall higher μ_e .

5.7 Influence of annealing atmosphere on the optoelectronic properties of In_2O_3:Zr

In view of the role of oxygen in the properties of In_2O_3:Zr upon thermal treatment, we annealed In_2O_3:Zr films of thickness from 15 nm to 100 nm at 200 °C in 0.5 mbar of H_2 or N_2 . Surprisingly, films annealed H_2 and N_2 did not crystallize fully, they show an amorphous microstructure with a relatively high crystallite-seed density (STEM in Figure 5.10). Given that O-atoms promote the structural re-arrangement required for the crystallization of In_2O_3, we propose that this phase change is promoted by O_2, [Pasquarelli et al., 2014, Adurodija et al., 2006, Medvedeva et al., 2017, Buchholz et al., 2014a]. Another (less likely) possibility is the increased pressure during air annealing triggers crystallization, nonetheless more investigations are required to further explain this effect. Figures 5.10(c) and (d) suggest that the size of the crystallite-seed depends also on the treatment atmosphere, since on average crystallites of films annealed in in H_2 are smaller than those treated in N_2 . Previous reports have shown that the crystallization temperature is dependent on the indium/oxygen ratio of the materials, of the deposition temperature, and ultimately in the route of oxygen incorporation [Pasquarelli et al., 2014, Adurodija et al., 2006]. These factors could potentially influence the microstrucure and the final size of the crystallite seeds.

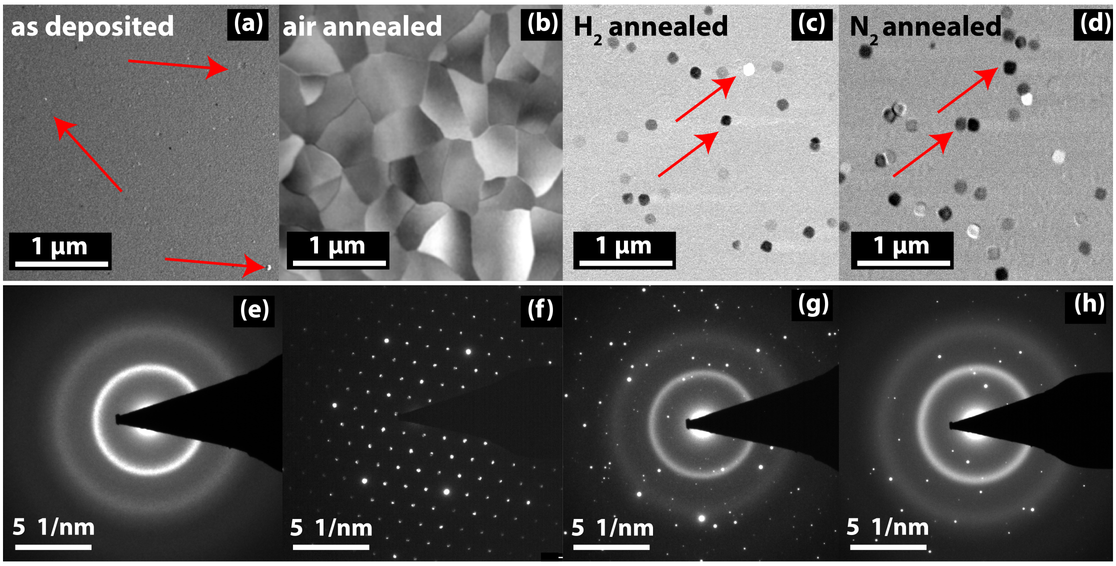

Figure 5.10 – STEM HAADF images of 50-nm-thick In_2O_3:Zr (a) as-deposited, (b) annealed in air, (c) annealed in H_2 and (d) N_2 atmospheres. The as-deposited films are amorphous with embedded nanometric-sized crystallites. The corresponding diffraction patterns confirm that the (e) as-deposited sample is mostly amorphous, (f) the sample annealed in air is crystalline and samples annealed in H_2 (c) and (g) and N_2 (d) and (h) have an amorphous microstructures with embedded crystallites of considerably higher grain size than those seen in the as-deposited film.

Figure 5.11 shows the electrical properties of the as-deposited and annealed films. The μ_e of films annealed in H_2 or N_2 is lower those annealed in air. Nonetheless, μ_e is improved compared to as-deposited films, possibly caused by local structural changes following the thermal treatments [Medvedeva et al., 2017, Buchholz et al., 2014a]. Differences in optoelectronic properties of films annealed in H_2 and N_2 atmospheres have their origin in point defects, as they were annealed at the same temperature and show similar microstructure. Annealing in H_2 and N_2 leads to a higher N_e as compared to films annealed in air. Annealing in a neutral atmosphere such as N_2 prevents the passivation of $\mathrm{V_O^{\bullet\bullet}}$ by oxygen from the air. Thermal treatments in H_2 atmosphere generate more N_e compared to an annealing in N_2 , since H atoms act as donors in In-based materials [Koida and Kondo, 2007b, Koida et al., 2010, Limpijumnong et al., 2009, Van De Walle, 2000]. Additionally H-atoms may also create additional $\mathrm{V_O^{\bullet\bullet}}$ by removing oxygen atoms from the surface of In_2O_3:Zr, as reported for other TCOs [Yamada et al., 2000, Rucavado et al., 2017, Kamiya et al., 2008b, King and Veal, 2011, Bielz et al., 2010]. Conversely, as compared with the as-deposited films, thermal treatments in N_2 and H_2 did not change μ_e importantly in films of 15 nm and 25 nm, which are the most sensitive to surface defects, suggesting that there is no overall $\mathrm{V_O^{\bullet\bullet}}$ passivation, and no introduction of $\mathrm{O_i''}$ and $\mathrm{O_{In}''}$
.

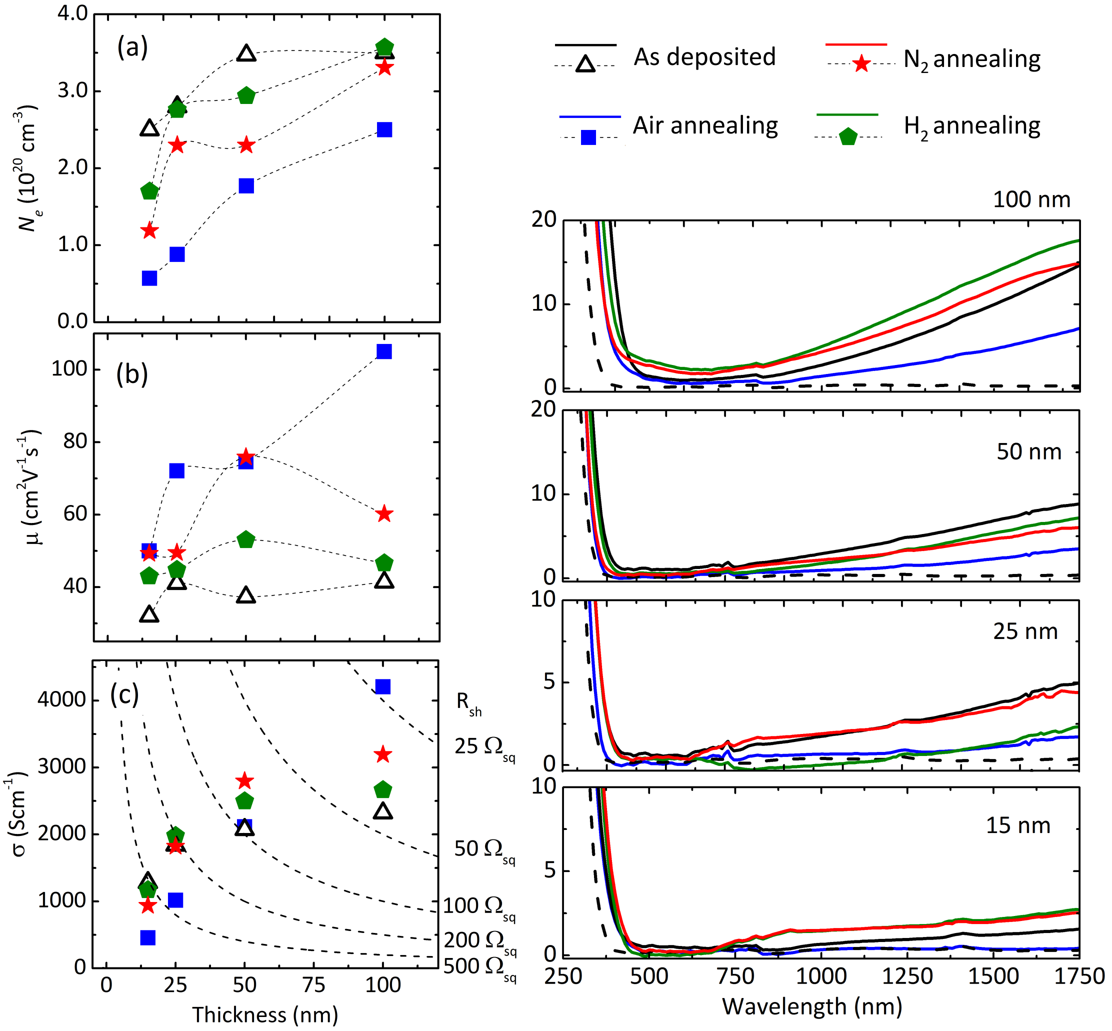

Figure 5.11 – Electrical properties of optimized In_2O_3:Zr as-deposited (empty symbols) and films annealed in H_2 and N_2 atmospheres (blue, green and red full symbols respectively). Films were deposited with r(O_2) of 0.33% and for different thickness. (a) N_e and (b) μ_e are dependent of the annealing atmosphere. In (c) the conductivity for each film is shown as function of thickness, in addition we plotted lines for constant R_{sheet}

5.8 In_2O_3:Zr films of thickness < 80 nm as front contact in silicon heterojunction solar cells

Given the optoelectronic properties of In_2O_3:Zr, the material is a promising candidate to replace the standard In_2O_3:Sn electrodes used in SHJ solar cells. On one side, 100-nm-thick In_2O_3:Zr films are more transparent than 100-nm-thick In_2O_3:Sn in the visible and near infrared, due to the wider bandgap and less free-carrier absorptance of In_2O_3:Zr ([Morales-Masis et al., 2018]). Moreover, decreasing the thickness of In_2O_3:Zr results in higher intensity of light transmitted through the TCO, due to the exponentially relation mentioned in Section

5.5. The sheet resistance of 50-nm-thick In_2O_3:Zr is similar to the standardly used electrodes (80-nm-thick In_2O_3:Sn with R_{sheet} between 90 Ω_{sq} and 100 Ω_{sq}). In SHJ solar cells, the TCO electrodes also serves as an antireflective coating (ARC) [De Wolf et al., 2012]. With a refractive index of ≈ 2 at wavelengths of 600 nm, 80-nm-thick TCO reduce the reflection of light from the cells. If the TCO thickness is < 80 nm, a second ARC must be used to minimize this optical loss mechanism. With a refractive index of 1.4 at wavelength of 600 nm, 100 nm of MgF_2 is an optimal secondary ARC to complement the antireflective properties of 40 nm of In_2O_3:Zr. To show that In_2O_3:Zr films with reduced thickness have great potential to replace In_2O_3:Sn electrodes, thus reducing the indium consumption, we sputtered 80 nm of In_2O_3:Zr, 40 nm of In_2O_3:Zr and 40 nm of In_2O_3:Zr and the standard In_2O_3:Sn electrode in SHJ solar cells. In addition, 100 nm of MgF_2 were evaporated in the 40 nm thick In_2O_3:Zr film. Following the TCO deposition and MgF_2 evaporation, Ag-fingers were screen printed and the cells parameters IV characteristics were measured under standard test conditions (AM 1.5G spectrum, 100 W cm^{-2} and 25 °C). Resulting solar cell parameters are shown in Table 5.1[3].

Table 5.1 – Performance of SHJ solar cells using 80 nm and 40-nm-thick In_2O_3:Zr as front electrode. The 40-nm-thick In_2O_3:Zr also has a MgF_2 film as second antireflective coating (ARC). The standard In_2O_3:Sn was used as reference electrode. In addition the R_{sheet} and the weighted absorptance ($A_{weighted}$) of the films are shown.

	80 nm In_2O_3:Zr	40 nm In_2O_3:Zr (no MgF_2)	40 nm In_2O_3:Zr (with MgF_2)	In_2O_3:Sn
Efficiency (%)	22.2	21.1	22.3	22.3
Fill factor (%)	77.1	76.7	76.7	77.7
J_{sc}(mA cm^{-2})	40.3	38.5	40.6	40.1
V_{oc} (mV)	715.6	714.7	714.5	714.6
R_{sheet} (Ω/sq)	25	95	95	93
$A_{weighted}$ (%)	1.6	0.6	0.6	4.3

Compared[4] to standard In_2O_3:Sn, the 80 nm In_2O_3:Zr shows higher J_{sc} and V_{oc} (+0.2 mA cm^{-2} and +1.0 mV respectively). The higher J_{sc} is a consequence of less parasitic absorptance in In_2O_3:Zr than in In_2O_3:Sn. The higher V_{oc} might be caused by a reduced sputtering damage during in the In_2O_3:Zr deposition [Morales-Masis et al., 2018]. On the other hand, the fill factor is lower in the cell using In_2O_3:Zr than in one with In_2O_3:Sn. Given that In_2O_3:Zr is more conductive than In_2O_3:Sn, and that In_2O_3:Zr and In_2O_3:Sn have similar contact resistance with Ag [Morales-Masis et al., 2018], possibly In_2O_3:Sn has lower contact resistance with the p-doped amorphous silicon than In_2O_3:Zr.

Thinning down the In_2O_3:Zr electrodes from 80 nm to 40 nm in the cells results in lower J_{sc} (-1.8 mA cm^{-2}) since for this TCO thickness, reflectance losses are not minimized. Depositing 100 nm of MgF_2 resulted in a J_{sc} gain of +0.5 mA cm^{-2} as compared with the cell with In_2O_3:Sn, and +0.3 mA cm^{-2} with the cell using 80 nm of In_2O_3:Zr due to an optimized anti-reflective condition.

---

[3] A more fair comparison between TCOs would also require the addition of MgF_2 as a second ARC with In_2O_3:Sn. This experiment was not performed due to time constrains.

[4] The R_{sheet} and $A_{weighted}$ shown in Table 5.1 were measured in films deposited on glass, with thickness of 100 nm and 50 nm instead.

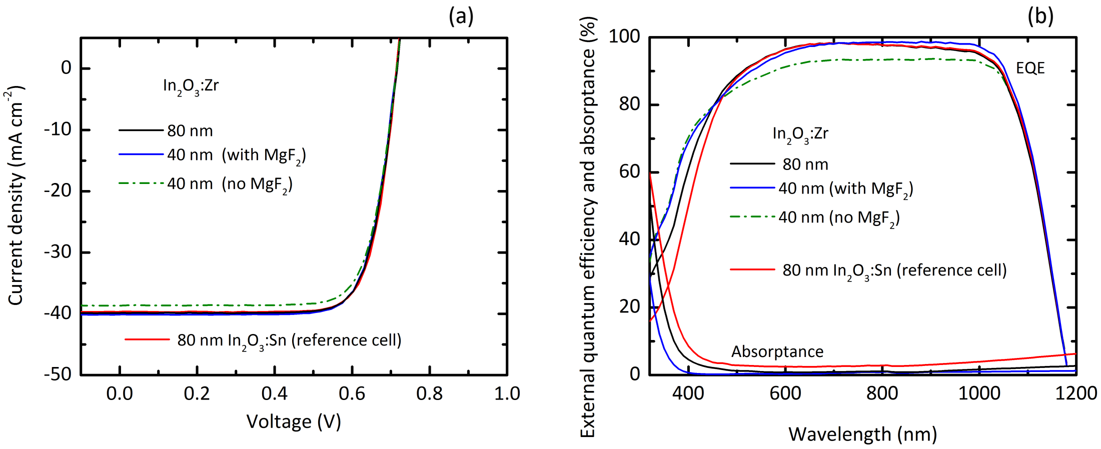

Figure 5.12 – (a) Light IV characteristics of SHJ solar cells with 80 nm and 40-nm-thick In_2O_3:Zr (with and without MgF_2 as second antireflective coating. (b) External quantum efficiency (EQE) of the cells shown in (a) and the corresponding optical absorptance of the front TCOs. The absorptance of the 40-nm-thick In_2O_3:Zr does not change with MgF_2 and is not shown here. As reference, In_2O_3:Sn electrode was also used in the cells and in the absorptance measurement.

External quantum efficiencies (EQE) of the solar cells and absorptance of the TCOs are shown in Figure 5.12(b). From 320 nm to 450 nm, lower EQE is measured for cells using 80-nm-thick TCOs as compared with the 40-nm-thick In_2O_3:Zr. This is caused by the higher parasitic absorptance of the 80-nm-thick TCOs as compared with the thinner films. This also explains partially the lower J_{sc} in the device using In_2O_3:Sn as front contact. In the wavelength range from 450 nm to 1050 nm, the 40 nm film without MgF_2 shows lower EQE, since for this film thickness the reflectance is not minimized, hence the 38.5 mA cm^{-2} seen in the IV-curve. The double-ARC material electrode has at the same time low optical absorptance and optimized antireflective parameters that leads to a photocurrent of 40.6 mA cm^{-2}, 0.5 mA cm^{-2} higher than the reference cell.

Several strategies could be implemented to further increase the efficiency of the In_2O_3:Zr-containing devices, on one hand the fill factor of cells can be incremented by either designing a TCO with a graded N_e (high N_e at the interface with the amorphous-Si contact), or by a better tuning of the a-Si contact. A thorough explanation of the In_2O_3:Zr/a-Si interface can be found in reference [Morales-Masis et al., 2018]. On the other hand, the high-σ of the TCO allows more space between the Ag-fingers, hence decreasing shadowing and increasing the J_{sc}.

Finally the high contact resistance between In_2O_3:Zr and p-type amorphous silicon could be avoided if the front of the cell is at the n-type contact, e.g. using a back emitter design. As a proof of concept, we sputtered 80 nm, 40 nm and 20 nm of In_2O_3:Zr in back-emitter cells and compare them with cells using the standard In_2O_3:Sn electrode.

5.9 Conclusion

In this chapter, we studied the optoelectronic properties of In_2O_3:Zr films with various thickness and described their electron transport and sources of conductivity in terms of thickness, donors and possible defects decreasing the mobility. To do this, we sputtered In_2O_3:Zr films with thickness changing from 100 nm to 15 nm and performed thermal treatments at atmospheric pressure and under N_2 and H_2 pressures. We found that annealing the films at atmospheric pressure results in a high quality crystalline microstructure while the oxygen present in the air passivates $V_O^{\bullet\bullet}$. These results in 100-nm-thick films with μ_e of 105 $cm^2V^{-1}s^{-1}$ and N_e of 2.5×10^{20} cm^{-3}. For films annealed in air, the carrier transport is limited by (i) optical phonons and (ii) ionized impurity scattering. The latter becomes dominant for films with a thickness < 100 nm since these films are more sensitive to ionized surface defects. Thermal treatments in H_2 seem to be optimal to achieve high conductivity with thin films (< 50 nm), by maintaining high free-carrier concentration. Conductivities as high as 1980 S cm^{-1} are achieved for 25-nm-thick films with optical absorptance close to the one on the glass substrate.

Furthermore, we demonstrated In_2O_3:Zr is an excellent candidate to replace In_2O_3:Sn as front electrodes in silicon heterojunction solar cells. Devices using 80-nm-thick In_2O_3:Zr have increased short-circuit current as compared with cells with In_2O_3:Sn electrodes of the same thickness. Finally, even higher J_{sc} gain was achieved by reducing the thickness of In_2O_3:Zr to 40 nm and implementing a secondary MgF_2 antireflective coating. A more complete experiment would include the usage of a second ARC with In_2O_3:Sn, nonetheless this results is promising alternative to reduce the amount of indium used in the front contact of silicon heterojunction solar cells.

6 Weighted Average Figure of Merit and TCO comparison

In this dissertation, the optical and electrical properties of TCOs were compared almost separately. In this Chapter we will introduce the average weighted figure of merit (FOM) and it will be used to compare the overall optoelectronic properties weighted under the solar spectrum. Finally we will make a general comparison of the TCOs designed in the previous chapters and we will compare them to the standard used material for silicon heterojunction solar cells, In_2O_3:Sn.

6.1 Solar spectrum and TCOs

As discussed earlier, the electrical conductivity of TCOs is fully controlled by μ_e and N_e . These two factors are intertwined and the simultaneous increase of both of them is challenging. In addition the increase of N_e alone has two important consequences in the optical properties: on one hand increasing N_e leads to an increase in free-carrier absorptance (α_{FCA}), which decreases the infrared transmitted light.

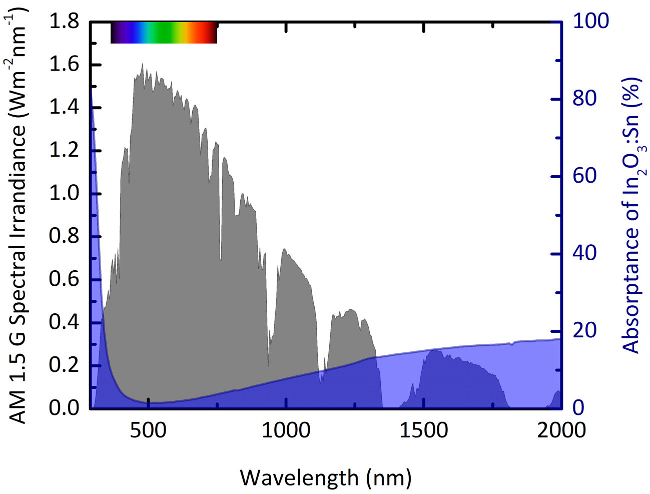

Figure 6.1 – (Left axis) Spectral irradiance from the Sun at AM 1.5 G compared with the (right axis) absorptance of In_2O_3:Sn. Increasing N_e results in higher absorptance in the infrared part of spectra and blue-shift of the fundamental absorption due to higher values of E_{opt}.

Conversely, increasing N_e also leads to a widening of the E_{opt} due to the Burstein-Moss shift. Here a conundrum is found between the detrimental effect of α_{FCA}, and the beneficial Burstein-Moss shift. To fairly compare the optical and electrical properties between TCOs while including a specific source of radiation, we introduce the weighted averaged figure of merit (FOM).

6.2 Weighted averaged figure of merit (FOM)

Up to now, we have used μ_e to optimize the TCOs, given that in general the high-μ_e results in low free carrier absorptance (α_{FCA}), and is also linked to lower absorptance in the visible part of the spectra due to defect passivation (as seen in Chapter 3) At this point we introduce an optimization approach which comprises the optical and electrical properties in a TCO. For a film with electrical conductivity of σ and thickness d, the FOM is defined as

$$FOM = \frac{\sigma \times d}{A_{weighted}} = \frac{1}{R_{sheet} \times A_{weighted}} \tag{6.1}$$

The FOM has units of Ω^{-1}. Nonetheless, for simplicity and to compare with results shown in reference [Morales-Masis et al., 2017a], the resulting FOM is multiplied by 1 Ω × 100%.

In Chapter 4 we used the simplified Figure of Merit (simplified-FOM), which does not take into account averaging the solar spectrum. The simplified-FOM is more useful for light emitting devices, accounting for the solar spectrum results useful for light absorbing devices. To ensure a fair comparison of TCOs, in Chapter 6 the FOM was calculated for all materials using Equation 6.1.

Finally, using the Figure of Merit to compare TCOs is useful because the influence of the solar spectrum is taken into account. Nonetheless the FOM is not guarantee of applicability directly in the optoelectronic devices where

$$A_{weighted} = \frac{\int I_{light}(\lambda) \times A(\lambda) d\lambda}{\int I_{light}(\lambda) d\lambda} \tag{6.2}$$

Where $A_{weighted}$ is the weighted absorptance, $A(\lambda)$ is the wavelength-dependent absorptance of TCOs and I_{light} (λ) is the 1 Sun air mass solar spectrum (AM 1.5G), shown in Figure 6.1. The solar spectrum is used due to its importance in solar cells. $A_{weighted}$ is averaged from 320 nm to 1200 nm, due to the application of this wavelength-range in silicon-based solar cells. Nonetheless, the integration limits can be tuned, and the spectral irradiance can be replaced by the irradiance of a light-emitting device, or by the spectral sensitivity of the eye [Morales-Masis et al., 2017a]. Hence, high FOM values are indication of high electrical conductivity and/or low absorptance in for the desired spectral range. Note that the calculated FOM is obtained using experimental measurements, since $A_{weighted}$ was calculated by integrating 1-TT-TR from spectrophotometry and R_{sheet} was measured using Hall effect measurement. Finally, it is worth mentioning that other figures of merit can be used in TCOs. An alternative FOM could be envisaged by considering other optical interactions, e.g. interaction with other surfaces or light trapping in the thin film. In this way the an FOM could be used to compare antireflective properties of the TCOs.

6.3 FOM for In_2O_3:Zr

We calculated the FOM for oxygen series of the annealed films shown in Figure 5.1 from Chapter 5.

Table 6.1 – Figure of merit (FOM), weighted absorptance ($A_{weighted}$) and sheet resistance (R_{sheet}) of annealed In_2O_3:Zr deposited with different $r(O_2)$.

$r(O_2)$ (%)	FOM(%)	$A_{Weighted}$	R_{sheet} (Ω_{sq})
0.00	0.1	13.5	91.5
0.16	1.5	3.3	20.3
0.33	2.6	1.6	23.7
0.62	2.6	0.6	60.0

The resulting FOM, R_{sheet} and $A_{Weighted}$, shown in Table 6.1, suggest that the optimal films in terms of σ and $A_{weighted}$ are the deposited with $r(O_2)$ of 0.16% and 0.33%, as they have higher FOM than the rest of the films. The high optical absorptance of the as-deposited films (not annealed) always results in low FOM values (not shown here). Therefore, considering the solar irradiance, optimum electrical properties are obtained for annealed films deposited with $r(O_2)$ of 0.33%. At this $r(O_2)$, the annealed film presents a μ_e of 105 $cm^2V^{-1}s^{-1}$, a N_e of 2.5×10^{20}

cm^{-3} , an average absorptance of 3.6% from 320 nm to 1200 nm and a $A_{weighted}$ of 1.61%. Increasing r(O_2) to 0.62% results in a similar FOM value (due to the reduced absorptance), but decreased μ_e and N_e . The results from the FOM suggest that there is an optimum r(O_2) content for solar cells which can benefit with a highly conductive TCO, (r(O_2) = 0.33%), and an ideal film for application which can profit more from transparency (r(O_2) = 0.62%).

For 100 nm In_2O_3:Zr films, a FOM value of 2.6% is achieved for the films deposited with r(O_2) of 0.33% and 0.62%. This is significantly larger than the reported FOM of In_2O_3:Sn and In_2O_3:H (0.3% and 1.8% respectively, as described in reference [Morales-Masis et al., 2017a]). On the other hand tungsten-doped and cerium-doped hydrogenated indium oxides (In_2O_3:W,H and In_2O_3:Ce,H) have reported FOM values of approximately 3.3%, placing In_2O_3:Zr just below in performance. The FOM difference is caused by μ_e of In_2O_3:W,H and In_2O_3:Ce,H, (higher than that of In_2O_3:Zr). This is possibly linked to a better passivation of surfaces and grain boundaries by H-atoms, since hydrogen gas or intentionally introduced water were used during deposition. In addition it is important to notice that In_2O_3:W,H and In_2O_3:Ce,H were deposited using ion plating, which could result in higher quality films [Morales-Masis et al., 2017a, Kobayashi et al., 2012]

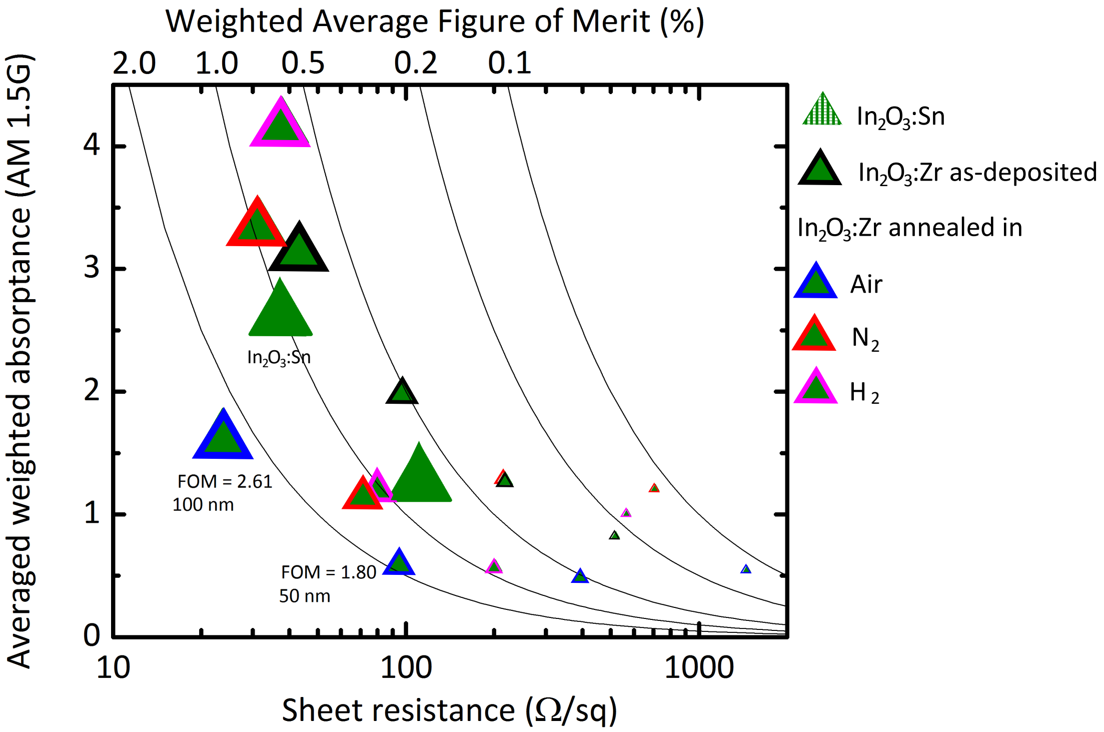

Figure 6.2 – Weighted average absorptance ($A_{weighted}$) versus the logarithm of the sheet resistance ($\log(R_{sheet})$) of In_2O_3:Zr films with thickness of 15 nm, 25 nm, 50 nm and 100 nm as-deposited and annealed in air, N_2 and H_2 atmospheres. The size of the markers is scaled linearly with the thickness of the samples. The FOM was calculated using Equation 6.1. The integration limits are from 390 nm to 1200 nm. In addition, the FOM for standard In_2O_3:Sn films are shown with green stripes. The solid lines mark constant FOM values of 2.0%, 1.0%, 0.2% and 0.1%

In Figure 6.2 the average absorptance is shown for films of thickness of 100 nm, 50 nm, 25 nm and 15 nm annealed in air, N_2 and H_2 as a function of the R_{sheet} . The lines in Figure 6.2 mark constant FOM values. The edge of each marker point indicates the annealing atmosphere, while its size is scaled with the film's thickness. The closer the markers are to origin of the graph, the higher the FOM.

The trade-off between $A_{weighted}$ and R_{sheet} values, indicate that the best film in terms of conductivity and absorptance is the 100-nm-thick film annealed in air, since the FOM value is 2.61%. In addition, all annealed 50-nm-thick films have a FOM > 1%, similar to that of Sn-doped In_2O_3, marked in the graph with stripes. Finally, if the device requirements have relaxed electrical constrains, i.e. can benefit more from a more transparent TCO rather than a highly conductive film, thermal annealing in H_2 of 25-nm-thick In_2O_3:Zr is convenient, since the FOM is close to 1%, higher that the as-deposited films and films annealed in air or N_2 . This film has a conductivity of 1980 S cm^{-1}, mainly because of the high N_e as compared with the other films and its thickness allows an average weighted absorptance of only 0.57%.

6.4 FOM of SnO_2 -based TCOs

In Figure 6.3 the $A_{weighted}$ is shown as function of R_{sheet} for Sn-based TCOs discussed in Chapters 3 and Chapter 4. The as-deposited ZTO film has a FOM of 0.08% which increases after thermal treatments. Annealing a-ZTO in H_2 at 200 °C and 500 °C , decreases sheet resistance to 142 Ω/sq and to 107 Ω/sq respectively, which results in FOM of 0.16% and 0.2%. Conversely, thermal treatments under atmospheric pressure result in important FOM shift to 0.16% and 0.20% for at 200 °C and 500 °C respectively. The relatively absorptance fo films annealed at 500 °C results in FOM of 0.2%. In contrast, films annealed in air at 200 °C show a good trade off between absorptance and R_{sheet} . ZTO films annealed under N_2 atmosphere at 500 °C show a FOM of 0.25%, highest among Sn-based films reported here. This is due to a decrease in R_{sheet} from 300 Ω/sq to 124 Ω/sq, accompanied with an important decrease in $A_{weighted}$.

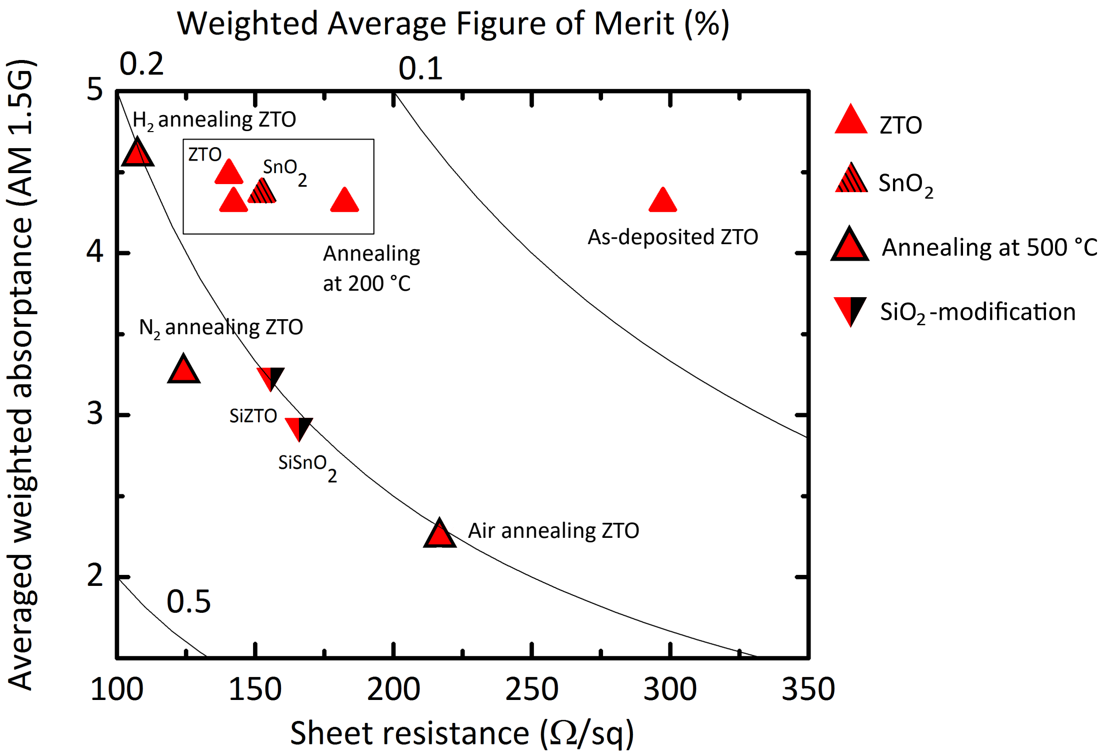

Figure 6.3 – Weighted average absorptance ($A_{weighted}$) versus sheet resistance (R_{sheet}) of ZTO and SnO_2 films with thickness of 150 nm as-deposited and annealed in air, N_2 and H_2 atmospheres. In addition the as-deposited and annealed SiZTO and $SiSnO_2$ films are also shown. The FOM was calculated using Equation 6.1. The integration limits are from 390 nm to 1200 nm.

The co-sputtering SnO_2 -based films with SiO_2 results in remarkable improvements, specially concerning $A_{weighted}$. At this point it is worth mentioning that these films were annealed at maximum temperatures of 200 °C , which decrease the thermal budget. While ZTO annealed at 200 °C in air shows an FOM of 0.16% and $A_{weighted}$ of 4.4%, the introduction of SiO_2 results in FOM of 0.20% and $A_{weighted}$ of 3.2%. The modification SnO_2 with SiO_2 showed a similar trend since the $A_{weighted}$ shifted from 4.4% to 3.2%. Nonetheless the FOM decreased after the addition of SiO_2 , mainly due to slight increase in R_{sheet} from 152 Ω/sq to 164 Ω/sq.

6.5 Comparison between TCOs

In Figure 6.4 the FOM of a selectrion of TCOs designed in this thesis are compared in terms of $A_{weighted}$ and R_{sheet} . In addition, the FOM of two optimized In_2O_3:Sn is shown to compare with In_2O_3:Zr and SnO_2 films. Resulting FOM for the two In_2O_3:Sn films are widely different from each other, since one is optimized for application as front electrode in SHJ solar cells while the other is optimized for application as back electrode in the same cell technology.

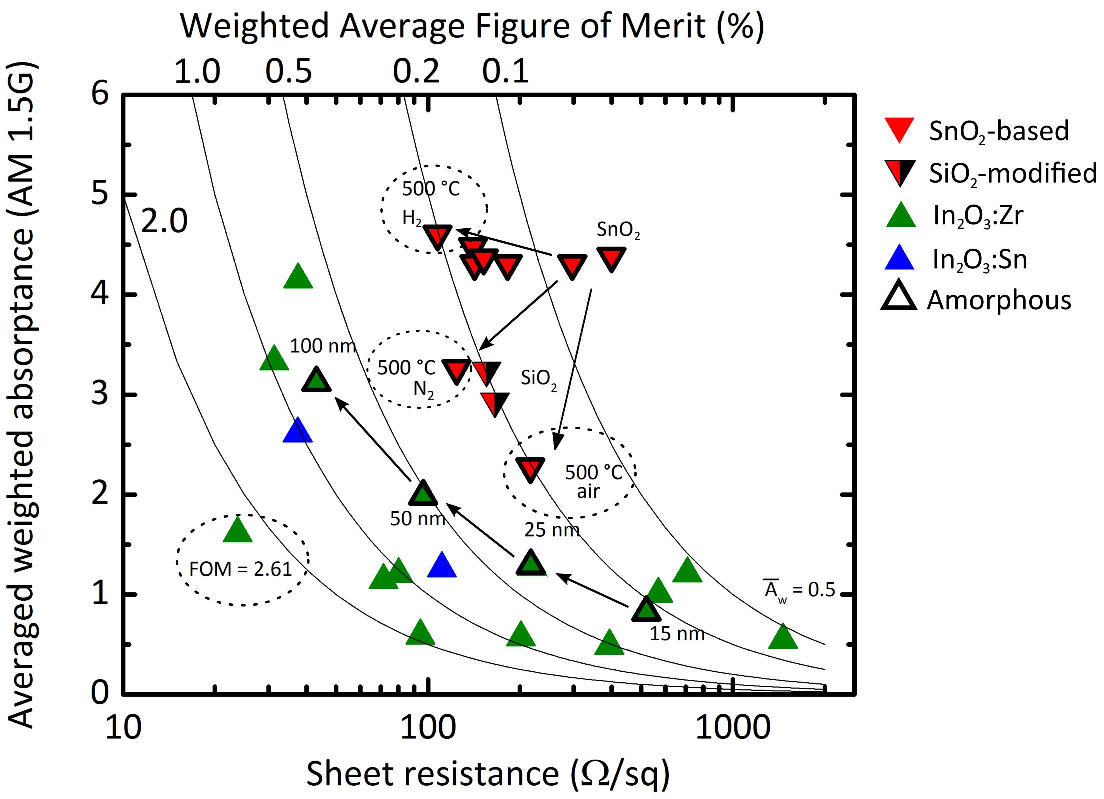

Figure 6.4 – Averaged weighted absorptance as function of sheet resistance (in logarithmic scale) for SnO_2 -based oxides (red), In_2O_3:Zr (green) and In_2O_3:Sn (blue). The amorphous films (or a mixture amorphous/crystalline) have a thick border in the markers, while crystallized films have no border. Films modified with SiO_2 are half red and half black. The lines show constant FOM values.

A separation in electrical and optical properties is seen for both families of materials. On

one hand, 150-nm-thick SnO_2 -based TCOs are restricted to FOM values between 0.06% (for as-deposited SnO_2) and 0.25% (for ZTO annealed in N_2 atmosphere). On the other hand, In_2O_3:Zr thin films, having thickness from 15 nm to 100 nm have a FOM spanning from 0.1% to 2.6% showing a R_{sheet} as low as 23 Ω/sq. The thinner In_2O_3:Zr films present a lower FOM, mainly due to higher a R_{sheet}. Nonetheless they exhibit a low absorptance of ≈ 0.5% and conductivity of 450 Scm^{-1}.
Two In_2O_3:Sn samples have a FOM of 0.7%, and 1.24%, $A_{weighted}$ between 1.3% and 2.6% and R_{sheet} between 40 Ω/sq and 100 Ω/sq. The large differences in the In_2O_3:Sn values highlight the significant influence of the oxygen partial pressure during deposition. The In_2O_3:Sn film with a $A_{weighted}$ of 1.3 is intended as a back transparent electrode in SHJ solar cells, while the film with a R_{sheet} of 40 Ω/sq is designed to work as front transparent electrode in SHJ solar cells, hence the striking differences. As mentioned in Chapter 1, In_2O_3:Sn is the standard material used for SHJ solar cells. But as seen in Figure 6.4, the electric and optical properties of In_2O_3:Zr are drastically better than those of In_2O_3:Sn. All 50-nm-thick In_2O_3:Zr (regardless of the annealing atmosphere) are more transparent and equally conductive as 100 nm of In_2O_3:Sn.

Finally, from Figure 6.4 it is clear that the optical and electrical properties of the studied In_2O_3-based TCOs are better than those of SnO_2 -based films. For example, the $A_{weighted}$ of 150 nm-tick a-ZTO annealed in air at 500 °C is very similar to that of as-deposited 50-nm-thick In_2O_3:Zr, but the low optical absorptance of the In-based film results in twice the FOM for In_2O_3:Zr. Why do these materials have so different optoelectronic properties? To answer this question we must analyse the differences in optoelectronic properties and correlate them with the effective mass, the structure, point defects and previous results from literature.

Effective mass m^*

An evaluation of the electron transport of these TCOs in terms of the effective mass is difficult, since the measured m^* values vary widely in literature, and calculations also provide different results. Fitting FTIR reflectance measurements with the Drude model, we obtained an m^* from $0.26m_e$ - $0.3m_e$ for a-ZTO. Obtaining the m^* of a-In_2O_3:Zr thin films was not possible, possibly due to the reduced thickness of the films. On the other hand, Hautier et al. made a systematic review of the effective masses in oxides, and virtually no difference is found in the m^* tensor of In_2O_3 and SnO_2 [Hautier et al., 2014]. On the other hand, Medvedeva calculates a slightly higher effective mass in SnO_2 than in In_2O_3 [Facchetti and Marks, 2010], which could partially explain the higher μ_e in In_2O_3-based TCOs. Nonetheless strong conclusions are difficult to extract just with the effective mass-difference between these TCOs. In addition, the hybrid nature of the conduction band, results an m^* insensitive to strong local distortions of the lattice [Medvedeva, 2007, Medvedeva et al., 2017]. Hence, the m^* is not expected to change importantly in a amorphous/crystalline transition.

Crystalline TCOs

Previous literature has reported of the growth of epitaxial single crystal (sc-) non-intentionally-doped $In_2O_3$and SnO_2 [1] ([Bierwagen and Speck, 2010, White et al., 2009] respectively). High-quality sc-SnO_2 shows an μ_e close to 100 $cm^2V^{-1}s^{-1}$ and a N_e of 2.7 × 10^{17} cm^{-3} at room temperature. Temperature dependent Hall effect measurements show that μ_e increases with decreasing temperature, achieving a maximum of ≈ 300 $cm^2V^{-1}s^{-1}$ at -173 °C . In contrast, sc-In_2O_3shows a μ_e of 200 $cm^2V^{-1}s^{-1}$ with a N_e of × 10^{17} cm^{-3} at room temperature. Decreasing the temperature to -173 °C resulted in an μ_e of ≈ 1000 $cm^2V^{-1}s^{-1}$. This shows that optical phonons limit the transport in both sc-TCOs. Nonetheless, the higher temperature sensitivity of sc-In_2O_3compared to sc-SnO_2 suggests ionized impurity scattering mechanism plays an important role limiting the electron transport in sc-SnO_2 . Therefore, even comparing single crystals the transport properties of In_2O_3-based TCOs are better than Sn-based oxides, possibly because of the higher overlap of s-orbitals in In_2O_3than in SnO_2 [Orita et al., 2001].

The microstructure of SnO_2 and In_2O_3 are strikingly different when deposited in similar conditions, e.g. temperature, sputtering power, working pressure. As seen in Chapter 5, In_2O_3:Zr films crystallize fully after thermal annealing at 200 °C . The high-quality crystallites with sizes from 300 nm to 500 nm indicate low density of defects within the grains, resulting in a high in-grain μ_e . The high-μ_e measured (Chapter 5) also indicate that grain boundaries are not limiting the electron transport in these films. In contrast, a-ZTO and SnO_2 films studied in Chapters 3 and 4 showed either a fully amorphous microstructure of a mixture of crystalline and amorphous phases[2] . The crystallites of size < 100 nm embedded in the amorphous phase could be sources of carrier scattering, given the introduction of grain boundaries.

Amorphous TCOs

Comparing amorphous In_2O_3- and SnO_2 -based films, it is possible to study the differences caused by point defects, independent of the crystal structure. In this work, the highest μ_e obtained for an amorphous SnO_2 -based film was ≈ 35 $cm^2V^{-1}s^{-1}$ (a-ZTO annealed « in air 500 °C), in contrast 50-nm-thick In_2O_3:Zr annealed at 200 °C in N_2 presents an amorphous microstructure and an μ_e of ≈ 75 $cm^2V^{-1}s^{-1}$. Surprisingly, the local structures around the metal cations of a-SnO_2 and a-In_2O_3 are fairly similar. Previous reports used X-ray absorption, to determine the metal-metal and metal-oxygen bond distances. The In-O and In-In bond-distances are 2.18 Å and 3.34 Å respectively [Buchholz et al., 2014b], while the Sn-O and Sn-Sn bond distances correspond to 2.05 Å and 3.26 Å [Zhu et al., 2014]. Therefore if we assume that these results are a good approximation to our amorphous materials, the atoms in a-SnO_2 -based films are more closely packed. Moreover In^{3+} and Sn^{4+} are both coordinated by 6 oxygen anions in their respective amorphous oxides. An important difference is that Sn in SnO_2 is easily reduced [Batzill and Diebold, 2005]. This could trigger the formation of V_O , therefore lower relaxations times (τ) in SnO_2 -based films are expected compared to In_2O_3-based materials. Conversely, the a-ZTO and a-In_2O_3:Zr discussed here, have a N_e of ≈ 6 × 10^{19} cm^{-3} and ≈ 2 × 10^{20} cm^{-3} respectively. The source of N_e in a-ZTO are mostly V_O which, as seen in Chapter 3, result in sub-bandgap states detrimental for μ_e and for $A_{weighted}$[3].

---

[1] Note that single sc-$In_2O_3$and sc-SnO_2 were grown at process temperatures of ~650 °C and ~1200 °C ([Bierwagen and Speck, 2010, White et al., 2009] respectively).

[2] Annealing a-ZTO at 600 °C crystallized the films to a rutile structure, but the electrical resistivity of the films was too high to measure with the available techniques. More information in reference [Landucci, 2019].

Conversely, the dopants in In_2O_3:Zr are $Zr_{In}^{\bullet}$, H-atoms and V_O . The V_O also form sub-badgap defects, as seen in Chapter 5, but these defects can be passivated by mild thermal treatments at 200 °C . In addition, the ionic radius of Zr^{4+} is similar to that of In^{3+} [Shannon, 1976], hence the $Zr_{In}^{\bullet}$ do not induce strain in In_2O_3, thus maintaining a relaxed atomic network.

Given these results, we conclude that the electron transport of SnO_2 -based films are inferior to In_2O_3-based TCOs due to: (i) SnO_2 -based films have higher density of ionized defects (or more sensitivity to ionized defects) than In_2O_3-based films, (ii) SnO_2 -based thin films have less favourable grain structure (small grains i.e. more boundaries) compared with In_2O_3-based films (iii) the rutile structure of SnO_2 is not ideal to promote electron transport (iv) Dopants in $In_2O_3$are less detrimental to the electron transport than in SnO_2 , and (v) in SnO_2 the Sn cations are easily reduced, creating more defects therefore decreasing μ_e .

6.6 Conclusion

Air-annealed 100-nm-thick In_2O_3:Zr presents a FOM of 2.61, this film results in the best optoelectronic properties of all the films evaluated in this dissertation. In addition, the optoelectronic properties of In_2O_3-based materials are better than SnO_2 -based films. This is visible in the optical and electrical evaluation from the FOM. To match the optoelectronic properties of In-based films, a change in paradigm is required to improve the optoelectronic properties of tin-based TCOs. The aforementioned weaknesses in SnO_2 -based TCOs could be surmounted with a different crystal structure. For example, La-doped $BaSnO_3$ is a TCO with a perovskite microstructure that enables a near ideal Sn-O-Sn bond angle, which results in m^* of $\approx 0.19m_e$ at the bottom of the conduction band [Niedermeier et al., 2017]. This enables μ_e values > 200 $cm^2V^{-1}s^{-1}$ with a N_e up to 4×10^{20} cm^{-3} [Kim et al., 2012, Krishnaswamy et al., 2017].

---

[3] In the a-ZTO films annealed at 500 °C in air, hydrogen forward scattering suggested that low H-concentrations (lower than the detection limit of the technique, i.e. 0.5%), therefore doping of a-ZTO via H-atoms is not considered in this case.

7 Conclusions and perspectives

This chapter synthesizes the conclusions from this dissertation and, based on these observation proposes research directions that could be meaningful for future projects in TCO physics, material development and device applications.
Overall this thesis sheds light on the defect-structure-property relationships on amorphous zinc tin oxide and zirconium-doped indium oxide. Furthermore, we propose techniques to mitigate the influence of defects on the optoelectronic properties of TCOs, using strategies compatible with the production of high-efficiency solar cells. Finally we use a figure of merit to categorize and compare the optical and electrical properties of the studied materials conjointly.

7.1 General Conclusions

7.1.1 Chapter 3

Amorphous zinc tin oxide (a-ZTO) has optical properties comparable to those of tin-doped indium oxide (In_2O_3:Sn), but its electrical properties lag behind those of indum-based TCOs. Using advanced electron microscopy techniques, we determined that there are no changes in the short- and medium-range order of the films with thermal treatments up to 500 °C for films deposited at 60 °C . Thus the voidless amorphous microstructure was preserved even after high-temperature treatments. Exploiting the structural stability of a-ZTO, we performed thermal treatments (up to 500 °C) in oxidizing, neutral and reducing atmospheres. Two temperature regimes were identified to modify the optoelectronic properties of a-ZTO. Annealing at temperatures < 300 °C resulted in improved electrical properties independent of the annealing atmosphere. In this temperature range, the optical properties did not change significantly. The effect of thermal treatments at high temperatures (300 °C to 500 °C) resulted in variations of the optoelectronic properties of the films that depend of the annealing atmosphere. Treatments in an oxygen-rich environment resulted in decreased subgap absorption and a drastic increase in μ_e of the films. In contrast, thermal treatments in reducing atmospheres resulted in increased N_e and subgap absorptance, resulting in 150-nm-thick films with R_{sheet}

values near 100 Ω/sq. Thermal treatments in N_2 at high temperatures resulted in a convenient compromise between optical and electrical properties. By combining Density functional theory (DFT) simulations and experiental results, we identified V_O as the dominating defect in a-ZTO. V_O act simultaneously as an intrinsic dopant and as a subgap state, limiting μ_e of the films. Thermal treatments in O_2-rich atmospheres resulted in the passivation of V_O , which triggered μ_e increase from ≈ 20 cm^{2}V^{-1}s^{-1} to ≈ 35 cm^{2}V^{-1}s^{-1} and the decrease in subgap absorptance. Conversely, thermal treatments in H_2 atmospheres could result in (i) the generation of more V_O , (ii) shifting the V_O subgap states deeper into the bandgap and (iii) the introduction of new defect levels associated with a Sn-H interaction. The combination of these three effects could potentially explain the increase of subgap absorptance after thermal treatments in H_2 . Finally, considering that the a-ZTO films annealed at 500 °C in air are free of macroscopic defects and have $\mu_e \approx 30$ cm^{2}V^{-1}s^{-1} , we suggest that this material has the optimal optoelectronic ftrade-off for amorphous indium-free TCOs.

7.1.2 Chapter 4

The high-temperature passivation scheme proposed in Chapter 3 might be problematic for temperature-sensitive technologies. Therefore, in Chapter 4 we investigated an alternative passivation route which relies on techniques compatible with low-thermal-budget technologies. For this we relied on co-sputtering of a-ZTO or tin oxide (SnO_2) together with silicon oxide (SiO_2). Tuning the content of SiO_2 in Sn-based TCOs resulted in a positive gain in the optoelectronic trade-off. The optical properties of SnO_2 -based films were substantially improved, due to a reduction of subgap absorptance in the visible and near-infrared part of spectrum. Conversely, the electrical properties of a-ZTO remain unchanged after co-deposition with SiO_2 and a mild thermal treatment at 200 °C . Furthermore, the addition of SiO_2 to Sn-based TCOs did not affect the microstructure drastically. The addition of Si to a-ZTO did not affect the amorphous structure, while the addition of Si to SnO_2 preserved a mixture of amorphous and crystalline phases. To explain the effect of SiO_2 on the optoelectronic properties of Sn-based TCOs, DFT calculations were performed on SnO_2 modified with silicon atoms. It was found that DFT calculations using the rutile structure of SnO_2 provide a feasible explanation for the change in the optoelectronic properties after the addition of SiO_2 to a-ZTO and SnO_2 . The calculations suggest that V_O in SnO_2 is stable with two charge states, q = 0 (V_O^x) and q = 2 ($V_O^{\bullet\bullet}$). While V_O^x creates a subgap defect deep in the middle of the bandgap, $V_O^{\bullet\bullet}$ results in shallow donors that do not contribute significantly to the detrimental subgap absorption. The calculations also suggest that the addition of Si atoms promotes the formation of $V_O^{\bullet\bullet}$ defects over V_O^x . Therefore, we demonstrate a low-temperature passivation route, practical for amorphous and crystalline Sn-based TCOs alike, which could be scalable to industrial applications in low-thermal-budget technologies. This passivation route should serve as an inspiration to design and discover oxides that could potentially play a similar role in other TCOs as SiO_2 does in SnO_2 and a-ZTO.

7.1.3 Chapter 5

Optimized zirconium-doped indium oxide (In_2O_3:Zr) shows outstanding optical and electrical properties. 100-nm-thick In_2O_3:Zr shows $\mu_e > 100$ $cm^2V^{-1}s^{-1}$, $N_e > 2 \times 10^{20}$ cm^{-3} and low optical absorptance in the visible and near-infrared spectrum. In Chapter 5 we investigated the electron transport, sources of conductivity, microstructure, dopants and defects limiting electron transport in In_2O_3:Zr. To do this, we fully characterized In_2O_3:Zr films with thicknesses from 100 nm to 15 nm annealed at atmospheric pressure, under N_2 and H_2 atmospheres. We found that the as-deposited films have an amorphous microstructure with embedded nanometric-size crystallites. When annealed in air, the crystallites trigger the full crystallization of the films to a bixbyite phase, common in In-based TCOs. In addition we found that thermal treatments under H_2 and N_2 atmospheres do not result in the full crystallization of the films, but rather in a mixed phase of relatively high crystallite density embedded in an amorphous matrix. The results for 100-nm-thick In_2O_3:Zr films show that a combination of ionized impurities and phonon scattering limits electron transport. Reducing the film's thickness to 15 nm resulted in electron transport limited by ionized impurities, possibly due to surface defects. Annealing in H_2 proved to be optimal for films of thickness < 50 nm, since the films maintained high N_e while the overall total transmittance is decreased due to the reduced thickness. Conductivities as high as 1980 S cm^{-1} are achieved for 25-nm-thick films, with optical absorptance close to that of the glass substrate.
Finally, we used 80-nm-thick In_2O_3:Zr as front electrodes in silicon heterojunction solar cells. The resulting electrical parameters show increased short-circuit current compared to cells with In_2O_3:Sn electrodes of the same thickness. Even higher J_{sc} gain was achieved by reducing the thickness of the In_2O_3:Zr to 40 nm and implementing a magnesium fluoride secondary anti-reflective coating. These results demonstrate that In_2O_3:Zr is an excellent candidate to replace In_2O_3:Sn as front electrodes, while reducing the amount of indium used in the front contacts in the solar cells.

7.1.4 Chapter 6

In Chapter 6 we introduced an alternative parameter to measure the optical and electrical properties of the TCOs studied in this dissertation. The average weighted figure of merit (FOM) considers simultaneously the sheet resistance of the films and the optical absorptance weighted with the irradiance of the Sun at AM 1.5 G. The FOM of the TCOs studied in this thesis were calculated and compared. Our TCOs showed FOM values which ranged from 0.08% to 2.6%, as-deposited a-ZTO the film with lowest FOM and 100-nm-thick crystalline In_2O_3:Zr the film with highest FOM. Within the thickness range studied, all the In-based films showed better optoelectronic properties than those based Sn-based TCOs.

The superior properties of the amorphous In_2O_3 (a-In_2O_3) compared to the a-ZTO are related to a lower N_e in the a-ZTO, i.e. a more-efficient dopant should be explored for a-ZTO and SnO_2 . The observed subgap states in a-ZTO also indicate a high defect density, linked mainly to undercoordinated tin cations. This is also a source of scattering, limiting μ_e in a-ZTO. These subgap defects are absent in a-In_2O_3, and based on the reported literature In-atoms have full coordination with oxygen leaving few undercoordinated atoms. The superior properties of the crystalline In_2O_3-based films are related mainly to their highly crystalline structure, formed by large single grains growing along the thickness of the films.

7.2 Perspectives

In this section I will describe some further ideas thought but not possible to pursue during the thesis work. The author hopes that this section will serve as inspiration to future researchers who will continue with TCO design for optoelectronic devices.

7.2.1 Alternative dopants for SnO_2 -based oxides

Tin-based oxides have been used widely in applications and their optoelectronic properties have been studied in depth. In Chapters 3 and 4, an in-depth study of the optoelectronic properties of SnO_2 and a-ZTO was performed, nonetheless, we did not explore extrinsic dopants. Recently a computational screening of the periodic table suggested three possible candidates to dope SnO_2 via oxygen substitution [Graužinytė et al., 2017]. I_O, Br_O and Cl_O, are expected to work as substitutional dopants in SnO_2 without introducing defects inside the bandgap. Preliminary work using an iodine-rich spin-coated substrate shows promising results for doping a-ZTO with iodine [Landucci, 2019]. Nonetheless the demonstration of an efficient non-absorbing dopant is still pending. Several new approaches could be envisaged to introduce these dopants into a TCO via sputtering, e.g. co-sputtering of SnO_2 and a dopant-rich material, or reactive sputtering using a dopant-containing gas.

7.2.2 Sputtered indium-free transparent conductive oxides with perovskite structure

Recent reports show that La-doped barium stannate ($BaSnO_3$:La) single crystals have a bandgap of ≈ 3.0 eV, μ_e of 320 $cm^2V^{-1}s^{-1}$ and N_e of 8×10^{19} cm^{-3} [Lee et al., 2012]. $BaSnO_3$:La presents a cubic perovskite structure which enables Sn-O-Sn angle close to 180° thus permitting a highly dispersed conduction band [Kim et al., 2012] which enables $m^* < 0.3\ m_e$ at the bottom of the conduction band [Niedermeier et al., 2017]. $BaSnO_3$:La with $\mu_e > 30$ $cm^2V^{-1}s^{-1}$ deposited by sputtering has not been demonstrated, given that structural defects limit μ_e to 20 $cm^2V^{-1}s^{-1}$ [Ganguly et al., 2015]. Films of $BaSnO_3$ with a perovskite structure have been deposited at temperatures > 700 °C over $SrTiO_3$ single crystal substrates by molecular beam epitaxy or pulsed laser deposition [Prakash et al., 2017, Niedermeier et al., 2017]. Sputtering deposition can be exploited to grow these perovskite oxides, by using high deposition temperatures and low power density to induce the perovskite phase formation. Alternatively,

---

In Chapter 3 we described a TCO composed of SnO_2 and ZnO, but Zn is not a dopant SnO_2 .

co-sputtering could be used to explore other oxide compositions, or alloying with $BaSnO_3$ for either doping or to discover novel structures with high conductivity and transparency but with lower crystallization temperatures compared to $BaSnO_3$.

7.2.3 Effect of ZrO_2 on In_2O_3:Zr

In Chapter 5, we mentioned that $\mathrm{Zr}_{\mathrm{In}}^{\bullet}$ acts as a substitutional dopant in In_2O_3:Zr [Koida and Kondo, 2006, Koida and Kondo, 2007a, Kanai, 1984]. But there are still open questions regarding the role of Zr atoms and ZrO_2 in In_2O_3:Zr films. Co-sputtering using an In_2O_3 target and a Zr-containing material (either In_2O_3:Zr, ZrO_2 or metallic Zr) could clarify whether the Zr acts solely as a dopant or whether it has a different role in the material. ZrO_2 could increase the dielectric permittivity of the material [Gessert et al., 2011], which could result in relevant positive consequences. Increasing of the dielectric permittivity could shift the plasma frequency to lower energies, thus decreasing α_{FCA} and increasing the film's transparency. In addition, a higher dielectric permittivity could modify the scattering from ionized impurities, since the associated coulomb potential of the charged defect points could be strongly screened by a higher dielectric constant.

7.2.4 In_2O_3:Zr in silicon heterojunction solar cells

In_2O_3:Zr has higher electrical conductivity and lower absorptance than In_2O_3:Sn. This was exploited in silicon heterojunction solar cells by decreasing the thickness of the front TCO electrodes which led to increased short-circuit currents (Chapter 5). Nonetheless other strategies could be envisaged to improve the electrical output of the solar cells. If the front TCO thickness is kept at the 80-nm-thick standard, maintaining the R_{sheet} of $\approx 25\ \Omega/\mathrm{sq}$, the front metallization of solar cells could be redesigned to reduce shadowing from the silver fingers in the cells. This could potentially boost the short-circuit current thus improving the conversion efficiency. In addition, the relatively low fill factors in cells using In_2O_3:Zr as the front electrode could be avoided using a different cell architecture. For example, rear-emitter silicon heterojunction solar cells have potentially more relaxed electrical restrictions for the front TCO [Bivour et al., 2014]. Therefore, several approaches could be envisaged in this using In_2O_3:Zr as the front electrode, e.g. depositing a TCO of thickness $\approx$ 50 nm and a secondary anti-reflective coating; or by depositing an 80-nm-thick In_2O_3:Zr with higher oxygen content, leading to a more transparent front electrode.

A Co-sputtering In-based and Sn-based TCOs as electrodes in silicon heterojunction solar cells

This dissertation shows results from TCO films based on a-ZTO, and In_2O_3:Zr separately. In this appendix I summarize additional experiments realized to test the effect of co-depositing a-ZTO and In_2O_3:Zr. We characterized the co-sputtered films and we used this film as front electrode in silicon heterojunction solar cells. Our motivation is to find an alternative technique to the one proposed in Chapter 5 to decrease the indium content in silicon heterojunction solar cells.

A.1 Film fabrication

The In-reduced TCO film was fabricated by sputtering a-ZTO, In_2O_3:Zr and SiO_2 simultaneously. The targets of a-ZTO and In_2O_3:Zr were submitted to an RF-power of 80 W (power density of 1.02 W cm^{-2}) while the SiO_2 target was subject to a RF-power of 10 W (0.13 W cm^{-2}). The flow of argon was kept constant at 10.0 sccm, while the Ar/O_2 flow was changed between 0.7 sccm and 2.0 sccm (The oxygen source is a mixture of 95% Ar and 5% O_2). These O_2 and Ar flow resulted in oxygen flow ratios ($r(O_2) = O_2/(Ar + O_2)$) from 0.28% to 0.61% during deposition.

The results presented here were obtained with the help of a semester student: Nicholas Paul Morgan. His contributions are gratefully acknowledged.

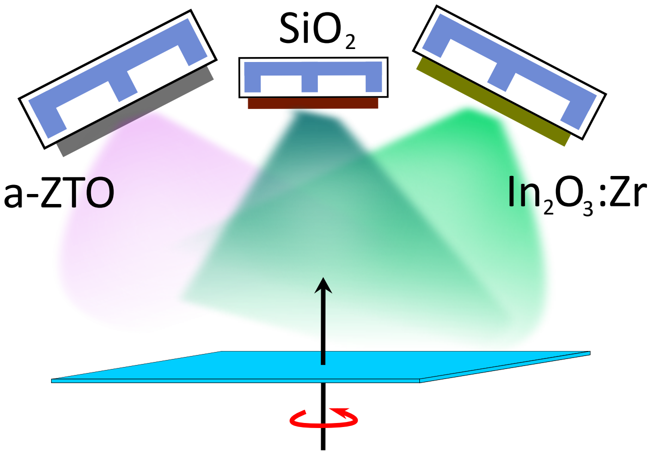

Figure A.1 – Scheme of a-ZTO, In_2O_3:Zr and SiO_2 co-sputtering. The power in the In_2O_3:Zr and a-ZTO targets was of 80 W and 10 W in the SiO_2 target. The O_2 partial pressure in the deposition chamber was tuned to optimize the films. The rotating sample enabled an homogeneous composition.

The temperature during deposition was of 100 °C and the base pressure was 10^{-6} mbar. Thirty minutes deposition resulted in 150-nm-thick films. The μ_e and N_e of the films were determined after deposition and after annealing at 200 °C for 30 minutes.

A.2 Optoelectronic properties

The μ_e and N_e of the as-deposited films is shown in Figure A.2(a) (full symbols). The μ_e increases with oxygen content, reaching a maximum of 40.8 $cm^2V^{-1}s^{-1}$ for films sputtered with r(O_2) of 0.61%. On the other hand, N_e decreases with O_2 content during deposition. Overall, annealing at 200 °C material resulted an increase in N_e and a decrease in μ_e as compared with the as-deposited samples (empty symbols in A.2(a)). The thermal treatment resulted in an increase of conductivity for films sputtered with r(O_2) of 0.45% and 0.53%, (Figure A.2(b)). The conductivity of samples sputtered with r(O_2) of 0.28% and 0.61% were to low to be measured with the Hall effect system after annealing. The TCO sputtered with r(O_2) of 0.53% presents a conductivity of 875 Scm^{-1}.

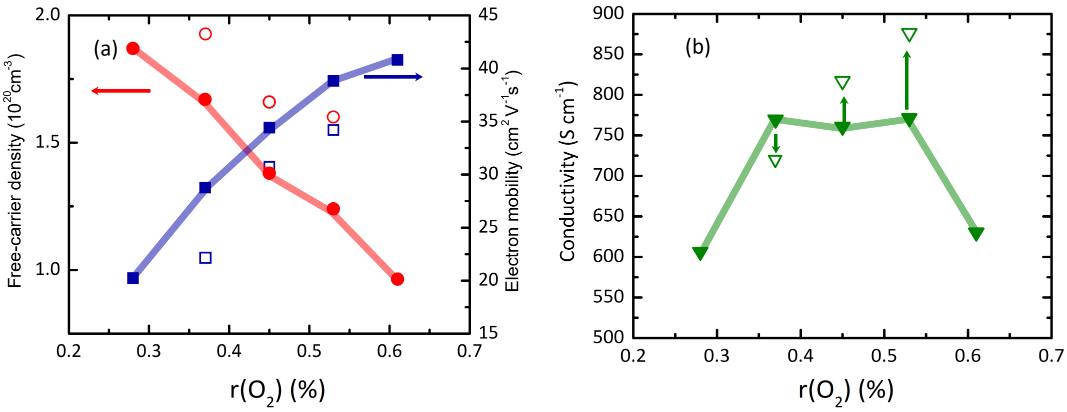

Figure A.2 – (a) N_e and μ_e of co-sputtered In_2O_3:Zr, a-ZTO and SiO_2 as function of r(O_2) during deposition. The electrical properties of chosen annealed films is shown in empty symbols. (b) Electric conductivity of films in (a), as-deposited and after annealing (full and empty symbols respectively).

The optical absorptance of the indium-reduced film sputtered with r(O_2) of 0.53% is compared with the absorptance of the a-ZTO, In_2O_3:Sn and In_2O_3:Zr. In the visible part of the spectra, the films absorb differently. In this spectral range a-ZTO shows higher absorption than the rest of the TCOs while In_2O_3:Sn and the co-sputtered (called ZITO from here on) film absorb less. In addition In_2O_3:Zr shows less absorption than the rest of the films in all the measured spectral range. In the near-infrared part of spectra, In_2O_3:Sn absorbs considerably more than In_2O_3:Zr and ZITO, mainly due to free-carrier absorption.

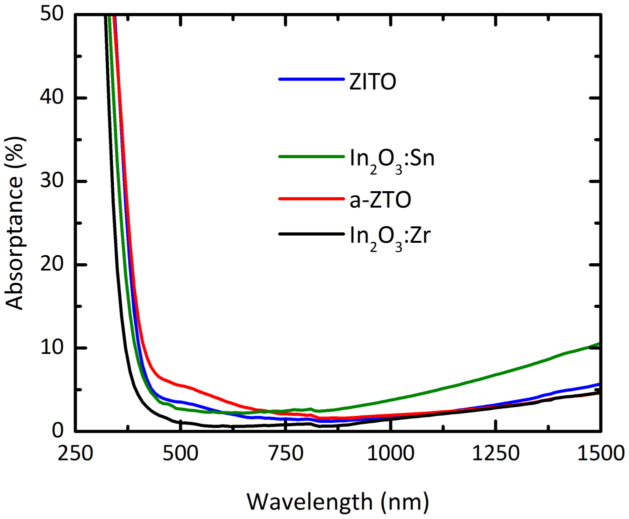

Figure A.3 – Optical absorptance of In_2O_3:Zr, In_2O_3:Sn, a-ZTO and the co-sputtered TCO (ZITO) deposited with an r(O_2) of 0.53%. The a-ZTO film and the co-sputtered film have a thickness of 150 nm, while In_2O_3:Zr and In_2O_3:Sn have a thickness of 100 nm.

A.3 Microstructure and composition

To study the film's microstructure, selected area electron diffraction patterns were acquired on the as-deposited and annealed ZITO. The smooth rings in the diffraction patterns indicate that the as-deposited and annealed films are amorphous. The metal composition of the films was determined by energy dispersive X-ray spectroscopy, the annealed films have metal composition Zn:Sn:In of 9:44:47. Silicon and zirconium were not detected due to the low concentration, possibly lower than the detection limit of the technique.

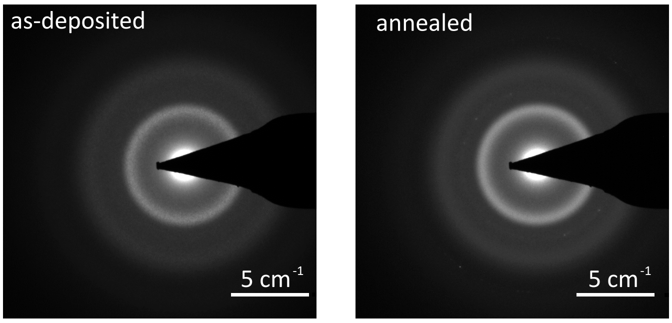

Figure A.4 – Electron diffraction patterns of as-deposited and annealed co-sputtered films

A.4 Application in silicon heterojunction solar cells

Silicon heterojunction (SHJ) solar cells were fabricated on a textured float-zone wafer. Plasma-enhanced chemical vapour deposition (PECVD) was used to deposit the intrinsic (i) and doped (p and n) amorphous silicon (a-Si:H) layers on each side. For front (back) emitter cells, the p-type (n-type) layer was deposited on the front (light-incoming) side of the wafer. The front TCO was then sputtered using a shadow mask to define a 2 cm × 2 cm cell areas. The front electrode was either In_2O_3:Sn, a-ZTO or the co-sputtering from targets of In_2O_3:Zr, a-ZTO and SiO_2 . On the rear side, In_2O_3:Sn and Ag were subsequently sputtered. Screen printing was used for the front Ag grid, and the device was finally cured at 210 °C for 20 minutes.

For the front TCO we sputtered the reference In_2O_3:Sn, a-ZTO and the co-sputtered IO:Zr/a-ZTO/SiO_2 with two different oxygen concentrations. The IV characteristics and the EQE are shown in Figure A.5(a) and (b) respectively.

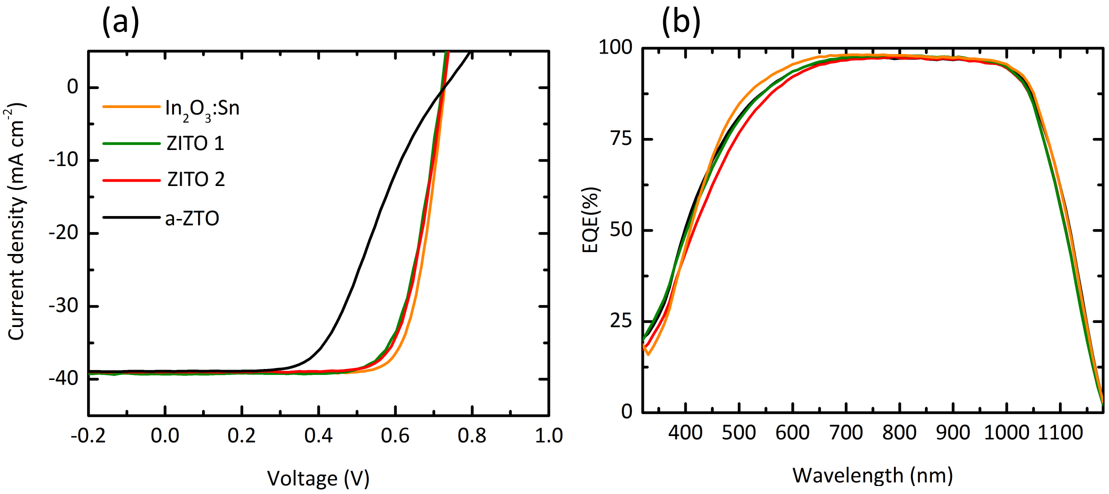

Figure A.5 – (a) IV-characteristics and (b) EQE as a function of wavelenght for the cells using the reference In_2O_3:Sn, a-ZTO and ZITO with two different oxygen contents, ZITO1 and ZITO2, with r(O_2) of 0.53% and 0.45% respectively.

Table A.1 – Performance parameters of SHJ solar cells (average values of 5 2 cm^2 × 2 cm^2 measured cells) using the co-sputtered TCO as front electrode. The results are compared with a reference cell with In_2O_3:Sn and a-ZTO front electrodes. The best-cell parameters are between parenthesis.

Front electrode	ZITO (r(O_2) = 0.53%)	ZITO (r(O_2) = 0.45%)	a-ZTO	In_2O_3:Sn
Efficiency (%)	20.3 (20.7)	20.3 (21.0)	14.2 (14.6)	21.1 (21.9)
Fill factor (%)	71.4 (73.0)	71.7(74.2)	49.9 (51.5)	74.7 (76.9)
J_{sc}(mA cm^{-2})	39.3 (39.3)	39.0 (39.0)	39.1 (38.9)	38.9 (39.1)
V_{oc} (mV)	721.5 (720.5)	724.4 (725.7)	726.6 (726.9)	726.9 (728.1)

A.5 Conclusions

The addition of In_2O_3 to a-ZTO improves its optoelectronic properties. The μ_e and N_e of the co-sputtered films at r(O_2) = 0.53% are ≈ 35 cm^{2}V^{-1}s^{-1} and 1.6 × 10^{20} cm^{-3} respectively. In contrast, the optimized a-ZTO grown and annealed at the same conditions results in μ_e of 25 cm^{2}V^{-1}s^{-1} and N_e of 10^{20} cm^{-3} . The optical properties also improved with the In_2O_3 addition as the absorptance decreased in the visible part of spectra. As compared with the standard In_2O_3:Sn front TCOs, the co-sputtered electrodes show a reduction of ≈ 50% in the indium content. Comparing the results from the IV measurement, the average efficiency decrease 0.8% with the usage of the co-sputtered TCO. The J_{sc} from all the measured cells remains fairly similar, nonetheless degraded passivation affected the V_{OC} while probably the lower conductivity affected the fill factor, therefore resulting in lower efficiency as compared with In_2O_3:Sn. However, further optimization of the co-sputtering and material optimization could solve these issues.

Bibliography

[Adachi, 2012] Adachi, S. (2012). *Optical properties of crystalline and amorphous semiconductors: Materials and fundamental principles.* Springer Science & Business Media.

[Adamo and Barone, 1999] Adamo, C. and Barone, V. (1999). Toward reliable density functional methods without adjustable parameters: The PBE0 model. *J. Chem. Phys.*, 110(13):6158–6170.

[Adurodija et al., 2006] Adurodija, F. O., Semple, L., and Brüning, R. (2006). Crystallization process and electro-optical properties of In2O3 and ITO thin films. *Journal of Materials Science*, 41(21):7096–7102.

[Agashe et al., 1988] Agashe, C., Marathe, B. R., Takwale, M. G., and Bhide, V. G. (1988). Structural properties of SnO2:F films deposited by spray pyrolysis technique. *Thin Films*, 164:261–264.

[Ágoston et al., 2009] Ágoston, P., Erhart, P., Klein, A., and Albe, K. (2009). Geometry, electronic structure and thermodynamic stability of intrinsic point defects in indium oxide. *Journal of Physics Condensed Matter*, 21(45).

[Agoston et al., 2010] Agoston, P., Korber, C., Klein, A., Puska, M. J., Nieminen, R. M., and Albe, K. (2010). Limits for n -type doping in In2O3and SnO2: A theoretical approach by first-principles calculations using hybrid-functional methodology. *Journal of Applied Physics*, 108(5).

[Albrecht et al., 2016] Albrecht, S., Saliba, M., Correa Baena, J. P., Lang, F., Kegelmann, L., Mews, M., Steier, L., Abate, A., Rappich, J., Korte, L., Schlatmann, R., Nazeeruddin, M. K., Hagfeldt, A., Grätzel, M., and Rech, B. (2016). Monolithic perovskite/silicon-heterojunction tandem solar cells processed at low temperature. *Energy & Environmental Science*, 9(1):81–88.

[Aldred and Pratt, 1963] Aldred, A. T. and Pratt, J. N. (1963). Vapor pressures or zinc, cadmium, antimony, and thallium. *Journal of Chemical & Engineering Data*, 8(3):429–431.

[Arai et al., 2017] Arai, T., Iimura, S., Kim, J., Toda, Y., Ueda, S., and Hosono, H. (2017). Chemical Design and Example of Transparent Bipolar Semiconductors. *Journal of the American Chemical Society*, 139(47):17175–17180.

[Banyamin et al., 2014] Banyamin, Z., Kelly, P., West, G., and Boardman, J. (2014). Electrical and Optical Properties of Fluorine Doped Tin Oxide Thin Films Prepared by Magnetron Sputtering. *Coatings*, 4(4):732–746.

[Battaglia et al., 2016] Battaglia, C., Cuevas, A., and De Wolf, S. (2016). High-efficiency crystalline silicon solar cells: status and perspectives. *Energy Environ. Sci.*, 9(5):1552–1576.

[Batzill and Diebold, 2005] Batzill, M. and Diebold, U. (2005). The surface and materials science of tin oxide. *Progress in Surface Science*, 79(2-4):47–154.

[Baur and Khan, 1971] Baur, W. H. and Khan, A. A. (1971). Rutile-type compounds. iv. sio2, geo2 and a comparison with other rutile-type structures. *Acta Crystallographica Section B*, 27(11):2133–2139.

[Bazzani et al., 2011] Bazzani, M., Neroni, A., Calzolari, A., and Catellani, A. (2011). Optoelectronic properties of Al:ZnO: Critical dosage for an optimal transparent conductive oxide. *Applied Physics Letters*, 98(12):121907.

[Bekisli et al., 2011] Bekisli, F., Stavola, M., Fowler, W. B., Boatner, L., Spahr, E., and Lüpke, G. (2011). Hydrogen impurities and shallow donors in SnO 2 studied by infrared spectroscopy. *Physical Review B*, 84(3):035213.

[Bielz et al., 2010] Bielz, T., Lorenz, H., Jochum, W., Kaindl, R., Klauser, F., Klötzer, B., and Penner, S. (2010). Hydrogen on In 2 O 3 : Reducibility, Bonding, Defect Formation, and Reactivity. *The Journal of Physical Chemistry C*, 114(19):9022–9029.

[Bierwagen and Speck, 2010] Bierwagen, O. and Speck, J. S. (2010). High electron mobility In2O3(001) and (111) thin films with nondegenerate electron concentration. *Applied Physics Letters*, 97(7):072103.

[Bikowski et al., 2016] Bikowski, A., Holder, A., Peng, H., Siol, S., Norman, A., Lany, S., and Zakutayev, A. (2016). Synthesis and Characterization of (Sn,Zn)O Alloys. *Chemistry of Materials*, 28(21):7765–7772.

[Birch, 1947] Birch, F. (1947). Finite Elastic Strain of Cubic Crystals. *Physical Review*, 71(11):809–824.

[Bivour et al., 2014] Bivour, M., Steinkemper, H., Jeurink, J., Schröer, S., and Hermle, M. (2014). Rear Emitter Silicon Heterojunction Solar Cells: Fewer Restrictions on the Optoelectrical Properties of Front Side TCOs. *Energy Procedia*, 55:229–234.

[Blöchl, 1994] Blöchl, P. E. (1994). Projector augmented-wave method. *Physical Review B*, 50(24):17953–17979.

[Blood and Orton, 1978] Blood, P. and Orton, J. W. W. (1978). Reports on Progress in Physics The electrical characterisation of semiconductors Related content This content was downloaded from IP address The electrical characterisation of semiconductors. Technical report.

[Boccara et al., 1980] Boccara, A. C., Fournier, D., and Badoz, J. (1980). Thermo-optical spectroscopy: Detection by the ”mirage effect”. *Applied Physics Letters*, 36(2):130–132.

[Boccard et al., 2016a] Boccard, M., Rodkey, N., and Holman, Z. C. (2016a). High-mobility Hydrogenated Indium Oxide without Introducing Water During Sputtering. *Energy Procedia*, 92:297–303.

[Boccard et al., 2016b] Boccard, M., Rodkey, N., and Holman, Z. C. (2016b). Properties of hydrogenated indium oxide prepared by reactive sputtering with hydrogen gas. In *2016 IEEE 43rd Photovoltaic Specialists Conference (PVSC)*, pages 2868–2870. IEEE.

[Brodsky, 1979] Brodsky, M. (1979). Topics in applied physics. vol. 36. amorphous semiconductors. *Springer-Verlag, xvi+ 337, 24 x 16 cm, illustrated, 1979.*

[Buchholz et al., 2014a] Buchholz, D. B., Ma, Q., Alducin, D., Ponce, A., Jose-Yacaman, M., Khanal, R., Medvedeva, J. E., and Chang, R. P. (2014a). The structure and properties of amorphous indium oxide. *Chemistry of Materials*, 26(18):5401–5411.

[Buchholz et al., 2014b] Buchholz, D. B., Ma, Q., Alducin, D., Ponce, A., Jose-Yacaman, M., Khanal, R., Medvedeva, J. E., and Chang, R. P. H. (2014b). The Structure and Properties of Amorphous Indium Oxide. *Chemistry of Materials*, 26(18):5401–5411.

[Burstein, 1954] Burstein, E. (1954). Anomalous optical absorption limit in insb. *Phys. Rev.*, 93:632–633.

[Butler et al., 2014] Butler, K. T., Buckeridge, J., Richard, C., Catlow, A., and Walsh, A. (2014). Crystal electron binding energy and surface work function control of tin dioxide. *PHYSICAL REVIEW B*, 89.

[Calnan and Tiwari, 2010] Calnan, S. and Tiwari, A. (2010). High mobility transparent conducting oxides for thin film solar cells. *Thin Solid Films*, 518(7):1839–1849.

[Choi et al., 2016] Choi, J. Y., Heo, K., Cho, K.-s., Hwang, S. W., Kim, S., and Lee, S. Y. (2016). Engineering of band gap states of amorphous SiZnSnO semiconductor as a function of Si doping concentration. *Scientific Reports*, 6(1):36504.

[Chopra and Das, 1983] Chopra, K. L. and Das, S. R. (1983). *Thin Film Solar Cells.* Springer.

[Chopra et al., 1983] Chopra, K. L., Major, S., and Pandya, D. K. (1983). Review Paper. *Thin Solid Films*, 102:1–46.

[Clatot et al., 2011] Clatot, J., Campet, G., Zeinert, A., Labrugère, C., Nistor, M., and Rougier, A. (2011). Low temperature Si doped ZnO thin films for transparent conducting oxides. *Solar Energy Materials and Solar Cells*, 95(8):2357–2362.

[Collins et al., 1979] Collins, G. S., Kachnowski, T., Benczer-Koller, N., and Pasternak, M. (1979). Application of the Mossbauer effect to the characterization of an amorphous tin-oxide system. *PHYSICAL REVIEW B*, 19.

[Correa Baena et al., 2015] Correa Baena, J. P., Steier, L., Tress, W., Saliba, M., Neutzner, S., Matsui, T., Giordano, F., Jacobsson, T. J., Srimath Kandada, A. R., Zakeeruddin, S. M., Petrozza, A., Abate, A., Nazeeruddin, M. K., Grätzel, M., and Hagfeldt, A. (2015). Highly efficient planar perovskite solar cells through band alignment engineering. *Energy & Environmental Science*, 8(10):2928–2934.

[Dabirian et al., 2016] Dabirian, A., Martin De Nicolas, S., Niesen, B., Hessler-Wyser, A., De Wolf, S., Morales-Masis, M., and Ballif, C. (2016). Tuning the Optoelectronic Properties of ZnO:Al by Addition of Silica for Light Trapping in High-Efficiency Crystalline Si Solar Cells. *Advanced Materials Interfaces*, 3(3).

[Dauzou et al., 2016] Dauzou, F., Bouten, P. C., Dabirian, A., Leterrier, Y., Ballif, C., and Morales-Masis, M. (2016). Mechanical integrity of hybrid indium-free electrodes for flexible devices. *Organic Electronics*, 35:136–141.

[De Wolf et al., 2012] De Wolf, S., Descoeudres, A., Holman, Z. C., and Ballif, C. (2012). High-efficiency Silicon Heterojunction Solar Cells: A Review. *Green*, 0(0):7–24.

[Delahoy and Guo, 2005] Delahoy, A. E. and Guo, S. Y. (2005). Transparent and semitransparent conducting film deposition by reactive-environment, hollow cathode sputtering. *Journal of Vacuum Science & Technology A: Vacuum, Surfaces, and Films*, 23(4):1215–1220.

[Dingle, 1955] Dingle, R. B. (1955). XCIV. Scattering of electrons and holes by charged donors and acceptors in semiconductors. *The London, Edinburgh, and Dublin Philosophical Magazine and Journal of Science*, 46(379):831–840.

[Dixon et al., 2016] Dixon, S. C., Scanlon, D. O., Carmalt, C. J., and Parkin, I. P. (2016). n-Type doped transparent conducting binary oxides: an overview. *J. Mater. Chem. C*, 4(29):6946–6961.

[Dugdale, 1977] Dugdale, J. S. (1977). *The electrical properties of metals and alloys*. E. Arnold London, London.

[Elangovan and Ramamurthi, 2005] Elangovan, E. and Ramamurthi, K. (2005). A study on low cost-high conducting fluorine and antimony-doped tin oxide thin films. *Thin Solid films*.

[Ellmer, 2001] Ellmer, K. (2001). Restivity of polycrystalline zinc oxide films: current status and physical limit. *J. Phys. D: Appl. Phys.*, 34:3097–3108.

[Ellmer, 2012] Ellmer, K. (2012). Past achievements and future challenges in the development of optically transparent electrodes. *Nature Photonics*, 6:808–816.

[Ellmer and Mientus, 2008] Ellmer, K. and Mientus, R. (2008). Carrier transport in polycrystalline ITO and ZnO:Al II: The influence of grain barriers and boundaries. *Thin Solid Films*, 516(17):5829–5835.

[Elsasser et al., 1990] Elsasser, C., Takeuchi, N., Ho, K. M., Chan, C. T., Braun, P., and Fahnle, M. (1990). Relativistic effects on ground state properties of 4d and 5d transition metals. *Journal of Physics: Condensed Matter*, 2(19):4371.

[Erginsoy, 1950] Erginsoy, C. (1950). Neutral impurity scattering in Semiconductors. *Phyiscal review*, 79(1013):22.

[Essig et al., 2018] Essig, S., Dréon, J., Rucavado, E., Mews, M., Koida, T., Boccard, M., Werner, J., Geissbühler, J., Löper, P., Morales-Masis, M., Korte, L., De Wolf, S., and Ballif, C. (2018). Toward Annealing-Stable Molybdenum-Oxide-Based Hole-Selective Contacts For Silicon Photovoltaics. *Solar RRL*, 2(4):1700227.

[Facchetti and Marks, 2010] Facchetti, A. and Marks, T. (2010). *Transparent electronics: from synthesis to applications*. John Wiley & Sons.

[Faure et al., 2012] Faure, C., Clatot, J., Teulé-Gay, L., Campet, G., Labrugère, C., Nistor, M., and Rougier, A. (2012). Co-sputtered ZnO:Si thin films as transparent conductive oxides. *Thin Solid Films*, 524:151–156.

[Fortunato et al., 2006] Fortunato, E., Pimentel, A., Gonçalves, A., Marques, A., and Martins, R. (2006). High mobility amorphous/nanocrystalline indium zinc oxide deposited at room temperature. *Thin Solid Films*, 502(1-2):104–107.

[Fox, 2010] Fox, M. (2010). *Optical Properties of Solids*. Oxford Master Series in Condensed Matter Physics, 2 edition.

[Frank and Kostlin, 1982] Frank, G. and Kostlin, H. (1982). Electrical Properties and Defect Model of Tin-Doped Indium Oxide Layers. *Applied Physics A*, 27:197–206.

[Frenzel et al., 2015] Frenzel, H., Tobias, D., Schlupp, P., Wenckstern, H. V., and Grundmann, M. (2015). Long-throw magnetron sputtering of amorphous Zn-Sn-O thin films at room temperature. *Physica Status Solidi (a)*, 1486(7):1482–1486.

[Fuchs and Bechstedt, 2008] Fuchs, F. and Bechstedt, F. (2008). Indium-oxide polymorphs from first principles: Quasiparticle electronic states. *Physical review B*.

[Fujiwara and Kondo, 2005] Fujiwara, H. and Kondo, M. (2005). Effects of carrier concentration on the dielectric function of ZnO:Ga and In 2O 3:Sn studied by spectroscopic ellipsometry: Analysis of free-carrier and band-edge absorption. *Physical Review B - Condensed Matter and Materials Physics*, 71(7):1–10.

[Gale, 1997] Gale, J. (1997). GULP: A computer program for the symmetry-adapted simulation of solids. *J. Chem. Soc., Faraday Trans.*, 93(4):629–637.

[Ganguly et al., 2015] Ganguly, K., Ambwani, P., Xu, P., Jeong, J. S., Mkhoyan, K. A., Leighton, C., and Jalan, B. (2015). Structure and transport in high pressure oxygen sputter-deposited BaSnO 3-δ. *Citation: APL Materials*, 3:62509.

[Gardner, 1940] Gardner, G. S. (1940). Handbook of chemistry. *Journal of the Franklin Institute*, 229(1):138–139.

[Gessert et al., 2011] Gessert, T., Burst, J., Li, X., Scott, M., and Coutts, T. (2011). Advantages of transparent conducting oxide thin films with controlled permittivity for thin film photovoltaic solar cells. *Thin Solid Films*, 519(21):7146–7148.

[Ginley and Perkins, 2011] Ginley, D. and Perkins, J. (2011). Handbook of Transparent Conductors. In *Handbook of transparent conductors*, pages 1–25. Springer.

[Granqvist, 2007] Granqvist, C. G. (2007). Transparent conductors as solar energy materials: A panoramic review. *Solar Energy Materials and Solar Cells*, 91(17):1529–1598.

[Graužinytė et al., 2017] Graužinytė, M., Goedecker, S., and Flores-Livas, J. A. (2017). Computational Screening of Useful Hole–Electron Dopants in SnO 2. *Chemistry of Materials*, 29(23):10095–10103.

[Guo and Hu, 2012] Guo, D. and Hu, C. (2012). First-principles study on the electronic structure and optical properties for sno_2 with oxygen vacancy. *Appl. Surf. Sci.*, 258(18):6987–6992.

[Hall and Racette, 1964] Hall, R. N. and Racette, J. H. (1964). Diffusion and solubility of copper in extrinsic and intrinsic germanium, silicon, and gallium arsenide. *Journal of Applied Physics*, 35(2):379–397.

[Han and Lee, 2015] Han, S. and Lee, S. Y. (2015). High performance of full swing logic inverter using all n-types amorphous ZnSnO and SiZnSnO thin film transistors. *Applied Physics Letters*, 106(21):212104.

[Hanyu et al., 2013] Hanyu, Y., Domen, K., Nomura, K., Hiramatsu, H., Kumomi, H., Hosono, H., and Kamiya, T. (2013). Hydrogen passivation of electron trap in amorphous In-Ga-Zn-O thin-film transistors. *Applied Physics Letters*, 103(20):202114.

[Harvey et al., 2006] Harvey, S. P., Mason, T. O., Gassenbauer, Y., Schafranek, R., and Klein, A. (2006). Surface versus bulk electronic/defect structures of transparent conducting oxides: I. Indium oxide and ITO. *Journal of Physics D: Applied Physics*, 39(18):3959–3968.

[Hautier et al., 2014] Hautier, G., Miglio, A., Waroquiers, D., Rignanese, G. M., and Gonze, X. (2014). How does chemistry influence electron effective mass in oxides? A high-throughput computational analysis. *Chemistry of Materials*, 26(19):5447–5458.

[Hlaing Oo et al., 2010] Hlaing Oo, W. M., Tabatabaei, S., McCluskey, M. D., Varley, J. B., Janotti, A., and Van de Walle, C. G. (2010). Hydrogen donors in SnO2 studied by infrared spectroscopy and first-principles calculations. *Physical Review B*, 82(19):193201.

[Ho et al., 1992] Ho, K. M., Elsasser, C., Chan, C. T., and Fahnle, M. (1992). First-principles pseudopotential calculations for hydrogen in 4d transition metals. I. Mixed-basis method for total energies and forces. *Journal of Physics: Condensed Matter*, 4(22):5189–5206.

[Hofmann et al., 2002] Hofmann, D. M., Hofstaetter, A., Leiter, F., Zhou, H., Henecker, F., Meyer, B. K., Orlinskii, S. B., Schmidt, J., and Baranov, P. G. (2002). Hydrogen: a relevant shallow donor in zinc oxide. *Physical review letters*, 88(4):045504.

[Holman et al., 2012] Holman, Z., Descoeudres, A., Barraud, L., Fernandez, F., Seif, J., De Wolf, S., and Ballif, C. (2012). Current Losses at the Front of Silicon Heterojunction Solar Cells. *IEEE Journal of Photovoltaics*, 2(1):7–15.

[Holman et al., 2013] Holman, Z. C., Filipič, M., Descoeudres, A., De Wolf, S., Smole, F., Topič, M., and Ballif, C. (2013). Infrared light management in high-efficiency silicon heterojunction and rear-passivated solar cells. *Journal of Applied Physics*, 113(1):013107.

[Hosono, 2013] Hosono, H. (2013). Exploring electro-active functionality of transparent oxide materials. *Japanese Journal of Applied Physics*, 52.

[Hosono et al., 1996a] Hosono, H., Yamashita, Y., Ueda, N., Kawazoe, H., and Shimidzu, K.-I. (1996a). New amorphous semiconductor: 2CdOPbO x. *Applied Physics Letters*, 68(5):661–663.

[Hosono et al., 1996b] Hosono, H., Yasukawa, M., and Kawazoe, H. (1996b). Novel oxide amorphous semiconductors: Transparent conducting amorphous oxides. *Journal of Non-Crystalline Solids*, 203:334–344.

[Ibach and Luth, 2009] Ibach, H. and Luth, H. (2009). *Solid-State Physics. An Introduction to Principles of Materials Science.* Springer.

[Ingenito et al., 2018] Ingenito, A., Nogay, G., Jeangros, Q., Rucavado, E., Allebé, C., Eswara, S., Valle, N., Wirtz, T., Horzel, J., Koida, T., Morales-Masis, M., Despeisse, M., Haug, F.-j., Löper, P., and Ballif, C. (2018). A passivating contact for silicon solar cells formed during a single firing thermal annealing. *Nature Energy*, 3(9):800–808.

[Ito et al., 2006] Ito, N., Sato, Y., Song, P., Kaijio, A., Inoue, K., and Shigesato, Y. (2006). Electrical and optical properties of amorphous indium zinc oxide films. *Thin Solid Films*, 496(1):99–103.

[Janotti and Van de Walle, 2007] Janotti, A. and Van de Walle, C. G. (2007). Hydrogen multi-centre bonds. *Nature Materials*, 6(1):44–47.

[Jayaraj et al., 2008] Jayaraj, M. K., Saji, K. J., Nomura, K., Kamiya, T., and Hosono, H. (2008). Optical and electrical properties of amorphous zinc tin oxide thin films examined for thin film transistor application. *Journal of Vacuum Science & Technology B*, 26(2):495–501.

[Jefferson et al., 2008] Jefferson, P. H., Hatfield, S. A., Veal, T. D., King, P. D. C., McConville, C. F., Zúñiga–Pérez, J., and Muñoz–Sanjosé, V. (2008). Bandgap and effective mass of epitaxial cadmium oxide. *Applied Physics Letters*, 92(2):022101.

[Jellison and Modine, 1996] Jellison, G. E. and Modine, F. A. (1996). Parameterization of the optical functions of amorphous materials in the interband region. *Appl. Phys. Lett*, 69:2137.

[Jiang et al., 2016] Jiang, J., Lu, Y., Meyer, B. K., Hofmann, D. M., and Eickhoff, M. (2016). Shift of optical absorption edge in SnO2 films with high concentrations of nitrogen grown by chemical vapor deposition. *Journal of Applied Physics*, 119(24):245703.

[Jost et al., 2016] Jost, G. C., Hamri, A. N., Kohler, F., and Hupkes, J. (2016). Reliability aspects of hydrogen-doped indium oxide. *Physica Status Solidi (A) Applications and Materials Science*, 213(7):1751–1759.

[Kamiya and Hosono, 2010] Kamiya, T. and Hosono, H. (2010). Material characteristics and applications of transparent amorphous oxide semiconductors. *NPG Asia Materials*, 2(1):15–22.

[Kamiya et al., 2008a] Kamiya, T., Nomura, K., Hirano, M., and Hosono, H. (2008a). Electronic structure of oxygen deficient amorphous oxide semiconductor a-InGaZnO 4- x : Optical analyses and first-principle calculations. *physica status solidi (c)*, 5(9):3098–3100.

[Kamiya et al., 2008b] Kamiya, T., Nomura, K., Hirano, M., and Hosono, H. (2008b). Electronic structure of oxygen deficient amorphous oxide semiconductor a-InGaZnO4-x: Optical analyses and first-principle calculations. *Physica Status Solidi (C) Current Topics in Solid State Physics*, 5(9):3098–3100.

[Kamiya et al., 2009a] Kamiya, T., Nomura, K., and Hosono, H. (2009a). Electronic structure of the amorphous oxide semiconductor a-InGaZnO4- x : Tauc-Lorentz optical model and origins of subgap states. *Physica Status Solidi A*, 206(5):860–867.

[Kamiya et al., 2009b] Kamiya, T., Nomura, K., and Hosono, H. (2009b). Origins of High Mobility and Low Operation Voltage of Amorphous Oxide TFTs: Electronic Structure, Electron Transport, Defects and Doping*. *Journal of Display Technology*, 5(12):273–288.

[Kamiya et al., 2009c] Kamiya, T., Nomura, K., and Hosono, H. (2009c). Origins of High Mobility and Low Operation Voltage of Amorphous Oxide TFTs: Electronic Structure, Electron Transport, Defects and Doping*. *Journal of Display Technology*, 5(12):468–483.

[Kamp et al., 2005] Kamp, B., Merkle, R., Lauck, R., and Maier, J. (2005). Chemical diffusion of oxygen in tin dioxide: Effects of dopants and oxygen partial pressure. *Journal of Solid State Chemistry*, 178(10):3027–3039.

[Kanai, 1984] Kanai, Y. (1984). Electrical Properties of In2O3 Single Crystals Doped with Metallic Donor Impurity. *Japanese Journal of Applied Physics*, 23(1):127.

[Kang et al., 2012] Kang, I., Park, C. H., Chong, E., and Lee, S. Y. (2012). Role of Si as carrier suppressor in amorphous Zn–Sn–O. *Current Applied Physics*, 12(SUPPL.4):S12–S16.

[Kılıç and Zunger, 2002] Kılıç, Ç. and Zunger, A. (2002). Origins of coexistence of conductivity and transparency in sno$_2$. *Phys. Rev. Lett.*, 88(9):095501.

[Kim et al., 2001] Kim, H., Horwitz, J. S., Kushto, G. P., Qadri, S. B., Kafafi, Z. H., and Chrisey, D. B. (2001). Transparent conducting Zr-doped thin films for organic light-emitting diodes. *Citation: Appl. Phys. Lett*, 78:1050.

[Kim et al., 2012] Kim, H. J., Kim, U., Kim, T. H., Kim, J., Kim, H. M., Jeon, B.-G., Lee, W.-J., Mun, H. S., Hong, K. T., Yu, J., Char, K., and Kim, K. H. (2012). Physical properties of transparent perovskite oxides (Ba,La)SnO3 with high electrical mobility at room temperature. *Physical Review B*, 86(16):165205.

[Kim et al., 2006] Kim, I., Ko, J., Kim, D., Lee, K., Lee, T., Jeong, J.-h., Cheong, B., Baik, Y.-J., and Kim, W. (2006). Scattering mechanism of transparent conducting tin oxide films prepared by magnetron sputtering. *Thin Solid Films*, 515(4):2475–2480.

[King et al., 2009] King, P. D. C., Lichti, R. L., Celebi, Y. G., Gil, J. M., Vilão, R. C., Alberto, H. V., Piroto Duarte, J., Payne, D. J., Egdell, R. G., McKenzie, I., McConville, C. F., Cox, S. F. J., and Veal, T. D. (2009). Shallow donor state of hydrogen in In2O3and SnO2: Implications for conductivity in transparent conductive oxides. *Physical Review B*, 80(8):081201.

[King and Veal, 2011] King, P. D. C. and Veal, T. D. (2011). Conductivity in transparent oxide semiconductors. *Journal of Physics: Condensed Matter*, 23(33):334214.

[Kizu et al., 2016] Kizu, T., Aikawa, S., Nabatame, T., Fujiwara, A., Ito, K., Takahashi, M., and Tsukagoshi, K. (2016). Homogeneous double-layer amorphous Si-doped indium oxide thin-film transistors for control of turn-on voltage. *Journal of Applied Physics*, 120(4):045702.

[Klein, 2013] Klein, A. (2013). Transparent conducting oxides: Electronic structure-property relationship from photoelectron spectroscopy with in situ sample preparation. *Journal of the American Ceramic Society*, 96(2):331–345.

[Kluth et al., 2003] Kluth, O., Schope, G., Hupkes, J., Agashe, C., Muller, J., Rech, B., and Rech (2003). Modified Thornton model for magnetron sputtered zinc oxide: film structure and etching behaviour. *Thin Solid Films*, 442:80–85.

[Knoops et al., 2015] Knoops, H. C. M., van de Loo, B. W. H., Smit, S., Ponomarev, M. V., Weber, J.-W., Sharma, K., Kessels, W. M. M., and Creatore, M. (2015). Optical modeling of plasma-deposited ZnO films: Electron scattering at different length scales. *Journal of Vacuum Science & Technology A: Vacuum, Surfaces, and Films*, 33(2):021509.

[Ko et al., 2007] Ko, J., Kim, I., Kim, D., Lee, K. S., Lee, T., Cheong, B., and Kim, W. (2007). Transparent and conducting Zn-Sn-O thin films prepared by combinatorial approach. *Applied Surface Science*, 253:7398–7403.

[Kobayashi et al., 2012] Kobayashi, E., Nakamura, N., and Watabe, Y. (2012). Reduction of Optical and Electrical Losses in Silicon Heterojunction Solar Cells by Hydrogenated Tungsten-doped In2O3. *Proceeding of 27th European Photovoltaic Solar Energy Conference and Exhibition*, (January):1619–1623.

[Kobayashi et al., 2015] Kobayashi, E., Watabe, Y., and Yamamoto, T. (2015). High-mobility transparent conductive thin films of cerium-doped hydrogenated indium oxide. *Applied Physics Express*, 8(1).

[Kohl, 1989] Kohl, D. (1989). Surface processes in the detection of reducing gases with SnO-Based devices. *Sensors and Actuators*, 18:71–113.

[Koida et al., 2007] Koida, T., Fujiwara, H., and Kondo, M. (2007). Hydrogen-doped In2O3 as High-mobility Transparent Conductive Oxide. *Japanese Journal of Applied Physics*, 46(28).

[Koida et al., 2017] Koida, T., Kaneko, T., and Shibata, H. (2017). *Materials*, 10(2).

[Koida and Kondo, 2006] Koida, T. and Kondo, M. (2006). High-mobility transparent conductive Zr-doped In2O3. *Applied Physics Letters*, 89(8):082104.

[Koida and Kondo, 2007a] Koida, T. and Kondo, M. (2007a). Comparative studies of transparent conductive Ti-, Zr-, and Sn-doped In2O3 using a combinatorial approach. *Journal of Applied Physics*, 101(6):063713.

[Koida and Kondo, 2007b] Koida, T. and Kondo, M. (2007b). Improved near-infrared transparency in sputtered in2O 3-based transparent conductive oxide thin films by Zr-doping. *Journal of Applied Physics*, 101(6):10–14.

[Koida et al., 2010] Koida, T., Kondo, M., Tsutsumi, K., Sakaguchi, A., Suzuki, M., and Fujiwara, H. (2010). Hydrogen-doped In2O3 transparent conducting oxide films prepared by solid-phase crystallization method. *Journal of Applied Physics*, 107(3).

[Koida et al., 2012] Koida, T., Shibata, H., Kondo, M., Tsutsumi, K., Sakaguchi, A., and Suzuki, M. (2012). Correlation between oxygen stoichiometry , structure , and opto-electrical properties in amorphous In2O3 : H films Correlation between oxygen stoichiometry , structure , and opto-electrical properties in amorphous In2O3:H films. *Journal of Applied Physics*, 111(063721):1–7.

[Koida et al., 2018] Koida, T., Ueno, Y., and Shibata, H. (2018). In 2 O 3 -Based Transparent Conducting Oxide Films with High Electron Mobility Fabricated at Low Process Temperatures. *physica status solidi (a)*, 215(7):1700506.

[Körner and Elsässer, 2010] Körner, W. and Elsässer, C. (2010). First-principles density functional study of dopant elements at grain boundaries in ZnO. *Physical Review B - Condensed Matter and Materials Physics*, 81(8):1–12.

[Körner and Elsässer, 2014] Körner, W. and Elsässer, C. (2014). Density-functional theory study of stability and subgap states of crystalline and amorphous Zn–Sn–O. *Thin Solid Films*, 555:81–86.

[Körner et al., 2012] Körner, W., Gumbsch, P., and Elsässer, C. (2012). Analysis of electronic subgap states in amorphous semiconductor oxides based on the example of Zn-Sn-O systems. *Physical Review B*, 86(16):165210.

[Körner et al., 2015] Körner, W., Urban, D., and Elsässer, C. (2015). Generic origin of subgap states in transparent amorphous semiconductor oxides illustrated for the cases of In-Zn-O and In-Sn-O. *Physica Status Solidi (a)*, 6:1–6.

[Körner et al., 2013] Körner, W., Urban, D. F., and Elsässer, C. (2013). Origin of subgap states in amorphous In-Ga-Zn-O. *Journal of Applied Physics*, 114(16):163704.

[Körner et al., 2014] Körner, W., Urban, D. F., Ramo, D. M., Bristowe, P. D., and Elsässer, C. (2014). Prediction of subgap states in Zn- and Sn-based oxides using various exchange-correlation functionals. *Physical Review B*, 90(19):195142.

[Kresse and Furthmüller, 1996] Kresse, G. and Furthmüller, J. (1996). Efficient iterative schemes for ab initio total-energy calculations using a plane-wave basis set. *Physical Review B*, 54(16):11169–11186.

[Krishnaswamy et al., 2017] Krishnaswamy, K., Himmetoglu, B., Kang, Y., Janotti, A., and Van de Walle, C. G. (2017). First-principles analysis of electron transport in BaSnO3. *Physical Review B*, 95(20):205202.

[Kroger and Vink, 1958] Kroger, F. A. and Vink, H. J. (1958). Phys. Chem. Solids. *J. Phys. Chem. Solids.*

[Kröger and Vink, 1958] Kröger, F. a. and Vink, H. J. (1958). Relations between the Concentrations of Imperfactions in Crystalline Solids. *Journal of Physics and Chemistry of Solids*, 5(I):208–223.

[Kumar et al., 2005] Kumar, B., Gong, H., and Akkipeddi, R. (2005). High mobility undoped amorphous indium zinc oxide transparent thin films. *Journal of Applied Physics*, 98(7):073703.

[Landucci, 2019] Landucci, F. (2019). *A multitechnique approach to asses the thermal stability in tin-based transparent conductive oxides.* PhD thesis, École Polytechnique Fédéral de Lausanne, Lausanne, Switzerland.

[Lany and Zunger, 2005] Lany, S. and Zunger, A. (2005). Anion vacancies as a source of persistent photoconductivity in ii-vi and chalcopyrite semiconductors. *Phys. Rev. B*, 72(3):035215.

[Lany and Zunger, 2007] Lany, S. and Zunger, A. (2007). Dopability, Intrinsic Conductivity, and Nonstoichiometry of Transparent Conducting Oxides. *Physical Review Letters*, 98(4):045501.

[Lechermann et al., 2004] Lechermann, F., Fähnle, M., Meyer, B., and Elsässer, C. (2004). Electronic correlations, magnetism, and structure of Fe-Al subsystems: An LDA+U study. *Physical Review B*, 69(16):165116.

[Lee et al., 2017] Lee, B. H., Lee, D.-y., Sohn, A., Park, S., Kim, D.-w., and Lee, S. Y. (2017). Direct investigation on energy bandgap of Si added ZnSnO system for stability enhancement by X-ray photoelectron spectroscopy. *Journal of Alloys and Compounds*, 715:9–15.

[Lee et al., 2012] Lee, H.-n., Kim, H.-j., Kim, C.-k., Dussaigne, A., Gonschorek, M., Malinverni, M., Hong, K. T., Lee, W.-j., Ju, C., Hoon, K., and Char, K. (2012). High Mobility in a Stable Transparent Perovskite Oxide. *Applied Physics Express*, 5(061102).

[Limpijumnong et al., 2009] Limpijumnong, S., Reunchan, P., Janotti, A., and Van de Walle, C. G. (2009). Hydrogen doping in indium oxide: An ab initio study. *Physical Review B*, 80(19):193202.

[Liu et al., 2016] Liu, C. P., Foo, Y., Kamruzzaman, M., Ho, C. Y., Zapien, J. A., Zhu, W., Li, Y. J., Walukiewicz, W., and Yu, K. M. (2016). Effects of Free Carriers on the Optical Properties of Doped CdO for Full-Spectrum Photovoltaics. *Physical Review Applied*, 6(6):1–12.

[Look et al., 2013] Look, D. C., Leedy, K. D., Kiefer, A., Claflin, B., Itagaki, N., Matsushima, K., and Suhariadi, I. (2013). Model for thickness dependence of mobility and concentration in highly conductive zinc oxide. *Optical Engineering*, 52(3):033801.

[Lupis, 1983] Lupis, C. H. P. (1983). *Chemical thermodynamics of materials*. North-Holland.

[Macco et al., 2015] Macco, B., Knoops, H., and Kessels, W. (2015). Electron Scattering and Doping Mechanisms in Solid-Phase-Crystallized In2O3:H Prepared by Atomic Layer Deposition. *ACS Applied Materials & Interfaces*, 7(30):16723–16729.

[Macco et al., 2016] Macco, B., Verheijen, M. A., Black, L. E., Barcones, B., Melskens, J., and Kessels, W. M. M. (2016). On the solid phase crystallization of In 2 O 3 :H transparent conductive oxide films prepared by atomic layer deposition. *Journal of Applied Physics*, 120(8):085314.

[Macco et al., 2014] Macco, B., Wu, Y., Vanhemel, D., and Kessels, W. M. (2014). High mobility In2O3: H transparent conductive oxides prepared by atomic layer deposition and solid phase crystallization. *Physica Status Solidi - Rapid Research Letters*, 8(12):987–990.

[Madelung, 2012] Madelung, O. (2012). *Semiconductors: data handbook*. Springer Science & Business Media.

[Marezio, 1966] Marezio, M. (1966). Refinement of the crystal structure of in_2o_3 at two wavelengths. *Acta Crystallographica*, 20(6):723–728.

[Masetti et al., 1983] Masetti, G., Severi, M., and Solmi, S. (1983). Modeling of carrier mobility against carrier concentration in arsenic-, phosphorus-, and boron-doped silicon. *IEEE Transactions on Electron Devices*, 30(7):764–769.

[Medvedeva, 2007] Medvedeva, J. E. (2007). Averaging of the electron effective mass in multicomponent transparent conducting oxides. *Europhysics Letters (EPL)*, 78(5):57004.

[Medvedeva et al., 2017] Medvedeva, J. E., Buchholz, D. B., and Chang, R. P. H. (2017). Recent Advances in Understanding the Structure and Properties of Amorphous Oxide Semiconductors. *Advanced Electronic Materials*, (Md):1700082.

[Meng et al., 2001] Meng, Y., Yang, X.-l., Chen, H.-x., Shen, J., Jiang, Y.-m., Zhang, Z.-j., and Hua, Z.-y. (2001). A new transparent conductive thin film In2O3:Mo. *Thin Solid Films*, 394(1-2):218–222.

[Mereu et al., 2015] Mereu, R., Le Donne, A., Trabattoni, S., Acciarri, M., and Binetti, S. (2015). Comparative study on structural, morphological and optical properties of Zn2SnO4 thin films prepared by r.f. sputtering using Zn and Sn metal targets and ZnO–SnO2 ceramic target. *Journal of Alloys and Compounds*, 626:112–117.

[Meyer et al., 1995] Meyer, B., Hummler, K., Elsasser, C., and Fahnle, M. (1995). Reconstruction of the true wavefunctions from the pseudowavefunctions in a crystal and calculation of electric field gradients. *Journal of Physics: Condensed Matter*, 7(48):9201–9217.

[Mi et al., 1999] Mi, Y., Odaka, H., and Iwata, S. (1999). Electronic Structures and Optical Properties of ZnO, SnO2 and In2O3. *Japanese Journal of Applied Physics*, 38(6A):3453–3458.

[Minami, 1999] Minami, T. (1999). Transparent and conductive multicomponent oxide films prepared by magnetron Transparent and conductive multicomponent oxide films prepared by magnetron sputtering. *Journal of Vacuum Science {&} Technology A: Vacuum, Surfaces, and Films*, 17(4):1765–1772.

[Minami et al., 1986] Minami, T., Sato, H., Nanto, H., and Takata, S. (1986). Highty Conductive and Transparent Silicon Doped Zinc Oxide Thin Films Prepared by RF Magnetron Sputtering. *Japanese Journal of Applied Physics*, 25(Part 2, No. 9):L776—-L779.

[Minami et al., 1994] Minami, T., Sonohara, H., Shinzo, T., and Hirotoshi, S. (1994). Highly Transparent and Conductive Zinc-Stannate Thin Films Prepared by RF Magnetron Sputtering. *Japanese Journal of Applied Physics*, 33:1693–1696.

[Mishra et al., 1995] Mishra, K. C., Johnson, K. H., and Schmidt, P. C. (1995). Electronic structure of antimony-doped tin oxide. 51.

[Mitoma et al., 2014] Mitoma, N., Aikawa, S., Gao, X., Kizu, T., Shimizu, M., Lin, M.-F., Nabatame, T., and Tsukagoshi, K. (2014). Stable amorphous In 2 O 3 -based thin-film transistors by incorporating SiO 2 to suppress oxygen vacancies. *Applied Physics Letters*, 104(10):102103.

[Mizokawa and Nakamura, 1974] Mizokawa, Y. and Nakamura, S. (1974). ESR study of the oxygen, hydrogen and nitrogen oxide on tin dioxide. *Japanese Journal of Applied Physics*, 13(S2):253–256.

[Mizuno et al., 1997] Mizuno, M., Miyamoto, T., Ohnishi, T., and Hayashi, H. (1997). Effects of Tin Doping and Oxygen Vacancies on the Electronic States of Indium Oxide. *Japanese Journal of Applied Physics*, 36(1):3408–3413.

[Morales-Masis et al., 2016] Morales-Masis, M., Dauzou, F., Jeangros, Q., Dabirian, A., Lifka, H., Gierth, R., Date, M., Hessler-Wyser, A., and Ballif, C. (2016). An Indium–Free Anode for

Large-Area Flexible OLEDs: Defect-Free Transparent Conductive Zinc Tin Oxide. *Advanced Functional Materials*, 26:384–392.

[Morales-Masis et al., 2017a] Morales-Masis, M., De Wolf, S., Woods-Robinson, R., Ager, J. W., and Ballif, C. (2017a). Transparent Electrodes for Efficient Optoelectronics. *Advanced Electronic Materials*, 3(5):1600529.

[Morales-Masis et al., 2014] Morales-Masis, M., Ding, L., Dauzou, F., Jeangros, Q., Hessler-Wyser, A., Nicolay, S., and Ballif, C. (2014). Hydrogen plasma treatment for improved conductivity in amorphous aluminum doped zinc tin oxide thin films. *APL Materials*, 2(9):096113.

[Morales-Masis et al., 2015] Morales-Masis, M., Nicolas, S., Holovsky, J., De Wolf, S., and Ballif, C. (2015). Low-Temperature High-Mobility Amorphous IZO for Silicon Heterojunction Solar Cells. *IEEE Journal of Photovoltaics*, pages 1–8.

[Morales-Masis et al., 2017b] Morales-Masis, M., Rucavado, E., Jeangros, Q., Landuchi, F., Hessler-Wyser, A., and Ballif, C. (2017b). High performance amorphous Zn-Sn-O: impact of composition, microstructure, and thermal treatments in the optoelectronic properties. Number February, page 101050D.

[Morales-Masis et al., 2018] Morales-Masis, M., Rucavado, E., Monnard, R., Barraud, L., Holovský, J., Despeisse, M., Boccard, M., and Ballif, C. (2018). Highly Conductive and Broadband Transparent Zr-doped In2O3 as Front Electrode for Solar Cells. *Journal of Photovolatics*.

[Moss, 1954] Moss, T. S. (1954). The interpretation of the properties of indium antimonide. *Proceedings of the Physical Society. Section B*, 67(10):775.

[Mryasov and Freeman, 2001] Mryasov, O. N. and Freeman, A. J. (2001). Electronic band structure of indium tin oxide and criteria for transparent conducting behavior. *Physical review B*, 64:233111.

[Mullings et al., 2014] Mullings, M. N., Hägglund, C., Tanskanen, J. T., Yee, Y., Geyer, S., and Bent, S. F. (2014). Thin film characterization of zinc tin oxide deposited by thermal atomic layer deposition. *Thin Solid Films*, 556:186–194.

[Narushima et al., 2002] Narushima, S., Orita, M., Hirano, M., and Hosono, H. (2002). Electronic structure and transport properties in the transparent amorphous oxide semiconductor 2CdOGeO2. *Physical Review B*, 66:1–8.

[Nastasi et al., 2014] Nastasi, M., Mayer, J., and Wang, Y. (2014). *Ion beam analysis: fundamentals and applications.* CRC Press Taylor & Francis Group, Boca Raton FL.

[Neil Ashcroft, 1976] Neil Ashcroft, D. M. (1976). *Solid State Physics.* Saunders College, Philadelphia, internatio edition.

[Newhouse et al., 2005] Newhouse, P. F., Park, C.-H., Keszler, D. A., Tate, J., and Nyholm, P. S. (2005). High electron mobility W-doped In2O3 thin films by pulsed laser deposition. *Applied Physics Letters*, 87(11):112108.

[Niedermeier et al., 2017] Niedermeier, C. A., Rhode, S., Ide, K., Hiramatsu, H., Hosono, H., Kamiya, T., and Moram, M. A. (2017). Electron effective mass and mobility limits in degenerate perovskite stannate BaSnO3. *Physical Review B*, 95(16):161202.

[Nogay et al., 2017] Nogay, G., Stuckelberger, J., Wyss, P., Rucavado, E., Allebé, C., Koida, T., Morales-Masis, M., Despeisse, M., Haug, F.-J., Löper, P., and Ballif, C. (2017). Interplay of annealing temperature and doping in hole selective rear contacts based on silicon-rich silicon-carbide thin films. *Solar Energy Materials and Solar Cells*, 173(June):18–24.

[Nomura et al., 2013] Nomura, K., Kamiya, T., and Hosono, H. (2013). Effects of Diffusion of Hydrogen and Oxygen on Electrical Properties of Amorphous Oxide Semiconductor, In-Ga-Zn-O. *ECS Journal of Solid State Science and Technology*, 2(1):P5–P8.

[Nomura et al., 2008] Nomura, K., Kamiya, T., Yanagi, H., Ikenaga, E., Yang, K., Kobayashi, K., Hirano, M., and Hosono, H. (2008). Subgap states in transparent amorphous oxide semiconductor, In–Ga–Zn–O, observed by bulk sensitive x-ray photoelectron spectroscopy. *Applied Physics Letters*, 92(20):202117.

[Orita et al., 2001] Orita, M., Ohta, H., Hirano, M., Narushima, S., and Hosono, H. (2001). Amorphous transparent conductive oxide InGaO 3 (ZnO) m (m< 4): a Zn4s conductor. *Philosophical Magazine Part B*, 81(5):501–515.

[Orton and Powell, 1980] Orton, J. W. and Powell, M. J. (1980). The Hall effect in polycrystalline and powdered semiconductors. Technical report.

[Oyama et al., 1992] Oyama, T., Hashimoto, N., Shimizu, J., Akao, Y., Kojima, H., Aikawa, K., and Suzuki, K. (1992). Low resistance indium tin oxide films on large scale glass substrate. *Citation: Journal of Vacuum Science & Technology A*, 10:1682.

[Özgür et al., 2005] Özgür, Ü., Alivov, Y. I., Liu, C., Teke, A., Reshchikov, M. A., Doğan, S., Avrutin, V., Cho, S.-J., and Morkoç, H. (2005). A comprehensive review of ZnO materials and devices. *Citation: Journal of Applied Physics*, 98:41301.

[Paier et al., 2006] Paier, J., Marsman, M., Hummer, K., Kresse, G., Gerber, I. C., and Ángyán, J. G. (2006). Screened hybrid density functionals applied to solids. *The Journal of Chemical Physics*, 124(15):154709.

[Pankove, 2012] Pankove, J. I. (2012). *Optical processes in semiconductors.* Courier Corporation.

[Pasquarelli et al., 2014] Pasquarelli, R. M., Van Hest, M. F. A. M., Parilla, P. A., Perkins, J. D., O'Hayre, R., and Ginley, D. S. (2014). Processing-phase diagrams: A new tool for solution-deposited thin-film development applied to the In5O(OPri)13-In 2O3 system. *Journal of Materials Chemistry C*, 2(13):2360–2367.

[Patnaik, 2003] Patnaik, P. (2003). *Handbook of inorganic chemicals*, volume 1. McGraw-Hill, Burlington, NJ, 1 edition.

[Peng et al., 2016] Peng, H., Bikowski, A., Zakutayev, A., and Lany, S. (2016). Pathway to oxide photovoltaics via band-structure engineering of SnO. *APL Materials*, 4(10):106103.

[Pisarkiewicz et al., 1989] Pisarkiewicz, T., Zakrzewska, K., and Leja, E. (1989). Scattering of charge carriers in transparent and conducting thin oxide films with a non-parabolic conduction band. *Thin Solid Films*, 174(PART 1):217–223.

[Prakash et al., 2017] Prakash, A., Xu, P., Faghaninia, A., Shukla, S., Iii, J. W. A., Lo, C. S., and Jalan, B. (2017). Wide bandgap BaSnO3 films with room temperature conductivity exceeding 104 S cm&minus;1. *Nature Communications*, 8(May):1–9.

[Preissler et al., 2013] Preissler, N., Bierwagen, O., Ramu, A. T., and Speck, J. S. (2013). Electrical transport, electrothermal transport, and effective electron mass in single-crystalline In2O3 films. *Physical Review B - Condensed Matter and Materials Physics*, 88(8):1–10.

[Proffit et al., 2012] Proffit, D. E., Ma, Q., Buchholz, D. B., Chang, R. P. H., Bedzyk, M. J., and Mason, T. O. (2012). Structural and Physical Property Studies of Amorphous Zn-In-Sn-O Thin Films. *Journal of the American Ceramic Society*, 95(11):3657–3664.

[Rashidi et al., 2013] Rashidi, N., Kuznetsov, V. L., Dilworth, J. R., Pepper, M., Dobson, P. J., and Edwards, P. P. (2013). Highly conducting and optically transparent Si-doped ZnO thin films prepared by spray pyrolysis. *Journal of Materials Chemistry C*, 1(42):6960.

[Robertson et al., 2006] Robertson, J., Xiong, K., and Clark, S. J. (2006). Band gaps and defect levels in functional oxides. *Thin Solid Films*, 496(1):1–7.

[Rucavado et al., 2018] Rucavado, E., Graužinytė, M., Flores-Livas, J. A., Jeangros, Q., Landucci, F., Lee, Y., Koida, T., Goedecker, S., Hessler-Wyser, A., Ballif, C., and Morales-Masis, M. (2018). New route for "cold-passivation" of defects in tin-based oxides. *The Journal of Physical Chemistry C*, 122(31):17612–17620.

[Rucavado et al., 2017] Rucavado, E., Jeangros, Q., Urban, D. F., Holovský, J., Remes, Z., Duchamp, M., Landucci, F., Dunin-Borkowski, R. E., Körner, W., Elsässer, C., Hessler-Wyser, A., Morales-Masis, M., and Ballif, C. (2017). Enhancing the optoelectronic properties of amorphous zinc tin oxide by subgap defect passivation : A theoretical and experimental demonstration. *Physical Review B*, 245204:1–10.

[Sallis et al., 2014] Sallis, S., Butler, K. T., Quackenbush, N. F., Williams, D. S., Junda, M., Fischer, D. A., Woicik, J. C., Podraza, N. J., White, B. E., Walsh, A., and Piper, L. F. J. (2014). Origin of deep subgap states in amorphous indium gallium zinc oxide: Chemically disordered coordination of oxygen. *Applied Physics Letters*, 104(23):2012–2016.

[Schleife et al., 2011] Schleife, A., Varley, J. B., Fuchs, F., Rödl, C., Bechstedt, F., Rinke, P., Janotti, A., and Van de Walle, C. G. (2011). Tin dioxide from first principles: Quasiparticle electronic states and optical properties. *Phys. Rev. B*, 83:035116.

[Schlossmacher et al., 2010] Schlossmacher, P., Klenov, D., Freitag, B., and von Harrach, H. (2010). Enhanced Detection Sensitivity with a New Windowless XEDS System for AEM Based on Silicon Drift Detector Technology. *Microscopy Today*, 18(04):14–20.

[Seto, 1975] Seto, J. Y. W. (1975). The electrical properties of polycrystalline silicon films The electrical properties of polycrystalline silicon films. *Journal of Applied Physics*, 46(1975):5247.

[Sha et al., 2010] Sha, M., Wu, G., Dou, Q., Tang, Z., and Fang, H. (2010). Double-layer formation of [Bmim][PF6] ionic liquid triggered by surface negative charge. *Langmuir : the ACS journal of surfaces and colloids*, 26(15):12667–72.

[Shannon, 1976] Shannon, R. D. (1976). Revised effective ionic radii and systematic studies of interatomic distances in halides and chalcogenides. *Acta Crystallographica Section A*, 32(5):751–767.

[Shard, 2014] Shard, A. G. (2014). Detection limits in XPS for more than 6000 binary systems using Al and Mg Kα X-rays. *Surface and Interface Analysis*, 46(3):175–185.

[Singh et al., 2008] Singh, A. K., Janotti, A., Scheffler, M., and Van de Walle, C. G. (2008). Sources of Electrical Conductivity in SnO2. *Physical Review Letters*, 101(5):055502.

[Sorar et al., 2011] Sorar, I., Saygin-Hinczewski, D., Hinczewski, M., and Tepehan, F. Z. (2011). Optical and structural properties of Si-doped ZnO thin films. *Applied Surface Science*, 257(16):7343–7349.

[Steinhauser, 2009] Steinhauser, J. (2009). *Low pressure chemical vapor deposited zinc oxide for silicon thin film solar cells.* Lulu. com.

[Stjerna et al., 1994] Stjerna, B., Olsson, E., and Granqvist, C. G. (1994). Optical and electrical properties of radio frequency sputtered tin oxide films doped with oxygen vacancies, F, Sb, or Mo. *Journal of Applied Physics*, 76(6):3797–3817.

[Summitt et al., 1964] Summitt, R., Marley, J. A., and Borrelli, N. F. (1964). The ultraviolet absorption edge of stannic oxide (sno_2). *J. Phys. Chem. Solids*, 25(12):1465–1469.

[Sundholm et al., 2012] Sundholm, E. S., Presley, R. E., Hoshino, K., Knutson, C. C., Hoffman, R. L., Mourey, D. A., Keszler, D. A., and Wager, J. F. (2012). Passivation of Amorphous Oxide Semiconductors Utilizing a Zinc-Tin-Silicon-Oxide Barrier Layer. *IEEE Electron Device Letters*, 33(6):836–838.

[Sze, 1981] Sze, S. M. (1981). *Physics of Semiconductor Devices.* John Wiley & Sons, Inc., 2 edition.

[Tanaka et al., 1997] Tanaka, I., Mizuno, M., and Adachi, H. (1997). Electronic structure of indium oxide using cluster calculations. Technical report.

[Tang et al., 2015] Tang, H., Ishikawa, K., Ide, K., Hiramatsu, H., Ueda, S., Ohashi, N., Kumomi, H., Hosono, H., and Kamiya, T. (2015). Effects of residual hydrogen in sputtering atmosphere on structures and properties of amorphous In-Ga-Zn-O thin films. *Journal of Applied Physics*, 118(20):205703.

[Tauc, 1968] Tauc, J. (1968). Optical properties and electronic structure of amorphous Ge and Si. *Materials Research Bulletin*, 3:37–46.

[Thornton, 1974] Thornton, J. A. (1974). Influence of apparatus geometry and deposition conditions on the structure and topography of thick sputtered coatings. *Citation: Journal of Vacuum Science and Technology*, 11:666.

[Tuna et al., 2010] Tuna, O., Selamet, Y., Aygun, G., and Ozyuzer, L. (2010). High quality ITO thin films grown by dc and RF sputtering without oxygen. *Journal of Physics D: Applied Physics*, 43(5):055402.

[Utsumi et al., 2003] Utsumi, K., Iigusa, H., Tokumaru, R., Song, P. K., and Shigesato, Y. (2003). sputtering using high density ceramic targets. *Thin Solid Films*, 445:229–234.

[Van De Walle, 2000] Van De Walle, C. G. (2000). Hydrogen as a cause of doping in zinc oxide. *Physical Review Letters*, 85(5):1012–1015.

[Vogel et al., 1996] Vogel, D., Krüger, P., and Pollmann, J. (1996). Self-interaction and relaxation-corrected pseudopotentials for II-VI semiconductors. *Physical Review B*, 54(8):5495–5511.

[Voyles and Muller, 2002] Voyles, P. M. and Muller, D. A. (2002). Fluctuation microscopy in the STEM. *Ultramicroscopy*, 93(2):147–159.

[Wager et al., 2008] Wager, J. F., Keszler, D. A., and Presley, R. E. (2008). *Devices*. Springer.

[Wahila et al., 2016] Wahila, M. J., Butler, K. T., Lebens-Higgins, Z. W., Hendon, C. H., Nandur, A. S., Treharne, R. E., Quackenbush, N. F., Sallis, S., Mason, K., Paik, H., Schlom, D. G., Woicik, J. C., Guo, J., Arena, D. A., White, B. E., Watson, G. W., Walsh, A., and Piper, L. F. J. (2016). Lone-Pair Stabilization in Transparent Amorphous Tin Oxides: A Potential Route to p-Type Conduction Pathways. *Chemistry of Materials*, 28(13):4706–4713.

[Walsh et al., 2008] Walsh, A., Da Silva, J. L. F., Wei, S.-H., Körber, C., Klein, A., Piper, L. F. J., Demasi, A., Smith, K. E., Panaccione, G., Torelli, P., Payne, D. J., Bourlange, A., and Egdell, R. G. (2008). Nature of the Band Gap of In 2 O 3 Revealed by First-Principles Calculations and X-Ray Spectroscopy. *Physical review letters*.

[Wardenga et al., 2015] Wardenga, H., Frischbier, M., Morales-Masis, M., and Klein, A. (2015). In Situ Hall Effect Monitoring of Vacuum Annealing of In2O3:H Thin Films. *Materials*, 8(2):561–574.

[Warmsingh et al., 2004] Warmsingh, C., Yoshida, Y., Readey, D. W., Teplin, C. W., Perkins, J. D., Parilla, P. A., Gedvilas, L. M., Keyes, B. M., and Ginley, D. S. (2004). High-mobility transparent conducting Mo-doped In2O3 thin films by pulsed laser deposition. *Journal of Applied Physics*, 95(7):3831–3833.

[Warner et al., 2015] Warner, E. J., Johnson, F., Campbell, S. a., and Gladfelter, W. L. (2015). Atomic layer deposition of tin oxide and zinc tin oxide using tetraethyltin and ozone. *Journal of Vacuum Science & Technology A: Vacuum, Surfaces, and Films*, 33:021517.

[Watts and Wolstenholme, 2003] Watts, J. and Wolstenholme, J. (2003). *Introduction to surface analysis by XPS and AES*. Wiley.

[Werner et al., 2018] Werner, J., Niesen, B., and Ballif, C. (2018). Perovskite/Silicon Tandem Solar Cells: Marriage of Convenience or True Love Story? - An Overview. *Advanced Materials Interfaces*, 5(1):1700731.

[Werner et al., 2016] Werner, J., Walter, A., Rucavado, E., Moon, S.-J., Sacchetto, D., Rienaecker, M., Peibst, R., Brendel, R., Niquille, X., De Wolf, S., Löper, P., Morales-Masis, M., Nicolay, S., Niesen, B., and Ballif, C. (2016). Zinc tin oxide as high-temperature stable recombination layer for mesoscopic perovskite/silicon monolithic tandem solar cells. *Applied Physics Letters*, 109(23):233902.

[White et al., 2009] White, M. E., Bierwagen, O., Tsai, M. Y., and Speck, J. S. (2009). Electron transport properties of antimony doped SnO2 single crystalline thin films grown by plasma-assisted molecular beam epitaxy. *Journal of Applied Physics*, 106(9):093704.

[Williams and Carter, 1996] Williams, D. and Carter, C. (1996). *Transmission Electron Microscopy, A Text Book for Materials Science*. Plenum Press, New-York.

[Wolfram-Research-Inc, 2016] Wolfram-Research-Inc (2016). Mathematica.

[Yaglioglu et al., 2006] Yaglioglu, B., Huang, Y.-J., Yeom, H.-Y., and Paine, D. C. (2006). A study of amorphous and crystalline phases in In2O3–10 wt.% ZnO thin films deposited by DC magnetron sputtering. *Thin Solid Films*, 496(1):89–94.

[Yamada et al., 2000] Yamada, N., Yasui, I., Shigesato, Y., Li, H., Ujihira, Y., and Nomura, K. (2000). Donor Compensation and Carrier-Transport Mechanisms in Tin-doped In 2 O 3 Films Studied by Means of Conversion Electron 119 Sn Mössbauer Spectroscopy and Hall Effect Measurements. *Japanese Journal of Applied Physics*, 39(Part 1, No. 7A):4158–4163.

[Yamazoe et al., 1979] Yamazoe, N., Fuchigami, J., Kishikawa, M., and Seiyama, T. (1979). Interactions of tin oxide surface with O2, H2O AND H2. *Surface Science*, 86(C):335–344.

[Yasukawa et al., 1995] Yasukawa, M., Hosono, H., Ueda, N., and Kawazoe, H. (1995). Novel Transparent and Electroconductive Amorphous Semiconductor : Amorphous AgSbO 3 Film. *Japanese Journal of Applied Physics*, 34(2):281 —- 284.

[Zhang and Ma, 1996] Zhang, D. H. and Ma, H. L. (1996). Scattering mechanisms of charge carriers in transparent conducting oxide films. *Applied Physics A Materials Science and Processing*, 62(5):487–492.

[Zhu et al., 2013] Zhu, Q., Ma, Q., Buchholz, D. B., Chang, R. P. H., Bedzyk, M. J., and Mason, T. O. (2013). Structural anisotropy in amorphous SnO2 film probed by X-ray absorption spectroscopy. *Applied Physics Letters*, 103(3):12–16.

[Zhu et al., 2014] Zhu, Q., Ma, Q., Buchholz, D. B., Chang, R. P. H., Bedzyk, M. J., and Mason, T. O. (2014). Structural and physical properties of transparent conducting, amorphous Zn-doped SnO2 films. *Journal of Applied Physics*, 115(3):33512.

Curriculum Vitae

Ph. D. Esteban Rucavado

Swiss permit B
Birth date 24.08.1984
Costarrican
Tel +41(0) 78 935 03 66
erucalea@gmail.com
Rue de la Cotê 47,
Neuchâtel 2000,
Switzerland

EDUCATION

2015-2019	Dr. Physics, Ecole Polytechnique Fédéral de Lausanne
2009-2011	Erasmus Mundus Master Nanoscience and Nanotechnology, KULueven/Chalmers University of Technology
2002-2007	Bachelor in Physics, University of Costa Rica

Technical skills: Thin film science and technology, characterization tools, data analysis and interpretation in terms of fundamental physical phenomena.

Personal skills: Self-motivated, independent, result driven, group-player, strong technical communication, multilingual, entrepreneurial-minded, international experience.

DOCTORAL PROJECT

2015 – present Photovoltaic and thin film electronics laboratory EPFL, Neuchâtel

Design and development of transparent and conductive thin films for applications in optoelectronic devices by sputtering systems, under the supervision of Prof. Christophe Ballif and the co-supervision of Dr. Monica Morales-Masis. The aim of my project is to analyze the optoelectronic properties of In-based and Sn-based transparent and conductive films and describe their behavior in terms of their atomic configuration and microstructure. Next to research activities, I am responsible of maintaining optical and electrical characterization systems, organizing laboratory supplies, recipe development and scheduling of target exchange in deposition systems.

Publications as first author:

- *Enhancing the optoelectronic properties of amorphous zinc tin oxide by subgap defect passivation : A theoretical and experimental demonstration*, *Physical Review B* (2017)
- *New route for "Cold-Passivation" of defects in tin-based oxides. Journal of Physical Chemistry C (2018)*
- *Zr-doped indium oxide: towards ultra-thin, high-performance electrodes*, manuscript in preparation

Special achievements and awards:

- *Best oral presentation* in European MRS Fall meeting 2017 (Symposium N on Advanced oxide materials – growth, characterization and applications).
- *First place* in SciVid Contest in Fall MRS 2017 co-awarded by the production "Let there be light". (1000 USD)
- *First place* in the Business Concept training 2017 – Innosuisse. Co-awarded by the project: "HitMEMS"

WORK EXPERIENCE

2012 – 2015	Lecturer in University of Costa Rica	University of Costa Rica

Teaching entry-level physics for engineering and science students. The aim was to give lectures to prepare students to high-level engineering courses. The topics covered were Newtonian mechanics, thermodynamics, wave dynamics and RC-circuits. Yearly lecturer scores above the department average.

2012 – 2015	Researcher	Center for energy and electrochemistry, University of Costa Rica

Researcher in the project: *Synthesis and characterization of modified nanoparticles by microwave assisted methods*. In this project the objectives were fulfilled and additionally, successful cooperation were stablished with private and state-run companies.

2006 – 2009	Student worker	Intel Corporation, San José, CR

Next to bachelor activities, I was a student-worker in the package quality and reliability department. My work was to support the daily activities and small research projects of the Package Failure analysis group.

Other experience

- “Business concept training - 2018”, Innosuisse-Neuchâtel
- Workshop “Entrepreneurship for physicist and engineers 2014” ICTP, Mexico
- Workshop “Molecular, atomic and optical physics 2007” Balseiro Insitute, Argentina.
- Social service: Main organizer and executer of “A day in Science”, activity for children from social-endangered communities (2013 - 2014).

OTHER SKILLS

- Software
    - Advanced knowledge: Mathematica, LaTeX, Microsoft office, OriginPro.
    - Basic knowledge: Matlab, C++.
- Languages
    - Spanish (Native speaker)
    - English (Academic level)
    - French (Working proficiency)

HOBBIES AND INTERESTS

I am a sports enthusiast: Rugby player (flanker/winger), hiking and trekking, running and snowboarding. I also enjoy cooking, reading and traveling. I am a founder member of Microcity Activity Department that organize activities at the Neuchâtel satellite campus of EPFL, among the activities we organized hiking trips, ski-weekends and cards tournaments.

Ce document a été imprimé au Centre d’impression EPFL,
imprimerie climatiquement neutre, certifiée myClimate.